HABILITATIONSSCHRIFT

# Collective quantum dynamics on a chip

Dmitry Krimer

Institut für Theoretische Physik
Technische Universität Wien
Wiedner Hauptstraße 8-10
1040 Wien
Österreich

Wien, April 2017

# Abstract

Over the past decade various setups in cavity quantum electrodynamics have been studied in terms of their potential for future technologies involving the storage and processing of quantum information. Among different hybrid quantum systems, those based on spin ensembles coupled to single-mode cavities have recently attracted much attention. Whereas it is nowadays possible to reach the regime of strong collective coupling between a cavity and a spin ensemble, necessary for the coherent transfer of quantum information, such hybrid quantum systems still suffer from a significant degree of decoherence resulting from an inhomogeneous broadening inherent in the ensemble. My research focuses on developing various theoretical approaches for understanding the collective non-Markovian dynamics of such non-Hermitian many-body systems aiming at their efficient control, as well as at the suppression of the decoherence induced by the ensemble broadening. Another line of my research deals with the complex quantum dynamics arising when two-level emitters are strongly coupled to a multimode cavity or photonic structures. All of my research is strongly oriented towards future practical realizations in different hybrid quantum systems.

# Contents

# 1 Introduction

Cavity quantum electrodynamic (cQED) is nowadays a rapily developing field whose technological importance cannot be overestimated. The history of cQED can be traced back to a very fundamental question on the interaction between an atom and an electromagnetic field, which is, "How long does it take for an atom in free space to decay back to its ground state once it has been excited by the field?" In 1930, this question was addressed by Weisskopf and Wigner [1], who demonstrated that the atom will not stay in its excited state forever but rather decay due to the interaction with the quantum electrodynamic (QED) vacuum. Moreover, the spectrum emitted by the atom in such a spontaneous decay can be well approximated by a Lorentzian function centered at the atomic transition frequency which additionally exhibits a slight Lamb shift [2]. Later it was realized that the QED vacuum can also be modified so that the local density of photonic states (LDOS) becomes structured in contrast to the simple free-space case. In his landmark paper in 1946, Purcell [3] was the first who discovered the dramatic enhancement of spontaneous emission of magnetic moment transitions if small metallic particles are mixed with a nuclear-magnetic medium. As was revealed in the early 1980s, spontaneous emission can not only be enhanced if the atom is surrounded with a resonant cavity but it can also be inhibited if the cavity has no modes at the transition frequency [4, 5]. Much of the earlier work focused on the resonant coupling to a single cavity mode, while coupling to the rest of the cavity modes was regarded as a parasitic influence and was either discarded or bulked into a total background spontaneous emission rate. Recent trends in experimental work, however, point towards highly complex and spatial open photonic structures, where the delineation between the cavity and the radiative environment becomes highly blurred (see, e.g., [6–8]).

The year 1963 witnessed another very important discovery [9] when Jaynes and Cummings proposed a fully quantized theory of a two-level atom coupled to a single cavity mode and showed that the atom is periodically re-excited in what is known as Rabi oscillations - a coherent exchange of the excitation between the atom and the cavity field. Some years later the quantized theory successfully explained the purely quantum phenomena such as a sequence of revivals and collapses of the Rabi oscillations [10]. The first experimental realization of quantum Rabi oscillations was carried out by Haroche et al., by placing Rydberg atoms in a high Q cavity and strongly coupling the atoms to it, thus establishing the experimental basis for a field that is now known as cQED [11]. Since that time many new techniques have been put forward to overcome the difficulties in trapping and manipulating atoms. A single rubidium atom strongly coupled to a nanoscale photonic crystal cavity [12] or to a whispering-gallery-mode of a bottle microresonator [13] are just a few recent examples.

One important aspect of strong coupling, which is reached when the coupling strength essentially exceeds the total decoherence rate in a system, is that it can be used for coherent information transfer between the electromagnetic field and the atom, which is a very interesting aspect in quantum information science. This technological interest triggered intensive material science studies towards the search for "artificial atoms" with tunable transition frequencies and coupling strengths over a wide range, as well as towards engineering of their environment to enhance the emitter-cavity coupling. Such "artificial atoms" usually possess two states decoupled from all other states, so that they effectively behave as two-level systems and can thus be referred to as quantum bits (qubits), to which quantum information can be encoded. Specifically, a large variety of solid-state qubits in complex photonic nanostructures, based e.g. on quantum dots or nitrogen vacancy centers in diamond (operating at optical frequencies), have been studied very intensively during the last decade (see [14] for a recent review). The most successful artificial systems that have been realized in this context so far are superconducting qubits radiating in the microwave region with controllable magnetic flux, electric charge or phase difference across a nano-fabricated Josephson junction (see the review [15]).

However, the strong emitter-cavity coupling naturally implies strong interactions also with other degrees of freedom leading to the detrimental influence of decoherence that limits the system's coherence times. Furthermore, there is not a single system available which would satisfy all the necessary criteria to build a quantum information processor. For instance, superconducting qubits are believed to be well suited for fast information processing, whereas photons in waveguides represent "flying" qubits valid for long-distance data transmission. Therefore, over the past decade various setups in cQED have been studied in terms of their potential for the storage and processing of quantum information. Particularly attractive in this context are so-called "hybrid quantum systems" (HQS), that conflate the individual advantages of different quantum technologies (see [16] for a recent review). Among recent realizations of such HQS, those based on spin, atomic or even molecular ensembles coupled to superconducting microwave cavities have attracted broad attention (see reviews [17, 18]). In such systems the spin or atomic ensemble plays the role of a quantum memory, to which quantum information is coherently stored and retrieved from at some later time. The cavity, in turn, serves as a quantum bus for the in- and output of information as well as for the coupling between several constituents of such HQS. The technology for building such devices has meanwhile advanced up to the degree that state-of-the-art experiments can be performed on a single superconducting chip, on which the corresponding ensemble is probed through the in- and out-coupling of a microwave field. Other interesting alternatives for HQS are achieved with opto- and nanomechanical systems, which enable the conversion between microwave and optical photons via phonons. Furthermore, they can effectively enhance the long-range interaction between distant spin qubits under certain conditions (see [19] for a recent review).

The most popular physical realizations of ensembles are based, for instance, on negatively charged nitrogen-vacancy (NV) defects in diamond [20–24], rare-earth spin ensembles [25, 26], or clouds of ultracold atoms [27, 28]. Despite the fact that each individual spin is coupled weakly to the cavity, one can nevertheless reach the strong coupling regime due to the large number of spins which are collectively coupled to the cavity mode. This nontrivial physics of cooperative dynamics intrinsically comprises complex collective phenomena such as “superradiance”, which was originally discovered in 1954 in a gas of two-level atoms independently interacting with a common radiation field (see the seminal paper by Dicke [29] and the review [30]). However, the constituents of a large spin ensemble experience different local environments that give rise to an inhomogeneous line broadening. The latter typically acts as the main source of decoherence leading to a drastic decrease of the coherence time, which is known to be the major bottleneck for the processing of quantum information in hybrid quantum technologies.

As a result, various protocols to ensure the controlled and reversible temporal dynamics in the presence of inhomogeneous broadening were recently the subject of many studies. One of the proposed techniques in this context is the so-called controlled reversible inhomogeneous broadening (CRIB) approach [31–33], which is based on a rather subtle preparation method and on the inversion of atomic detunings during the temporal evolution. Most of the techniques developed for this purpose are based on photon-echo type approaches in cavity or cavity-less setups and operate at optical or microwave frequencies, such as those dealing with spin-refocusing [34, 35], with atomic frequency combs (AFC) [36–43], with electromagnetically induced transparency (EIT) [44], with off-resonant Raman atomic transitions [45] or with the concept of impedance matching condition [46–48]. Traditionally, these architectures operate in the optical region and require additional high-intensity control fields. The resulting large number of excitations is prone to spoil the delicate quantum information that is encoded in states with extremely low numbers of excitations. Other sophisticated concepts based on preselecting the optimal spectral portion of the inhomogeneously broadened ensemble also have been proposed [49, 50]. They rely, however, on a strong modification of the intrinsically predefined density profile that is again very challenging to implement experimentally. Very recent studies propose to access long-lived dark or subradiant states in atomic or spin ensembles for efficient information storage [51–55]. Also new setup designs without any inhomogeneous broadening such as those based on magnon modes strongly coupled to a cavity have recently been realized [56, 57]. In this case, however, the gradient memory is characterized by relatively large intrinsic losses which impose limitations on the achievable time span of the revival dynamics. Although modern experiments mentioned above are definitely a step forward towards the realization of efficient memory devices, most of them are operating far from the single quantum excitation regime and still suffer from various limitations. On the other hand, these experiments provide an ideal setting for the observation of a large variety of complex collective nonlinear many-body phenomena on a chip, so that the understanding of their dynamics becomes of central importance both in terms of fundamental research as well as in view of potential future applications.

In my own theoretical work presented here, many of the issues discussed above play an important role, in particular various aspects of quantum non-Markovian dynamics in hybrid quantum systems and their efficient control. The goal of this habilitation thesis is to provide a concise overview of recent results from my research, which are more extensively presented in the appended manuscripts. The predictions and concepts following from my theoretical work can be generally applied to different physical realizations of HQS based on, e.g., rare-earth spin ensembles, ultracold atoms, magnons, ensembles of qubits, etc. coupled to a single-mode cavity or on a single artificial atom simultaneously coupled to a large discrete number of modes in arbitrary photonic structures. In particular, my theoretical concepts and methods have been directed towards the example of one specific experimental realization sketched in Fig. 1, namely a $\lambda/2$ superconducting microwave coplanar waveguide resonator magnetically coupled with a spin ensemble of negatively charged NV centers in diamond.

The corresponding experiments were carried out in the group of Prof. Hannes-Jörg Schmiedmayer and Dr. Johannes Majer from the Institute of Atomic and Subatomic Physics, TU Wien. In the framework of a fruitful collaboration comprising also the group's former PhD students, Dr. Stefan Putz and Dr. Robert Amsüss, as well as the current PhD student, Dipl.-Ing. Andreas Angerer, our predictions have lead to the first experimental realization of the "cavity protection effect" as well as to the realization of a resonant scheme which ensures efficient energy feeding into strongly coupled spin-cavity system [58, 59]. Our recently proposed procedure of burning narrow spectral holes in the spin density at polaritonic positions [54, 60] has meanwhile also been successfully implemented in the experiment [55]. In our very recent joint work [61], we have also revealed nontrivial nonlinear spin-cavity dynamics and critical slowing down of the cavity population and demonstrated a very good agreement between theoretical and experimental results. Many other theoretical predictions summarized in the following sections are waiting for their future experimental confirmation in hybrid quantum systems.

This thesis is organized as follows. In section 2 we briefly present a theoretical framework and some results on non-Markovian dynamics of a single-mode cavity strongly coupled to an inhomogeneously broadened spin ensemble. We also demonstrate how the decoherence induced by the inhomogeneous broadening can be suppressed in the strong-coupling regime [I,II]. Section 3 focuses on the spectral engineering which allows us to substantially suppress the decoherence [III,IV] and to achieve long-lived revival dynamics [V]. The question about optimal control of non-Markovian dynamics will also be addressed in this section [VI]. Section 4 is devoted to the nonlinear phenomena such as an amplitude bistability and critical slowing down of the cavity population for the same system as in previous sections [VII]. Finally, in section 5 we briefly discuss a theoretical framework based on a Green's function technique as well as the main results obtained on non-Markovian quantum dynamics of an emitter inside an open multimode cavity [VIII]. We also present some results on a quantum feedback in a cQED system based on an open cavity coupled to a structured continuum [IX].

I D. O. Krimer, S. Putz, J. Majer, and S. Rotter, "Non-Markovian dynamics of a single-mode cavity strongly coupled to an inhomogeneously broadened spin ensemble", Phys. Rev. A **90**, 043852 (2014).

*Contributions: conceiving the ideas, devising the theoretical framework, performing numerical calculations, writing the manuscript.*

II S. Putz, D. O. Krimer, R. Amsüss, A. Valookaran, T. Nöbauer, J. Schmiedmayer, S. Rotter, and J. Majer "Protecting a spin ensemble against decoherence in the strong-coupling regime of cavity QED", Nature Physics **10**, 720 (2014) **(shared first-authorship)**.

*Contributions: conceiving the ideas, devising the theoretical framework, modelling the experiment, writing the manuscript.*

III D. O. Krimer, B. Hartl, and S. Rotter, "Hybrid quantum systems with collectively coupled spin states: suppression of decoherence through spectral hole burning", Phys. Rev. Lett. **115**, 033601 (2015).

*Contributions: conceiving the ideas, devising the theoretical framework, performing numerical calculations, writing the manuscript.*

IV S. Putz, A. Angerer, D. O. Krimer, R. Glattauer, W. J. Munro, S. Rotter, J. Schmiedmayer, and J. Majer, "Spectral hole burning and its application in microwave photonics", Nature Photonics **11**, 36 (2017).

*Contributions: conceiving the ideas, devising the theoretical framework, modelling the experiment.*

V D. O. Krimer, M. Zens, S. Putz, and S. Rotter, "Sustained photon pulse revivals from inhomogeneously broadened spin ensembles", Laser & Photonics Review **10**, 1023 (2016).

*Contributions: conceiving the ideas, devising the theoretical framework, performing numerical calculations, writing the manuscript.*

VI D. O. Krimer, B. Hartl, F. Mintert, and S. Rotter, "Optimal control of non-Markovian dynamics in a single-mode cavity strongly coupled to an inhomogeneously broadened spin ensemble", Phys. Rev. A **96**, 043837 (2017).

*Contributions: conceiving the ideas, devising the theoretical framework, writing the manuscript.*

VII A. Angerer, S. Putz, D. O. Krimer, T. Astner, M. Zens, R. Glattauer, K. Streltsov, W. J. Munro, K. Nemoto, S. Rotter, J. Schmiedmayer, and J. Majer, "Dynamical Exploration of Amplitude Bistability in Engineered Quantum Systems", Science Adv. **3**, e1701626 (2017).
*Contributions: conceiving the ideas, devising the theoretical framework, modelling the experiment.*

VIII D. O. Krimer, M. Liertzer, S. Rotter, and H.E. Türeci, "Route from spontaneous decay to complex multimode dynamics in cavity QED", Phys. Rev. A **89**, 033820 (2014).
*Contributions: conceiving the ideas, devising the theoretical framework, performing numerical calculations, writing the manuscript.*

IX J. Kabuss, D. O. Krimer, S. Rotter, K. Stannigel, A. Knorr, and A. Carmele, "Analytical Study of Quantum Feedback Enhanced Rabi Oscillations", Phys. Rev. A **92**, 053801 (2015).
*Contributions: interpretation of the results, formulation of the conditions for the asymptotically undamped dynamics.*

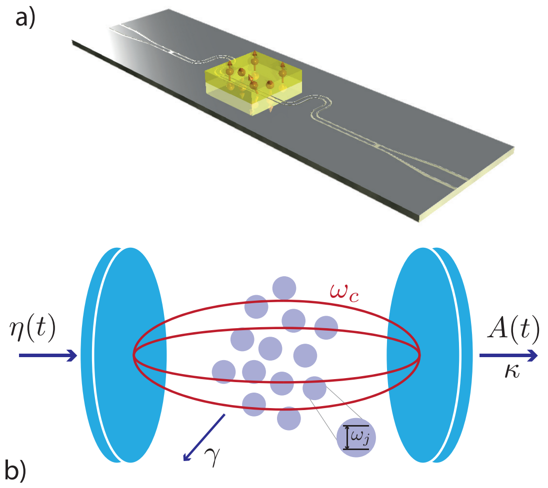

Figure 1. Sketch of the hybrid quantum system:

**(a)** A spin ensemble (yellow) coupled to a transmission-line resonator (gray) confining the electromagnetic field inside a small volume.

**(b)** Scheme of the spin ensemble-cavity coupled system. An incoming signal $\eta(t)$ passes through the cavity characterized by a frequency $\omega_c$ which is coupled to a spin ensemble with each individual spin of frequency $\omega_j$. The transmitted signal is proportional to the cavity amplitude, $A(t)$. $\kappa$ and $\gamma$ stands for the cavity and spin losses, respectively.

## 2 Non-Markovian dynamics of a single-mode cavity strongly coupled to an inhomogeneously broadened spin ensemble

This section gives a brief overview over the main aspects of the temporal dynamics in a HQS consisting of a large spin ensemble coupled with a single-mode cavity via magnetic or electric dipole interaction. We also address an important question arising in the context of possible realizations of coherent-control schemes, which is how the decoherence caused by the inhomogeneous distribution can be suppressed in the strong-coupling regime - a phenomenon known as "cavity protection". Some results on the resonant collective spin-cavity dynamics are also presented.

### 2.1 Theoretical model

The theoretical approach introduced in this section is general, but in what follows it will be compared with one specific experimental realization, namely a $\lambda/2$ superconducting microwave coplanar waveguide resonator magnetically coupled with a spin ensemble of negatively charged NV centers in diamond (see Fig. 1). To account for the spin-cavity dynamics we start from the Tavis-Cummings Hamiltonian ($\hbar = 1$) [62]

$$\mathcal{H} = \omega_c a^\dagger a + \frac{1}{2}\sum_j^N \omega_j \sigma_j^z + i\sum_j^N \left[g_j \sigma_j^- a^\dagger - g_j^* \sigma_j^+ a\right] - i\left[\eta(t) a^\dagger e^{-i\omega_p t} - \eta^*(t) a e^{i\omega_p t}\right], \quad (1)$$

where $a^\dagger$ and $a$ are standard creation and annihilation operators of the single cavity mode with frequency $\omega_c$ and $\sigma_j^+$, $\sigma_j^-$, $\sigma_j^z$ are the Pauli operators associated with each individual spin of frequency $\omega_j$. An incoming signal is characterized by the carrier frequency $\omega_p$ and by the amplitude $\eta(t)$ whose time variation is much slower as compared to $1/\omega_p$. The interaction part of $\mathcal{H}$ is written in the rotating-wave approximation (terms $\propto a\sigma_j^-$, $a^\dagger \sigma_j^+$ are neglected), where $g_j$ stands for the coupling strength of the $j$-th spin. We assume that the distance between spins is large enough such that the dipole-dipole interactions between spins can be neglected.

Although the individual spin coupling strengths $g_j$ are very small, one can nevertheless reach the strong coupling regime due to the large number of spins which are collectively coupled to the cavity mode. The effect of collective coupling is particularly evident when reducing the interaction term to a collective term $\Omega(S^- a^\dagger - S^+ a)$ [63], where the collective spin operators are given by $S^\pm = \Omega^{-1} \cdot \sum_j^N g_j \sigma_j^\pm$. The prefactor $\Omega^2 = \sum_j^N g_j^2$ stands for an effective coupling strength, which scales up a single coupling strength, $g_j$, by a factor of $\sqrt{N}$. Thus, thanks to this collective coupling it becomes possible to reach the strong coupling regime by taking large ensembles (see, e.g., [20, 23] for NV spin ensembles).

Next, one can derive the Heisenberg operator equations, for the cavity and spin operators, $\dot{a} = i[\mathcal{H}, a] - \kappa a$, $\dot{\sigma}_k^- = i[\mathcal{H}, \sigma_k^-] - \gamma \sigma_k^-$, respectively. Here $\kappa$ and $\gamma$ stand for the total dissipative cavity and spin losses. Then, a set of equations for the expectation values (semiclassical approach), $A(t) \equiv \langle a(t) \rangle$ and $B_k(t) \equiv \langle \sigma_k^-(t) \rangle$, can be derived in the frame rotating with the probe frequency $\omega_p$. During the derivations a few simplifications and approximations are used, which are valid for various experimental realizations. One of the main assumptions is the limit of low input powers of an incoming signal, so that the number of microwave photons in the cavity remains small as compared to the total number of spins participating in the coupling. Thus, the Holstein-Primakoff-approximation [64], $\langle \sigma_k^{(z)} \rangle \approx -1$, always holds implying that the spin motion develops in the vicinity of the south pole of the Bloch sphere. Furthermore, the energy of photons of the external bath, $k_B T$, is assumed to be substantially smaller than that of cavity photons, $k_B T \ll \hbar \omega_c$. Therefore, the influence of the external bath on the cavity can be neglected. Another restrictions is that the effective collective coupling strength of the spin ensemble, $\Omega$, satisfies the inequality $\Omega \ll \omega_c$, justifying the rotating-wave approximation. Finally, the spatial size of the spin ensembles is considered to be sufficiently smaller than the wavelength of a cavity mode. With all these simplifications the equations for the cavity and spin amplitudes become

$$\dot{A}(t) = -\left[\kappa + i\Delta_c\right] A(t) + \sum\nolimits_k g_k B_k(t) - \eta(t), \tag{2a}$$

$$\dot{B}_k(t) = -\left[\gamma + i\Delta_k\right] B_k(t) - g_k A(t), \tag{2b}$$

where $\Delta_c = \omega_c - \omega_p$ and $\Delta_k = \omega_k - \omega_p$ are the detunings with respect to the probe frequency.

Owing to the large number of spins within the ensemble, there are a lot of spins in each frequency subinterval around $\omega_s$ which make a non-negligible contribution to the dynamics. One can thus define a continuous spectral density as $\rho(\omega) = \sum_k g_k^2 \delta(\omega - \omega_k)/\Omega^2$, where $\Omega$ is the collective coupling strength introduced above, satisfying the normalization condition $\int d\omega \rho(\omega) = 1$. As it turns out, one should take special care when choosing the functional profile of the spectral distribution for the spin density, $\rho(\omega)$, which describes its inhomogeneous broadening and which plays a crucial role for the dynamics. The specific shape of $\rho(\omega)$ can typically be determined by a careful comparison with the experiment based on stationary [21] or dynamical [59] transmission measurements. In the following a $q$-Gaussian distribution will be used, which phenomenologically describes very well the shape of the spin spectral density in the experiment [59, 65]

$$\rho(\omega) = C \cdot \left[1 - (1-q)(\omega - \omega_s)^2/\Delta^2\right]^{1/(1-q)}. \tag{3}$$

Here $q = 1.39$ and $\rho(\omega)$ is centered around the cavity frequency $\omega_s = \omega_c = 2\pi{\cdot}2.6915$ GHz having a full-width at half maximum $\gamma_q = 2\Delta\sqrt{(2^q-2)/(2q-2)} = 2\pi \cdot 9.4$ MHz. The cavity decay rate, $\kappa/2\pi = 0.4$ MHz (half-width at half-maximum) and the coupling strength $\Omega/2\pi = 8.56$ MHz.

By formally integrating Eq. (2b) with respect to time for the spin expectation values and inserting them into Eq. (2a), one arrives at the following Volterra equation for the cavity amplitude

$$\begin{aligned} \dot{A}(t) = &-[\kappa + i\Delta_c]A(t) + \sum\nolimits_k g_k\, B_k(T_1)\; e^{-[\gamma + i\Delta_k](t-T_1)} - \eta(t) - \\ &\Omega^2 \int_0^\infty d\omega\, \rho(\omega) \int_{T_1}^t d\tau\, A(\tau)\, e^{-[\gamma + i\Delta_\omega](t-\tau)}, \end{aligned} \tag{4}$$

where $\Delta_\omega = \omega - \omega_p$, $B_k(T_1)$ are the initial spin amplitudes at $t = T_1$. Note that the last term in Eq. (4) strongly depends on the exact shape of the spin density distribution $\rho(\omega)$ and is responsible for the non-Markovian feedback of the spin ensemble on the cavity, so that the cavity amplitude at time $t$ depends on all previous events $\tau < t$.

It is worth noting that the above predictions are valid not only in the semiclassical but also in the quantum case, when all spins are initially in the ground state and the cavity mode $a$ contains initially a single photon, $|1, \Downarrow\rangle$. It can be shown that the probability for a photon to reside in the cavity at time $t > 0$, $N(t) = \langle 1, \Downarrow | a^\dagger(t) a(t) | 1, \Downarrow\rangle$, reduces to $N(t) = |\langle 0, \Downarrow | a(t) | 1, \Downarrow\rangle|^2 = |A(t)|^2$, where $A(t)$ is the solution of Eq. (4) with the initial condition $A(t = 0) = 1$ (external drive $\eta(t) = 0$).

### 2.1.1 Integration of the Volterra equation for the cavity amplitude

One can formally integrate Eq. (4) in time and simplify the resulting double integral on the right-hand side by partial integration considering the case when the cavity is initially empty, $A(T_1) = 0$, and all spins are in the ground state, $B_k(T_1) = 0$. To speed up numerical calculations and to make it numerically tractable, the whole time integration can be divided into successive subintervals, $T_n \leq t \leq T_{n+1}$, with $n = 1, 2, ....$ This allows us to derive the recurrence relation for the cavity amplitude for the $n$-th time interval, $A^{(n)}(t)$, which depends on all previous events at $t < T_n$.

Finally, we end up with the following expression for $A^{(n)}(t)$

$$A^{(n)}(t) = \int_{T_n}^{t} d\tau\, \mathcal{K}(t-\tau) A^{(n)}(\tau) + \mathcal{D}^{(n)}(t) + \mathcal{F}^{(n)}(t), \tag{5}$$

where the non-Markovian feedback within the $n$-th time interval is provided by the memory kernel function $\mathcal{K}(t-\tau)$

$$\mathcal{K}(t-\tau) = \Omega^2 \int_{0}^{\infty} d\omega\, \rho(\omega)\, \frac{e^{-[\gamma+i\Delta_\omega](t-\tau)} - e^{[\kappa+i\Delta_c](t-\tau)}}{[\gamma + i\,\Delta_\omega] - [\kappa + i\,\Delta_c]}. \tag{6}$$

The driving term $\mathcal{D}^{(n)}(t)$ in Eq. (5),

$$\mathcal{D}^{(n)}(t) = -\int_{T_n}^{t} d\tau\, \eta^{(n)}(\tau)\, e^{-[\kappa+i\Delta_c](t-\tau)}, \tag{7}$$

includes an arbitrarily shaped, weak incoming-pulse $\eta^{(n)}(t)$, defined in the time interval $[T_n, T_{n+1}]$. The memory contributions from all previous time intervals for $t < T_n$ are given both through the amplitude $A^{(n-1)}(T_n)$ and through the memory integrals $\mathcal{I}^{(n)}(\omega)$, which are contained in the function

$$\mathcal{F}^{(n)}(t) = \Bigg\{ A^{(n-1)}(T_n)\, e^{-[\kappa+i\Delta_c](t-T_n)} + \tag{8}$$

$$\Omega^2 \int_{0}^{\infty} d\omega\, \rho(\omega) \frac{e^{-[\gamma+i\Delta(\omega)](t-T_n)} - e^{-[\kappa+i\Delta_c](t-T_n)}}{[\gamma + i\,\Delta_\omega] - [\kappa + i\,\Delta_c]} \cdot \mathcal{I}^{(n)}(\omega) \Bigg\},$$

where

$$\mathcal{I}^{(n)}(\omega) = \mathcal{I}^{(n-1)}(\omega)\, e^{-[\gamma+i\Delta_\omega](T_n-T_{n-1})} + \int_{T_{n-1}}^{T_n} d\tau\, A^{(n-1)}(\tau)\, e^{-[\gamma+i\Delta_\omega](T_n-\tau)}, \tag{9}$$

In accordance with the initial conditions introduced above at $t = T_1$, $A^{(0)}(T_1) = 0$ and $\mathcal{I}^{(1)}(\omega) = 0$, so that $\mathcal{F}^{(1)}(t)$ vanishes in the first time interval, $\mathcal{F}^{(1)}(t) = 0$ ($T_1 \leq t \leq T_2$).

### 2.1.2 Laplace transformation of the Volterra equation

In order to get insight into all possible dynamical behaviors of our system and to make analytical estimates for different regimes, one can perform a Laplace transform of the Volterra equation (4) (see [58] for more details), which is briefly sketched below. (This approach is relevant for the other sections as well.) Let us assume that all spins are initially in the ground state and the cavity mode $a$ contains initially a single photon, $A(0) = 1$. One can then multiply Eq. (4) by

$e^{-st}$ ($s = \sigma + i\omega$ is the complex variable) and integrate both sides of the equation with respect to time to obtain the expression for the Laplace transform. By performing the inverse Laplace transformation we get the formal solution for the cavity amplitude $A(t)$ which is as follows

$$A(t) = \frac{e^{i(\omega_c - i\gamma)t}}{2\pi i} \int_{\sigma - i\infty}^{\sigma + i\infty} \frac{e^{st} ds}{s + \kappa - \gamma + i\omega_c + \Omega^2 \int_0^\infty \dfrac{d\omega F(\omega)}{s + i\omega}}, \tag{10}$$

where $\sigma > 0$ is chosen such that the real parts of all singularities of $\tilde{A}(s)$ are smaller than $\sigma$. It turns out that the integral in the denominator of Eq. (10) has a jump when passing across the negative part of the imaginary axis leading to the branch cut in the complex plane of $s$. By setting the denominator of the integrand in Eq. (10) to zero, one can derive the equations for simple poles, $s_j = \sigma_j + i\omega_j$. Next, the Cauchy's theorem for closed contours can be applied to evaluate the formal integral (10) and, finally, the following expression for the cavity amplitude is derived

$$A(t) = e^{i\omega_c t} \left\{ \Omega^2 \int_0^\infty d\omega e^{-i\omega t} U(\omega) + \sum_j R_j \right\}, \tag{11}$$

where

$$U(\omega) = \lim_{\sigma \to 0^+} \left\{ \frac{\rho(\omega)}{\left(\omega - \omega_c - \Omega^2 \delta(\omega) + i(\kappa - \gamma)\right)^2 + (\pi \Omega^2 \rho(\omega) + \sigma)^2} \right\}. \tag{12}$$

is the kernel function and

$$\delta(\omega) = \mathcal{P} \int_0^\infty \frac{d\tilde{\omega} \rho(\tilde{\omega})}{\omega - \tilde{\omega}} \tag{13}$$

has the meaning of the nonlinear Lamb shift of the cavity frequency $\omega_c$, which depends on the spin spectral distribution, $\rho(\omega)$. Here $\mathcal{P}$ stands for the Cauchy principal value and $R_j$ is the contribution of poles (if at all existing), the expression for which can be found in [58].

## 2.2 Non-Markovian spin-cavity dynamics

The typical experimental results of the dynamics under the action of rectangular pulse for different values of the probe frequency $\omega_p$ are displayed in Fig. 2. This pulse has a duration substantially longer than the resulting period of damped Rabi oscillations and the inverse of the total decay rate, so that the system sets into a steady state before the signal is turned off. One clearly sees two polaritonic peaks in the structure of the transmission which are split by the Rabi frequency $\Omega_R$. These peaks correspond to two effective eigenstates of the coupled system

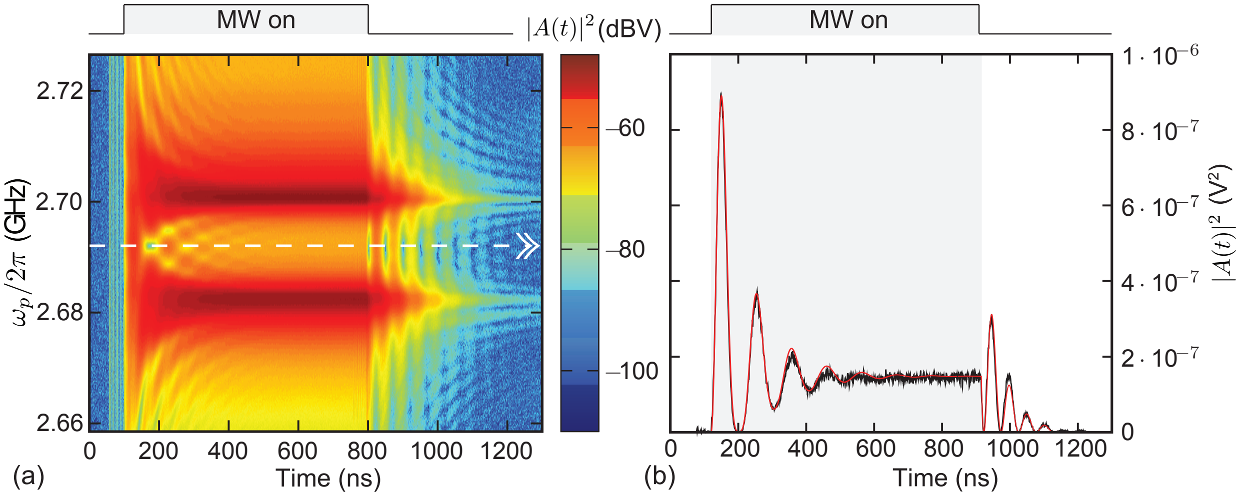

Figure 2. *(adapted from [59]).* **(a)** Time domain measurements of the cavity transmission under the action of a rectangular microwave pulse through the cavity vs. time and probe frequency $\omega_p$ (the spins are on resonance with the cavity, $\omega_s = \omega_c$). The observation of a strong mode-splitting into the two hybridized modes $|\Psi_\pm\rangle \approx \frac{1}{\sqrt{2}}(|0\rangle_c|1\rangle_s \pm |1\rangle_c|0\rangle_s)$ (see dark red enhancements split by the Rabi frequency $\Omega_R/2\pi = 19.2$ MHz) confirm that the system is in the deep strong-coupling regime. **(b)** The dynamics at the resonant probe frequency $\omega_p = \omega_s = \omega_c$ [white dashed line in (a)] is compared with the theoretical prediction for the cavity probability amplitude $|A(t)|^2$ (experiment: black, theory: red). Excellent agreement is achieved when incorporating the $q$-Gaussian shape (3) for the spectral spin distribution.

represented by symmetric and antisymmetric superposition of the cavity and spin eigenstates, $|\Psi_\pm\rangle \approx (|0\rangle_c|1\rangle_s \pm |1\rangle_c|0\rangle_s)/\sqrt{2}$. To accurately describe the collective spin-cavity dynamics, we set up the Volterra integral equation (5) for the cavity amplitude that contains a memory kernel (6) with information about all previous events in the system. Our numerical calculations show an excellent agreement with the experimental results only if the $q$-Gaussian shape (3) for the spin density is taken underlining that a precise knowledge of the inhomogeneous spin distribution is crucial for the understanding of time domain measurements [58, 59]. After turning on and switching off the microwave pulse coherent Rabi oscillations occur between the cavity and the spin ensemble, which are reproduced very accurately including their damping [see Fig. 2(b)]. Interestingly, the first Rabi peak shows a pronounced overshoot after switching off the microwave drive, at which the energy stored in the spin ensemble is coherently released back into the cavity. These oscillations are a hallmark of the non-Markovian character of the system dynamics in the strong-coupling regime.

We have also found a very efficient scheme, which allows us to reach high excitation levels in the spin ensemble with a driving signal that has only limited power to avoid heating up the hybrid quantum device. For that purpose, the cavity is pumped by a pulse whose driving amplitude is periodically modulated with the Rabi period, $2\pi/\Omega_R$, and the driving frequency is kept in resonance, $\omega_p = \omega_c = \omega_s$. Note that at this resonant driving the steady-state Rabi

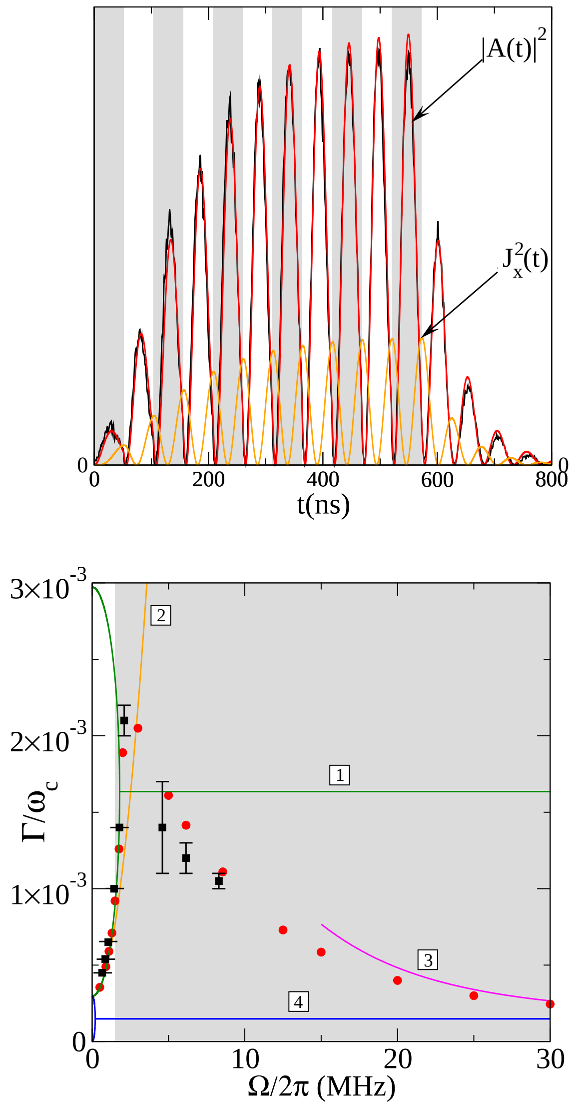

Figure 3. *(adapted from [58, 59])*. **(a)** Resonant dynamics under the action of 11 successive rectangular microwave pulses, phase switched by $\pi$ (alternating gray and white vertical bars). This specific driving corresponds to the largest enhancement of both the cavity amplitude $|A(t)|^2$ and the $x$-component of the collective spin $J_x^2(t)$ which coherently exchange the energy during the course of time. *Red curve*: results of numerical calculations for $|A(t)|^2$. *Orange curve*: results of numerical calculations for $J_x^2(t)$. *Black curve*: $|A(t)|^2$ measured in the experiment. The last white area corresponds to the damped dynamics when the driving signal is switched off.

**(b)** Decay rate $\Gamma$ of the the cavity mode $|A(t)|^2$ versus coupling strength $\Omega$ [58, 59]. *Red curve*: decay rates extracted from the full numerical calculations. *Black symbols*: experimentally observed decay rates. *Green curve (1)*: Decay rate under the assumption of a Lorentzian distribution of the spin density. The overdamped regime ($\Omega/2\pi < 1.8$ MHz) is characterised by two exponents given by $\Gamma = \Delta + \kappa \pm \sqrt{(\Delta - \kappa)^2 - 4\Omega^2}$. The regime of underdamped oscillations ($\Omega/2\pi > 1.8$ MHz) has the constant decay rate, $\Gamma = \Delta + \kappa$. *Orange curve (2)*: $\Gamma$ derived under Markovian approximation, $\Gamma = 2[\kappa + \pi\Omega^2\rho(\omega_s)]$. *Magenta curve (3)*: an estimate for $\Gamma$ within the strong coupling regime with a well-resolved Rabi splitting in the limit of $\Omega \to \infty$, $\Gamma = \kappa + \pi\Omega^2\rho(\omega_s \pm \Omega)$. *Blue curve (4)*: the decay rate in the absence of dephasing.

oscillation amplitude [Fig. 3(a)] exceeds the stationary amplitude reached under the action of a long rectangular pulse [Fig. 2(b)] by two orders of magnitude, although the net power injected into the cavity is exactly the same in both cases. It is worth noting that the cavity and spin ensemble coherently exchange their energy during the course of time, so that the cavity amplitude $|A(t)|^2$ oscillates in antiphase with respect to the spin ensemble component $J_x^2(t)$, see Fig. 3(b).

## 2.3 Total decoherence and the cavity protection effect

In a next step we address an important question arising in the context of possible realizations of coherent-control schemes, which is how to efficiently suppress the decoherence in the spin-cavity dynamics. The total decoherence in the system consists of two major contributions: The first one is due to dissipative cavity losses, while the second one originates from the inhomogeneous broadening of the spin ensemble which leads to the dephasing of spins during the time evolution. Actually, precisely this dephasing mechanism gives the dominant contribution to the decoherence (the spin dissipation $\gamma$ is negligible in our case). Our starting point here is a Laplace transform of the Volterra equation briefly discussed in section 2.1.2 from which we estimate the total rate of decoherence to be

$$\Gamma \approx \kappa + \pi\Omega^2\rho(\omega_s \pm \Omega), \tag{14}$$

also in agreement with a stationary analysis [66]. Thus, the value of $\Gamma$ is determined by the spin density $\rho(\omega)$, evaluated close to the maxima of the two polaritonic peaks, $\omega = \omega_s \pm \Omega$, split by the Rabi frequency $\Omega_R \approx 2\Omega$ due to strong coupling.

It follows from the above estimate that for spectral distributions $\rho(\omega)$ whose tails fall off faster than $1/\omega^2$, an increasing coupling strength inevitably leads to a reduction of the decay rate $\Gamma$, so that the system will finally be protected against decoherence, a phenomenon referred to as "cavity protection effect" [66, 67]. It is not hard to see that our $q$-Gaussian satisfies such a requirement, whereas a Lorentzian spin distribution does not. As a consequence, the latter does not protect the cavity against decoherence, featuring a constant decay rate in the strong coupling regime [see green line in Fig. 3(b)]. To clarify the role played by the non-Lorentzian inhomogeneous broadening, we classify the dynamics by calculating and measuring the total decay rate $\Gamma$ of the cavity amplitude squared, $|A(t)|^2$, from its steady state value for different coupling strengths $\Omega$, see Fig. 3(b). While the maximally reachable value in the experiment already leads to a considerable reduction of $\Gamma$ by 50$\%$ below its maximum, our numerical results for the $q$-Gaussian predict a further reduction of the decay rate with increasing coupling strength by an order of magnitude [see Fig. 3(b)]. It is important to note, that the minimal possible value for the decay rate reached in the limit of large $\Omega$ is $\kappa$ as the decay rate for a bare cavity without diamond is $2\kappa$. This can be explained by the fact that due to the strong coupling between the spin ensemble and the cavity, the excitation is trapped by $50\%$ within the spin ensemble which has a negligible direct decay rate during the course of our experiment.

Physically, the "cavity protection effect" can be understood as follows: In the presence of inhomogeneous spin broadening, the polariton states, defined as superpositions of the cavity mode with the superradiant (bright) spin-wave modes, become coupled to the sub-radiant (dark) spin-wave modes [58, 67]. This coupling acts as the main source of decoherence, leading to a strong damping of the polariton modes. However, for strong enough coupling strength, the Rabi-splitting of the polariton peaks opens up a gap for the super-radiant polaritons. If the spectral profile of the inhomogeneous spin distribution decays sufficiently fast for increasing gap size, an energetic decoupling of the super-radiant polaritons from the sub-radiant spin-wave modes occurs, leading to a suppressed damping of the polaritons and to a corresponding decrease of their peak linewidth.

This section was devoted to the study of the dynamics in a single-mode resonator strongly coupled to a spin ensemble. It is demonstrated that a precise knowledge of the inhomogeneous spin distribution is crucial both for a qualitative and a quantitative understanding of the temporal spin-cavity dynamics. It is also shown how the decoherence from inhomogeneous broadening can be substantially diminished using the "cavity protection effect", resulting in considerably extended coherence times in HQS. However, to fully bring to bear the potential of the "cavity protection" effect discussed above requires going to very high values of the coupling strength, which can be achieved, for example, by increasing the spin concentration within a spin ensemble. An increased spin concentration, however, would cause non-negligible dipole-dipole interactions between spins which spoil the effects under consideration and should be explored separately. Very recently, we proposed a method that circumvents this problem [54], which is the subject of the next section.

## 3 Spectral engineering and optimal control of non-Markovian dynamics

In this section we present an alternative way to overcome the detrimental influence of inhomogeneous broadening and show how to drastically suppress the decoherence reaching the values for the decay rates which lie significantly below the fundamental limit set by the "cavity protection effect". For this purpose we propose a very elementary concept of hole burning into the spin spectral density at judiciously chosen frequencies that requires only a reduced experimental effort. We then demonstrate that engineering the spin spectral density to acquire a comb-like structure leads to coherent revival dynamics and show how to drastically improve the performance of the resulting multimode regime. Finally, we present an efficient optimal control scheme based on Volterra equations and demonstrate the viability of our approach in terms of explicit storage and readout sequences that will serve as a starting point towards the realization of more demanding full quantum mechanical optimal control schemes.

### 3.1 Burning narrow spectral holes close to the polaritonic peaks

We begin our analysis from the analytical estimate (14) for the decoherence rate in the strong coupling regime, $\Gamma \approx \kappa + \pi\Omega^2\rho(\omega_s \pm \Omega)$, and take this relation literally, assuming that the decoherence rate can be strongly suppressed by burning two spectral holes into the spin distribution $\rho(\omega)$ close to the positions of the polaritonic peaks, $\omega = \omega_s \pm \Omega$, such that $\rho(\omega_s \pm \Omega) = 0$. At the same time, the width of the holes has to be chosen very small, such as to remove only a negligible fraction of the spins by the hole burning. It is important to note that for this strategy the precise shape of the spin density distribution plays practically no role since only the values of

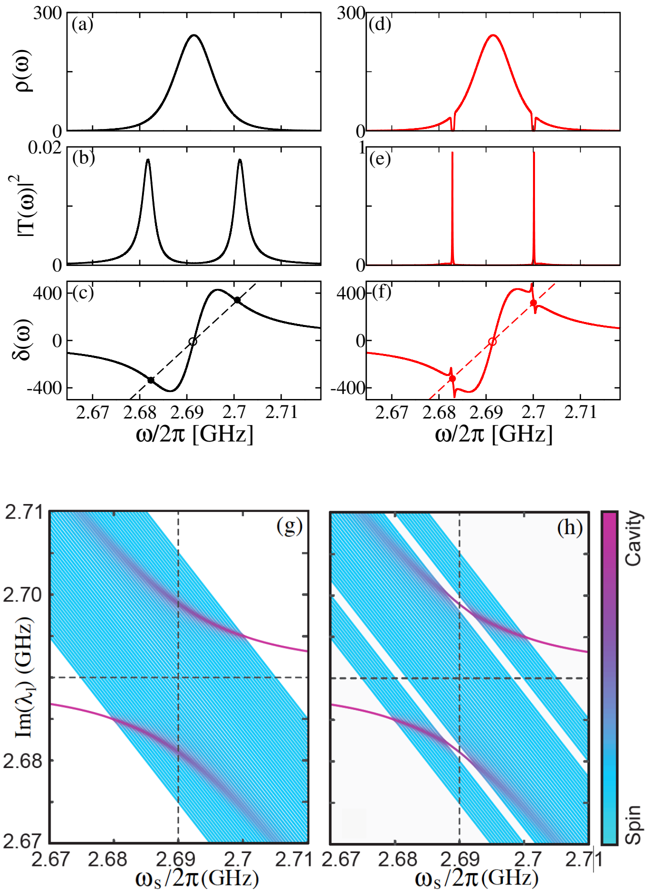

Figure 4. *(adapted from [54, 55])*. Comparison of the cavity coupled to the inhomogeneously broadened spin ensemble without and with hole burning in the spin density profile. Top row: The $q$-Gaussian spin density distribution, $\rho(\omega)$, without [**(a)**] and with hole burning [**(d)**] at $\omega_h = \omega_s \pm \Omega$. Both holes are of equal width. Second row: Transmission $T(\omega)$ without [**(b)**] and with hole burning [**(e)**] in $\rho(\omega)$ (note different $y$-axes scale). Third row: The corresponding nonlinear Lamb shift $\delta(\omega)$. Filled circles label resonance values $\omega_r$ of the transmission $T(\omega)$ occurring at the intersections between the Lamb shift $\delta(\omega)$ and the dashed line $(\omega - \omega_c)/\Omega^2$. At empty circles such intersections are non-resonant.

**(g,h)**: Solution of the eigenvalue problem as a function of the mean spin frequency $\omega_s$ of the spectral density $\rho(\omega)$ shown in (a) and, respectively, in (d). The cavity content, $|A_l|^2$, of the normalised eigenvector, $\psi_l = (A_l, B_l^k)$, versus eigenfrequencies Im$(\lambda_l)$ and $\omega_s$ is represented by the color gradient (color bar on the right in log scale). Two polariton modes in a bath of subradiant states are visible in (g). Spectral hole burning at $\omega_h = \omega_s \pm \Omega$ creates long-lived dark states which become partially visible.

$\rho(\omega)$ at $\omega = \omega_s \pm \Omega$ do contribute to the total decoherence rate.

To demonstrate the efficiency of this approach explicitly, we first perform a stationary analysis of the transmission $T(\omega)$ through the microwave resonator as a function of the probing frequency $\omega$ [by putting $\dot{A}(t) = \dot{B}_k(t) = 0$ into Eqs. (2a,2b)]. This quantity, which is directly accessible in the experiment [58, 59], provides direct access to the occupation amplitude of the cavity [$T(\omega) \propto A(\omega)$]. Assuming $\gamma \to 0$, the transmission $T(\omega)$ acquires the following form,

$$T(\omega) = \frac{i\kappa}{\omega - \omega_c - \Omega^2\delta(\omega) + i[\kappa + \pi\Omega^2\rho(\omega)]}, \tag{15}$$

where $\delta(\omega)$ is the nonlinear Lamb shift given by Eq. (13). In the reference case taken from our previous studies [58, 59], $\rho(\omega)$ is given by Eq. (3) and has no holes, see Fig. 4(a). In this case the transmission $|T(\omega)|^2$ displays the well-resolved double-peak structure typical for the strong-coupling regime, see Fig. 4(b). If one now burns two narrow holes into the spin density at the relevant positions $\omega_h = \omega_s \pm \Omega$, see Fig. 4(d), and reevaluate $|T(\omega)|^2$, a more than 50-fold increase in the corresponding peak values is observed, see Fig. 4(e). This dramatic change is all the more surprising considering that the relative number of spins removed from $\rho(\omega)$ through the hole burning is less than $3\%$.

To understand this behavior it is best to analyze the real and imaginary parts of the denominator of $T(\omega)$, see Eq. (15). For the observed transmission resonances at $\omega = \omega_r$ with a maximum value of $T(\omega_r) = 1$ to occur, two conditions are satisfied simultaneously: (i) $(\omega_r - \omega_c)/\Omega^2 = \delta(\omega_r)$ and (ii) $\rho(\omega_r) = 0$. Consider first condition (i): In the reference case without holes, see Fig. 4(c), the nonlinear Lamb shift $\delta(\omega)$ displays rather smooth variations in the vicinity of the resonant frequencies $\omega_r$, determined by the intersection of $\delta(\omega)$ and a straight line $(\omega - \omega_c)/\Omega^2$. In contrast, for the case with hole burning, see Fig. 4(f), $\delta(\omega)$ exhibits rapid variations around the two resonance points within a very narrow spectral interval. As a consequence, the resultant transmission peaks become substantially sharper. Due to the second condition (ii) they also dramatically increase in height. Note, that no resonance occurs at $\omega = \omega_c$ because $\rho(\omega)$ has a maximum at this point and condition (ii) is strongly violated, see Fig. 4(c),(f). A close examination of the structure of $T(\omega)$ shows, furthermore, that the narrow transmission peaks resultant from the hole burning do not replace the broad polaritonic peaks present in the reference case, but rather get to sit on top of them. As will be seen below, these two different resonance widths in $T(\omega)$ set two different time scales in the dynamics with, in particular, the sharp peaks in the transmission giving rise to an asymptotically slowly decaying dynamics with a strongly suppressed decoherence.

### 3.2 Eigenvalue analysis and the concept of dark states

The physics of spectral hole burning discussed above can be thoroughly understood and most vividly illustrated by solving the eigenvalue problem of our hybrid spin-cavity system and analyzing the resulting spectra. For this purpose one can discretise the spectral spin distribution $\rho(\omega)$ in the frequency domain, which is described by the $q$-Gaussian shape (3), by performing the transformation, $g_j = \Omega \cdot [\rho(\omega_j)/\sum_l \rho(\omega_l)]^{1/2}$, where $\Omega^2 = \sum_j g_j^2$ as before stands for the collective coupling strength. Since in total we deal with a sizable number of spins ($N \approx 10^{12}$), this problem can be made numerically tractable by dividing spins into many subgroups with approximately the same coupling strengths, so that the numerical values for $g_j$ above represent a coupling strength within each subgroup rather than an individual coupling strength. One can then substitute $A(t) = A \cdot \exp(-\lambda t)$, $B_k(t) = B^k \cdot \exp(-\lambda t)$ as well as $\eta(t) = 0$ into Eqs. (2a, 2b) for the cavity and spin expectation values to derive the complex eigenvalue problem for $\lambda$, which can be represented as, $\mathcal{L}\psi_l = \lambda_l \psi_l$, where

$$\mathcal{L} = \begin{pmatrix} \kappa & -g_1 & -g_2 & ... & -g_N \\ g_1 & \gamma + i(\omega_1 - \omega_c) & 0 & ... & 0 \\ g_2 & 0 & \gamma + i(\omega_2 - \omega_c) & ... & 0 \\ ... & ... & ... & ... & ... \\ g_N & 0 & 0 & ... & \gamma + i(\omega_N - \omega_c) \end{pmatrix}, \tag{16}$$

and $\psi_l = (A \quad B_1 \quad B_2 \; ... \; B_N)^T$ being the eigenvector which represents the collective spin-cavity excitation belonging to the eigenvalue $\lambda_l$.

The results of the corresponding numerical calculations are presented in Fig. 4(g,h), where the cavity content, $|A_l|^2$, of the normalized eigenvector $\psi_l$ is plotted as a function of the mean frequency $\omega_s$ of $\rho(\omega)$ and the calculated collective eigenfrequency Im$(\lambda_l)$ for two cases, without [Fig. 4(g)] and with hole burning [Fig. 4(h)]. In the absence of hole burning, one can clearly observe two polaritonic peaks in the structure of the spectrum, which are shown by purple colour in Fig. 4(g). Additionally, there is a major number of pure spin eigenvectors colored in blue in the same figure, which contain a negligibly small amount of cavity content. As a result, these states are decoupled from the cavity being not accessible by transmission spectroscopy and are, therefore, referred to as dark states - a concept that was originally introduced as a particular state of a three-level atom driven by two fields, which cannot absorb or emit photons [68]. However, as a result of hole burning a certain amount of these collective dark states acquire a significant cavity content [Fig. 4(h)], so that the cavity can "decay" into any of these states, and as a result, they become visible. It is worth noting that the decay rates of such engineered dark states are bounded from below just by a single spin decay rate $\gamma$ and, in fact, can be substantially smaller than the dissipation rate of the bare cavity $\kappa$, since in our system the inequality, $\gamma \ll \kappa$, always holds (see also the next section).

### 3.3 Dynamics in the presence of hole burning

To reach our ultimate goal of understanding the influence of the spectral hole burning on the resultant dynamics, we now study the time evolution of $A(t)$ governed by the Volterra equation (4) explicitly for the resonant case $\omega_p = \omega_c = \omega_s$. To prove that all predictions are valid not only in the semiclassical but also in the quantum case, the case when all spins are initially in the ground state and the cavity mode $a$ contains initially a single photon, $|1, \Downarrow\rangle$, is considered. The probability for a photon to reside in the cavity at time $t > 0$, $N(t) = \langle 1, \Downarrow | a^\dagger(t) a(t) | 1, \Downarrow \rangle$, reduces to $N(t) = |\langle 0, \Downarrow | a(t) | 1, \Downarrow \rangle|^2 = |A(t)|^2$, where $A(t)$ is the solution of Eq. (4) with the initial condition $A(t = 0) = 1$ and $B_k(t = 0) = 0$ (external drive $\eta(t) = 0$). For the case without hole burning this solution is represented by the damped Rabi oscillations [see Fig. 5(a)]

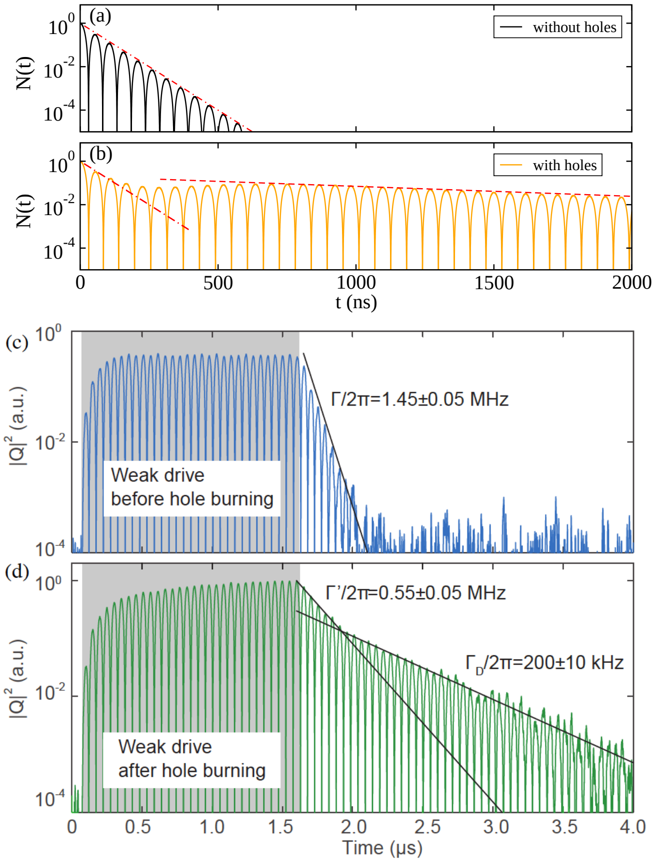

Figure 5. *(adapted from [54, 55]). Theory*: Decay of the cavity occupation $N(t) = \langle 1,\downarrow|a^\dagger(t)a(t)|1,\downarrow\rangle$ from the initial state, for which a single photon with frequency $\omega_c$ resides in the cavity and all spins are unexcited. The asymptotic decay $Ce^{-\Gamma t}$ with and without hole burning (see red lines) is determined by the constants $\Gamma/2\pi = 3\,\text{MHz}$ in (a) and a drastically reduced $\Gamma = 0.42\kappa = 2\pi \cdot 0.17\,\text{MHz}$ in (b). The holes in $\rho(\omega)$ have a width $\Delta_h/2\pi = 1.4\,\text{MHz}$ and are burnt at $t = 0$ at $\omega_h = \omega_s \pm \Omega$.

*Experiment*: (c) Linear dynamical response for a sinusoidally modulated weak pulse. (d) The substantially improved coherence time is shown by probing the system as in (c), but $5\mu$s after spectral holes are burnt at $\omega_s/2\pi \pm 9.6$ MHz with a band width $\Delta/2\pi = 235$ kHz and the cavity was emptied.

found already previously (see section 2.2). By burning narrow holes in $\rho(\omega)$ at $\omega_h = \omega_s \pm \Omega$ (immediately before $t = 0$)[1], one observes very similar transient dynamics, which is followed, however, by a crossover to Rabi oscillations with a much slower asymptotic decay [see Fig. 5(b)].

Quite remarkably, the total decay rate $\Gamma$ in this asymptotic time limit turns out to be substantially smaller than the fundamental limit of half the bare cavity decay rate $\kappa$ set by the recently proposed "cavity protection effect" (see section 2.3). Apparently a new type of physics is at work here being directly related to the emergence of long-lived engineered dark states introduced in the previous section, which are characterized by a decay rate substantially smaller than $\kappa$. (Note that the main requirement for our theory to be applied is that the losses exhibited by each individual constituent in the ensemble, $\gamma$, are substantially smaller as compared to the bare cavity decay rate, $\kappa$, which is well fulfilled here.) From the mathematical point of view such a slow asymptotic behavior can also be associated with the contribution of two poles in the Laplace transform of Eq. (11), which appear when the holes in $\rho(\omega)$ reach a critical depth. The pole contributions also stabilize the long-time behavior when the holes are shifted away from the polaritonic peaks

---

[1] Experimentally, our approach was implemented [55] by modulating the high-intensity harmonic field that drives the cavity at its resonance frequency with a sum of two sinusoidal envelopes with spectral components near the polaritonic positions, $\eta(t) \sim \sin(\pm\Omega_R t/2)\cdot\exp(-i\omega_c t)$, i.e., the result is a drive at polaritonic frequencies, $\omega_c \pm \Omega_R/2$. When being strong enough in intensity this two-frequency drive will eventually excite all spins in the ensemble at these frequencies to a mixture between ground and excited state. As a result, these spins will be effectively removed from the coupling process with the cavity and a further application of the weak resonant driving signal, $\eta(t) \sim \exp(-i\omega_c t)$ cannot change this balance. Thus, it is equivalent to saying that we have burned two holes into the spin distribution located at $\omega_c \pm \Omega_R/2$.

[54], but the optimal hole positions remain close to the polaritonic peaks. Note that despite the considerable photon loss $(N(t) \ll 1)$ for long times the phase coherence is very well preserved here, a clear signature of which is the stable form of the Rabi oscillations. In this way a high "visibility" can be achieved that is needed for the efficient processing of quantum information [38].

In Fig. 5(c,d) we present the experimental results [55] for the case when the system is driven with a weak ($<10^{-5}$ photons per spin) sinusoidally modulated pulse. In the absence of spectral holes the unchanged system decay rate $\Gamma/2\pi \sim 1.45\,$MHz is observed after switching off the driving tone, see Fig. 5(c). Applying a hole burning pulse, and waiting 5 $\mu$s after the signal has decayed, the system is probed again. After the weak probe pulse is switched off, different decay rates are clearly distinguishable in the Rabi oscillations, see Fig. 5(d). At first a reduced decay rate, $\Gamma'/2\pi \sim 550\,$kHz, is observed due to the created spectral holes and reduced damping of the bright polariton modes. This first decay is followed by a crossover to a second much slower decay, $\Gamma_D/2\pi \sim 200\,$kHz, featuring long-lived Rabi oscillations as the hallmark of the created dark states. Furthermore, by burning four spectral holes at special positions [55] it is possible to create multiple pairs of dark states, such that two revivals in the Rabi oscillations appear (not shown here), which is a clear signature of the coherent dark states beating against each other. This is a first step towards the realization of a solid-state microwave frequency comb, in which one could ideally address up many long lived dark states in one polariton mode.

### 3.4 Photon pulse revivals from inhomogeneously broadened spin ensembles

The above concept of hole burning is rather general and also applicable to more sophisticated cases - it will thus be referred to as spectral engineering of the spin density [60]. In this section we demonstrate how to overcome the problem of decoherence by burning well-placed holes into the comb-shaped spectral spin density leading to spectacular performance in the multimode regime. The resulting multimode dynamics is ideally suited for the purpose of developing efficient memory elements due to a constructive rephasing of spins in the ensemble and a collective coherent reemission of the stored information at predetermined moments of time.

Starting point of our analysis is an arrangement of several inhomogeneously broadened spin ensembles coupled to a single cavity mode with frequency $\omega_c$. The spin ensembles are assumed to be prepared with mean frequencies that are equidistantly spaced at intervals of $\Delta\omega$, such that $\omega_s^{(\mu)} = \omega_c \pm n_\mu \Delta\omega$, resulting in a comb-shaped spectral density $F(\omega)$. While this approach is general we will be referring in the following to one particular experimental realization based on magnetic coupling of NV-ensembles residing in several diamonds coupled to a superconducting microwave resonator. Note that by an appropriate aligning of the diamonds with respect to an external magnetic field and by exploiting the Zeeman effect, the mean frequencies of the

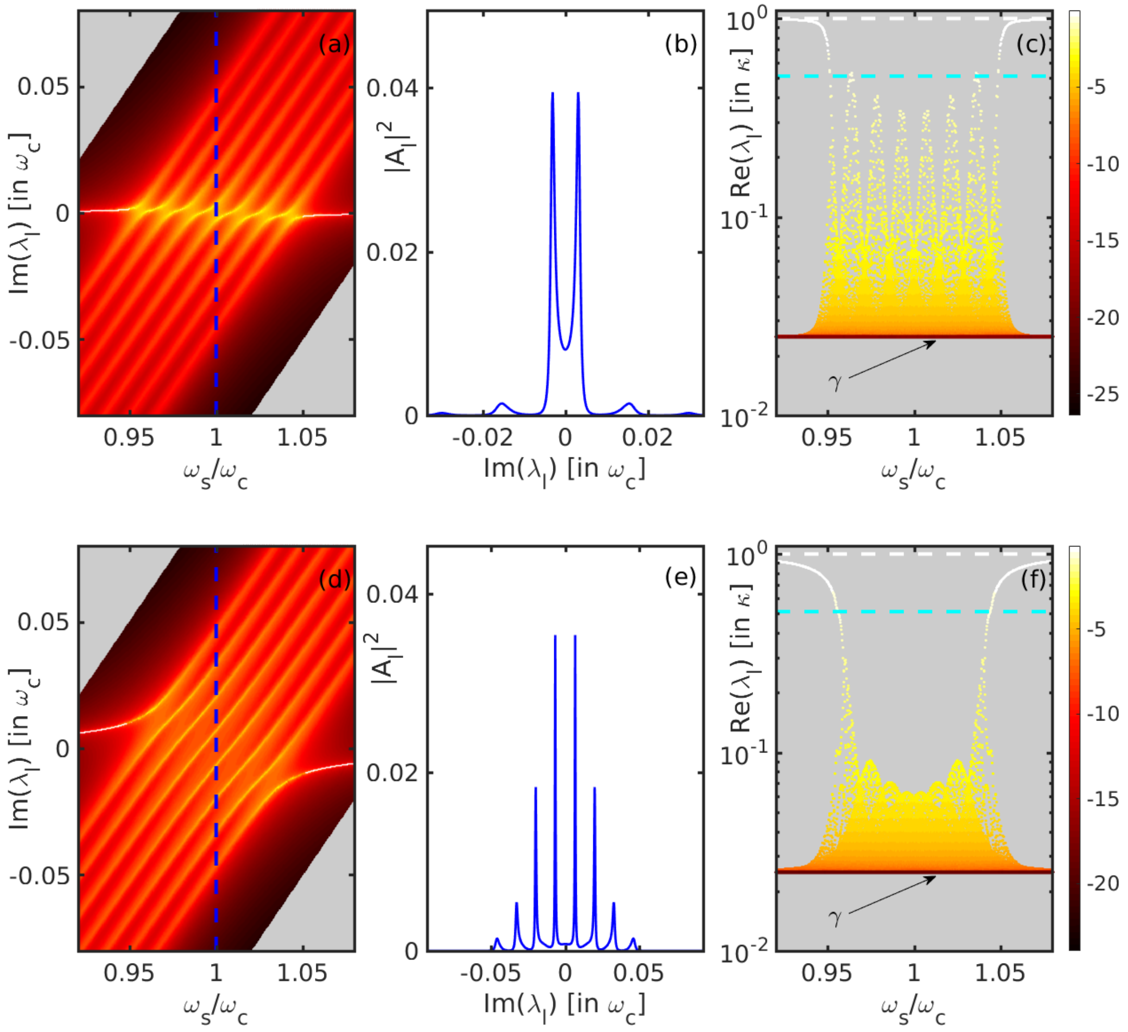

Figure 6. *(taken from [60])*. *Upper row*: **Single-mode strong coupling regime**. Solution of the eigenvalue problem at $\Omega/2\pi = 8\,\text{MHz}$ as a function of the mean spin frequency $\omega_s$ of the spectral function $F(\omega) = \sum_{\mu=1}^{M} \Omega_\mu^2/\Omega^2 \cdot \rho_\mu(\omega)$, consisting of seven equally spaced $q$-Gaussians [given by Eq. (3)] of equal width, $\gamma_q/2\pi = 9.4\,\text{MHz}$. $F(\omega)$ has peaks at frequencies $\omega_s^{(\mu)} = \omega_c \pm n_\mu \Delta\omega$ with the spacing, $\Delta\omega/2\pi = 40\,\text{MHz}$. The cavity frequency $\omega_c$ coincides with the mean frequency of the central $q$-Gaussian, $\omega_s = \omega_c = 2\pi \cdot 2.6915\,\text{GHz}$. Spin ensembles have coupling strengths distributed as $\Omega_\mu^2/\Omega^2 = \exp[-(\omega_c - \omega_s^{(\mu)})^2/2\sigma_G^2]$, with $\sigma_G/2\pi = 150\,\text{MHz}$.
(a) The cavity content, $|A_l|^2$, of the normalised eigenvector, $\psi_l = (A_l, B_l^k)$, versus eigenfrequencies Im($\lambda_l$) and $\omega_s$ is represented by the color gradient (color bar on the right in log scale): two prominent polariton modes are clearly distinguishable from a bath of dark states at fixed value of $\omega_s$. (b) the cavity content $|A_l|^2$ versus Im($\lambda_l$) for the resonant case, $\omega_s = \omega_c$, along the vertical cut shown in (a) (dashed blued line). (c) $|A_l|^2$ versus decay rates, Re($\lambda_l$), and $\omega_s$ with the same coloring as in (a). Cyan dashed line: the minimally reachable decay rate achieved due to the cavity protection effect, $\Gamma/2 \approx \kappa/2$ (limit of $\gamma \ll \kappa$), with $\kappa = 2\pi \cdot 0.4\,\text{MHz}$ (HWHM of the cavity decay) and $\gamma = 2\pi \cdot 0.01\,\text{MHz} \ll \kappa$ (HWHM of the spin decay). White dashed line: decay rate of a bare cavity mode, $\kappa$.
*Lower row*: **Multimode strong coupling regime**. Solution of the same eigenvalue problem as above, but for an increased coupling strength $\Omega/2\pi = 26\,\text{MHz}$ (notation and colors are the same as in the upper row). Eight polariton modes are clearly distinguishable with an almost equidistant spacing, see (e) for the resonant case, $\omega_s = \omega_c$. In all calculations $N = 1200$ spins were used.

spin ensembles, $\omega_s^{(\mu)}$, can be efficiently tuned in a rather wide spectral interval [20, 21]. Let us first investigate how the eigenvalues and the corresponding eigenstates of this hybrid cavity-spin system look like using the method described in sec. 3.2. For this purpose one can derive and solve numerically the non-Hermitian eigenvalue problem $\mathcal{L}\psi_l = \lambda_l\psi_l$, with $\psi_l = (A_l, B_l^k)^T$ being the eigenvector which represents the collective spin-cavity excitation belonging to the eigenvalue $\lambda_l$. Note that Im$(\lambda_l)$ plays the role of the collective eigenfrequency and Re$(\lambda_l) > 0$ is the rate at which $\psi_l$ decays. When solving this eigenvalue problem one always has to keep the same shape for the spectral function $F(\omega)$ but shift the whole structure in the frequency domain by detuning the mean spin frequency $\omega_s$ of the central ensemble with respect to the cavity $\omega_c$. The only other variable parameter is the value of the collective coupling strength $\Omega$, that is tuned from the limit where the cavity mode is strongly coupled solely to the central spin subensemble to the regime of "multimode strong coupling".

The results of numerical calculations are presented in Fig. 6 where the cavity content, $|A_l|^2$, of the normalized eigenvector, $\psi_l$, is displayed as a function of $\omega_s$ and the calculated collective eigenfrequency Im$(\lambda_l)$ [(a),(d)] or decay rate Re$(\lambda_l)$ [(c),(f)]. We begin with the regime where the value for the coupling strength of each spin ensemble separately is large enough to ensure strong coupling to the cavity. In this "single-mode strong coupling limit" one observes an avoided crossing in Fig. 6(a) whenever the resonance condition with the $\mu$-th ensemble is met, $\omega_s^{(\mu)} = \omega_c$. The other off-resonant spin ensembles in turn give rise to a small dispersive contribution only. The most pronounced avoided crossing is observed when the cavity is at resonance with the central spin ensemble, $\omega_s = \omega_c$, where two symmetric polaritonic peaks in the structure of $|A_l|^2$ occur, see Fig. 6(b). It is also seen from Fig. 6(c) [yellow symbols] that a large fraction of eigenstates, $\psi_l$, decays with some intermediate values of the decay rate which lie within the interval $\gamma <$ Re$\lambda_l < \kappa$. (Here $\kappa$ and $\gamma \ll \kappa$ are the dissipative cavity and spin losses, respectively.) This can be explained by the fact that such eigenvectors represent an entangled spin-cavity state, where both the cavity and spin contents are essentially nonzero.

With a further increase of the coupling strength, the distance between two polaritonic peaks depicted in Fig. 6(b), which is approximately as large as $2\Omega$, increases and the peak line shapes become substantially sharper (not shown). Such a peak narrowing can be attributed to the "cavity protection effect" (see sec. 2.3). At even larger values of $\Omega$ the usual form of the avoided crossings eventually disappears, being replaced instead by a comb-shaped structure with parallel stripes characterised by a large cavity content, see yellow curves in Fig. 6(d). Such a picture is, however, valid only for moderate values of detuning of $\omega_s$ from $\omega_c$, whereas for large detuning we are in the dispersive regime [see Fig. 6(d,f)]. A comb-shaped structure of $|A_l|^2$ with almost equally spaced polaritonic peaks is clearly seen at resonance, $\omega_s = \omega_c$, indicating the multimode strong coupling between all spin ensembles and the cavity mode [see Fig. 6(e)].

The shapes of $|A_l|^2$ versus Im($\lambda_l$) at $\omega_s = \omega_c$ for both the multimode and the single-mode strong coupling regime reproduce exactly the corresponding shapes of the kernel function $U(\omega)$ obtained in the framework of the Laplace transform technique sketched in sec. 2.1.2. Thus these two alternative concepts represent two sides of the same coin: all complex features which appear in the structure of the eigenvalue spectrum displayed in Fig. 6 are correspondingly reflected in the properties of the kernel function (12) and the nonlinear Lamb shift (13) (see also [60] for more details).

### 3.4.1 Suppression of decoherence in the multimode strong-coupling regime

The narrow peaks in the frequency domain displayed in Fig. 6(e) are exactly those that are responsible for the pulsed emission in the time domain (see [60] for details). Next, we explore the question of how to suppress the decoherence in the multimode strong-coupling regime [60]. For this purpose one can take advantage of the strategy [54] introduced in sec. 3.1, that for single-mode strong-coupling the decoherence induced by the spin broadening can be strongly suppressed simply by burning two narrow spectral holes in the spin spectral density close to the maxima of the two polaritonic peaks as shown here in Fig. 6(b). The working principle of this effect is based on the creation of long-lived collective dark states (see sec. 3.2) in the spin ensemble that only have very little cavity content and may thus even outperform the ultimate limit for the decoherence rate of the cavity protection effect given by $\Gamma = \kappa$ for $\gamma \ll \kappa$ [54]. (Note that the decay rate for a bare cavity without spin ensembles coupled to it is $2\kappa$.) Mathematically, this effect can also be associated with rapid variations of the nonlinear Lamb shift around the holes' positions and with contribution of poles in the Laplace transform of the Volterra equation derived above [54].

The most natural extension of this hole-burning approach to the multimode regime would demand that the positions of the burnt spectral holes remain close to the polaritonic peaks of which we observe altogether eight in Fig. 6(e), corresponding to the seven spin-subensembles. It was therefore proposed [60] to burn eight narrow spectral holes into the spectral distribution $F(\omega)$ at frequencies which correspond to the maxima of the cavity content, $|A_l|^2$, shown in Fig. 6(e) (or, equivalently, to the maxima of the Laplace transformed kernel function $U(\omega)$, see sec. 2.1.2). This hole burning is essentially a nonlinear process, which can not be captured by the Volterra equation, but the system dynamics may very well be described right after the holes have been burnt. For this purpose one can directly integrate the Volterra equation (4) numerically in time, resulting in the time evolution for both the quantum and the semiclassical case, which looks qualitatively very similar for both cases (see Fig. 7, where the results for the semiclassical case are presented only). For these results the holes are assumed to be burnt at $t = 0$ keeping their shape during the whole time interval shown in Fig. 7, a property which is well-fulfilled in recent

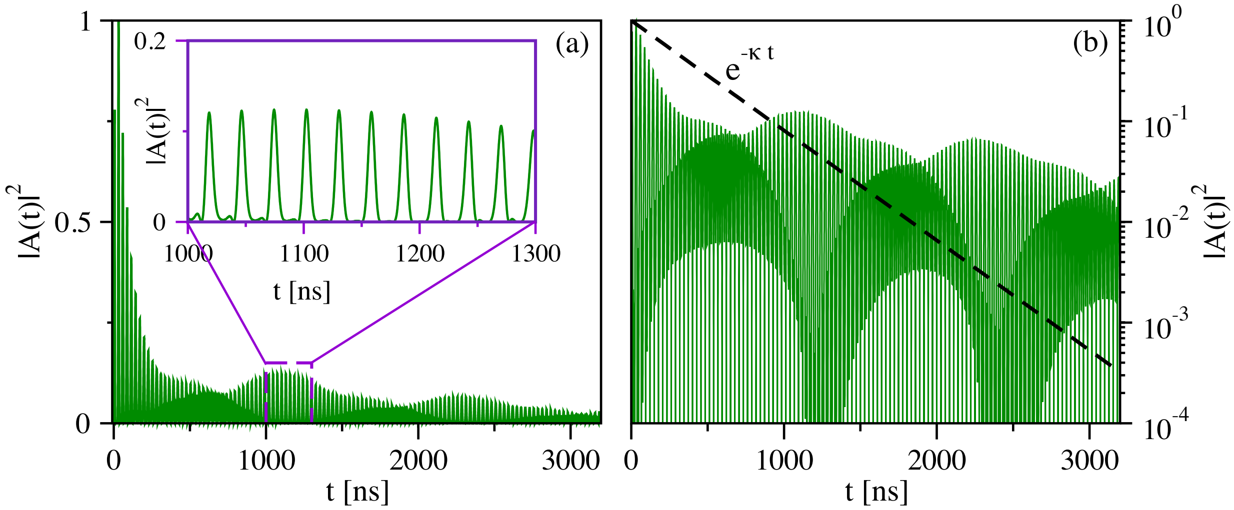

Figure 7. *(taken from [60]).* (a) Cavity probability amplitude $|A(t)|^2$ versus time $t$ under the action of an incident short rectangular pulse of duration $6$ ns after eight holes are burnt at $t = 0$ close to the eight polaritonic peaks depicted in Fig. 6(e). The distance between temporal peaks (revival time) is, $T_{rev} \approx 2\pi/\Delta\omega$, where $\Delta\omega$ is the spacing in a comb-shaped spectral density $F(\omega)$. (b) Same as (a) with the ordinate plotted on a logarithmic scale. The decay process with the minimal decay rate reachable by the cavity protection effect, $e^{-\kappa t}$, with $\kappa/2\pi = 0.4$ MHz is depicted by the dashed line (limit of $\gamma \ll \kappa$). The decay rate of $|A(t)|^2$ for a bare cavity without spin ensembles coupled to it is given by $e^{-2\kappa t}$ (not shown).

experiments where the hole lifetime was estimated to be as large as $27\,\mu$s [55].

Most importantly, it is very clearly seen in Fig. 7 that the pulsed emission from the spin ensemble, which is characterized by the revival time, $T_{rev} \approx 2\pi/\Delta\omega$, persists over a drastically increased time interval as compared to the corresponding case without hole burning (not shown). This suppression of decoherence is not only a quantitative improvement, but it breaks the barrier achievable when making maximal use of the “cavity protection effect”. To illustrate this explicitly, in Fig. 7(b) the results from Fig. 7(a) are replotted on a logarithmic scale and compared with the minimal exponential decay $e^{-\kappa t}$ of the fully cavity-protected ensemble. It turns out that the probabilities $|A(t)|^2$ for the photon pulse revivals significantly exceed this barrier such that, e.g., at $t \sim 3\,\mu s$ after the driving pulse, the values for $|A(t)|^2$ are two orders of magnitude above those achievable through cavity-protection.

In summary we presented a novel approach to suppress the decoherence in quantum memories based on inhomogeneously broadened spin ensembles coupled to a cavity. The main idea of the proposed hole burning technique is, as the name indicates, to burn narrow spectral holes in the spin density at the polaritonic peak positions through the cavity or from the outside. After such a preparatory step, the quantum information (as stored, e.g., in a qubit [23]) may be transferred through the cavity bus to the spins from where it is reemitted back into the cavity at periodic time intervals in the form of Rabi oscillations or pulsed revivals without requiring any further refocusing techniques.

## 3.5 Optimal control of non-Markovian dynamics

Having understood in detail the spin-cavity dynamics and how to efficiently suppress the decoherence caused by inhomogeneous broadening, we now take advantage of these findings and move on to another important question related to the optimal control of the information stored into and retrieved from a spin ensemble. In this context it is worth noting that owing to the tight field confinement inside a cavity, one can achieve a better storage and retrieval efficiency as compared to cavity-less setups [37, 38]. Another advantage of using a cavity is that the phase initially encoded in the cavity amplitude is very well preserved during the course of time, a clear signature of which is the stable form of the Rabi oscillations and pulsed revivals which we observed so far. Furthermore, in contrast to established echo techniques [34–40, 69] our scheme only involves low-intensity write and readout signals and therefore diminishes the influence of noise caused by writing and reading pulses. We develop a very efficient semiclassical optimization technique [70] based on a set of Volterra integral equations similar to those in Eq. (4), which allows us to write information into a spin ensemble coupled to a single cavity mode by means of optimized microwave pulses and to retrieve it at some later time in the form of well-separated cavity responses. The applicability of this approach is also demonstrated in conjunction with a previously described spectral hole-burning technique that allows us to reach storage times going far beyond the dephasing time of the inhomogeneously broadened ensemble.

The aim is to look at the transfer of states from the cavity to the spin ensemble, its storage over a well-defined period of time, and its transfer back to the cavity. Our control scheme thus consists of a *write* and *readout section*, with a variable *delay section* in between. Starting from a polarized state with all spins in their ground state, we construct (i) two write pulses $\eta^{(W)}_{|0\rangle}(t)$ and $\eta^{(W)}_{|1\rangle}(t)$ that encode the respective logical states $|0\rangle$ and $|1\rangle$ in the spin ensemble. During the *delay section* (ii) the information is subject to dephasing by the inhomogeneous ensemble broadening and the external drive is optimized here to reduce the cavity amplitude $A(t) \equiv \langle a(t) \rangle$ (to prevent the information in the spin ensemble from leaking back to the cavity prematurely). In the *readout section* (iii) the readout pulse $\eta^{(R)}(t)$ is switched on that maps the two logical states of the spin ensemble on two mutually orthogonal states of the cavity field. Note that the write pulses (i) are specific for the input states $|0\rangle$ and $|1\rangle$, but pulses (ii) and (iii) are generic as they are designed without prior knowledge of the information stored in the ensemble. The goal of the work [70] was to find optimal time-dependent choices for the write and readout pulses, such that the resulting cavity responses have minimal temporal overlap in analogy to time-binned qubits where information is stored in the occupation amplitudes of two well distinguishable time bins [37, 71].

A typical result of this optimization using the standard method of Lagrange multipliers (first

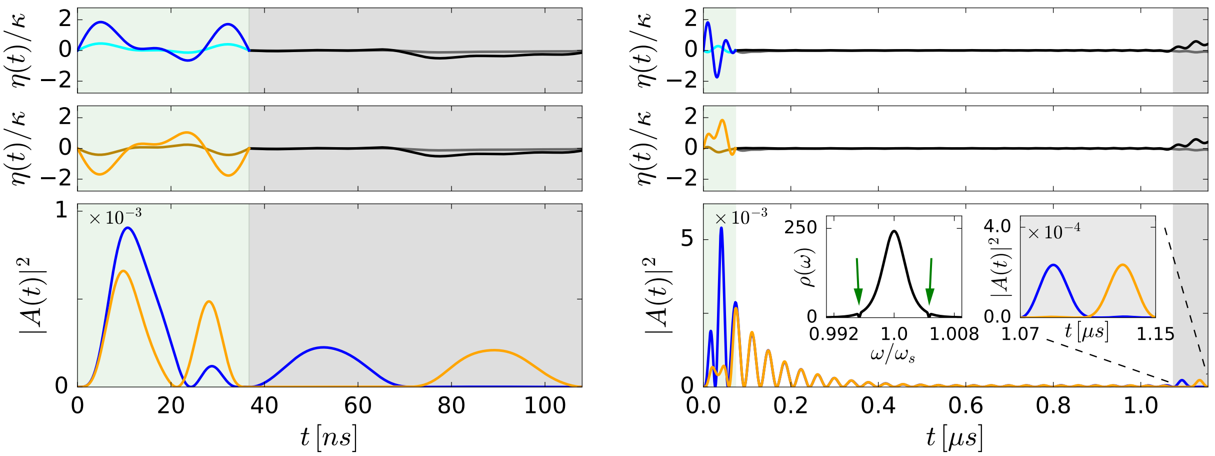

Figure 8. *(taken from [70]).* Preparation of the spin ensemble configurations, $|0\rangle$ and $|1\rangle$, for a spin density following a $q$-Gaussian distribution (3) with $q = 1.39$ centered around the cavity frequency $\omega_s = \omega_c$ and a full-width at half maximum $\gamma_q/2\pi = 9.4\,\text{MHz}$. This form for $\rho(\omega)$ was established in our previous studies by a careful comparison with the experiment [59, 65]. *Right column:* two holes were burnt into $\rho(\omega)$ at frequencies $\omega_s \pm \Omega$ (green arrows in the inset) to suppress decoherence [54, 55] and to make room for a delay section [white area] between the write [green area] and readout [gray area] sections. *First/second row*: real [blue/orange] and imaginary parts [cyan/brown] of the optimized write pulse $\eta^{(W)}_{|0/1\rangle}(t)$ for state $|0/1\rangle$ and of the generic readout pulse $\eta^{(R)}(t)$ [black and gray]. *Third row:* $|A(t)|^2$ for the resulting non-overlapping cavity responses $A^{(R)}_{|0\rangle}(t)$ [blue] and$A^{(R)}_{|1\rangle}(t)$ [orange]. The carrier frequency of all pulses, $\omega_p = \omega_c = 2\pi \cdot 2.6915\,\text{GHz}$, and the coupling strength $\Omega/2\pi = 12.5\,\text{MHz}$. The ratio of the powers between the readout and write pulses is 0.068 (0.013) for the case without (with) hole burning. The amplitudes of all pulses are presented in units of $\kappa/2\pi = 0.4\,\text{MHz}$.

without a delay section) is depicted in Fig. 8 (left column), where the amplitudes of all optimized pulses as well as those of the resulting cavity responses are depicted. One can indeed see that the two different configurations stored in the spin ensemble, $|0\rangle$ and $|1\rangle$, are retrieved by the same readout pulse in the form of two well-separated cavity responses. The storage efficiency can be quantified in terms of the ratio of integrated cavity amplitudes during the readout and write section, which turns out to be $\approx 40\,\%$ for the configurations $|0\rangle$ and $|1\rangle$ shown in Fig. 8 (left column). One can then incorporate the hole burning scheme introduced before in the present analysis, which leads to an increase of the dephasing time from $1/\Gamma \sim 75\,\text{ns}$ [the case shown in Fig. 8 (left column)] to microsecond time scales [see Fig. 8 (right column)] for which one can now meaningfully introduce a delay section in between the write and the readout section. In Fig. 8 (right column) we show that with parameters taken from recent experiments [55] one can extend the storage time and thereby the method's temporal range of control beyond one micro-second.

With these long coherence times one can now store coherent superpositions of the two spin configurations, $|0/1\rangle$. Those can be created by the corresponding superposition $\eta^{(W)}(t) = \alpha \cdot \eta^{(W)}_{|0\rangle}(t) + \beta \cdot \eta^{(W)}_{|1\rangle}(t)$ of the respective write pulses, and, ideally, the corresponding superposition of time-binned cavity responses would be observed under the application of the readout pulse $\eta^{(R)}(t)$. As it turns out, however, the cavity response induced by the readout pulse imposes the constraint, $\alpha + \beta = 1$, to retrieve an appropriate superposition of cavity outputs [70]. Together with the normalization $|\alpha|^2 + |\beta|^2 = 1$ this implies that for the amplitudes $\alpha_x = 1 - x \pm i\sqrt{x(1-x)}$ and $\beta_x = x \mp i\sqrt{x(1-x)}$ with $x \in [0, 1]$ the desired cavity response will be obtained. As a result, the proposed storage sequence does not only work for the two basis states $|0/1\rangle$, but, indeed for a one-dimensional set of coherent superpositions, such as for a rebit [71, 72]. Quite remarkably, when being only interested in reading out the parameters $\alpha$ and $\beta$ (and not in further processing the resulting cavity response) one is not restricted by the above rebit parametrization, but has the full qubit parameter space at one's disposal [70].

In summary, we present here an efficient optimization technique applicable to different experimental realizations based on an inhomogeneously broadened spin ensemble coupled to a single cavity mode. Generalizing this scheme to the full quantum-mechanical level is the obvious next step to make our protocol an essential building block for the development of future optimal control schemes with the perspective of advancing the storage capabilities for quantum information.

## 4 Spin-cavity nonlinear dynamics on a chip

In our previous sections many new and exciting physics of the non-Markovian spin-cavity dynamics was obtained in the framework of a linear integral Volterra equation for the cavity amplitude. This approach has a restricted validity being applicable only in the limit of weak driving powers, when the Holstein-Primakoff-approximation is justified [64], so that the spin motion develops in the vicinity of the south pole of the Bloch sphere. Arbitrary spin deviations are definitely a new degree of freedom, which considerably enrich the resulting dynamics and can give rise to new dynamical behaviours potentially interesting for novel types of coherent-control schemes. Therefore, a next logical line of research consists in the generalization of our theory such that it will allow us to describe the large spin deviations from its initial unexcited state. In this section we briefly present the results on bistability and nonlinear dynamics of a spin ensemble strongly coupled to a single mode cavity driven by external pulses [61]. The resulting dynamics is described in the framework of Maxwell-Bloch equations and the effect of inhomogeneous broadening of the spin ensemble is treated as in the previous sections. We also discuss the effect of a critical slowing down of the cavity population which lasts for a very long time, a timescale many orders of magnitude longer than the longest time scale associated with the system.

## 4.1 Theoretical model

In general, to describe the temporal spin-cavity dynamics in the presence of inhomogeneous broadening, allowing for large spin deviations from their unexcited states, one can begin with a quantum master equation for the spin-cavity density matrix of the following form, $d\rho/dt = -i\,[\,\mathcal{H},\rho\,] + \mathcal{L}_D(\rho)$. Here $\mathcal{H}$ stands for the Tavis-Cummings Hamiltonian (1) and $\mathcal{L}_D(\rho)$ is the Lindblad operator which accounts for the system-environment interaction and can be represented in the following form,

$$\mathcal{L}_D(\rho) = \kappa\,(2a\rho a^\dagger - a^\dagger a\,\rho - \rho\,a^\dagger a) + \gamma_h \sum_{j=1}^{N} (2\sigma_j^-\,\rho\,\sigma_j^+ - \sigma_j^+\sigma_j^-\,\rho - \rho\,\sigma_j^+\sigma_j^-) + \gamma_p \sum_{j=1}^{N} (\sigma_j^z\rho\,\sigma_j^z - \rho\,).$$

Here we explicitly distinguish between two different time scales, $T_2 = 1/\gamma_\perp$ and $T_1 = 1/\gamma_\parallel$ (where $\gamma_\perp = \gamma_h + 2\gamma_p$ and $\gamma_\parallel = 2\gamma_h$), associated with nonradiative dephasing of the spins (fast process) and their spontaneous decay (slow process), respectively. Using this formalism, one can derive a first-order ordinary differential equation (ODE) for the expectation value of any operator $\hat{O}$, which is given by, $d\langle\hat{O}\rangle/dt = \text{Trace}\Big(-i[\,\hat{O},\mathcal{H}\,]\rho + \hat{O}\mathcal{L}_D(\rho)\Big)$. However, a set of equations for the spin and cavity expectation values, $\langle a\rangle$, $\langle\sigma_j^-\rangle$ and $\langle\sigma_j^z\rangle$, will not form a closed set of ODEs because it will contain the second-order expectation values like $\langle\sigma_j^- a^\dagger\rangle$ etc. Thus, it would be necessary to derive equations for $\langle\sigma_j^- a^\dagger\rangle$, which will, in turn, depend on the third-order correlations of spin and cavity operators and so on. In other words, to solve this problem exactly one should solve in general an infinite hierarchy of equations. To close the resulting system of ODEs the remaining higher-order correlations will be approximated by means of the lower-order ones using the so-called generalized cumulant expansion method [73–75]. The problem is drastically simplified if a complete factorization between cavity photons and the spin ensemble is assumed, i.e. when the expressions like $\langle\sigma_j^- a^\dagger\rangle$ are assumed to factorize into $\langle\sigma_j^-\rangle\langle a^\dagger\rangle$. After carefully analyzing the correlation properties between cavity photons and the spin ensemble, one can indeed conclude that this approximation is very well fulfilled for a large spin ensemble driven by a coherent signal.

Thus, using this mean-field approximation, $\langle\sigma_j^- a^\dagger\rangle \approx \langle\sigma_j^-\rangle\langle a^\dagger\rangle$, a set of first order ODEs can be derived, which is formally equivalent to the well known Maxwell-Bloch equations [76]:

$$\begin{aligned}
\dot{a} &= -\kappa a + \sum\nolimits_j g_j\sigma_j^- + \eta \\
\dot{\sigma}_j^- &= -\left(\gamma_\perp + i\Theta_j\right)\sigma_j^- + g_j\sigma_j^z a \\
\dot{\sigma}_j^z &= -\gamma_\parallel\left(1+\sigma_j^z\right) - 2g_j\left(\sigma_j^- a^\dagger + \sigma_j^+ a\right),
\end{aligned} \tag{17}$$

where from now on all symbols are used for the corresponding expectation values rather than for the operators. If not specified otherwise, all notations and parameters are the same as in

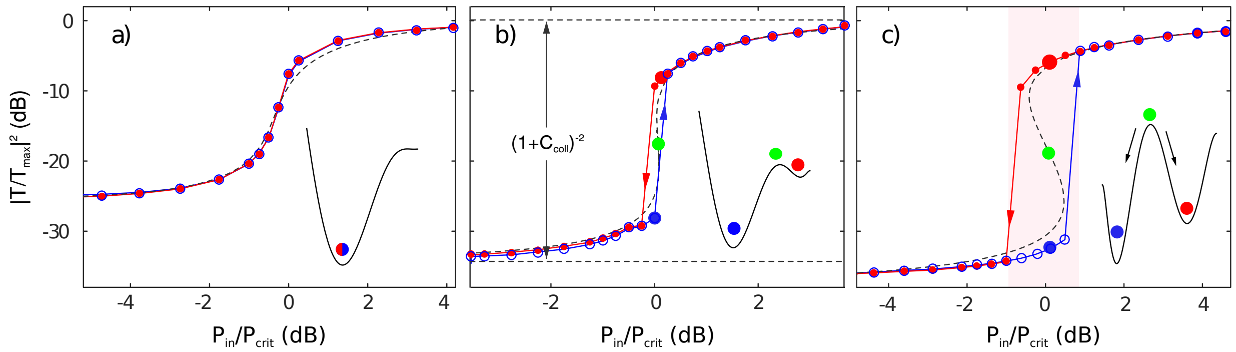

Figure 9. *(taken from [61]).* Steady state bistability transmission measurements through the cavity as a function of increasing (blue) and decreasing (red) input power $\mathrm{P_{in}}$. In (a) the transmission measurements are plotted for the cooperativity value $C_{\mathrm{coll}} \approx 18$ and $\kappa/2\pi = 1.2\,$MHz using two subensembles in resonance with the cavity. (b) The same transmission measurement with $C_{\mathrm{coll}} \approx 49$ and $\kappa/2\pi = 0.44\,$MHz. A small bistablity area is visible where no steady states exist and the system jumps from one steady state to the other. (c) The same measurement as in (a) with an increased cooperativity of $C_{\mathrm{coll}} \approx 78$ (by using all four NV subensembles in resonance with the cavity), again with $\kappa/2\pi = 0.44\,$MHz. The dashed curves: numerical solutions of Eqs. (18). Dashed lines in (b): asymptotic solutions in the limit of large and small driving amplitudes $\eta$. Two critical values of $\eta$, at which a jump between two stable branches occurs, are characterized by a saddle-node bifurcation. For all three cases also a sketch of the corresponding potential is depicted that shows the occurrence of either one or two stable solutions (red and blue symbols) and one unstable solution for (b,c) (green symbol) at a fixed value of $\eta$.

the previous sections. The relaxation rates are ordered as $\kappa > \gamma_\perp \gg \gamma_\parallel = 10^{-4}\,$Hz, such that the spin inversion is by far the slowest process. $\Theta_j$ are frequency detunings with respect to the ensemble central frequency to account for inhomogeneous broadening and numerical values for $g_j$ represent a coupling strength within each subgroup by dividing the $q$-Gaussian into many frequency subintervals as it is done in sec. 3.2. Setting the time derivatives to zero, one gets the following steady state solution,

$$|a|^2=\frac{\eta^2}{\kappa^2}\left(1-\sum\nolimits_j C_j\sigma_j^z\right)^{-2},\quad \sigma_j^z=-\left(1+\frac{4g_j^2|a|^2\gamma_\perp}{\gamma_\parallel(\gamma_\perp^2+\Theta_j^2)}\right)^{-1}, \tag{18}$$

where the dimensionless parameter $C_j = g_j^2/\left[\kappa\gamma_\perp\left(1+\Theta_j^2/\gamma_\perp^2\right)\right]$ is the single spin cooperativity. The collective system cooperativity is given accordingly by $C_{\mathrm{coll}} = \sum_j C_j$.

## 4.2 Amplitude bistability and quench dynamics

First, the steady state bistable behavior is searched for in the experiment [61] by measuring the transmitted intensities through the cavity defined by $|\mathrm{T}|^2 = \mathrm{P_{out}}/\mathrm{P_{in}}$ as a function of the input drive intensity $\mathrm{P_{in}} \approx \eta^2/\kappa$ and outgoing intensity $\mathrm{P_{out}} \approx |a|^2\,\kappa$. The drive power is raised in a stepwise manner, slow enough to allow the system to reach a steady state for each stimulus $\mathrm{P_{in}}$. For weak driving pulses the intra-cavity intensity is not sufficient to saturate the spin ensemble ($\sigma_j^z \sim -1$) and is thus given by $|a|^2 \approx \frac{\eta^2}{\kappa^2}\frac{1}{(1+C_{\mathrm{coll}})^2}$. As the power level increases, the cavity field

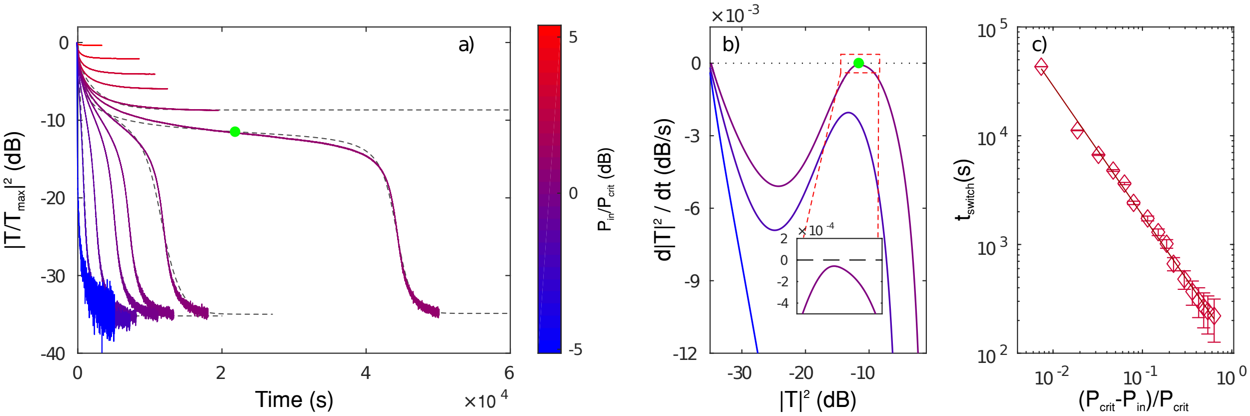

Figure 10. (taken from [61]). Quench dynamics for high cooperativity $C_{\text{coll}} \approx 78$. In (a) the intra-cavity intensity $|\mathrm{T}|^2/|\mathrm{T}_{\max}|^2$ is plotted vs. time for different drive intensities, where the time to reach a steady state strongly depends on the input intensity. For drive intensities larger than a critical drive value $\mathrm{P}_{\text{crit}}$ (defined as the power where the system undergoes the phase transition from the lower to the upper branch, see Fig. 9) the spin ensemble remains saturated and a system sets into a state lying on the upper branch, whereas in the opposite case it starts to collectively decay into a state lying on the lower branch. Close to the critical drive $\mathrm{P}_{\text{crit}}$ the transient dynamics is extremely enchanced and approaches $4 \cdot 10^4$ s. The dashed curves are numerical solutions of Eqs. (17) (see [61]). In (b) the phase diagram, $\mathrm{d}|\mathrm{T}|^2/\mathrm{d}t$ vs. $|\mathrm{T}|^2$, is shown for the decay towards a steady state (black dotted line) for different input drivings $\mathrm{P}_{\text{in}}$. For driving powers close to $\mathrm{P}_{\text{crit}}$ the derivative $\mathrm{d}|\mathrm{T}|^2/\mathrm{d}t$ approaches the values close to zero resulting in very slow transient dynamics. The switching time between the upper and lower branch is displayed in (c) as a function of the distance to $\mathrm{P}_{\text{crit}}$. Close to the critical drive the switching time diverges, and the time to reach a steady state becomes arbitrarily long. The solid red line is a fitting function of the form $t_{\text{switch}} \sim |\mathrm{P}_{\text{in}} - \mathrm{P}_{\text{crit}}|^{-\alpha}$ (with $\alpha = 1.2$).

bleaches the spins ($\sigma_j^z \approx \sigma_j^- \sim 0$) such that the Rabi-splitting vanishes and the spin system decouples from the cavity. The intra-cavity intensity $|a|^2 \approx \frac{\eta^2}{\kappa^2}$ is that of an empty cavity from which spins are completely decoupled. We identify the power level for which the transition between both cases occurs at the critical drive $\mathrm{P}_{\text{crit}}$.

This nonlinear saturation behavior is a necessary precursor for the observation of amplitude bistability. However, whether or not it is observable in the experiment is determined by the system's collective cooperativity. This is apparent from Eq. (18), where larger cooperativity values result in stronger nonlinearity and thus in a larger phase seperation. In Fig. 9 we present steady state bistability measurements for three cooperativity values $C_{\text{coll}} = 18, 49, 78$. The lowest value $C_{\text{coll}} = 18$ does not show bistability [Fig. 9(a)], but increasing the cooperativity up to $C_{\text{coll}} = 49$ leads to the onset of bistable behavior [Fig. 9(b)]. With further increase of the cooperativity, a very pronounced amplitude bistability within a 2dB range shows up [see Fig. 9(c) for $C_{\text{coll}} \approx 78$]. This steady state bistability behavior is well reproduced by numerical calculations when the effect of inhomogeneous broadening is taken into account [dashed lines in Fig. 9(a-c)].

Having obtained such a clear evidence of the amplitude bistability, one can focus next on the temporal behavior of the hybrid system exploring the quench dynamics. Here the system is prepared in a certain initial steady state in which the spin ensemble is completely saturated and constantly driven with $\mathrm{P}_{\mathrm{in}} \gg \mathrm{P}_{\mathrm{crit}}$. Then, the driving power is abruptly switched to a lower driving level and the system transmission is monitored. The measurements are repeated several times, by preparing the system always in the same initial state and switching driving powers to different lower values. When the system is driven close to the bifurcation point ($\mathrm{P}_{\mathrm{in}} \approx \mathrm{P}_{\mathrm{crit}}$) the timescales needed to settle in a stationary state become as long as $4 \cdot 10^4$ s (see Fig. 10). Such a behavior is referred to as critical slowing down [77].

This dynamical behavior can also be described in the framework of Maxwell-Bloch equations (17), which predict that the system features two fixed points at which a saddle-node bifurication occurs. A branch with unstable solutions connects two stable branches, one being weakly driven, with de-excited and ordered spins, and the other one being strongly driven, with unordered and saturated spins [see Fig. 9(c)]. Starting from the strongly driven upper branch with a large intracavity intensity, the saturated spin system ($\sigma_j^z \approx \sigma_j^- \sim 0$) is entirely decoupled from the cavity. This prohibits collective decay into the cavity leaving the extremely small longitudinal relaxation rate $\gamma_{\|}$ as the dominant decay channel. In the opposite limit of drive intensities much smaller than the critical value, the spin system starts to collectively decay through the cavity early on with a rate much larger than $\gamma_{\|}$ and no critical slowing down is observed.

At the critical driving intensity, the saturation due to the drive and decay of the spin system are equal and opposite in effect allowing an everlasting decay to occur without the system reaching its fixed point. If however, the drive intensity is slightly smaller than the critical drive, one observes a critical slowing down of the decay, but eventually the collective decay in the system prevails leading to a buildup of spin correlations, and, eventually, to a faster decay of the spins as well as the cavity population. This behavior is demonstrated in Fig. 10(a-c) where close to a critical drive the system evolves towards the upper unstable fixed point, with a time derivative that can approach zero arbitrarily closely [inset in Fig. 10(b)]. Small deviations from the critical drive lead to a speed up in decay until the system relaxes to a stable steady state. The time it takes to go from the upper to the lower branch diverges close to the critical drive according to $t_{\mathrm{switch}} \sim |\mathrm{P}_{\mathrm{in}} - \mathrm{P}_{\mathrm{crit}}|^{-\alpha}$ with $\alpha \sim 1.2$, as shown in Fig. 10(c). This algebraic divergence is characteristic for nonlinear systems exhibiting saddle-node bifurications [78]. One can also find here a very good agreement between measurements and numerical numerical solutions of Eqs. (17) [see Fig. 10(a)].

In conclusion, we have shown how a hybrid system composed of a superconducting resonator coupled to a spin ensemble in diamond can be used to explore amplitude bistability in new regimes of cQED, with unusual decay rates where the spin life-time is much longer than other decay constants in the system. We have demonstrated a critical slowing down of the cavity population which is of the order of ten hours, a timescale several orders of magnitude longer

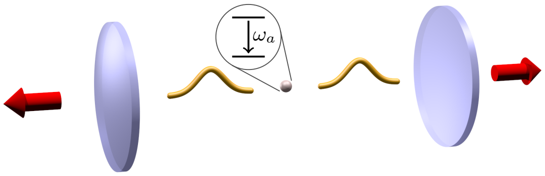

Figure 11. Two-level system (TLS) with transition frequency $\omega_a$ inside an open cavity.

than that observed so far for this effect. In our future studies we intend to go beyond the semiclassical thermodynamic limit governed by the Maxwell-Bloch equations and investigate the mesoscopic case with a moderate number of spins. This regime is very interesting from the technological perspective and is realized e.g. in metamaterials [79, 80] based on an ensemble of superconducting qubits for which the role of quantum correlations becomes stronger as compared to the semiclassical case. From the fundamental point of view it is very important to explore a non-trivial route from a few body- to many-body physics on a chip.

## 5 Non-Markovian quantum dynamics of an emitter inside an open multimode cavity

Up until now, we discussed many interesting aspects of the spin-cavity dynamics as well as their possible applications in a system of many spins strongly coupled to a single-mode cavity. In search of new physical realizations interesting in the context of hybrid quantum technology, we next investigate the reverse situation, i.e., a single-mode cavity strongly coupled to many two-level emitters. Namely, we overview in this section some of the main features of the non-Markovian quantum dynamics of an emitter inside an open multimode cavity, focusing on the case where the emitter is resonant with high-frequency cavity modes (see Fig. 11). Based on a Green's function technique suited for open photonic structures, we explore the route from spontaneous decay to complex multimode dynamics in cQED [65]. We also discuss under which conditions a single emitter-cavity system, which is initially in the weak coupling regime, can be driven into the strong coupling regime via the quantum feedback mechanism in a cQED system based on a half cavity set-up coupled to a structured continuum (the research on this project was carried out in close collaboration with the group of Prof. Andreas Knorr from TU Berlin [81]).

### 5.1 Theoretical model

The system under study is a cavity QED setup consisting of a two-level system (TLS) with transition frequency $\omega_a$ placed inside a multimode cavity. The method presented here is valid for an arbitrarily complex open cavity geometry but for the sake of transparency we discuss here a Fabry-Pérot cavity formed by two highly reflecting mirrors, see Fig. 11. To describe the excitation dynamics of the TLS one can start with the Hamiltonian written in terms of the modes-of-the-universe approach [82], which makes no distinction between the cavity and its environment,

$$\mathcal{H}=(\hbar\omega_a/2)\cdot\sigma_z+\int d\omega\hbar\omega a^\dagger(\omega)\,a(\omega)+\hbar\sqrt{\xi/\pi}\cdot\int d\omega[g(\omega,\mathbf{r})\,a(\omega)\sigma^+ +g^\star(\omega,\mathbf{r})\,a^\dagger(\omega)\sigma^-]. \tag{19}$$

Here $a^\dagger(\omega)$ and $a(\omega)$ are standard creation and annihilation operators of a photon and $\sigma^\pm$, $\sigma_z$ are the Pauli operators associated with the TLS. The interaction part of $\mathcal{H}$ is written in the electric dipole and rotating-wave approximation, where $g(\omega,\mathbf{r})$ are the coupling amplitudes with the dimension of frequency, and $\xi$ stands for the dimensionless coupling strength proportional to the dipole moment squared. Due to the rotating wave approximation, non-resonant terms ($\propto a_\lambda\sigma^-$, $a_\lambda^\dagger\sigma^+$) are absent in this Hamiltonian, such that the number of excitations is conserved. We can thus make the following ansatz for the time evolution of the system, $|\Psi(t)\rangle = c(t)e^{-i\omega_a t/2}|u\rangle|0\rangle + \int d\omega c_\omega(t)|l\rangle|1_\omega\rangle e^{-i(\omega-\omega_a/2)t}$, where the ket-vectors $|u\rangle$ and $|l\rangle$ stand for the atom in the upper and lower states, respectively, and the ket-vectors $|0\rangle$ and $|1_\omega\rangle$ represent the vacuum state and a single photon with the frequency $\omega$. Solving the Schrödinger equation with this ansatz, $\mathcal{H}|\Psi(t)\rangle = i\hbar\partial_t|\Psi(t)\rangle$, we arrive at the following Volterra equation for the excited state amplitude of the TLS, $c(t)$,

$$\dot{c}(t) = -\frac{\xi}{\pi}\int_0^t dt'\int_0^\infty d\omega F(\omega)e^{-i(\omega-\omega_a)(t-t')}c(t'), \tag{20}$$

where $F(\omega) = \rho(\mathbf{r}_a,\omega)\cdot|g(\omega)|^2$ is the spectral function, featuring the local density of photonic states (LDOPS), $\rho(\mathbf{r}_a,\omega)$, evaluated at the emitter position $\mathbf{r} = \mathbf{r}_a$ and $g(\omega)$ determines the coupling strength to the emitter where a high-frequency cutoff function is also included (see [65] for details). It is important to note that Eq. (20) written for the excited state amplitude $c(t)$ with LDOPS $F(\omega)$ is formally equivalent to the Volterra equation (4) formulated for the cavity amplitude $A(t)$ with the spectral spin density $\rho(\omega)$, apart from dissipative rates which do not explicitly enter in the former case. Therefore, the methods introduced in sec. 2.1 for solving Eq. (4) can be directly applied here to solve Eq. (20).

To make contact with the physics of an open cavity, one can evaluate the LDOPS for a one-dimensional cavity of length $L$ bounded at $x = 0, L$ by two thin semi-transparent mirrors modelled by dielectric slabs of width $d \ll L$ with refractivity index $n$ (see Fig. 11). For such an open system the LDOPS is given exactly by the imaginary part of the Green's function [83], $\rho(x_a,\omega) = -2\omega\cdot\operatorname{Im}G^+(x_a,x_a,\omega)/\pi$, where the retarded Green's function (labeled by $+$) satisfies the Helmholtz equation $(\partial_x^2 + n^2\omega^2)\,G^+(x,x_a,\omega) = -\delta(x-x_a)$ for all $x\in\mathbb{R}$ with purely outgoing, so-called "constant-flux" boundary conditions. The expression for $\rho(x_a,\omega)$ can be analytically calculated for this geometry [65]. Note that, due to the openness of the cavity, the LDOPS is a continuous function, corresponding to a continuum of extended modes which are notably different from the discrete set of cavity modes.

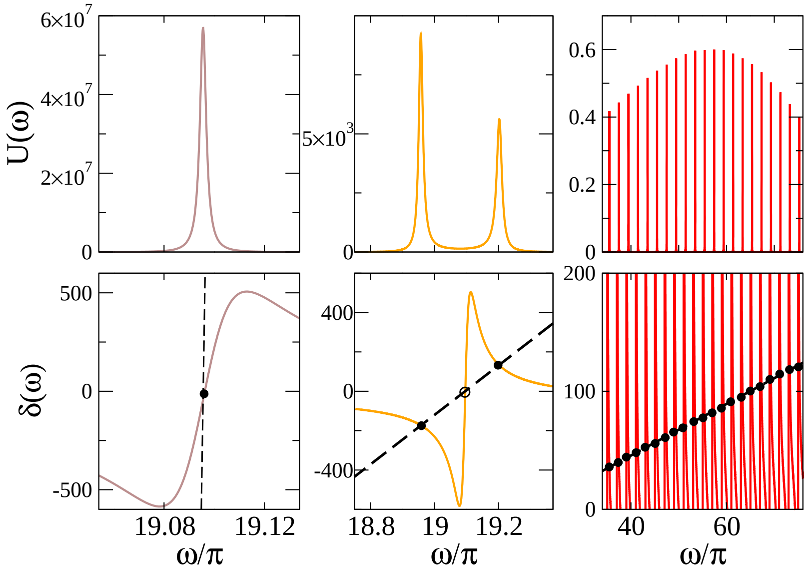

Figure 12. *(taken from [65])*. Route from single- to multimode coupling regime for different coupling strengths $\xi$. *Upper row*: Dimensionless kernel function $U(\omega)$. *Lower row*: Dimensionless nonlinear Lamb shift $\delta(\omega)$ for the same $\omega$-interval as above (note the different zooms for the three columns). *Left column*: weak coupling regime for $\xi = 4 \cdot 10^{-6}$ with a single peak in $U(\omega)$ (Purcell modified spontaneous decay). *Middle column*: strong coupling regime for $\xi = 2.5 \cdot 10^{-3}$ with a well-resolved Rabi splitting in $U(\omega)$ (regime of damped Rabi oscillations). *Right column*: Multimode strong coupling regime for $\xi = 1.44$ with a multi-peak structure in $U(\omega)$ consisting of almost equidistant peaks (regime of revivals). Filled circles label resonance values $\omega_r$ of the kernel $U(\omega)$ occurring at the intersections between the Lamb shift $\delta(\omega)$ and the dashed line $(\omega - \omega_a)/\xi$. At empty circles (not shown in right column) such intersections are non-resonant and do not lead to a corresponding peak in $U(\omega)$ (see text). The transition frequency $\omega_a \approx 19\pi$ of the TLS coincides with the 10th resonance of the spectral function $F(\omega)$. The reflectivity parameter $\eta = 0.1$ is such that the mirror reflectivity $|r(\omega_a)|^2 = 0.9$. Frequency $\omega$ is measured here in units of the inverse half the cavity round trip time.

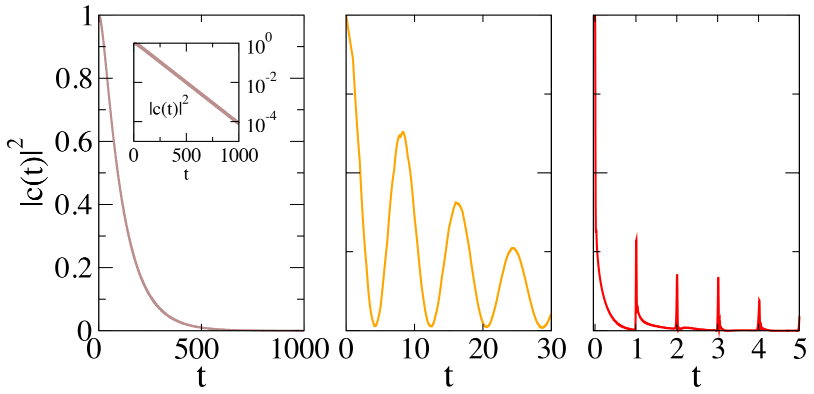

Figure 13. *(taken from [65])*. Temporal evolution of the excited state probability $|c(t)|^2$ of the TLS for the three cases shown in Fig. 12. Time $t$ is measured here in units of half the cavity round trip time. *Left panel*: Weak coupling regime ($\xi = 4 \cdot 10^{-6}$) featuring spontaneous decay (also shown in log-lin scale in the inset). *Middle panel*: Strong coupling regime ($\xi = 2.5 \cdot 10^{-3}$) with damped Rabi oscillations. *Right panel*: Multi-mode strong coupling regime ($\xi = 1.44$) featuring pulsed revivals at multiple integers of half the cavity round trip time.

### 5.2 Route from spontaneous decay to complex multimode dynamics

One can now proceed to solve Eq. (20) for a single excitation, initially stored in the TLS, $c(0) = 1$. Applying the Laplace transformation in the same fashion as in sec. 2.1.2, the following expression for the amplitude $c(t)$ can be derived

$$c(t) = \frac{\xi}{\pi}\, e^{i\omega_a t} \int_0^\infty d\omega\, U(\omega)\, e^{-i\omega t}, \tag{21}$$

with the kernel function $U(\omega)$ and the nonlinear Lamb shift $\delta(\omega)$ given by Eqs. (12,13) upon replacing $\rho(\omega)$, $\Omega^2$ and $\omega_c$ by, respectively, $F(\omega)$, $\xi$, and $\omega_a$, and setting two dissipative rates to zero.

Obviously, the dominant frequency components entering the dynamics of $c(t)$ are those which are resonant in the kernel function $U(\omega)$. A *necessary* condition for such resonances to occur is that the first term in the denominator of $U(\omega)$ vanishes,

$$(\omega_r - \omega_a)/\xi = \delta(\omega_r)\,. \tag{22}$$

This resonance condition is satisfied at the frequencies $\omega_r$, determined by the intersection of the nonlinear Lamb shift $\delta(\omega)$ and a straight line $(\omega - \omega_a)/\xi$. Since, according to Eq. (13), every resonance in $F(\omega)$ produces a dip followed by a peak in the Lamb shift, there may be several such intersections, corresponding to multiple solutions of Eq. (22). The corresponding resonances in the kernel $U(\omega)$ can, however, be suppressed, whenever the spectral function $F(\omega)$ has a maximum at the same resonance frequency. This is the case if the kernel $U(\omega) = 1/[\xi^2 F(\omega)]$ goes through a minimum at $\omega = \omega_r$.

Based on these observations, one can now investigate the crossover from weak to strong coupling upon variation of the coupling strength $\xi$; all other parameters, like the spectral function $F(\omega)$ and the mirror's reflectivity factor $\eta$ will be left unchanged. At very weak coupling, $\xi = 10^{-4}$ (left panel of Fig. 12), the straight line in Eq. (22) is very steep and thus leads just to a single intersection, corresponding to a single resonance at $\omega_r \approx \omega_a$. All quantities in $U(\omega)$ can thus be evaluated at $\omega_a$ to very good accuracy and the kernel function reduces to a Lorentzian centered around the slightly shifted frequency $\omega_a + \xi\delta(\omega_a)$ with the width $\xi F(\omega_a)$. By extending the integration limit in Eq. (21) to $-\infty$, the Purcell modified exponential decay of the TLS inversion [3] is reproduced, in good agreement with a numerical solution of the Volterra equation, Eq. (21) (left panel in Fig. 13). This is the overdamped dynamics of the TLS in the weak coupling limit of cQED.

As $\xi$ increases to $\xi = 2.5 \cdot 10^{-3}$ we enter the strong coupling regime, as indicated by the straight line now being flat enough to intersect the nonlinear Lamb shift at three points (middle panel of Fig. 12). Note that these *three* intersections give rise to only *two* resonances $\omega_r$ in the kernel

$U(\omega)$ since the middle frequency is very close to the resonance of $F(\omega)$ (see discussion above). As a consequence, the kernel function $U(\omega)$ has a double peak structure that is characteristic of the single-mode vacuum Rabi splitting [9]. This energy splitting introduces a new frequency scale, the Rabi frequency, which is easily estimated from the resonance condition (22) to be $\sqrt{2\omega_a\xi}$. The inverse of the peak width provides the time scale at which the Rabi oscillations decay, as confirmed by independent numerical solutions of Eq. (21) (middle panel of Fig. 13).

With further increase of the coupling strength to $\xi = 1.44$, the straight line starts to intersect neighboring resonances of $\delta(\omega)$, involving an increasing number of cavity modes. Thus, within the multimode strong coupling regime it is possible to couple to many cavity modes, including those that reside far away from the transition frequency $\omega_a$ (right panel of Fig. 12). Note that, similar to the situation above, only every second intersection with the Lamb shift produces a resonance in the kernel $U(\omega)$ which, correspondingly, takes on a multi-peaked profile. If, as in our case, these peaks also have an equidistant spacing to each other, then the interference between these resonant modes produces a train of pulses in the probability of the excited state $|c(t)|^2$, corresponding to pulsed revivals of the TLS inversion (right panel of Fig. 13). With the revival time being equal to half the cavity round trip time, the straightforward explanation of this phenomenon is the repetitive emission and subsequent reabsorption of radiation by the TLS, when it is back-reflected by the cavity boundaries. As such, this effect relies on the fact that the phases acquired from all possible paths starting from and returning to the position of the TLS differ only by integer multiples of $2\pi$, a condition which strongly depends on the position of the TLS in the cavity. Indeed, if we move the TLS away from the cavity center, a much more irregular type of dynamics emerges (not shown).

In this section we showed that the conventionally observed regimes of spontaneous decay or Rabi oscillations at the very strong emitter-cavity coupling are followed by periodic quantum revivals of the atomic inversion on a time scale associated with the cavity round-trip time. In this new multimode strong-coupling regime, the emitter sends out a pulse during the de-excitation process and gets re-excited when this pulse returns after back-reflection from the ends of the cavity. We show that the crucial parameter to capture the crossovers between these regimes is the nonlinear Lamb shift, accounted for exactly in our formalism.

### 5.3 Quantum feedback enhanced Rabi oscillations

A coherent energy exchange between an atom and a cavity requires that an atom-cavity coupling exceeds any photon loss and radiative decay processes. Therefore, besides technological progress to increase the quality factor of the cavities, a promising alternative for the stabilization of desired quantum regimes is quantum feedback achieved either via the external control e.g. by continuous measurements [84], or via various delayed feedback control schemes [85, 86]. In this section we

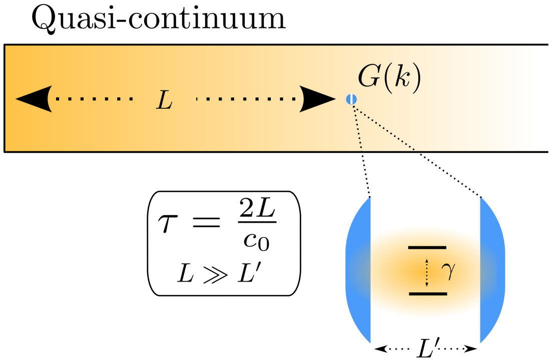

Figure 14. *(taken from [81]).* Implementation of an intrinsic quantum feedback mechanism via a quasicontinuum, realized by a photonic crystal waveguide with length $L$, which is supposed to be considerably larger than the cavity length $L'$. The waveguide is a half cavity and allows to exchange cavity photons with waveguide photons due to the photon leakage $G(k)$. The photons inside the cavity interact with a single emitter (coupling strength $\Omega$).

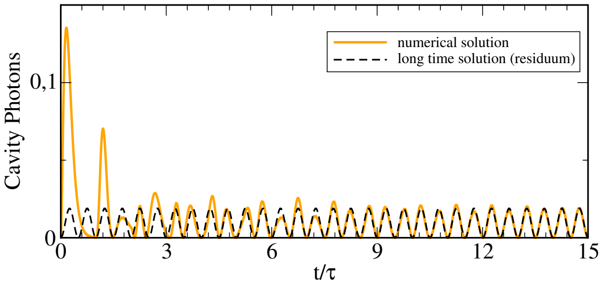

Figure 15. Comparison between numerics (orange curve) and long time solution determined by the residuum contribution only (black curve) for an initially excited TLS $c_e(0) = 1$ and $\kappa/\Omega = 2$, where $\kappa = \pi G_0^2/(2c_0)$. After several $\tau$, the analytical long time solution and the numerics coincide.

present an interesting strategy to stabilize single-emitter cQED via a quantum feedback from an external structured continuum. Specifically, we consider the photon leakage mechanism shaped by an external mirror and discuss how the initial weak atom-cavity coupling can be driven into the strong coupling regime. For this purpose the conditions for this stabilization phenomenon are specified, among which the phase relation between the cavity mode and the delay time imposed by the external mirror plays a decisive role [81]. The system under study consists of a microcavity system of length $L'$ with a two-level emitter coupled to a single cavity mode (see Fig. 14). Furthermore, the cavity exhibits photon loss due to its coupling to external modes. An external mirror, placed in a distance of $L \gg L'$, introduces a boundary condition to the external mode structure and causes a feedback of lost cavity photons into the cavity. This kind of quantum self-feedback can be realized via a shaped mode continuum in a photonic waveguide. Due to the finite cavity-mirror distance $L$ and the quasicontinuous mode structure of the semiinfinite lead, a delay mechanism is introduced into the system at $\tau = 2L/c_0$ with $c_0$ being the speed of light in vacuum. To describe the corresponding physics one begins with the following Hamiltonian within the rotating-wave and dipole approximation:

$$H/\hbar = -\Omega \left(\sigma^- a^\dagger + \sigma^+ a\right) - \int \mathrm{d}k G(k,t)\; a^\dagger d_k + G^*(k,t)\; d_k^\dagger a, \tag{23}$$

where a rotating frame is chosen in correspondence to the free energy contribution of the Hamiltonian. The emitter is described via the Pauli matrices with $\sigma^\pm$ being the raising and lowering operators of the two level system, respectively. In the following, the atomic energy is assumed to be in resonance with the single cavity mode. A photon annihilation (creation) in the cavity is described with the bosonic operator $a^\dagger(a)$ and $\Omega$ is the coupling between the two-level system and the cavity mode. The cavity photons interact with the external modes $d_k^\dagger$ in front of the mirror via the tunnel Hamiltonian coupling elements $G(k,t) = G_0 \sin(kL) \exp[i(\omega_0 - \omega_k)t]$, which due to the interference with the back-reflected signal from the mirror depend both on time $t$ and on the wavenumber $k$ [81]. Here $G_0$ stands for the bare tunnel coupling strength and $\omega_0$ and $\omega_k$ are the frequencies of a single cavity mode and half-cavity modes, respectively. Note that this specific form of $G(k,t)$ determines the nature of the feedback on the cavity.

If no other loss channels or pump mechanism are introduced, the system dynamics described by the Hamiltonian (23) can be solved in the Schrödinger picture, so that in the single photon limit, the total wave function reads:

$$|\Psi(t)\rangle = c_e(t)|e,0,\{0\}\rangle + c_g(t)|g,1,\{0\}\rangle + \int \mathrm{d}k \; c_{g,k}(t)|g,0,\{k\}\rangle, \tag{24}$$

where $|e,0,\{0\}\rangle$ denotes the excited state of the TLS with the cavity and the waveguide being in the vacuum state, $|g,1,\{0\}\rangle$ stands for a single photon residing in the cavity and the TLS as well as the radiation field in the waveguide being in the ground state. Finally, $|g,0,\{k\}\rangle$ describes the ground state of the TLS with exactly one photon in the waveguide of mode $k$.

Writing the Schrödinger equation, one can derive a set of linear ODEs with respect to the amplitudes $c_e(t)$, $c_g(t)$ and $c_{g,k}(t)$ and use the simplest initial conditions assuming that at $t_0 = 0$ the TLS is in the excited state, $c_e(t_0) = 1$, and there are neither photons inside the cavity, $c_g(t_0) = 0$, nor in the external region, $c_{g,k}(t_0) = 0$. To introduce a delay time corresponding to $\tau = 2L/c_0 = 2\pi/\Omega$, a mirror resonator distance $L = \pi c_0/\Omega$ is chosen. The resulting set of ODEs for the amplitudes can also be solved using the Laplace transform method (see sec. 2.1.2). Importantly, a slow asymptotic behavior of the coupled system is directly related to the singularities in the contour integral of the Laplace transformed function, which are found by setting its denominator to zero. As it turns out, the corresponding singularity condition can be matched if, for instance, $\Omega\tau = 2\pi m$ and, at the same time, the cavity frequency is chosen such that $\omega_0\tau = 2\pi l$, where $l, m$ are integer numbers. As a result one ends up with a purely coherent asymptotic solution characterized by a minimum of dephasing and a maximum amplitude, corresponding to the fact that the pole does not contain any decaying term.

In Fig. 15, the numerical solution and the analytical asymptotic solution are plotted for $\tau = 2\pi/\Omega$ (i.e. when $m = 1$) up to several $\tau$. The agreement is excellent with the long time solution accurately recovering the amplitude and the oscillation frequency of the exact numerical solution. It turns out that the effect of stabilized Rabi oscillations in the long time limit depends strongly on the chosen time delay $\tau$, which has to be chosen such to satisfy aforementioned conditions that lead to asymptotically undamped Rabi oscillations. Furthermore, the factor $\exp(i\omega_0\tau)$ plays a crucial role to decide whether quantum feedback leads to a stabilized Rabi oscillation or to a damped feedback situation. However, the effect depends only quantitatively (rather than qualitatively) on the cavity loss $\kappa$ and coupling strength $\Omega$, besides the obvious restriction that both of them are unequal to zero. To gain an intuitive explanation of the effect of recovered Rabi oscillations in the weak coupling limit, one can visualize the resulting cavity dynamics in the framework of the photon-path representation using the von Neumann expansion [81]. With this expansion, one can represent the dynamics as a series of single scattering events by multiple application of the scattering matrix, which swaps the excitation from $c_e$ to $c_g$ and includes the cavity loss and the gain from the feedback. In other words, the strong coupling feature is produced by a destructive interference effect of the photon paths at the point of tunneling between cavity and waveguide.

In summary, in this chapter we address a very important question in the context of possible cQED applications, which is how to reach and stabilize the regime of the quantum-feedback-induced Rabi oscillations. The results obtained show that the stabilization of Rabi oscillations for a system being initially in the weak-coupling regime (before the feedback modifies the system dynamics) depends strongly on the chosen time delay. The latter has to be chosen such as to satisfy certain conditions between the system parameters that lead to asymptotically undamped Rabi oscillations.

## 6 Summary of the attached articles

In [58] I developed a theoretical framework to describe the collective non-Markovian spin-cavity dynamics of a system consisting of a large spin ensemble coupled with a single-mode cavity via magnetic or electric dipole interaction. For that purpose a Volterra integral equation was set up for the cavity amplitude that contains a memory kernel with information about all previous events in the system. My numerical calculations showed excellent agreement with the experimental results [59], and underline that a precise knowledge of the inhomogeneous spin distribution is crucial for the understanding of time domain measurements. Based on this theory it was possible to predict, on the example of one particular experimental realization [59], how the decoherence induced by the inhomogeneous distribution of the constituents of a large ensemble can be suppressed in the strong-coupling regime - a phenomenon known as "cavity protection". To demonstrate the potential of this effect for coherent control schemes, we showed how appropriately chosen microwave pulses can dramatically increase the amplitude of coherent oscillations between the cavity and the spin ensemble. Furthermore, my theoretical analysis disclosed a non-trivial crossover between Markovian and non-Markovian dynamics which is realized by varying the collective coupling strength.

In two other studies [54, 55], we could recently find an alternative way to overcome the detrimental influence of inhomogeneous broadening: In particular, I theoretically predicted that the decoherence induced by the spin broadening can be strongly suppressed by burning two narrow spectral holes in the spin spectral density at judiciously chosen frequencies [54]. Using this procedure we found an increase of the coherence time by more than an order of magnitude as compared to the case without hole burning - a scenario that has been confirmed in a recent experiment [55].

In [60] I generalized our hole-burning concept to more sophisticated profiles of an engineered spin spectral density. Specifically, when the ensembles feature a comb-shape structure to give rise to repetitive photon pulse revivals, we demonstrated how the burning of narrow holes in this atomic frequency comb leads to a dramatic prolongation of the revival dynamics. I found that the positions of the holes are generally incommensurate with the positions of the peaks in the frequency comb - a result that follows directly from our theory for the multimode strong coupling regime.

In [70], we developed an efficient optimal control scheme and demonstrated the viability of our approach in terms of explicit storage and readout sequences for a spin ensemble strongly coupled to a single-mode cavity. Our technique based on Volterra equations relies solely on very weak control pulses, and as consequence, diminishes the influence of noise caused by writing and reading pulses in contrast to established echo techniques which require additional high-intensity control fields. The applicability of our approach was also demonstrated in conjunction with the above-mentioned spectral hole-burning technique [54, 55, 60] that allows us to reach storage times going far beyond the dephasing time of the inhomogeneously broadened ensemble.

In [61] I went beyond the Volterra equation approach and developed a theoretical framework which is capable of capturing the essential features of nonlinear dynamics and amplitude bistability observed in the experiment dealing with an inhomogeneously broadened ensemble strongly coupled to a single mode cavity driven by external pulses [61]. We also unraveled a very unusual effect of a critical slowing down of the cavity population which exceeds the longest time scale associated with the system by many orders of magnitude.

In another study [65] based on a Green's function technique suited for open photonic structures, we analyzed the non-Markovian quantum dynamics of an emitter inside an open multimode cavity, focusing on the case where the emitter is resonant with high-frequency cavity modes. Solving the Volterra equation for the temporal decay through Laplace transform allowed me to obtain the decay dynamics together with a corresponding graphical analysis which provides an intuitive understanding of the different regimes observed. On top of the familiar exponential decay and damped Rabi oscillations in the weak and strong coupling regime, respectively, I identified, for very strong coupling, a regime where the emitter couples to multiple modes, leading to pulsed revivals of its initial excitation.

In [81] we found an approach to stabilize single-emitter cQED via a quantum feedback mechanism induced by an external mirror. Specifically, we analyzed under which conditions a system consisting of an emitter weakly coupled to a cavity, which, in turn, is coupled to a structured continuum, can be driven into the strong coupling regime. Furthermore, we determined the theoretical limit for a feedback effect on the single excitation level and extended our investigation from the weak- to the strong coupling regime. By expanding our solution with the von Neumann series, we could demonstrate that the effect relies on a destructive interference effect of incoming and outgoing photon wave packages and illustrated this in a photon-path representation picture.

## 7 Outlook

Cavity QED is a rapidly developing field which is of central importance both from a practical, application-minded interest, and from a fundamental point of view. The envisioned future technologies deal with secure communication and quantum sensing, with the implementation of elementary operations for quantum information processing as well as for its coherent storage and retrieval. Another promising applications will be based on various quantum architectures, which enable on-chip quantum simulations necessary for the understanding of the dynamics in open quantum many-body systems.

The experimental success achieved in various physical realizations has reached an important stage where one can now in principle engineer composite systems to exploit the best properties of their individual constituents. Such a hybridization between different elements leads to new device functionalities, which otherwise would not be possible to reach. However, there are still many practical limitations caused by decoherence, which is known to be the major bottleneck for the processing of quantum information in hybrid quantum technology. Furthermore, a general theoretical framework covering all aspects of many-body quantum dynamics in these systems is still missing.

Specifically, the presence of a sizeable number of constituents (spins, qubits etc) within an ensemble coupled to a cavity permits the introduction of the semiclassical approach so that the problem is formally reduced to the Maxwell-Bloch equations for the cavity and spin amplitudes. The opposite limit with a few spins (of the order of fifteen) is computationally tractable by numerically solving the Lindblad master equation. However, adequate theoretical tools applicable in a mesoscopic limit are not well-established, which is realized in various quantum metamaterials such as those based on an ensemble of superconducting qubits coupled to a microwave cavity. We believe that in this case the density-matrix renormalization group method (or, even more general, Tensor Network methods) can be appropriately adjusted, which has turned into the numerical method of choice for studying the physics in strongly correlated quantum lattice systems.

A whole range of new and previously unexplored physics is expected to be uncovered in different cavity QED setups upon variation of the external drive and of the collective coupling strength. In particular, we anticipate that very intriguing dynamical regimes and bifurcation scenarios will be found as a result of the complex interplay between several ingredients characteristic for quantum non-Hermitian many-body system such as entanglement, “superradiance”, and the Dicke-model quantum phase transitions.

# 8 Acknowledgements

First and foremost, I am deeply indebted to Prof. Stefan Rotter for all kind of support, insightful ideas, guidance, useful advice and numerous valuable discussions on different exciting topics in physics, which he has offered me during my stay in his group. I am also very grateful to him for giving me many opportunities to travel and for keeping a very warm and inspiring working atmosphere in the group, which allowed me to learn also on many other interesting topics not necessarily related to this thesis.

My work has benefited a lot from the collaborations with the experimental group of Prof. Hannes-Jörg Schmiedmayer and Dr. Johannes Majer from the Institute of Atomic and Subatomic Physics, TU Wien. My special thanks are to the current and former members of this group, in particular, to Dr. Stefan Putz, Dipl.-Ing. Andreas Angerer and Dr. Robert Amsüss.

I have also enjoyed working together with several very good project, Bachelor and Diploma students. In particular, I am grateful to Dipl.-Ing. Benedikt Hartl, Dipl.-Ing. Matthias Zens and Dipl.-Ing. Kevin Pichler (former Diploma students of Prof. Rotter and of myself). My special thanks go to Dr. Adrian Girschik for our excellent collaboration on the quantum theory classes. I am also very grateful to Dr. Matthias Liertzer for very fruitful discussions - he was a great office mate for several years.

I would also like to thank all local and international colleagues that have been involved in fruitful discussions on various topics of my thesis, in particular, Dr. Alexander Carmele (TU Berlin), Dr. Himadri Dhar (TU Wien), Dr. Julia Kabuss (TU Berlin), Prof. Sergej Kilin (National Academy of Sciences of Belarus, Minsk), Prof. Anreas Knorr (TU Berlin), Prof. Konstantinos Makris (University of Crete), Dr. Florian Mintert (Imperial College, London), Prof. Sergey Moiseev (Kazan Quantum Center), Prof. William Munro (NTT Basic Research Laboratories, Kanagawa), Prof. Kae Nemoto (National Institute of Informatics, Tokyo), Dr. Mikhail Pletyukhov (RWTH Aachen), Prof. Peter Rabl (TU Wien), Prof. Helmut Ritsch (University of Innsbruck), Prof. Hong Tang (Yale University), Prof. Aleksey Ustinov (KIT, Karlsruhe), and Prof. Chang-Ling Zou (University of Science and Technology of China). I also should not forget to acknowledge the nice and friendly atmosphere at the Institute for Theoretical Physics and perfect support provided by the institute's secretaries, Mrs. Heike Höller and Mrs. Sylvia Riedler.

Last but certainly not least I would like to express deep gratitude to my wife Oksana and daughter Margaret for their permanent encouragement and support.

# 9 References

[1] V. Weisskopf and E. Wigner, “Berechnung der natürlichen linienbreite auf grund der diracschen lichttheorie,” *Zeitschrift für Physik*, vol. 63, no. 1, pp. 54–73, 1930.

[2] W. E. Lamb and R. C. Retherford, “Fine structure of the hydrogen atom by a microwave method,” *Phys. Rev.*, vol. 72, pp. 241–243, Aug 1947.

[3] E. M. Purcell, “Proceedings of the american physical society,” *Phys. Rev.*, vol. 69, p. 681, Jun 1946.

[4] D. Kleppner, “Inhibited spontaneous emission,” *Phys. Rev. Lett.*, vol. 47, pp. 233–236, Jul 1981.

[5] R. G. Hulet, E. S. Hilfer, and D. Kleppner, “Inhibited spontaneous emission by a rydberg atom,” *Phys. Rev. Lett.*, vol. 55, pp. 2137–2140, Nov 1985.

[6] L. Sapienza, H. Thyrrestrup, S. Stobbe, P. D. Garcia, S. Smolka, and P. Lodahl, “Cavity quantum electrodynamics with anderson-localized modes,” *Science*, vol. 327, no. 5971, pp. 1352–1355, 2010.

[7] P. V. Ruijgrok, R. Wüest, A. A. Rebane, A. Renn, and V. Sandoghdar, “Spontaneous emission of a nanoscopic emitter in a strongly scattering disordered medium,” *Opt. Express*, vol. 18, pp. 6360–6365, Mar 2010.

[8] X.-W. Chen, M. Agio, and V. Sandoghdar, “Metallodielectric hybrid antennas for ultrastrong enhancement of spontaneous emission,” *Phys. Rev. Lett.*, vol. 108, p. 233001, Jun 2012.

[9] E. T. Jaynes and F. W. Cummings, “Comparison of quantum and semiclassical radiation theories with application to the beam maser,” *Proceedings of the IEEE*, vol. 51, pp. 89–109, Jan 1963.

[10] J. H. Eberly, N. B. Narozhny, and J. J. Sanchez-Mondragon, “Periodic spontaneous collapse and revival in a simple quantum model,” *Phys. Rev. Lett.*, vol. 44, pp. 1323–1326, May 1980.

[11] S. Haroche and J.-M. Raimond, *Exploring the Quantum: Atoms, Cavities, and Photons*. Oxford University Press, 2006.

[12] J. D. Thompson, T. G. Tiecke, N. P. de Leon, J. Feist, A. V. Akimov, M. Gullans, A. S. Zibrov, V. Vuletić, and M. D. Lukin, “Coupling a single trapped atom to a nanoscale optical cavity,” *Science*, vol. 340, no. 6137, pp. 1202–1205, 2013.

[13] C. Junge, D. O’Shea, J. Volz, and A. Rauschenbeutel, “Strong coupling between single atoms and non-transversal photons,” *Phys. Rev. Lett.*, vol. 110, p. 213604, May 2013.

[14] P. Lodahl, S. Mahmoodian, and S. Stobbe, “Interfacing single photons and single quantum dots with photonic nanostructures,” *Rev. Mod. Phys.*, vol. 87, pp. 347–400, May 2015.

[15] J. Clarke and F. K. Wilhelm, “Superconducting quantum bits,” *Nature*, vol. 453, pp. 1031–1042, 06 2008.

[16] G. Kurizki, P. Bertet, Y. Kubo, K. Mølmer, D. Petrosyan, P. Rabl, and J. Schmiedmayer, “Quantum technologies with hybrid systems,” *Proceedings of the National Academy of Sciences*, vol. 112, no. 13, p. 3866, 2015.

[17] Z.-L. Xiang, S. Ashhab, J. Q. You, and F. Nori, “Hybrid quantum circuits: Superconducting circuits interacting with other quantum systems,” *Rev. Mod. Phys.*, vol. 85, pp. 623–653, Apr 2013.

[18] C. Simon and et al., “Quantum memories,” *Europ. Phys. J. D*, vol. 58, no. 1, pp. 1–22, 2010.

[19] M. Aspelmeyer, T. J. Kippenberg, and F. Marquardt, “Cavity optomechanics,” *Rev. Mod. Phys.*, vol. 86, pp. 1391–1452, Dec 2014.

[20] R. Amsüss, C. Koller, T. Nöbauer, S. Putz, S. Rotter, K. Sandner, S. Schneider, M. Schramböck, G. Steinhauser, H. Ritsch, J. Schmiedmayer, and J. Majer, “Cavity qed with magnetically coupled collective spin states,” *Phys. Rev. Lett.*, vol. 107, p. 060502, Aug 2011.

[21] K. Sandner, H. Ritsch, R. Amsüss, C. Koller, T. Nöbauer, S. Putz, J. Schmiedmayer, and J. Majer, “Strong magnetic coupling of an inhomogeneous nitrogen-vacancy ensemble to a cavity,” *Phys. Rev. A*, vol. 85, p. 053806, May 2012.

[22] Y. Kubo, F. R. Ong, P. Bertet, D. Vion, V. Jacques, D. Zheng, A. Dréau, J.-F. Roch, A. Auffeves, F. Jelezko, J. Wrachtrup, M. F. Barthe, P. Bergonzo, and D. Esteve, “Strong coupling of a spin ensemble to a superconducting resonator,” *Phys. Rev. Lett.*, vol. 105, p. 140502, Sep 2010.

[23] Y. Kubo, C. Grezes, A. Dewes, T. Umeda, J. Isoya, H. Sumiya, N. Morishita, H. Abe, S. Onoda, T. Ohshima,

V. Jacques, A. Dréau, J.-F. Roch, I. Diniz, A. Auffeves, D. Vion, D. Esteve, and P. Bertet, "Hybrid quantum circuit with a superconducting qubit coupled to a spin ensemble," *Phys. Rev. Lett.*, vol. 107, p. 220501, Nov 2011.

[24] Y. Kubo, I. Diniz, A. Dewes, V. Jacques, A. Dréau, J.-F. Roch, A. Auffeves, D. Vion, D. Esteve, and P. Bertet, "Storage and retrieval of a microwave field in a spin ensemble," *Phys. Rev. A*, vol. 85, p. 012333, Jan 2012.

[25] S. Probst, H. Rotzinger, S. Wünsch, P. Jung, M. Jerger, M. Siegel, A. V. Ustinov, and P. A. Bushev, "Anisotropic rare-earth spin ensemble strongly coupled to a superconducting resonator," *Phys. Rev. Lett.*, vol. 110, p. 157001, Apr 2013.

[26] M. Nilsson and S. Kröll, "Solid state quantum memory using complete absorption and re-emission of photons by tailored and externally controlled inhomogeneous absorption profiles," *Optics Communications*, vol. 247, no. 4, pp. 393 – 403, 2005.

[27] A. Imamoglu, "Cavity qed based on collective magnetic dipole coupling: Spin ensembles as hybrid two-level systems," *Phys. Rev. Lett.*, vol. 102, p. 083602, Feb 2009.

[28] J. Verdú, H. Zoubi, C. Koller, J. Majer, H. Ritsch, and J. Schmiedmayer, "Strong magnetic coupling of an ultracold gas to a superconducting waveguide cavity," *Phys. Rev. Lett.*, vol. 103, p. 043603, Jul 2009.

[29] R. H. Dicke, "Coherence in spontaneous radiation processes," *Phys. Rev.*, vol. 93, pp. 99–110, Jan 1954.

[30] M. Gross and S. Haroche, "Superradiance: An essay on the theory of collective spontaneous emission," *Physics Reports*, vol. 93, no. 5, p. 301, 1982.

[31] S. A. Moiseev and S. Kröll, "Complete reconstruction of the quantum state of a single-photon wave packet absorbed by a doppler-broadened transition," *Phys. Rev. Lett.*, vol. 87, p. 173601, Oct 2001.

[32] B. Kraus, W. Tittel, N. Gisin, M. Nilsson, S. Kröll, and J. I. Cirac, "Quantum memory for nonstationary light fields based on controlled reversible inhomogeneous broadening," *Phys. Rev. A*, vol. 73, p. 020302, Feb 2006.

[33] W. Tittel, M. Afzelius, T. Chaneliére, R. L. Cone, S. Kröll, S. A. Moiseev, and M. Sellars, "Photon-echo quantum memory in solid state systems," *Laser & Photonics Reviews*, vol. 4, no. 2, pp. 244–267, 2010.

[34] B. Julsgaard and K. Mølmer, "Fundamental limitations in spin-ensemble quantum memories for cavity fields," *Phys. Rev. A*, vol. 88, p. 062324, Dec 2013.

[35] C. Grezes, B. Julsgaard, Y. Kubo, M. Stern, T. Umeda, J. Isoya, H. Sumiya, H. Abe, S. Onoda, T. Ohshima, V. Jacques, J. Esteve, D. Vion, D. Esteve, K. Mølmer, and P. Bertet, "Multimode storage and retrieval of microwave fields in a spin ensemble," *Phys. Rev. X*, vol. 4, p. 021049, Jun 2014.

[36] N. Gisin, S. A. Moiseev, and C. Simon, "Storage and retrieval of time-bin qubits with photon-echo-based quantum memories," *Phys. Rev. A*, vol. 76, p. 014302, Jul 2007.

[37] M. U. Staudt, S. R. Hastings-Simon, M. Nilsson, M. Afzelius, V. Scarani, R. Ricken, H. Suche, W. Sohler, W. Tittel, and N. Gisin, "Fidelity of an optical memory based on stimulated photon echoes," *Phys. Rev. Lett.*, vol. 98, p. 113601, Mar 2007.

[38] H. de Riedmatten, M. Afzelius, M. U. Staudt, C. Simon, and N. Gisin, "A solid-state light-matter interface at the single-photon level," *Nature*, vol. 456, pp. 773–777, 12 2008.

[39] P. Jobez, I. Usmani, N. Timoney, C. Laplane, N. Gisin, and M. Afzelius, "Cavity-enhanced storage in an optical spin-wave memory," *New Journal of Physics*, vol. 16, no. 8, p. 083005, 2014.

[40] S. A. Moiseev and J.-L. L. Gouët, "Rephasing processes and quantum memory for light: reversibility issues and how to fix them," *Journal of Physics B: Atomic, Molecular and Optical Physics*, vol. 45, no. 12, p. 124003, 2012.

[41] M. Sabooni, Q. Li, S. Kröll, and L. Rippe, "Efficient quantum memory using a weakly absorbing sample," *Phys. Rev. Lett.*, vol. 110, p. 133604, Mar 2013.

[42] K. I. Gerasimov, S. A. Moiseev, V. I. Morosov, and R. B. Zaripov, "Room-temperature storage of electromagnetic pulses on a high-finesse natural spin-frequency comb," *Phys. Rev. A*, vol. 90, p. 042306, Oct 2014.

[43] R. A. Akhmedzhanov, L. A. Gushchin, A. A. Kalachev, S. L. Korableva, D. A. Sobgayda, and I. V. Zelensky, "Atomic frequency comb memory in an isotopically pure 143 nd 3+ :y 7 lif 4 crystal," *Laser Physics Letters*,

vol. 13, no. 1, p. 015202, 2016.

[44] I. Novikova, N. B. Phillips, and A. V. Gorshkov, "Optimal light storage with full pulse-shape control," *Phys. Rev. A*, vol. 78, p. 021802, Aug 2008.

[45] S. A. Moiseev, "Off-resonant raman-echo quantum memory for inhomogeneously broadened atoms in a cavity," *Phys. Rev. A*, vol. 88, p. 012304, Jul 2013.

[46] M. Afzelius and C. Simon, "Impedance-matched cavity quantum memory," *Phys. Rev. A*, vol. 82, p. 022310, Aug 2010.

[47] S. A. Moiseev, S. N. Andrianov, and F. F. Gubaidullin, "Efficient multimode quantum memory based on photon echo in an optimal qed cavity," *Phys. Rev. A*, vol. 82, p. 022311, Aug 2010.

[48] T. Chanelière, "Strong excitation of emitters in an impedance matched cavity: the area theorem, $\pi$-pulse and self-induced transparency," *Opt. Express*, vol. 22, pp. 4423–4436, Feb 2014.

[49] G. Bensky, D. Petrosyan, J. Majer, J. Schmiedmayer, and G. Kurizki, "Optimizing inhomogeneous spin ensembles for quantum memory," *Phys. Rev. A*, vol. 86, p. 012310, Jul 2012.

[50] J. Cai, F. Jelezko, N. Katz, A. Retzker, and M. B. Plenio, "Long-lived driven solid-state quantum memory," *New Journal of Physics*, vol. 14, no. 9, p. 093030, 2012.

[51] X. Zhu, Y. Matsuzaki, R. Amsüss, K. Kakuyanagi, T. Shimo-Oka, N. Mizuochi, K. Nemoto, K. Semba, W. J. Munro, and S. Saito, "Observation of dark states in a superconductor diamond quantum hybrid system," *Nat Commun*, vol. 5, p. 3424, 04 2014.

[52] M. O. Scully, "Single photon subradiance: Quantum control of spontaneous emission and ultrafast readout," *Phys. Rev. Lett.*, vol. 115, p. 243602, Dec 2015.

[53] W. Guerin, M. O. Araújo, and R. Kaiser, "Subradiance in a large cloud of cold atoms," *Phys. Rev. Lett.*, vol. 116, p. 083601, Feb 2016.

[54] D. O. Krimer, B. Hartl, and S. Rotter, "Hybrid quantum systems with collectively coupled spin states: Suppression of decoherence through spectral hole burning," *Phys. Rev. Lett.*, vol. 115, p. 033601, Jul 2015.

[55] S. Putz, A. Angerer, D. O. Krimer, R. Glattauer, W. J. Munro, S. Rotter, J. Schmiedmayer, and J. Majer, "Spectral hole burning and its application in microwave photonics," *Nature Photonics*, vol. 11, pp. 36–39, 01 2017.

[56] X. Zhang, C.-L. Zou, N. Zhu, F. Marquardt, L. Jiang, and H. X. Tang, "Magnon dark modes and gradient memory," *Nat Commun*, vol. 6, p. 8914, 11 2015.

[57] X. Zhang, C. Zou, L. Jiang, and H. X. Tang, "Superstrong coupling of thin film magnetostatic waves with microwave cavity," *Journal of Applied Physics*, vol. 119, no. 2, 2016.

[58] D. O. Krimer, S. Putz, J. Majer, and S. Rotter, "Non-markovian dynamics of a single-mode cavity strongly coupled to an inhomogeneously broadened spin ensemble," *Phys. Rev. A*, vol. 90, p. 043852, Oct 2014.

[59] S. Putz, D. O. Krimer, R. Amsüss, A. Valookaran, T. Nobauer, J. Schmiedmayer, S. Rotter, and J. Majer, "Protecting a spin ensemble against decoherence in the strong-coupling regime of cavity qed," *Nature Physics*, vol. 10, pp. 720–724, 10 2014.

[60] D. O. Krimer, M. Zens, S. Putz, and S. Rotter, "Sustained photon pulse revivals from inhomogeneously broadened spin ensembles," *Laser & Photonics Reviews*, vol. 10, no. 6, pp. 1023–1030, 2016.

[61] A. Angerer, S. Putz, D. O. Krimer, T. Astner, M. Zens, R. Glattauer, K. Streltsov, W. J. Munro, K. Nemoto, S. Rotter, J. Schmiedmayer, and J. Majer, "Ultralong relaxation times in bistable hybrid quantum systems," *Science Advances*, vol. 3, no. 12, p. e1701626, 2017.

[62] M. Tavis and F. W. Cummings, "Exact solution for an $n$-molecule¯radiation-field hamiltonian," *Phys. Rev.*, vol. 170, pp. 379–384, Jun 1968.

[63] C. Emary and T. Brandes, "Chaos and the quantum phase transition in the dicke model," *Phys. Rev. E*, vol. 67, p. 066203, Jun 2003.

[64] H. Primakoff and T. Holstein, "Many-body interactions in atomic and nuclear systems," *Phys. Rev.*, vol. 55, pp. 1218–1234, Jun 1939.

[65] D. O. Krimer, M. Liertzer, S. Rotter, and H. E. Türeci, "Route from spontaneous decay to complex multimode dynamics in cavity qed," *Phys. Rev. A*, vol. 89, p. 033820, Mar 2014.

[66] I. Diniz, S. Portolan, R. Ferreira, J. M. Gérard, P. Bertet, and A. Auffèves, "Strongly coupling a cavity to

inhomogeneous ensembles of emitters: Potential for long-lived solid-state quantum memories," *Phys. Rev. A*, vol. 84, p. 063810, Dec 2011.

[67] Z. Kurucz, J. H. Wesenberg, and K. Mølmer, "Spectroscopic properties of inhomogeneously broadened spin ensembles in a cavity," *Phys. Rev. A*, vol. 83, p. 053852, May 2011.

[68] M. Fleischhauer, A. Imamoglu, and J. P. Marangos, "Electromagnetically induced transparency: Optics in coherent media," *Rev. Mod. Phys.*, vol. 77, pp. 633–673, Jul 2005.

[69] M. Gündoğan, P. M. Ledingham, K. Kutluer, M. Mazzera, and H. de Riedmatten, "Solid state spin-wave quantum memory for time-bin qubits," *Phys. Rev. Lett.*, vol. 114, p. 230501, Jun 2015.

[70] D. O. Krimer, B. Hartl, F. Mintert, and S. Rotter, "Optimal control of non-markovian dynamics in a single-mode cavity strongly coupled to an inhomogeneously broadened spin ensemble," *Phys. Rev. A*, vol. 96, p. 043837, Oct 2017.

[71] J. Brendel, N. Gisin, W. Tittel, and H. Zbinden, "Pulsed energy-time entangled twin-photon source for quantum communication," *Phys. Rev. Lett.*, vol. 82, pp. 2594–2597, Mar 1999.

[72] J. Batle, A. R. Plastino, M. Casas, and A. Plastino, "Understanding quantum entanglement: Qubits, rebits and the quaternionic approach," *Optics and Spectroscopy*, vol. 94, no. 5, pp. 700–705, 2003.

[73] R. Kubo, "Generalized cumulant expansion method," *J. Phys. Soc. Jpn.*, vol. 17, no. 7, p. 1100, 1962.

[74] D. Meiser, J. Ye, D. R. Carlson, and M. J. Holland, "Prospects for a millihertz-linewidth laser," *Phys. Rev. Lett.*, vol. 102, p. 163601, Apr 2009.

[75] K. Henschel, J. Majer, J. Schmiedmayer, and H. Ritsch, "Cavity qed with an ultracold ensemble on a chip: Prospects for strong magnetic coupling at finite temperatures," *Phys. Rev. A*, vol. 82, p. 033810, Sep 2010.

[76] R. Bonifacio and L. A. Lugiato, *Theory of Optical Bistability*, pp. 61–92. Berlin, Heidelberg: Springer Berlin Heidelberg, 1982.

[77] Grynberg, G. and Cribier, S., "Critical exponents in dispersive optical bistability," *J. Physique Lett.*, vol. 44, no. 12, pp. 449–453, 1983.

[78] C. Kuehn, "Scaling of saddle-node bifurcations: degeneracies and rapid quantitative changes," *Journal of Physics A: Mathematical and Theoretical*, vol. 42, no. 4, p. 045101, 2009.

[79] P. Macha, G. Oelsner, J.-M. Reiner, M. Marthaler, S. André, G. Schön, U. Hübner, H.-G. Meyer, E. Il'ichev, and A. V. Ustinov, "Implementation of a quantum metamaterial using superconducting qubits," *Nat Commun*, vol. 5, p. 5146, 10 2014.

[80] K. V. Shulga, P. Yang, G. P. Fedorov, M. V. Fistul, M. Weides, and A. V. Ustinov, "Observation of a collective mode of an array of transmon qubits," *JETP Lett.*, vol. 105, p. 47, 2017.

[81] J. Kabuss, D. O. Krimer, S. Rotter, K. Stannigel, A. Knorr, and A. Carmele, "Analytical study of quantum-feedback-enhanced rabi oscillations," *Phys. Rev. A*, vol. 92, p. 053801, Nov 2015.

[82] R. J. Glauber and M. Lewenstein, "Quantum optics of dielectric media," *Phys. Rev. A*, vol. 43, pp. 467–491, Jan 1991.

[83] E. Economou, *Green's Functions in Quantum Physics*. Springer Series in Solid-State Sciences, Springer, 2006.

[84] X. Zhou, I. Dotsenko, B. Peaudecerf, T. Rybarczyk, C. Sayrin, S. Gleyzes, J. M. Raimond, M. Brune, and S. Haroche, "Field locked to a fock state by quantum feedback with single photon corrections," *Phys. Rev. Lett.*, vol. 108, p. 243602, Jun 2012.

[85] F. Albert, C. Hopfmann, S. Reitzenstein, C. Schneider, S. Höfling, L. Worschech, M. Kamp, W. Kinzel, A. Forchel, and I. Kanter, "Observing chaos for quantum-dot microlasers with external feedback," *Nature Communications*, vol. 2, p. 366, 06 2011.

[86] A. L. Grimsmo, A. S. Parkins, and B.-S. Skagerstam, "Rapid steady-state convergence for quantum systems using time-delayed feedback control," *New Journal of Physics*, vol. 16, no. 6, p. 065004, 2014.

PHYSICAL REVIEW A **90**, 043852 (2014)

# Non-Markovian dynamics of a single-mode cavity strongly coupled to an inhomogeneously broadened spin ensemble

Dmitry O. Krimer,[1,*] Stefan Putz,[2] Johannes Majer,[2] and Stefan Rotter[1]
[1]*Institute for Theoretical Physics, Vienna University of Technology, Wiedner Hauptstrasse 8-10/136, 1040 Vienna, Austria*
[2]*Vienna Center for Quantum Science and Technology, Atominstitut, Vienna University of Technology, Stadionallee 2, 1020 Vienna, Austria*

(Received 25 July 2014; published 24 October 2014)

We study the dynamics of a spin ensemble strongly coupled to a single-mode resonator driven by external pulses. When the mean frequency of the spin ensemble is in resonance with the cavity mode, damped Rabi oscillations are found between the spin ensemble and the cavity mode which we describe very accurately, including the dephasing effect of the inhomogeneous spin broadening. We demonstrate that a precise knowledge of this broadening is crucial both for a qualitative and a quantitative understanding of the temporal spin-cavity dynamics. On this basis we show that coherent oscillations between the spin ensemble and the cavity can be enhanced by a few orders of magnitude, when driving the system with pulses that match special resonance conditions. Our theoretical approach is tested successfully with an experiment based on an ensemble of negatively charged nitrogen-vacancy centers in diamond strongly coupled to a superconducting coplanar single-mode waveguide resonator.

DOI: 10.1103/PhysRevA.90.043852 PACS number(s): 42.50.Pq, 42.50.Ct, 42.50.Gy, 61.72.jn

## I. INTRODUCTION

Over the past decade various setups in cavity quantum electrodynamics (QED) have been studied in terms of their potential for future technologies involving the storage and processing of quantum information. Among different hybrid quantum systems [1], the ones based on spin, atomic or even molecular ensembles coupled to superconducting microwave cavities have recently attracted much attention [2–10] (see Fig. 1). In such systems the spin or atomic ensemble plays the role of a quantum memory, to which the quantum information is coherently stored and retrieved from at some later time. The cavity, in turn, serves as a quantum bus for the in- and output of information as well as for the coupling between several constituents of such hybrid quantum systems (see, e.g., [5]). One of the necessary conditions for the coherent transfer of quantum information between an ensemble and a cavity is the strong coupling between them. Fortunately, various spin ensembles, as, for instance, negatively charged nitrogen-vacancy (NV) defects in diamond [2–6], rare-earth spin ensembles [7], clouds of ultracold atoms [9,11] or magnons in yttrium iron garnet with or without doping [12,13], may satisfy this requirement when being collectively coupled to [14]. We also note that in recent proposals the direct coupling of a qubit to such spin ensembles has been suggested without any cavity being involved [15,16].

Here we study the dynamics of a superconducting cavity strongly coupled to an ensemble of negatively charged NV centers. Each individual NV center can possess a sufficiently long coherence time [17] needed for the coherent transfer of quantum information. However, since the local magnetic dipole-dipole couplings of NV centers constituting the ensemble to the bath of magnetic impurities (such as nitrogen atoms not converted into NV centers) slightly differ from each other, the NV electron spin resonance line of a large ensemble is inhomogeneously broadened [18]. This line broadening acts as the main source of decoherence, and constitutes a significant drawback of this solid-state spin ensemble leading to a drastic decrease of its coherence time. Several approaches including echo-type refocusing techniques [19,20] have meanwhile been suggested to overcome this limitation. Recent stationary transmission studies demonstrate that the decoherence can be strongly suppressed altogether [21,22] when the spin density has a spectral distribution with tails that decay sufficiently fast [3,21,22]. In this paper we report on a detailed time-dependent study for exactly such a case and demonstrate how the corresponding dynamics can be efficiently captured using a Volterra integral equation for the cavity amplitude [23]. The excellent correspondence between our theoretical model and a corresponding experiment allows us to closely look into the fascinating features following from a pulsed driving of this hybrid quantum system in the strong-coupling regime.

Our paper is organized as follows. In Sec. II we present the theoretical framework of our problem and summarize the most important assumptions made. We sketch the general form of the equations obtained, describing the two methods for solving the Volterra equation in Appendices A and B. Furthermore, we discuss the specific experimental realization of our theory. In Sec. III, we consider the dynamics under the action of a long rectangular microwave pulse which allows us to obtain the precise form for the spin density and its parameters by detailed comparison with the experimental results. We also present analytical results for a Lorentzian spin density distribution and demonstrate which features are captured by this approximation and which are not. Section IV will then address the question of how the decoherence in our system caused by inhomogeneous broadening changes as a function of the coupling strength. We show that a non-Lorentzian functional profile of the spin distribution leads to a strong suppression of decoherence for large values of the coupling strength—an effect known as "cavity protection" [21,22]. Finally, in Sec. V, we propose a scheme which allows us to induce giant coherent oscillations between the cavity and our spin ensemble as well as to transfer energy into the spin ensemble very efficiently.

---

[*] dmitry.krimer@gmail.com

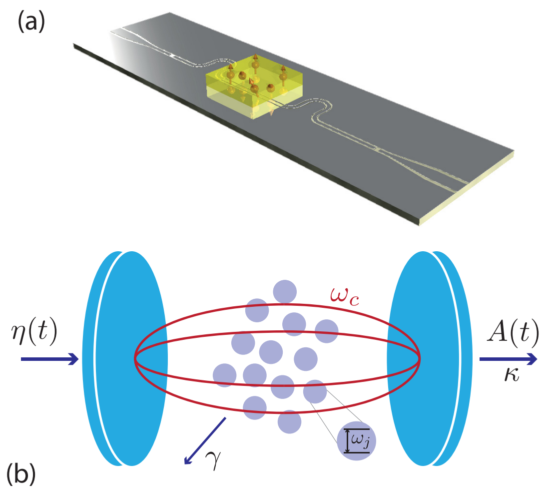

FIG. 1. (Color online) Sketch of the hybrid quantum system studied in this paper: (a) a spin ensemble (yellow) coupled to a transmission-line resonator (gray) confining the electromagnetic field inside a small volume. (b) Scheme of the spin ensemble-cavity coupled system. An incoming signal $\eta(t)$ passes through the cavity characterized by a frequency $\omega_c$ which is coupled to a spin ensemble with each individual spin of frequency $\omega_j$. The transmitted signal is proportional to the cavity amplitude $A(t)$. $\kappa$ and $\gamma$ stand for the cavity and spin losses, respectively.

## II. THEORETICAL MODEL

We study the temporal dynamics of a system consisting of a large spin ensemble coupled with a single-mode cavity via magnetic or electric dipole interaction. We assume that the distance between spins is large enough such that the dipole-dipole interactions between spins can be neglected. Our starting point is the Tavis-Cummings Hamiltonian ($\hbar = 1$) [24],

$$\mathcal{H} = \omega_c a^\dagger a + \frac{1}{2}\sum_j^N \omega_j \sigma_j^z + i\sum_j^N [g_j \sigma_j^- a^\dagger - g_j^* \sigma_j^+ a] - i[\eta(t) a^\dagger e^{-i\omega_p t} - \eta(t)^* a e^{i\omega_p t}], \quad (1)$$

where $a^\dagger$ and $a$ are standard creation and annihilation operators of the single cavity mode with frequency $\omega_c$ and $\sigma_j^+, \sigma_j^-, \sigma_j^z$ are the Pauli operators associated with each individual spin of frequency $\omega_j$. An incoming signal is characterized by the carrier frequency $\omega_p$ and by the amplitude $\eta(t)$ whose time variation is much slower as compared to $1/\omega_p$. The interaction part of $\mathcal{H}$ is written in the dipole and rotating-wave approximation (terms $\propto a\sigma_j^-, a^\dagger\sigma_j^+$ are neglected), where $g_j$ stands for the coupling strength of the $j$th spin.

Despite the fact that each individual spin is coupled weakly to the cavity, one can nevertheless reach the strong-coupling regime due to the large number of spins which are collectively coupled to the cavity mode (see, e.g., [2,5,9] for NV spin ensembles). The effect of collective coupling is particularly evident when reducing the interaction term to a collective term $\Omega(S^- a^\dagger - S^+ a)$ [25], where the collective spin operators are given by $S^\pm = N^{-1/2}\sum_j^N \sigma_j^\pm$. The prefactor $\Omega^2 = \sum_j^N g_j^2$ stands for an effective coupling strength, which scales up a single coupling strength $g_j$, by a factor of $\sqrt{N}$, so that $\Omega$ can be sufficiently enhanced for the realization of the strong-coupling regime. In this formulation the effective spin waves that are excited by the cavity mode can be identified as superradiant collective Dicke states which are effectively damped by the coupling to subradiant states in the ensemble [14,21,22]. Note that the rotating-wave approximation mentioned above is applicable only if $\Omega \ll \omega_c$.

Next, we derive the Heisenberg operator equations, for the cavity and spin operators, $\dot{a} = i[\mathcal{H},a] - \kappa a, \dot{\sigma}_k^- = i[\mathcal{H},\sigma_k^-] - \gamma\sigma_k^-$, respectively. Here $\kappa$ and $\gamma$ stand for the total dissipative cavity and spin losses. Strictly speaking, the noise operators should also be added to the right-hand side of these equations in order to preserve the commutation relations. However, their expectation values vanish as was shown already in earlier works [21,22] on the example of an NV ensemble and therefore these terms are not included here explicitly. These Heisenberg equations describe the dynamics to a very high accuracy, provided that the energy of photons of the external bath is substantially smaller than that of cavity photons, $kT \ll \hbar\omega_c$. We then write a set of equations for the expectation values, $\langle a(t)\rangle$ and $\langle \sigma_k^-(t)\rangle$ in the frame rotating with the probe frequency $\omega_p$. In what follows the amplitude of the pumping signal $\eta(t)$ is taken to be rather small and therefore the number of the excited spins is always small compared to the ensemble size. This allows us to simplify these equations further by setting $\langle \sigma_k^z \rangle \approx -1$ (Holstein-Primakoff-approximation [26]). With all these simplifications the equations for the cavity and spin amplitudes become

$$\dot{A}(t) = -[\kappa + i(\omega_c - \omega_p)]A(t) + \sum_k g_k B_k(t) - \eta(t), \quad (2a)$$

$$\dot{B}_k(t) = -[\gamma + i(\omega_k - \omega_p)]B_k(t) - g_k A(t), \quad (2b)$$

where $A(t) \equiv \langle a(t)\rangle$ and $B_k(t) \equiv \langle \sigma_k^-(t)\rangle$.

### A. Experimental realization

In the following, we will compare our theoretical model with one specific experimental realization, namely a $\lambda/2$ superconducting microwave coplanar waveguide resonator magnetically coupled with a spin ensemble of negatively charged NV centers in diamond. The corresponding experiment is carried out in a standard dilution refrigerator with a synthetic diamond placed on top of a resonator cooled to millikelvin temperatures (~25 mK) (see [23] for more details). The concentration of NV centers in diamond is sufficiently low and the distance between spins is still large enough, so that the dipole-dipole interactions between spins is negligibly small justifying the assumption of our model. By applying an external magnetic field, two degenerate subensembles, which can effectively be considered as a single subensemble, are brought into resonance with the cavity, whereas the other subensembles make a slight dispersive contribution only and their influence is neglected here (see, e.g., [2,3,23] for more details). The individual spins are distributed around the mean frequency $\omega_s = 2\pi 2.6915$ GHz, with the width $\Delta \ll \omega_s$, which is of the order of 10 MHz. The coupling strength of each individual spin with a cavity mode is typically of the order of $g_j/2\pi \sim 10$ Hz [9]. However, the effective coupling

$\Omega$ is enhanced by a factor of $\sqrt{N}$ with the ensemble size $N \sim 10^{12}$, so that $\Omega$ can reach values as large as 10 MHz which is sufficient to reach the strong-coupling regime. Note that the energy of thermal photons is substantially smaller than that of microwave photons, $kT \ll \hbar\omega_c$, resulting in an occupation probability of the ensemble in the ground state which is larger than 0.99. In what follows, the cavity frequency was taken to be always equal to the spin mean frequency, $\omega_c = \omega_s = 2\pi 2.6915$ GHz. Therefore the inequality $\Omega \ll \omega_c$ always holds and the rotating-wave approximation is very well fulfilled. Note also that the spin dissipation is much smaller than the cavity dissipation, $\gamma \ll \kappa$, so that the former does not contribute to the dynamics realized in the experiment. We thus omitted $\gamma$ everywhere, except when necessary for the calculation of some integrals which would otherwise be singular.

### B. Setting up the Volterra integral equation

Owing to the large number of spins within the ensemble ($N \sim 10^{12}$), there are a lot of spins in each frequency subinterval around $\omega_s$ which make a non-negligible contribution to the dynamics. We can thus introduce a continuous spectral density as $\rho(\omega) = \sum_k g_k^2 \delta(\omega - \omega_k)/\Omega^2$, where $\Omega^2 = \sum_j^N g_j^2$ is the collective coupling strength of the spin ensemble to the cavity, satisfying the normalization condition $\int d\omega \rho(\omega) = 1$. As we shall see below, one should take special care when choosing the functional profile of the spectral distribution for the spin density $\rho(\omega)$, which describes its inhomogeneous broadening and which plays a crucial role for the dynamics.

To go to the continuous limit (in frequency) we carry out the following formal replacement from the discrete function $F(\omega_k)$ to the continuous one, $F(\omega)$: $\sum_k F(\omega_k) \to \Omega^2 \int d\omega \rho(\omega) F(\omega)$. By integrating Eq. (2b) in time, each individual spin amplitude, $B_k(t)$, can be expressed in terms of the cavity amplitude, $A(t)$, as

$$B_k(t) = B_k(0) e^{-i(\omega_k - \omega_p - i\gamma)t} - g_k \int_0^t d\tau e^{-i(\omega_k - \omega_p - i\gamma)(t-\tau)} \cdot A(\tau), \tag{3}$$

where $B_k(0)$ is the initial spin amplitude. Substituting Eq. (3) into Eq. (2a) we arrive at the Volterra equation for the cavity amplitude $A(t)$,

$$\dot{A}(t) = -i(\omega_c - \omega_p - i\kappa)A(t) + \sum_k g_k B_k(0) e^{-i(\omega_k - \omega_p - i\gamma)t} - \Omega^2 \int_0^\infty d\omega \rho(\omega) \int_0^t d\tau e^{-i(\omega - \omega_p - i\gamma)(t-\tau)} A(\tau) - \eta(t). \tag{4}$$

After integrating Eq. (4) in time, performing lengthy but straightforward algebraic calculations and assuming that the cavity is initially empty, $A(0) = 0$, and all spins are initially in the ground state, $B_k(0) = 0$, we end up with the following Volterra equation for the cavity amplitude,

$$A(t) = \int_0^t d\tau \mathcal{K}(t - \tau) A(\tau) + \mathcal{F}(t), \tag{5}$$

which contains the kernel function $\mathcal{K}(t - \tau)$,

$$\mathcal{K}(t - \tau) = \Omega^2 \int_0^\infty d\omega \frac{\rho(\omega)[e^{-i(\omega - \omega_c + i\kappa)(t-\tau)} - 1]}{i(\omega - \omega_c + i\kappa)} \times e^{-i(\omega_c - \omega_p - i\kappa)(t-\tau)}, \tag{6}$$

and the function $\mathcal{F}(t)$,

$$\mathcal{F}(t) = -\int_0^t d\tau\, \eta(\tau) e^{-i(\omega_c - \omega_p - i\kappa)(t-\tau)}, \tag{7}$$

where the amplitude $\eta(t)$ represents an arbitrarily shaped incoming pulse or a sequence of pulses. Note that the kernel function $\mathcal{K}(t - \tau)$ accounts for memory effects and leads in general to a non-Markovian feedback of the NV ensemble on the cavity. In Appendices A and B we give a detailed description of the two methods which allow us to solve the Volterra equation in a very efficient way.

Having calculated the cavity amplitude $A(t)$, we can find the expectation values of the collective spin operator, $J_x + iJ_y = \sum_k g_k B_k(t)/[2(\sum_i g_i^2)^{1/2}]$, which in the continuous limit and for the initial conditions $A(0) = 0$ and $B_k(0) = 0$ introduced above read as follows:

$$J_x + iJ_y = -\frac{\Omega}{2} \int_0^\infty d\omega \rho(\omega) \int_0^t d\tau e^{-i(\omega - \omega_c)(t-\tau)} A(\tau). \tag{8}$$

The $z$ component of the expectation value of the collective spin operator, $J_z = \sum_k \langle \sigma_k^z \rangle / (2\sqrt{N})$, remains $J_z \approx -\sqrt{N}$, in accordance with the approximations discussed above.

Note that Eqs. (2a) and (2b), as well as the resulting Volterra equation (4) are linear equations with respect to the cavity and spin amplitudes, $A(t)$ and $B_k(t)$, respectively. We can thus always rescale our solution by multiplying the amplitude of the driving signal $\eta(t)$, by an arbitrary scaling factor. In the following we take the amplitude of the incoming signal equal to the cavity decay rate, $\eta = \kappa$. Note that such a choice corresponds to the situation when the incoming signal, being in a coherent state, gives rise to a single photon in the empty cavity on average. The experimental curves will be appropriately rescaled with a constant prefactor such as to match the corresponding theoretical curves.

## III. DYNAMICS UNDER THE ACTION OF A LONG PULSE

In order to choose an appropriate form for the spectral density $\rho(\omega)$, we compare our numerical results with the experiment performed within the strong-coupling regime. Specifically, we apply a rectangular microwave pulse [$\eta(t) = \eta$ for $0 \leqslant t \leqslant \tau_d$ and $\eta(t) = 0$ otherwise; see Eq. (7)], with the resonance carrier frequency ($\omega_p = \omega_c = \omega_s$). This pulse has a duration $\tau_d$ substantially longer than the resulting period of damped Rabi oscillations and the inverse of the total decay rate, so that the system sets into a steady state before the signal is turned off [see Fig. 2(a)]. Note that the total decay rate describes the overall decoherence in our system which consists of two contributions: The first one is due to dissipative cavity losses $\kappa$, while the second one originates from the inhomogeneous broadening of the spin ensemble which leads to the dephasing of spins during the time evolution. As we shall see below, this dephasing mechanism gives the dominant

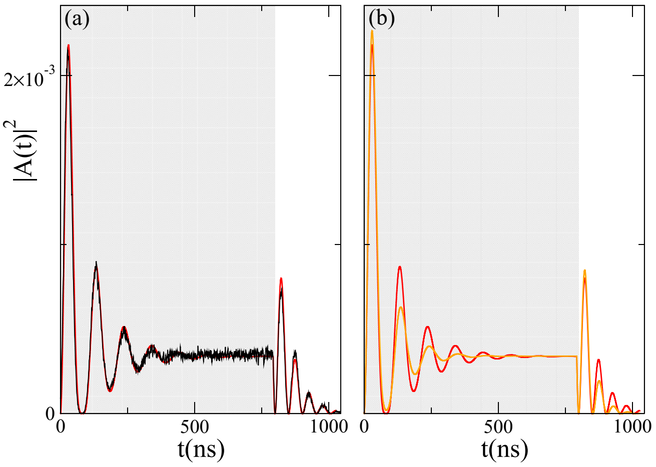

FIG. 2. (Color online) Cavity probability amplitude $|A(t)|^2$ versus time $t$ under the action of an incident long rectangular pulse of duration 800 ns with the carrier frequency matching the resonance condition, $\omega_p = \omega_c = 2\pi 2.6915$ GHz, where $\omega_c$ stands for the cavity resonance frequency. Gray (white) area indicates a time interval during which the pumping signal is on (off). (a) (Taken from [23].) Red (gray) curve shows numerical results for the cavity transmission at a coupling strength $\Omega/2\pi = 8.56$ MHz. In the calculations the spectral density is modeled by a $q$-Gaussian distribution. The frequency of Rabi oscillations, $\Omega_R = 2\pi 19.2$ MHz. Black curve shows experimental results for the cavity transmission. (b) Red (gray) curve is the same as in (a). Orange (light gray) curve shows results of numerical calculations assuming a Lorentzian distribution of the spin density.

contribution to the decoherence (the spin dissipation $\gamma$ is negligible in our case).

In accordance with our previous study [3,23], we obtain a very good agreement between theory and experiment, when taking a $q$ Gaussian [27] as the distribution function for the spectral density defined as

$$\rho(\omega) = C\left[1 - (1-q)\frac{(\omega-\omega_s)^2}{\Delta^2}\right]^{\frac{1}{1-q}}. \tag{9}$$

Here $q$ is the dimensionless shape parameter, $1 < q < 3$, $\gamma_q = 2\Delta\sqrt{\frac{2^q-2}{2q-2}}$ is the full width at half maximum (FWHM), and $C$ is the normalization constant. Note that for $q \to 1$ and $q = 2$ we recover a Gaussian and Lorentzian distribution, respectively. From the comparison with the experiment, we extracted the following parameters used in our calculations: $q = 1.39$, $\gamma_q/2\pi = 9.4$ MHz, and $\kappa/2\pi = 0.8$ MHz (FWHM of the cavity decay). We have also tested other lineshapes for describing the spectral spin density such as the stable alpha distribution, but found them to be less suitable for describing the experimentally observed data.

An interesting and, at first sight, surprising fact is that the first Rabi peak of the cavity amplitude after switching off the microwave signal is approximately twice as large as the steady-state amplitude, as seen in Fig. 2(a). This overshoot effect takes place after the incoming signal is turned off, because the energy stored in the spin ensemble is released back to the cavity and interferes constructively with the energy stored there (see Appendix C for more details). It will be shown in the next section that this overshoot appears only if the coupling strength is larger than a certain critical value. In addition to this condition, the overshoot effect also requires a finite amount of energy being stored in the spin ensemble, but does not show up if it is in the ground state and the field inside the cavity is described by a Fock state, as, for instance, when it is fed with a single photon (see Appendix B).

### A. Dynamics for a Lorentzian spin density distribution

To illustrate the importance of the spectral spin distribution, we have also tried to achieve an agreement with the experiment when assuming a Lorentzian instead of a $q$-Gaussian distribution for the spectral density,

$$\rho(\omega) = \frac{\Delta}{\pi[(\omega-\omega_s)^2 + \Delta^2]}. \tag{10}$$

For this purpose, we adapt the parameters such that the period of the resulting Rabi oscillations and the cavity amplitude at the steady state agree with the measurements [see Fig. 2(b)]. As seen there, the Lorentzian predicts a sufficiently larger decay rate as compared to that observed in the experiment [compare the values of the Rabi peaks during damped Rabi oscillations for the $q$ Gaussian and for the Lorentzian distributions shown in Fig. 2(b)]. Such an inadequate overestimation of the total decay rate becomes particularly pronounced in the case of even higher values of the coupling strength as those used in Fig. 2 (see Sec. IV for more details). Nevertheless, it is very instructive to consider at first the simple picture associated with a Lorentzian distribution, because in this case the problem can be solved analytically giving intuitive insights into the dynamical properties of our system. By plugging the Lorentzian distribution (10) into Eq. (4) and assuming that the cavity is initially empty, $A(0) = 0$, and spins are unexcited, $B_k(0) = 0$, we obtain the following Volterra equation (in the frame rotating with $\omega_p$) under the action of a rectangular microwave pulse introduced above for $t \leqslant \tau_d$:

$$\dot{A}(t) = -\kappa A(t) - \Omega^2 \int_0^t d\tau e^{-\Delta(t-\tau)} A(\tau) - \eta. \tag{11}$$

By differentiating Eq. (11) with respect to time, and after doing some algebra, the above equation reduces to the one for a damped harmonic oscillator driven by a time-independent external force,

$$\ddot{A}(t) + [\Delta + \kappa]\dot{A}(t) + [\Omega^2 + \Delta\kappa]A(t) + \eta\Delta = 0. \tag{12}$$

The solution of Eq. (11), which is also the one of Eq. (12), can be represented as $A(t) = \alpha e^{\lambda_1 t} + \beta e^{\lambda_2 t}$, so that the dynamics is characterized by two exponents, namely,

$$\lambda_{1,2} = [-(\Delta+\kappa) \pm \sqrt{(\Delta-\kappa)^2 - 4\Omega^2}]/2. \tag{13}$$

In the strong-coupling regime the dynamics is underdamped, the expression under the square root is negative, and the system exhibits damped oscillations with the Rabi frequency,

$$\Omega_R = \sqrt{4\Omega^2 - (\Delta-\kappa)^2}, \tag{14}$$

and the decay rate of $|A(t)|^2$ is $\Gamma = \Delta + \kappa$. It is worth noting that for the case shown in Fig. 2(b), the expression (14) for the Rabi frequency can be approximated as $\Omega_R \approx 2\Omega$. Finally, we obtain the following expression for the cavity amplitude for $t \leqslant \tau_d$,

$$A(t) = -\frac{\Delta\eta}{\Omega^2 + \Delta\kappa} + \frac{\eta e^{-(\Delta+\kappa)t/2}}{2\Omega_R(\Omega^2 + \Delta\kappa)} \times \left[2\Omega_R \Delta \cos(\Omega_R t/2) - \left[\Omega_R^2 - \Delta^2 + \kappa^2\right] \sin(\Omega_R t/2)\right]. \quad (15)$$

The reason why $A(t) \in \mathbb{R}$ in Eq. (15) is due to the fact that the Lorentzian distribution (10) is symmetric with respect to $\omega_s$, and $\omega_p = \omega_c = \omega_s$. For the same reason the $y$ component of the collective spin $J_y = 0$, whereas $J_x(t)$ can easily be determined from Eq. (2a),

$$J_x(t) = \frac{\sum_k g_k B_k(t)}{2\Omega} = \frac{\dot{A}(t) + \kappa A(t) + \eta}{2\Omega}. \quad (16)$$

Indeed, by inserting the solution (15) into this equation we get

$$J_x(t) = \frac{\eta\Omega}{2(\Omega^2 + \Delta\kappa)} - \frac{\eta\Omega e^{-(\Delta+\kappa)t/2}}{2\Omega_R(\Omega^2 + \Delta\kappa)} \times \left[(\Delta + \kappa)\sin(\Omega_R t/2) + \Omega_R \cos(\Omega_R t/2)\right]. \quad (17)$$

By differentiating Eq. (2a) with respect to time twice, making use of Eq. (12), and performing straightforward algebraic calculations, we find that $J_x(t)$ obeys also the following equation:

$$\ddot{J}_x(t) + \Delta \dot{J}_x(t) + \Omega^2 J_x(t) - \frac{\kappa\Omega}{2} A(t) - \frac{\eta\Omega}{2} = 0. \quad (18)$$

Therefore in the case of a Lorentzian distribution the dynamics can be modeled by two coupled damped harmonic oscillators governed by Eqs. (12) and (18).

Thus, after switching on a rectangular microwave signal our system exhibits damped Rabi oscillations and it tends finally to a steady state,

$$A_{\mathrm{st}} = -\frac{\Delta\eta}{\Omega^2 + \Delta\kappa}, \quad J_x^{\mathrm{st}} = \frac{\eta\Omega}{2(\Omega^2 + \Delta\kappa)}, \quad J_y^{\mathrm{st}} = 0, \quad (19)$$

provided that the pulse duration is long enough, i.e., $\tau_d \gg 1/(\Delta + \kappa)$. (Note that this condition is very well fulfilled in Fig. 2.) Inserting the Lorentzian profile (10) into Eq. (C6) from Appendix C yields the equation for the cavity amplitude $A(t)$, which governs the decay process from the steady state given by Eq. (19):

$$\dot{A}(t) = -\kappa A(t) + \frac{\eta\Omega^2 \cdot e^{-\Delta t}}{\Omega^2 + \kappa\Delta} - \Omega^2 \int_0^t d\tau e^{-\Delta(t-\tau)} A(\tau), \quad (20)$$

where, for the sake of simplicity, the time is counted from zero as the pulse is turned off. As discussed in detail before and also in Appendix C, the second term in Eq. (20) stands for the excitation stored in the spin ensemble, which is coherently released back into the cavity, after switching off the microwave pulse. Similarly as done above, we can derive from Eq. (20) a damped harmonic oscillator equation, $\ddot{A}(t) + [\Delta + \kappa]\dot{A}(t) + [\Omega^2 + \Delta\kappa]A(t) = 0$, so that finally the damped Rabi oscillations of the cavity amplitude and the $x$ component of the collective spin to the ground state for $t \geqslant \tau_d$ are solved by

$$A(t) = \frac{\eta \cdot e^{-(\Delta+\kappa)(t-\tau_d)/2}}{2\Omega_R(\Omega^2 + \Delta\kappa)}\left[-2\Omega_R\Delta\cos(\Omega_R(t-\tau_d)/2) + \left(\Omega_R^2 - \Delta^2 + \kappa^2\right)\sin(\Omega_R(t-\tau_d)/2)\right], \quad (21)$$

$$J_x(t) = \frac{\eta\Omega e^{-(\Delta+\kappa)(t-\tau_d)/2}}{2\Omega_R(\Omega^2 + \Delta\kappa)}\left[(\Delta + \kappa)\sin\left(\Omega_R(t-\tau_d)\right) + \Omega_R \cos(\Omega_R(t-\tau_d)/2)\right]. \quad (22)$$

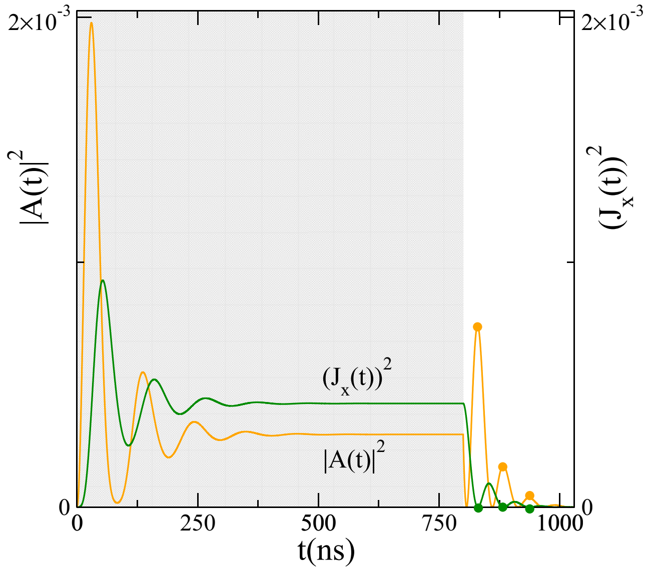

FIG. 3. (Color online) Cavity probability amplitude $|A(t)|^2$ and the corresponding $x$ component of the collective spin $J_x^2(t)$ versus time $t$ under the action of an incident long pulse assuming a Lorentzian spin distribution, given by Eqs. (15) and (21), and (17) and (22), respectively. $|A(t)|^2$ coincides with the orange (light gray) curve from Fig. 2(b). Symbols designate the maxima and minima of $|A(t)|^2$ and $J_x^2(t)$ during the damped Rabi oscillations. The carrier frequency matches the resonance condition, $\omega_p = \omega_c = 2\pi 2.6915$ GHz, and the frequency of Rabi oscillations, $\Omega_R = 2\pi 19.2$ MHz. Gray (white) area indicates the time interval during which the pumping signal is on (off).

In Fig. 3, $|A(t)|^2$ and $J_x^2(t)$, defined by Eqs. (15) and (21) and by Eqs. (17) and (22), respectively, are plotted versus time $t$. Note that this analytical solution for the cavity probability, $|A(t)|^2$, perfectly coincides with the one found numerically which is depicted in Fig. 2(b). (For that reason the analytical solution is not shown in this figure.) One sees that the cavity and spin ensemble exchange their energies during the time evolution, so that maxima of $A^2(t)$ correspond to minima of $J_x^2(t)$ or, in other words, the energy inside the cavity is maximal at those moments of time, when the energy stored in the ensemble is entirely emitted back into the cavity.

Let us summarize the collective spin dynamics under the action of a long pulse governed by Eqs. (17) and (22) in the $\omega_p$-rotating frame. Since $J_z \approx -\sqrt{N}$ is always valid, our dynamics is restricted to the vicinity of the pole of the Bloch sphere. Additionally, $J_y = 0$ owing to symmetry arguments. As a rectangular microwave signal is turned on, the $x$ component $J_x(t)$ exhibits damped Rabi oscillations starting

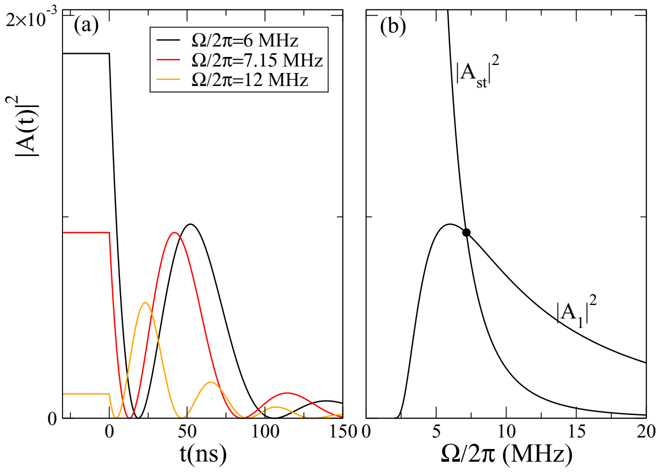

FIG. 4. (Color online) Damped Rabi oscillations from the stationary state which the system exhibits after the action of an incident long pulse assuming a Lorentzian spin distribution. (a) Cavity probability amplitude given by Eq. (21), versus time for three different values of the coupling strengths, $\Omega/2\pi = 6, 7.15$ and 12 MHz [black, red (gray), orange (light gray)]. The carrier frequency matches the resonance condition, $\omega_p = \omega_c = 2\pi 2.6915$ GHz. The lowest value for the stationary state corresponds to the highest value of $\Omega$ in accordance with Eq. (19). (b) The amplitude of the stationary state $|A_{\rm st}|^2$ and the amplitude of the first maximum $|A_1|^2$, versus coupling strength $\Omega$ during the damped Rabi oscillations [see Eqs. (19) and (23)]. Black symbol designates the intersection between these two curves at the value of coupling strength $\Omega/2\pi = 7.15$ MHz, below which the overshoot effect is absent.

from the ground state and tends towards a steady state $J_x^{\rm st}$. After the signal is switched off, $J_x(t)$ again undergoes damped Rabi oscillations and returns to its initial state on the pole of the Bloch sphere. These spin components in the $\omega_p$-rotating frame are connected with those in the laboratory frame as follows: $J_x^{\rm lab}(t) = J_x(t)\cos(\omega_p t)$, $J_y^{\rm lab}(t) = J_x(t)\sin(\omega_p t)$, and $J_z^{\rm lab}(t) = J_z(t) \approx -\sqrt{N}$. From these expressions follows that in the laboratory frame high frequency oscillations are superimposed on the damped Rabi oscillations found in the $\omega_p$ frame. Moreover, the steady state in the $\omega_p$ frame is represented by a simple precession around the $z$ axis in the laboratory frame.

We show in Fig. 4 that the first Rabi peak of the cavity amplitude after switching off the driving pulse may exceed the corresponding steady-state value (overshoot effect), if the value of the coupling strength is above a certain threshold. As discussed earlier in this section, this effect is in principle possible due to the fact that in the steady state at constant driving nonzero energy is preliminarily stored in the spin ensemble. However, the smaller the coupling strength $\Omega$ is, the larger the value of the cavity amplitude $|A_{\rm st}|$, and the weaker the excitation of the spin ensemble $|J_x^{\rm st}|$; see Eq. (19). In the limiting case of $\Omega \to 0$, there is no coupling to the spin ensemble, and it remains unexcited, $J_x^{\rm st} = 0$, whereas $|A_{\rm st}|$ acquires its maximal value, $|A_{\rm st}| = \eta/\kappa$. The overshoot effect can be easily quantified analytically by searching for the first maximum of the decaying cavity amplitude (21), which is found to be

$$A_1^2 = A_{\rm st}^2 e^{-\frac{2(\Delta+\kappa)}{\Omega_R}\arccos[-(\Delta-\kappa)/(2\Omega)]}. \tag{23}$$

We present $A_1^2$ and $A_{\rm st}^2$ versus coupling strength $\Omega$ in Fig. 4(b), where one can see that the overshoot effect is realized for $\Omega/2\pi > 7.15$ MHz (for the Lorentzian distribution). Note that the strong-coupling regime, the hallmark of which are Rabi oscillations, terminates at $\Omega/2\pi = 2$ MHz, where $A_1 = 0$. At lower values of the coupling strength the oscillations do not occur and the dynamics becomes Markovian (see Sec. IV for more details).

### B. Dynamics for the *q*-Gaussian spin density distribution

After considering the case of a Lorentzian distribution for the spin density, which allows us to capture some of the important features of the dynamics, we return to the case of the $q$-Gaussian density profile to describe the dynamics accurately and to demonstrate a qualitatively new effect not existing in the framework of the Lorentzian distribution, i.e., the so-called cavity protection effect (see Sec. IV).

In Fig. 5 we present the coherent energy exchange between cavity and spin ensemble under the action of the long pulse, which looks rather similar to the one shown in Fig. 3 for the Lorentzian distribution. For the latter, however, our analysis predicts an overestimated decay rate with deviations that grow to an unacceptable degree for higher values of the coupling strengths as will be demonstrated in Sec. IV. Another

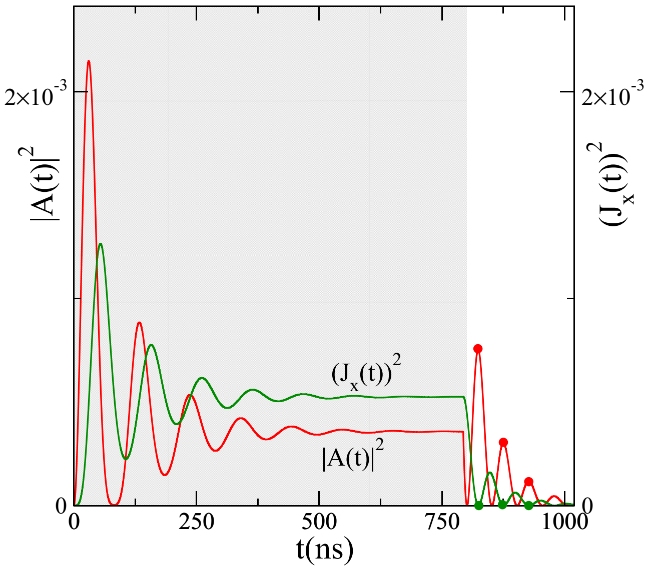

FIG. 5. (Color online) Cavity probability amplitude, $|A(t)|^2$, and the corresponding $x$ component of the collective spin $J_x^2(t)$, versus time $t$ under the action of an incident long pulse for the $q$-Gaussian spin distribution. $|A(t)|^2$ coincides with the red (gray) curve from Fig. 2(b). Symbols designate the maxima and minima of, respectively, $|A(t)|^2$ and $J_x^2(t)$ during the damped Rabi oscillations. The carrier frequency matches the resonance condition, $\omega_p = \omega_c = 2\pi 2.6915$ GHz, and the coupling strength $2\Omega = 2\pi 17.12$ MHz. The frequency of the resulting Rabi oscillations, $\Omega_R = 2\pi 19.2$ MHz. Gray (white) area indicates the time interval during which the pumping signal is on (off).

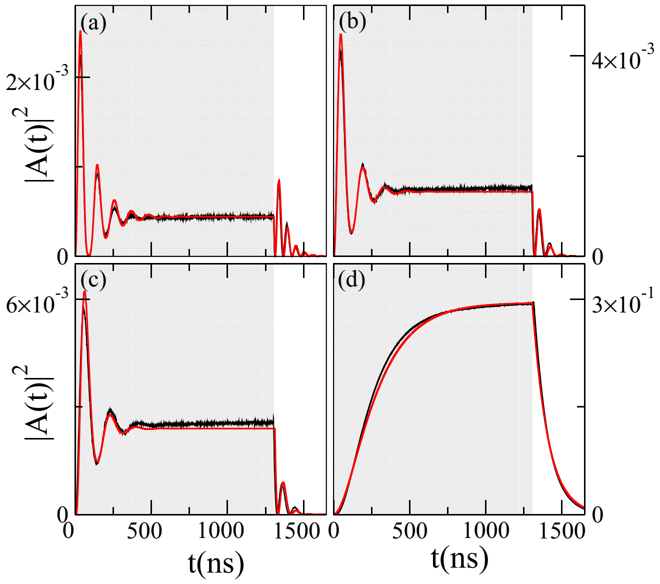

FIG. 6. (Color online) Cavity probability amplitude, $|A(t)|^2$, versus time $t$ under the action of an incident long pulse with the carrier frequency matching the resonance condition, $\omega_p = \omega_c = 2\pi 2.6915$ GHz. The coupling strength $2\Omega$ is (a) $2\pi 15.8$ MHz; (b) $2\pi 12.0$ MHz; (c) $2\pi 10.2$ MHz; (d) $2\pi 2.12$ MHz. Gray (white) area indicates the time interval during which a pumping signal is on (off). [Red (gray) curves] results of numerical calculations; (black curves) experimental results for the cavity transmission.

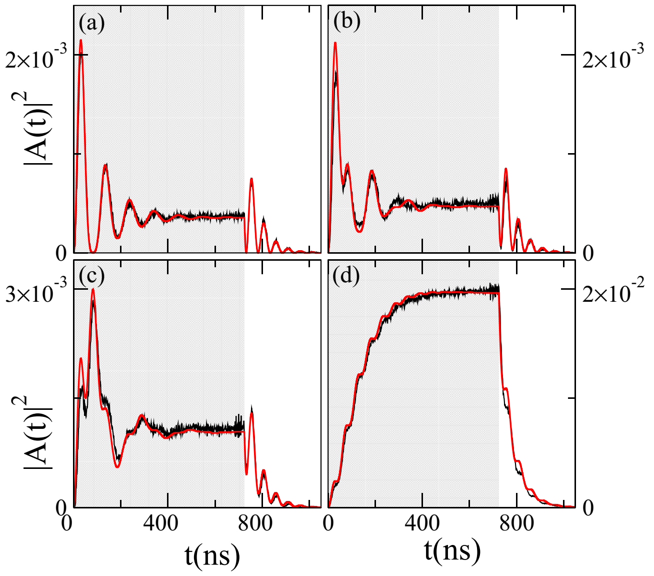

FIG. 7. (Color online) Cavity probability amplitude, $|A(t)|^2$, versus time $t$ under the action of an incident long pulse for different values of the carrier frequency: (a) $\omega_p = \omega_c$; (b) $\omega_p = \omega_c \pm \Omega_R/8$; (c) $\omega_p = \omega_c \pm \Omega_R/4$; (d) $\omega_p = \omega_c \pm \Omega_R/2$, where $\omega_c = 2\pi 2.6915$ GHz and $\Omega_R = 2\pi 19.2$ MHz are, respectively, the cavity and Rabi frequencies. Gray (white) area indicates the time interval during which the driving signal is on (off). Red (gray) curves show results of numerical calculations for the coupling strength $2\Omega = 2\pi 17.12$ MHz. Black curves show experimental results for the cavity transmission.

signature of the non-Lorentzian line shape of our spectral spin distribution $\rho(\omega)$ is that the Rabi frequency $\Omega_R$ deviates significantly from twice the value of the coupling strength $2\Omega$. In other words, our hybrid cavity-spin system cannot be modeled as two coupled damped harmonic oscillators as in the case of a purely Lorentzian spin distribution.

In Fig. 6 we show the dynamics under the action of a long pulse for the resonant case, $\omega_p = \omega_c = \omega_s$, but for different values of the coupling strength $\Omega$ [29]. One can see in Figs. 6(a)–6(d) that the steady-state value, $|A_{\mathrm{st}}|$, increases as $\Omega$ decreases, which is in line with Eq. (C5). One can also see that the value of the first Rabi peak decreases with a decrease of the coupling strength. As a result, the overshoot effect fades away gradually; finally the Rabi oscillations disappear, implying that we enter the regime of Markovian dynamics. As discussed in Sec. III A these features are also qualitatively captured when approximating the spin density by the Lorentzian distribution.

Next, we keep the value for the coupling strength constant (staying in the strong-coupling regime) and vary the probe frequency (see Fig. 7). The larger the mismatch from the resonance condition, $\omega_p = \omega_c = \omega_s$, the less visible the Rabi oscillations, so that finally they become completely blurred. The reason for this behavior is the following: As the probe frequency $\omega_p$ gets increasingly detuned from the central spin frequency $\omega_s$, the phase in the exponential function of Eq. (4) increases at those frequencies where the contribution of $\rho(\omega)$ is non-negligible. As a consequence, during subsequent time integration the resulting integral becomes small due to the fast oscillations of the exponential function, so that the effect of strong coupling smears out. In this case the dynamics is reminiscent of the Markovian regime which occurs right at the resonance condition but for small values for $\Omega$ [see Fig. 6(d)].

We would like to emphasize that in our numerical calculations shown in Figs. 6 and 7, we vary only the values for the coupling strength and probe frequency, whereas all other parameters are kept the same as those in Fig. 2(a). Still, the agreement between our theoretical model and the experiment is found to be excellent.

## IV. CLASSIFICATION OF THE DYNAMICS

To clarify the role played by the non-Lorentzian inhomogeneous broadening, we classify the dynamics by calculating and measuring the total decay rate $\Gamma$ of the cavity amplitude squared, $|A(t)|^2$, from its steady-state value for different coupling strengths $\Omega$. For the sake of simplicity, we focus on the resonant case, $\omega_p = \omega_c = \omega_s$, only. It should be stressed that the total decay rate $\Gamma$ is independent of the initial conditions (see also [23]), so that we can start from simpler initial conditions corresponding to the case when only a single photon is populating the cavity and the spin ensemble is in the ground state, $|1,G\rangle = a^{\dagger}(t=0)|0\rangle$ ($|0\rangle$ corresponds to the vacuum state). In this case it is possible to get a relatively simple form for the Laplace transform of the Volterra equation and to considerably speed up the calculations (see Appendix B). One can prove that the Volterra equation (4) is indeed the governing equation for $A(t)$ also in this case with the initial condition, $A(t=0) = 1$ and $B_k(t=0) = 0$, by virtue of the following arguments. Acting with the Heisenberg operator equations on the bra- and ket-vectors $\langle 0|$ and $a^{\dagger}(t=0)|0\rangle$,

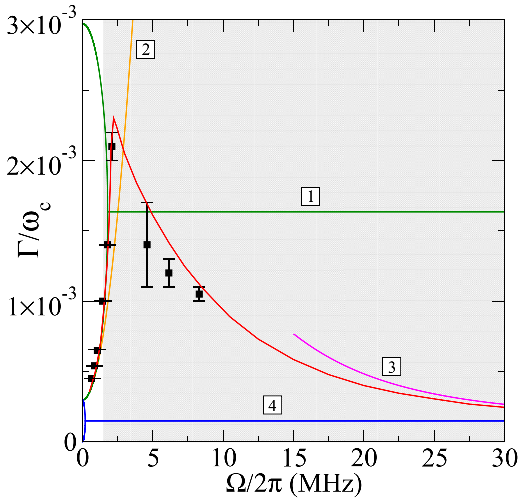

FIG. 8. (Color online) Decay rate $\Gamma$ of the the cavity mode $|A(t)|^2$ versus coupling strength $\Omega$. (Red curve) Decay rates extracted from the full numerical calculations with the $q$-Gaussian spin distribution. (Black symbols) Experimentally observed decay rates. [Green curve (1)] Decay rate under the assumption of a Lorentzian distribution of the spin density. The overdamped regime ($\Omega/2\pi < 1.8$ MHz) is characterised by two exponents given by $\Gamma = \Delta + \kappa \pm \sqrt{(\Delta-\kappa)^2 - 4\Omega^2}$. The regime of underdamped oscillations ($\Omega/2\pi > 1.8$ MHz) with the Rabi frequency (14) has the constant decay rate, $\Gamma = \Delta + \kappa$. [Orange curve (2)] $\Gamma$ derived under Markovian approximation, $\Gamma = 2[\kappa + \pi\Omega^2\rho(\omega_s)]$. [Magenta curve (3)] An estimate for $\Gamma$ within the strong-coupling regime with a well-resolved Rabi splitting in the limit of $\Omega \to \infty$, $\Gamma = \kappa + \pi\Omega^2\rho(\omega_c \pm \Omega)$. [Blue curve (4)] The decay rate in the absence of dephasing. For $\Omega/2\pi < 0.2$ MHz the overdamped regime is characterized by two exponents $\Gamma = \kappa \pm \sqrt{\kappa^2 - 4\Omega^2}$. In the opposite case, $\Omega/2\pi > 0.2$ MHz, the regime of underdamped Rabi oscillations takes place with the Rabi frequency $\sqrt{4\Omega^2 - \kappa^2}$ and the constant decay rate $\Gamma = \kappa$. (White region) Markovian dynamics. (Gray region) Non-Markovian dynamics.

respectively, it can be shown that the corresponding equations for the expectation values coincide with Eqs. (2a) and (2b) from Sec. II. The only formal difference now is that the amplitudes $A(t)$ and $B_k(t)$ are given as $A(t) \equiv \langle 0|a(t)a^\dagger(t=0)|0\rangle$ and $B_k(t) \equiv \langle 0|\sigma_k^-(t)a^\dagger(t=0)|0\rangle$, respectively. Thus the variable $A(t)$ describes the probability amplitude for a photon to be in the cavity at time $t$, if it was there initially, $A(t=0) \equiv \langle 0|a(t=0)a^\dagger(t=0)|0\rangle = \langle 1,G|1,G\rangle = 1$.

The results are presented in Fig. 8, where we show that the decay rate varies surprisingly strongly and in a nonmonotonous fashion with $\Omega$ covering a range of almost one order of magnitude (see the red curve in this figure). Before going to further details, let us analyze at first how the decay rate $\Gamma$ behaves as a function of the coupling strength under different simplifying assumptions.

For the case of a Lorentzian distribution for the spin density, the decay process is characterized by two exponents given by Eq. (13). If $4\Omega^2 > (\Delta-\kappa)^2$, then the Rabi oscillations are underdamped and the total decay rate reduces to $\Gamma = \Delta + \kappa$. In the opposite case, we are dealing with a pure exponential decay without oscillations (overdamped regime) with $\Gamma = \Delta + \kappa \pm \sqrt{(\Delta-\kappa)^2 - 4\Omega^2}$. Thus, the Lorentzian distribution gives rise to qualitatively different behavior for the decay process as compared to the $q$-Gaussian one, since $\Gamma$ remains constant in the whole range of $\Omega$ within the strong-coupling regime. However, as is unambiguously seen in Fig. 8, the nonmonotonic behavior obtained in the framework of the $q$-Gaussian spin density distribution is supported by our experimental data thereby confirming our initial assumption for the shape of this distribution.

In the absence of inhomogeneous broadening, when the spin density function is written as $\rho(\omega) = \delta(\omega - \omega_s)$, the expressions for the decay rate are obtained from those for a Lorentzian distribution by setting its width to zero, $\Delta = 0$. Thus, in the regime of underdamped oscillations we get $\Gamma = \kappa$, whereas in the overdamped regime, $\Gamma = \kappa \pm \sqrt{\kappa^2 - 4\Omega^2}$. Correspondingly, the blue lines in Fig. 8 determine the lowest border for possible decay rates reached in our system, because the values for $\Gamma$ in the presence of inhomogeneous broadening should always be larger than the corresponding ones in the case when it is absent. It is seen from Fig. 8 that this condition is indeed always fulfilled.

Next, we apply the so-called Markov approximation in Eq. (4) with respect to the cavity amplitude $A(t)$ which implies that the memory effects caused by a feedback from the NV ensemble onto the cavity are disregarded. Specifically, we shift the initial time of integration on the right-hand side of Eq. (4) to $-\infty$, put $A(\tau) \approx A(t)$, and make use of the Sokhotski-Plemelj theorem (C5) in the limit of $\gamma \to 0$, when performing the integration with respect to $\omega$. Under all these assumptions the third term on the right-hand side of Eq. (4) reduces to ($\omega_p = \omega_s$),

$$-\Omega^2 \int_0^\infty d\omega\rho(\omega) \int_0^t d\tau e^{-i(\omega-\omega_s-i\gamma)(t-\tau)} A(\tau)$$

$$\approx i\Omega^2 A(t) \int_0^\infty \frac{d\omega\rho(\omega)}{\omega - \omega_s - i\gamma} = -\pi\Omega^2\rho(\omega_s)\cdot A(t). \quad (24)$$

Note that the principal value does not appear in the above equation because $\rho(\omega)/(\omega-\omega_s)$, is an antisymmetric function with respect to the singular point, $\omega = \omega_s$. In the simplest case when there is no driving and all spins are initially in the ground state, the Volterra equation (4) reduces to $\dot{A}(t) = -[\kappa + \pi\Omega^2\rho(\omega_s)]A(t)$. Therefore, the Markov approximation leads to a pure exponential decay with the decay rate, $\Gamma = 2[\kappa + \pi\Omega^2\rho(\omega_s)]$. The spin ensemble density thus gives rise to a significant enhancement of the cavity decay rate as compared to the one for a bare cavity, $\Gamma = 2\kappa$. Remarkably, this effect has a direct analogy to the Purcell enhancement of the spontaneous emission rate of a single emitter inside a cavity [28] which appears due to the increase of the local density of photonic states at the emitter position as compared to the vacuum case. The Markov approximation, however, loses its validity at fairly low coupling strengths, starting to deviate from the real values of $\Gamma$ already at $\Omega/2\pi \approx 1.5$ MHz (see Fig. 8). The hallmark of non-Markovianity of the resulting dynamics are Rabi oscillations setting in at higher values of $\Omega$.

In a next step we put forward an analytical estimate for the decay rate in the limit of very strong coupling ($\Omega \to \infty$) employing the Laplace transform of our Volterra equation summarized in Appendix B. For that purpose we use recently developed concepts for another cavity QED problem dealing with non-Markovian quantum dynamics of a single emitter inside an open multimode cavity [30]. The key insight from that study is that the dominant frequency components contributing to the dynamics of $A(t)$ are those which are resonant in its Laplace transform, $U(\omega)$, given by Eq. (B7). For such resonances to occur we find the following requirement on the nonlinear Lamb shift (B8), $\omega_r - \omega_c = \Omega^2\delta(\omega_r)$. In the limit of sufficiently large values of the coupling strength the Laplace transform, $U(\omega)$, has a well-resolved double-peak structure with two resonance frequencies given approximately by $\omega_r \approx \omega_c \pm \Omega$. Furthermore, $A(t)$ essentially displays damped Rabi oscillations of the form, $A(t) \sim \cos(\Omega t)e^{-[\kappa+\pi\Omega^2\rho(\omega_c\pm\Omega)]t/2}$, due to the Fourier transforms of the two curves in $U(\omega)$ centered at these two resonance frequencies. One can see in Fig. 8 that such an estimate for the decay rate, $\Gamma = \kappa + \pi\Omega^2\rho(\omega_c \pm \Omega)$, works rather well if $\Omega/2\pi \geqslant 25$ MHz. Thus, in contrast to the Markovian dynamics, the relevant frequencies which contribute to the value of the decay rate are those associated with two resonant peaks in $U(\omega)$. Remarkably, a pair of poles in the complex plane occurring for $\Omega/2\pi \geqslant 25$ MHz do not spoil this asymptotic behavior (see Appendix B). Note that our expression for the decay rate in the limit of $\Omega \to \infty$ coincides with the one obtained in [22], where the behavior of poles of the stationary transmission has been analyzed.

### Cavity protection effect

It follows from the above analysis that for spectral distributions $\rho(\omega)$ whose tails fall off faster than $1/\omega^2$, an increasing coupling strength inevitably leads to a reduction of the decay rate $\Gamma$, so that the system will finally be protected against decoherence, a phenomenon referred to as "cavity protection effect" [21,22]. It is not hard to see that our $q$ Gaussian satisfies such a requirement, whereas a Lorentzian spin distribution does not. As a consequence, the latter does not protect the cavity against decoherence, featuring a constant decay rate in the strong-coupling regime (see green line in Fig. 8). In contrast, our numerical analysis for the $q$ Gaussian shows that for a collective coupling strength of $\Omega/2\pi \sim 25$ MHz, the decay rate induced is already suppressed below 8% of its maximal value at $\Omega/2\pi \sim 2.25$ MHz. It is interesting to note that the minimal possible value for the decay rate reached in the limit of large $\Omega$ is $\kappa$ whereas the decay rate for a bare cavity without diamond is $2\kappa$. This can be explained by the fact that due to the strong coupling between the spin ensemble and the cavity, the excitation is trapped by 50% within the spin ensemble which has a negligible direct decay rate during the course of our experiment.

Physically, the "cavity protection effect" can be understood as follows: In the presence of inhomogeneous spin broadening, the polariton states, defined as superpositions of the cavity mode with the superradiant (bright) spin-wave modes, become coupled to the subradiant (dark) spin-wave modes [21]. This coupling acts as the main source of decoherence, leading to a strong damping of the polariton modes. However, for strong enough coupling strength, the Rabi splitting of the polariton peaks opens up a gap for the super-radiant polaritons. If the spectral profile of the inhomogeneous spin distribution decays sufficiently fast for increasing gap size, an energetic decoupling of the super-radiant polaritons from the subradiant spin-wave modes occurs, leading to a suppressed damping of the polaritons and to a corresponding decrease of their peak linewidth.

## V. COHERENTLY DRIVEN SPIN ENSEMBLES

In a next step we address an important question arising in the context of possible realizations of coherent-control schemes, which is how to reach high excitation levels in the spin ensemble with a driving signal that has only limited power to avoid heating up the hybrid quantum device. We have seen in Sec. III A that the assumption of a Lorentzian distribution for the spin density leads to a simplified picture reducing the dynamics to the one of two coupled damped harmonic oscillators, where one of them stands for the cavity and the other for the spin ensemble. Furthermore, the expectation value of the collective spin operator can formally be excluded, so that we end up with a single equation for the cavity amplitude which has the same form as the equation for a damped and driven harmonic oscillator. Therefore, if our system is subjected to a periodic driving force, a resonance is expected to occur when the driving frequency is equal to the characteristic frequency of the system. Based on this reduced model, we conjecture that coherent cavity oscillations, and as a consequence, spin ensemble oscillations with a large amplitude can also be achieved for the $q$-Gaussian spin distribution. Also in this case the system needs to be driven periodically, so that the period of $\eta(t)$ matches the resonance condition given by the Rabi period, $T_R = 2\pi/\Omega_R$.

By pumping the cavity by a sequence of rectangular pulses with a carrier frequency $\omega_p = \omega_c = \omega_s$, phase switched by $\pi$, we indeed reveal a strongly resonant structure of $|A(t)|^2$ as a function of pulse duration $\tau$ and time $t$ (see Fig. 9). The corresponding increase of $|A(t)|^2$ can reach two orders of magnitude as compared to the case when the system is driven by a long rectangular pulse [see Fig. 2(a)], provided that the resonance condition is met, $\tau = 2\pi/\Omega_R$ (see Fig. 10). Note

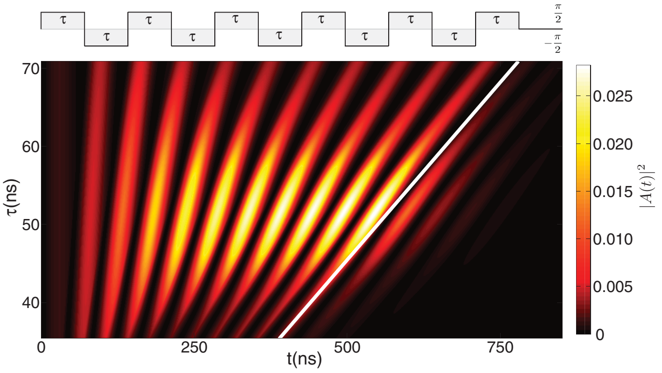

FIG. 9. (Color online) Cavity probability amplitude $|A(t)|^2$ under the action of 11 successive rectangular microwave pulses with carrier frequency $\omega_p = \omega_c = \omega_s = 2\pi 2.6915$ GHz, phase switched by $\pi$, as a function of time and pulse duration $\tau$. The white line indicates the corresponding moment of times, $11\tau$, at which the driving signal is switched off. The coupling strength $2\Omega/2\pi = 17.12$ MHz.

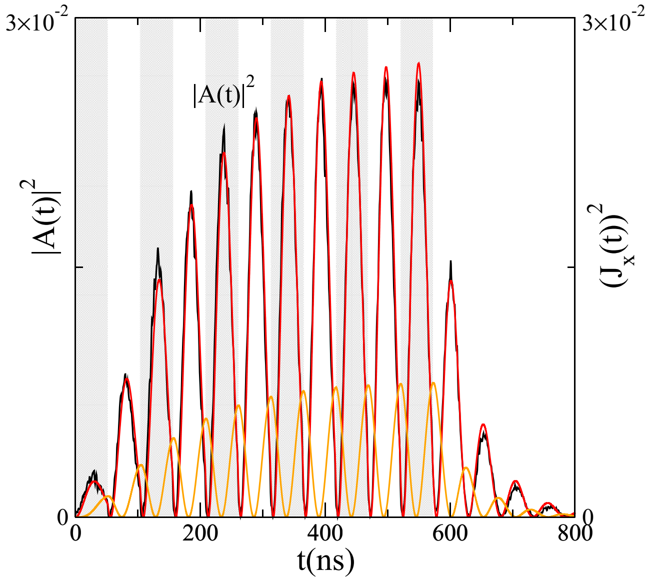

FIG. 10. (Color online) Resonant dynamics under the action of 11 successive rectangular microwave pulses (horizontal cut of Fig. 9 at $\tau = 2\pi/\Omega_R = 52$ ns). This specific driving corresponds to the largest enhancement of both the cavity amplitude $|A(t)|^2$ and the $x$ component of the collective spin $J_x^2(t)$ which coherently exchange the energy during course of time. [Red (gray) curve] Results of numerical calculations for $|A(t)|^2$. (Black curve) $|A(t)|^2$ measured in the experiment. [Orange (light gray) curve] Results of numerical calculations for $J_x^2(t)$. The alternating gray and white vertical bars designate the pulses sketched at the top of Fig. 9. The last white area corresponds to the damped dynamics when the driving signal is switched off.

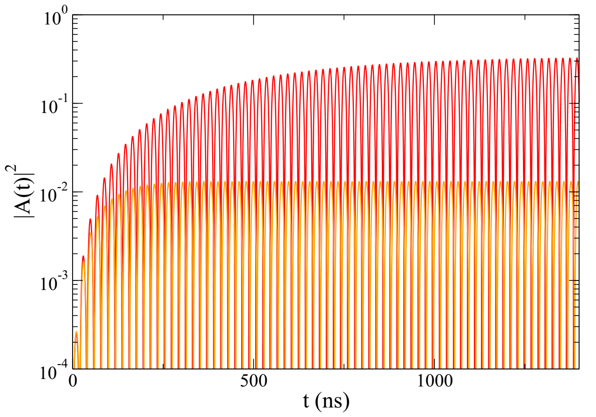

FIG. 11. (Color online) Resonant dynamics under the action of 70 successive rectangular microwave pulses ($\omega_p = \omega_c = \omega_s$) for a pulse duration $\tau = 2\pi/\Omega_R = 19.5$ ns. [Red (gray) curve] Numerical results for the $q$-Gaussian spin distribution. The coupling strength is chosen to be $\Omega/2\pi = 25$ MHz. In this case the value for the total decay rate $\Gamma$ (see Fig. 8) is 3.7 times smaller than that for $\Omega/2\pi = 8.56$ MHz used so far in Figs. 9 and 10. [Orange (light gray) curve] Corresponding numerical results for the Lorentzian spin distribution.

that the net power injected into the cavity, when applying a long rectangular pulse or a sequence of rectangular pulses phase switched by $\pi$, is exactly the same as we are just periodically changing the sign of the amplitude. Also in both cases the cavity and spin ensemble coherently exchange their energy, so that the cavity amplitude $|A(t)|^2$ oscillates in antiphase with respect to the spin ensemble component $J_x^2(t)$.

In Fig. 11 we present results for such a resonant driving both for a $q$ Gaussian and for a Lorentzian profile of the spectral distribution for the spin density. We take the value of the coupling strength, $\Omega/2\pi = 25$ MHz, for which the decoherence effect caused by the $q$-Gaussian form of the inhomogeneous broadening is strongly suppressed. Indeed, the resulting total decay rate shown in Fig. 8 for this value of $\Omega$ is 3.7 times smaller than that for $\Omega/2\pi = 8.56$ MHz used so far in Figs. 9 and 10 and 5.4 times smaller than the total decay rate predicted in the framework of the Lorentzian distribution. For this situation we see that the giant oscillations of the cavity probability amplitude, $|A(t)|^2$, induced by the resonant driving are a factor of 20 larger than what would be predicted for by a Lorentzian functional profile. This clear signature of the "cavity-protection effect" paves the way for the realization of sophisticated coherent-control schemes in the strong-coupling regime of QED.

In a further study we take the probe frequency out of resonance with the cavity $\omega_p \neq \omega_c$. (The condition $\omega_c = \omega_s$, however, always holds.) In Fig. 12 we present the maximal value of the cavity amplitude, $\max[|A(t)|^2]$, reached during coherent oscillations to which the system sets in under the action of incident rectangular pulses of duration $\tau$ that are phase switched by $\pi$. We deduce from this figure that the cavity amplitude experiences maximal growth at the resonance

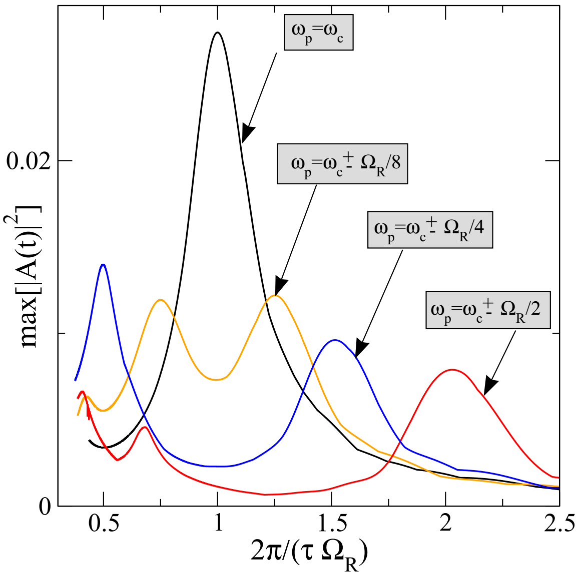

FIG. 12. (Color online) The maximal value of the cavity probability amplitude $|A(t)|^2$, $\max[|A(t)|^2]$, reached during coherent oscillations to which the system sets in under the action of incident rectangular pulses of duration $\tau$ that are phase switched by $\pi$. We consider four different values for the carrier frequency of our periodic driving signal: $\omega_p = \omega_c$; $\omega_p = \omega_c \pm \Omega_R/8$; $\omega_p = \omega_c \pm \Omega_R/4$; $\omega_p = \omega_c \pm \Omega_R/2$, where $\omega_c = 2\pi\,2.6915$ GHz and $\Omega_R = 2\pi\,19.2$ MHz are, respectively, the cavity and Rabi frequencies.

condition, $\omega_p = \omega_c = \omega_s$. It is worth noting that for the off-resonant cases ($\omega_p \neq \omega_c$) the right peak of $\max[|A(t)|^2]$ appears exactly at such values of $\pi/\tau$ which correspond to the mismatching value of the probe frequency from the resonant case ($\omega_p = \omega_c$). A similar tendency is also seen for the left peak for not too high values of the mismatch from the resonance condition.

## VI. CONCLUSIONS

We have studied in detail the dynamics of an inhomogeneously broadened spin ensemble interacting with a single cavity mode. For that purpose we numerically solved the Volterra integral equation for the cavity amplitude which explicitly contains the spin distribution function describing the inhomogeneous broadening of the spin ensemble. By assuming a Lorentzian functional profile for the spin density, we solved the problem analytically. This analytical solution provides an intuitive understanding of some important features of the resulting spin-cavity dynamics, such as an overshoot effect resulting from the constructive interference between the energy stored in the spin ensemble and in the cavity. Several features of the temporal dynamics in the strong-coupling regime are, however, specifically due to the $q$-Gaussian spectral spin density which we find to be realized in our experiment. In particular, the non-Lorentzian functional profile of the spin distribution allows us to observe as well as to accurately describe a phenomenon known as "cavity protection effect" [21,22] for large values of the coupling strength. This effect results in a complete suppression of the decoherence induced by inhomogeneous broadening in the strong-coupling regime. To highlight the potential of this effect for the implementation of coherent-control schemes, we reveal how an appropriately chosen pulse sequence can excite giant coherent oscillations between the cavity and the spin ensemble. We classify the dynamics as a function of the coupling strength and the probe frequency covering both Markovian and non-Markovian regimes.

## ACKNOWLEDGMENTS

We would like to thank R. Amsüss, B. Hartl, F. Mintert, T. Nöbauer, P. Rabl, J. Schmiedmayer, and A. Valookaran for helpful discussions. D.O.K. and S.R. acknowledge funding by the Austrian Science Fund (FWF) through Project No. F49-P10 (SFB NextLite). The experimental effort has been supported by the TOP grant of TU Vienna. S.P. acknowledges support by the Austrian Science Fund (FWF) in the framework of the Doctoral School "Building Solids for Function" (Project No. W1243).

## APPENDIX A: DIRECT TIME INTEGRATION OF THE VOLTERRA EQUATION

Although Eq. (5) has a relatively simple form, it is a challenging task to solve it numerically. There are two reasons for that: First, in order to calculate the cavity amplitude at time $t$, one should know the amplitude $A(\tau)$ at all previous instants, $\tau < t$ (memory effect). Second, an integration with respect to the frequency in the kernel function $\mathcal{K}(t-\tau)$ has to be performed for each $t$ and $\tau < t$ [see Eq. (6)]. The smallest possible time scale in our problem is given by $T = 2\pi/\omega_p \sim 0.4$ ns. To achieve a very good accuracy of the calculations, we solve the equation on a temporal mesh with uniform spacing, choosing a time step $dt \sim 0.05$ ns (see, e.g., [31] for more details about the method). The direct discretization of $\mathcal{K}(t-\tau)$ on the time interval of the order of $\mu$s (typical time of measurements) leads to a high-dimensional matrix (of a size typically exceeding $10^4 \times 10^4$), which, together with the integration with respect to frequency, makes the problem computationally intractable by way of a direct numerical solution.

To overcome this problem and to speed up the calculations drastically, we divide the whole time integration into many successive subintervals, $T_n \leqslant t \leqslant T_{n+1}$, with $n = 1,2,\ldots$. Such a time division can, in principle, be implemented arbitrarily but we choose it to be adapted to our experimental realization. Specifically, for a sequence of rectangular pulses with phase inversion, the driving amplitude is unchanged within each subinterval, so that $\eta(t)$ is written as $\eta_n = (-1)^{n+1}\cdot\eta$, where $n = 1,2,3,\ldots$. Thus, in order to proceed with the integration on the $n$th time interval, which starts from the initial value $A^n(T_n)$, we have to provide the result of integration obtained in the previous step, $A^{(n-1)}(T_n)$. The recurrence relation (time runs within $T_n \leqslant t \leqslant T_{n+1}$ for $n = 1,2,3,\ldots$) then reads

$$A^{(n)}(t) = \int_{T_n}^{t} d\tau\,\mathcal{K}(t-\tau)A^{(n)}(\tau) + \mathcal{F}^{(n)}(t), \tag{A1}$$

where the kernel function $\mathcal{K}(t-\tau)$ is defined by Eq. (6) and

$$\begin{aligned}\mathcal{F}^{(n)}(t) = {} & e^{-i(\omega_c-\omega_p-i\kappa)(t-T_n)}\Bigg\{A^{(n-1)}(T_n) \\ & + \Omega^2\int_0^\infty d\omega\,\frac{\rho(\omega)[e^{-i(\omega-\omega_c+i\kappa)(t-T_n)}-1]}{i(\omega-\omega_c+i\kappa)}\cdot\mathcal{I}_n(\omega)\Bigg\} \\ & - \frac{i\eta_n}{\omega_c-\omega_p-i\kappa}[1-e^{-i(\omega_c-\omega_p-i\kappa)(t-T_n)}]. \end{aligned} \tag{A2}$$

Note also that the memory on previous events enters not only through the amplitude $A^{(n-1)}(T_n)$ but also through the function,

$$\begin{aligned}\mathcal{I}_n(\omega) = {} & e^{-i(\omega-\omega_p)(T_n-T_{n-1})}\mathcal{I}_{n-1}(\omega) \\ & + \int_{T_{n-1}}^{T_n} d\tau\, e^{-i(\omega-\omega_p)(T_n-\tau)}A^{(n-1)}(\tau). \end{aligned} \tag{A3}$$

The initial conditions at $t = T_1 = 0$ are defined as $A(T_1) = 0$ and $\mathcal{I}_1(\omega) = 0$ if the cavity is empty and spins are in the ground state.

The above technique allows us to solve Eq. (5) accurately while being very efficient in terms of computational time. We have tested the accuracy of our numerical results by varying the discretization both in time and frequency in a wide range obtaining excellent agreement with the experimental results, thereby confirming the accuracy of our method.

## APPENDIX B: LAPLACE TRANSFORM OF THE VOLTERRA EQUATION

In order to speed up the calculations of the decay rate for different values of the coupling strengths $\Omega$, and to derive an analytical expression for it in the limit of $\Omega \to \infty$, we perform

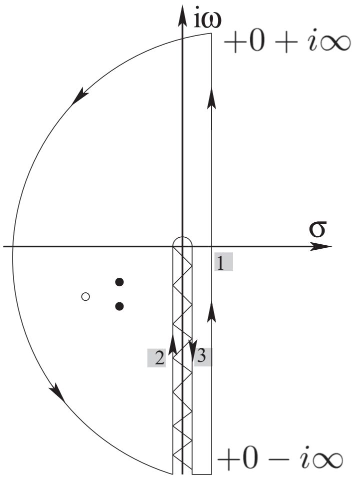

FIG. 13. Contour completion in the complex plane $s=\sigma+i\omega$ for the calculation of the inverse Laplace transform. Those contours which give nonzero contribution are designated by numbers. (Open circle) The pole which appears in the regime of weak coupling for $\Omega/2\pi \leqslant 1.7$ MHz (Markovian dynamics). (Two solid circles) Two poles which show up in the strong-coupling regime for $\Omega/2\pi \geqslant 25$ MHz. The zigzag line corresponds to the branch cut along the negative part of the imaginary axis.

a Laplace transformation of the Volterra equation,

$$\dot{A}(t) = -\kappa A(t) - \Omega^2 \int_0^\infty d\omega\rho(\omega) \int_0^t d\tau e^{-i(\omega-\omega_p)(t-\tau)} A(\tau), \tag{B1}$$

assuming that the decay process starts from the most simple initial condition, $A(t=0)=1$, when the cavity is fed with a single photon and the spin ensemble is in the ground state. For the sake of simplicity we consider the resonant case only, $\omega_p=\omega_c=\omega_s$. To carry out the Laplace transformation we multiply Eq. (B1) by $e^{-\mathrm{st}}$ and integrate both sides of the equation with respect to time from 0 to $\infty$ (see, e.g., [32] for more details). Here $s=\sigma+i\omega$ is the complex variable so that we reformulate our problem by solving it in the complex plane of $s$. After straightforward calculations, the algebraic equation for the Laplace transform, $\tilde{A}(s)=\int_0^\infty dt\, e^{-\mathrm{st}}A(t)$, is derived which is solved by

$$\tilde{A}(s) = \frac{1}{s+\kappa+\Omega^2\int_0^\infty \frac{d\omega\rho(\omega)}{s+i(\omega-\omega_c)}}. \tag{B2}$$

By performing the inverse Laplace transformation, $A(t)=\frac{1}{2\pi i}\int_{\sigma-i\infty}^{\sigma+i\infty} ds\, e^{\mathrm{st}}\tilde{A}(s)$, we obtain the following formal solution for the cavity amplitude $A(t)$,

$$A(t) = \frac{e^{i\omega_c t}}{2\pi i}\int_{\sigma-i\infty}^{\sigma+i\infty} \frac{e^{\mathrm{st}}ds}{s+\kappa+i\omega_c+\Omega^2\int_0^\infty \frac{d\omega\rho(\omega)}{s+i\omega}}, \tag{B3}$$

where $\sigma>0$ is chosen such that the real parts of all singularities of $\tilde{A}(s)$ are smaller than $\sigma$. It can be proved that the integral in the denominator of Eq. (B3) has a jump when passing across the negative part of the imaginary axis leading to the branch cut in the complex plane of $s$ (see Fig. 13 and also [30]).

By setting the denominator of the integrand in Eq. (B3) to zero, we derive the following equations for a simple pole, $s_j=\sigma_j+i\omega_j$,

$$\sigma_j = -\frac{\kappa}{1+\Omega^2\int_0^\infty \frac{d\omega\rho(\omega)}{\sigma_j^2+(\omega_j+\omega)^2}}, \tag{B4}$$

$$\omega_j = -\omega_c + \Omega^2\int_0^\infty \frac{d\omega\rho(\omega)(\omega_j+\omega)}{\sigma_j^2+(\omega_j+\omega)^2}. \tag{B5}$$

It turns out that a single solution to Eqs. (B4) and (B5) exists within the weak-coupling regime in a rather narrow interval of the coupling strengths, $\Omega/2\pi \leqslant 1.7$ MHz. [It is seen that in the limit of $\Omega \to 0$, Eqs. (B4) and (B5) are solved by $\sigma_j \sim -\kappa$ and $\omega_j=-\omega_c$, respectively.) We also find a pair of poles with $\sigma_1=\sigma_2<0$, $|\sigma_{1,2}| \lll \kappa$, and $\omega_{1,2}=-\omega_c\pm\epsilon$ in the strong-coupling regime for large values of the coupling strength starting from $\Omega/2\pi\approx 25$ MHz. Note that both $|\sigma_{1,2}|$ and $\epsilon$ grow with increasing $\Omega$.

Next, we apply Cauchy's theorem to a closed contour to evaluate the original integral Eq. (B3) taking into account that only a few paths of those shown in Fig. 13 contribute. Finally, we end up with the following expression for the cavity amplitude $A(t)$:

$$A(t) = e^{i\omega_c t}\left\{\Omega^2\int_0^\infty d\omega e^{-i\omega t}U(\omega) + \sum_j R_j\right\}, \tag{B6}$$

where

$$U(\omega) = \lim_{\sigma\to 0^+}, \\ \times\left\{\frac{\rho(\omega)}{(\omega-\omega_c-\Omega^2\delta(\omega)+i\kappa)^2+(\pi\Omega^2\rho(\omega)+\sigma)^2}\right\} \tag{B7}$$

is the kernel function and

$$\delta(\omega) = \mathcal{P}\int_0^\infty \frac{d\tilde{\omega}\rho(\tilde{\omega})}{\omega-\tilde{\omega}} \tag{B8}$$

can be interpreted as the nonlinear Lamb shift of the cavity frequency $\omega_c$. Here $\mathcal{P}$ stands for the Cauchy principal value and $R_j$ is the contribution of poles (if at all existing),

$$R_j = \frac{e^{(\sigma_j+i\omega_j)t}}{1-\Omega^2\int_0^\infty \frac{d\omega\rho(\omega)}{[\sigma_j+i(\omega_j+\omega)]^2}}. \tag{B9}$$

## APPENDIX C: DECAY PROCESS FROM THE STEADY STATE

After applying a long rectangular pulse, both the cavity amplitude and spin ensemble settle to a finite value in the steady state (see Figs. 2, 3, and 5). Here we explore the decay process from this steady-state solution in more detail. To avoid cumbersome expressions we present, without loss of generality, the results for the resonant case only, $\omega_p=\omega_c=\omega_s$. To obtain a stationary solution, we set the time derivatives in Eqs. (2a) and (2b) to zero, $\dot{A}(t)=\dot{B}_k(t)=$

0, go to the continuous limit (in frequency), and finally derive the following expressions for the cavity amplitude and for the expectation values of the following collective spin operators,

$$A_{\mathrm{st}} = \frac{\eta}{-\kappa + i\Omega^2 \int_0^\infty d\omega \frac{\rho(\omega)}{\omega - \omega_s - i\gamma}}, \tag{C1}$$

$$J_x^{\mathrm{st}} + iJ_y^{\mathrm{st}} = \frac{\sum_k g_k B_k^{\mathrm{st}}}{2\Omega} = \frac{iA_{\mathrm{st}}\Omega}{2}\int_0^\infty d\omega \frac{\rho(\omega)}{\omega - \omega_s - i\gamma}. \tag{C2}$$

It can be easily proved, that the expressions above are real because the $q$ Gaussian is symmetric with respect to $\omega_s$, and as a consequence, $J_y^{\mathrm{st}} = 0$ and $A_{\mathrm{st}} \in \mathbb{R}$. Note that the second term in the Volterra equation (4) stands for the energy coming back to the cavity from the initial (steady) state of a spin ensemble, which in the continuous limit is found to be

$$\sum_k g_k B_k^{\mathrm{st}} e^{-i(\omega_k - \omega_s - i\gamma)t}$$
$$= iA_{\mathrm{st}}\Omega^2 \int d\omega \rho(\omega) \frac{e^{-i(\omega-\omega_s-i\gamma)t}}{\omega - \omega_s - i\gamma}, \tag{C3}$$

leading to the following Volterra equation,

$$\dot{A}(t) = -\kappa A(t) + iA_{\mathrm{st}}\Omega^2 \int_0^\infty d\omega\rho(\omega)\frac{e^{-i(\omega-\omega_s-i\gamma)t}}{\omega-\omega_s-i\gamma} - \Omega^2\int_0^\infty d\omega\rho(\omega)\int_0^t d\tau e^{-i(\omega-\omega_s-i\gamma)(t-\tau)}A(\tau). \tag{C4}$$

From this expression we can conclude that the energy which is first stored and then released from the spin ensemble is exactly the reason for the pronounced overshoot in the cavity amplitude [see the example shown in Fig. 2(a)]. Note that if initially the spin ensemble is in the ground state, $B_k(0) = 0$, then the overshoot effect will never occur, as is the case for initial conditions described in Appendix B (the cavity is fed with a single photon and a spin ensemble is in the ground state).

Next, employing the Sokhotski-Plemelj theorem, in the limit of $\gamma \to 0$,

$$\int_0^\infty \frac{d\omega F(\omega)}{\omega - \omega_s - i\gamma} = \mathcal{P}\int_0^\infty \frac{d\omega F(\omega)}{\omega - \omega_s} + i\pi F(\omega_s),$$

where $\mathcal{P}$ denotes the Cauchy principal value, Eqs. (C1) and (C4) are finally reduced to (the resonance case, $\omega_p = \omega_c = \omega_s$, is considered only)

$$A_{\mathrm{st}} = -\frac{\eta}{\kappa + \pi\Omega^2\rho(\omega_s)}, \tag{C5}$$

and

$$\dot{A}(t) = -\kappa A(t) + A_{\mathrm{st}}\Omega^2\left\{\int_0^\infty d\omega\rho(\omega)\frac{\sin[(\omega-\omega_s)t]}{\omega-\omega_s} - \pi\rho(\omega_s)\right\} - \Omega^2\int_0^\infty d\omega\rho(\omega)\int_0^t d\tau e^{-i(\omega-\omega_s-i\gamma)(t-\tau)}A(\tau). \tag{C6}$$

This equation describes the damped Rabi oscillations from the steady state after switching off a long pulse for a general form of the spin density, including both Lorentzian and $q$-Gaussian distributions [see results presented in Figs. 2(a) and 2(b)].

[1] J. Q. You and F. Nori, Phys. Today **58**(11), 42 (2005).

[2] R. Amsüss, Ch. Koller, T. Nöbauer, S. Putz, S. Rotter, K. Sandner, S. Schneider, M. Schramböck, G. Steinhauser, H. Ritsch, J. Schmiedmayer, and J. Majer, Phys. Rev. Lett. **107**, 060502 (2011).

[3] K. Sandner, H. Ritsch, R. Amsüss, Ch. Koller, T. Nöbauer, S. Putz, J. Schmiedmayer, and J. Majer, Phys. Rev. A **85**, 053806 (2012).

[4] Y. Kubo, F. R. Ong, P. Bertet, D. Vion, V. Jacques, D. Zheng, A. Dréau, J.-F. Roch, A. Auffeves, F. Jelezko, J. Wrachtrup, M. F. Barthe, P. Bergonzo, and D. Esteve, Phys. Rev. Lett. **105**, 140502 (2010).

[5] Y. Kubo, C. Grezes, A. Dewes, T. Umeda, J. Isoya, H. Sumiya, N. Morishita, H. Abe, S. Onoda, T. Ohshima, V. Jacques, A. Dréau, J.-F. Roch, I. Diniz, A. Auffeves, D. Vion, D. Esteve, and P. Bertet, Phys. Rev. Lett. **107**, 220501 (2011).

[6] Y. Kubo, I. Diniz, A. Dewes, V. Jacques, A. Dréau, J.-F. Roch, A. Auffeves, D. Vion, D. Esteve, and P. Bertet, Phys. Rev. A **85**, 012333 (2012).

[7] S. Probst, H. Rotzinger, S. Wünsch, P. Jung, M. Jerger, M. Siegel, A. V. Ustinov, and P. A. Bushev, Phys. Rev. Lett. **110**, 157001 (2013).

[8] P. Rabl, D. DeMille, J. M. Doyle, M. D. Lukin, R. J. Schoelkopf, and P. Zoller, Phys. Rev. Lett. **97**, 033003 (2006).

[9] J. Verdú, H. Zoubi, Ch. Koller, J. Majer, H. Ritsch, and J. Schmiedmayer, Phys. Rev. Lett. **103**, 043603 (2009).

[10] Z.-L. Xiang, X.-Y. Lü, T.-F. Li, J. Q. You, and F. Nori, Phys. Rev. B **87**, 144516 (2013).

[11] A. Imamoglu, Phys. Rev. Lett **102**, 083602 (2009).

[12] H. Huebl, C. W. Zollitsch, J. Lotze, F. Hocke, M. Greifenstein, A. Marx, R. Gross, and S. T. B. Goennenwein, Phys. Rev. Lett. **111**, 127003 (2013).

[13] Y. Tabuchi, S. Ishino, T. Ishikawa, R. Yamazaki, K. Usami, and Y. Nakamura, Phys. Rev. Lett. **113**, 083603 (2014).

[14] R. H. Dicke, Phys. Rev. **93**, 99 (1954).

[15] X. Zhu, S. Saito, A. Kemp, K. Kakuyanagi, S. Karimoto, H. Nakano, W. J. Munro, Y. Tokura, M. S. Everitt, K. Nemoto, M. Kasu, N. Mizuochi, and K. Semba, Nature (London) **478**, 221 (2011).

[16] S. Saito, X. Zhu, R. Amsüss, Y. Matsuzaki, K. Kakuyanagi, T. Shimo-Oka, N. Mizuochi, K. Nemoto, W. J. Munro, and K. Semba, Phys. Rev. Lett. **111**, 107008 (2013).

[17] N. Bar-Gill, L. M. Pham, A. Jarmola, D. Budker, and R. L. Walsworth, Nature Comm. **4**, 1743 (2013).

[18] P. L. Stanwix, L. M. Pham, J. R. Maze, D. Le Sage, T. K. Yeung, P. Cappellaro, P. R. Hemmer, A. Yacoby, M. D. Lukin, and R. L. Walsworth, Phys. Rev. B **82**, 201201(R) (2010).

[19] C. Grezes, B. Julsgaard, Y. Kubo, M. Stern, T. Umeda, J. Isoya, H. Sumiya, H. Abe, S. Onoda, T. Ohshima, V. Jacques, J. Esteve, D. Vion, D. Esteve, K. Mølmer, and P. Bertet, Phys. Rev. X **4**, 021049 (2014).

[20] H. Wu, R. E. George, J. H. Wesenberg, K. Mölmer, D. I. Schuster, R. J. Schoelkopf, K. M. Itoh, A. Ardavan, J. J. L. Morton, and G. A. D. Briggs, Phys. Rev. Lett. **105**, 140503 (2010).

[21] Z. Kurucz, J. H. Wesenberg, and K. Mølmer, Phys. Rev. A **83**, 053852 (2011).

[22] I. Diniz, S. Portolan, R. Ferreira, J. M. Gerard, P. Bertet, and A. Auffeves, Phys. Rev. A **84**, 063810 (2011).

[23] S. Putz, D. O. Krimer, R. Amsüss, A. Valookaran, T. Nöbauer, J. Schmiedmayer, S. Rotter, and J. Majer, Nature Physics **10**, 720 (2014).

[24] M. Tavis and F. W. Cummings, Phys. Rev. **170**, 379 (1968).

[25] C. Emary and T. Brandes, Phys. Rev. E **67**, 066203 (2003).

[26] H. Primakoff and T. Holstein, Phys. Rev. **55**, 1218 (1939).

[27] C. Tsallis, *Introduction to Nonextensive Statistical Mechanics: Approaching a Complex World* (Springer, New York, 2009).

[28] E. M. Purcell, Phys. Rev. **69**, 681 (1946).

[29] In order to reduce $\Omega$, we repeatedly apply a driving signal in our experiment with substantially higher power than the one used elsewhere in the paper, such that a non-negligible number of NV spins gets excited (see [23] for more details). In this way, we effectively diminish the number of spins in ground state $N$, which are coupled to the cavity, and as a consequence, the coupling strength $\Omega \sim \sqrt{N}$ decreases as well. During this pulse sequence, which consists of $\sim 10^5$ traces each of 1.6-$\mu$s duration used for further averaging, the coupling strength remains almost constant, however, a non-negligible amount of spins gets excited leading to a slight decrease of the coupling strength on this overall time interval of 0.1 s. As a result, a slight upward inclination of the steady-state value $|A_{\rm st}|$ becomes visible in the experimental curves of Fig. 6, since $|A_{\rm st}|$ increases with decreasing $\Omega$ in accordance with Eq. (C5).

[30] D. O. Krimer, M. Liertzer, S. Rotter, and H. E. Türeci, Phys. Rev. A **89**, 033820 (2014).

[31] W. H. Press, S. A. Teukolsky, W. T. Vetterling, and B. P. Flannery, *Numerical Recipes: The Art of Scientific Computing* (Cambridge University Press, New York, 2007).

[32] K. F. Riley, M. P. Hobson, and S. J. Bence, *Mathematical Methods for Physics and Engineering* (Cambridge University Press, Cambridge, 2006).

nature physics

LETTERS

# Protecting a spin ensemble against decoherence in the strong-coupling regime of cavity QED

S. Putz[1,2†], D. O. Krimer[3†], R. Amsüss[1], A. Valookaran[1], T. Nöbauer[1,4], J. Schmiedmayer[1], S. Rotter[3*] and J. Majer[1,2*]

**Hybrid quantum systems based on spin ensembles coupled to superconducting microwave cavities are promising candidates for robust experiments in cavity quantum electrodynamics (QED) and for future technologies employing quantum mechanical effects[1-4]. At present, the main source of decoherence in these systems is inhomogeneous spin broadening, which limits their performance for the coherent transfer and storage of quantum information[5-7]. Here we study the dynamics of a superconducting cavity strongly coupled to an ensemble of nitrogen–vacancy centres in diamond. We experimentally observe how decoherence induced by inhomogeneous broadening can be suppressed in the strong-coupling regime—a phenomenon known as 'cavity protection'[5,7]. To demonstrate the potential of this effect for coherent-control schemes, we show how appropriately chosen microwave pulses can increase the amplitude of coherent oscillations between the cavity and spin ensemble by two orders of magnitude.**

The processing of quantum information requires special devices that can store and manipulate quantum bits. Hybrid quantum systems[2] combine the advantages of different systems to overcome their individual physical limitations. In this context superconducting microwave cavities have emerged as ideal tools for realizing strong coupling to qubits[3,4,8–12] for the transfer of excitations on the single-photon level[13,14]. For the storage of quantum information the negatively charged nitrogen–vacancy (NV) centres in diamond show great potential, especially owing to their long coherence times (up to one second[15]) and to the combination of microwave and optical transitions which makes them an easily accessible and controllable qubit[16]. Coherently passing quantum information between such a spin and a cavity requires that they are strongly coupled to each other. As has recently been shown[4,10–12], this limit can be reached by collective coupling to a large spin ensemble, in which case the coupling strength is increased by the square root of the ensemble size. However, this collective coupling comes with a considerable downside: in a solid-state environment a spin is always prone to inhomogeneous broadening. In particular, for an ensemble of NV centres, magnetic dipolar interaction with excess nuclear and electron spins in the diamond crystal leads to an inhomogeneous broadening of the spin transition[17], which acts as the dominant source of decoherence. Several approaches, including echo-type refocusing techniques[18,19], have been suggested to overcome this limitation. Here we will concentrate on recent theoretical proposals which rely on the specific shape of the inhomogeneous spectral spin distribution $\rho(\omega)$ of the NV centre ensemble. In our explicitly time-dependent study we will demonstrate the so-called 'cavity-protection effect'[5,7], which was predicted in these proposals but has remained so far unobserved.

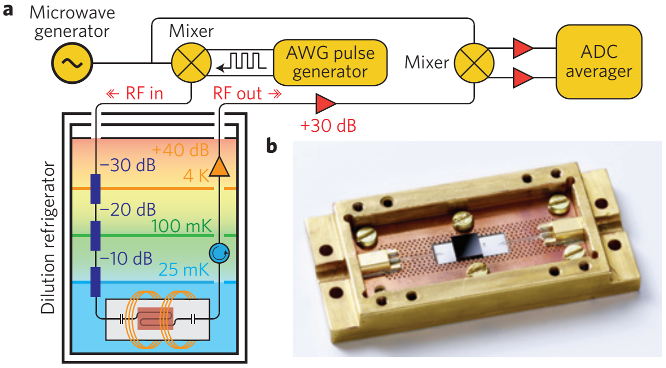

**Figure 1 | Experimental set-up. a**, The superconducting coplanar waveguide resonator with the diamond on top is cooled to ∼25 mK in a dilution refrigerator. In our homodyne detection measurements, the input microwave signal is split into two paths, both serving as a reference signal as well as for testing and controlling our experiment. Outside the cryostat both signal paths are combined by a frequency mixer and the quadratures I and Q are recorded with a fast analog-to-digital converter (ADC) with subnanosecond time resolution. AWG: arbitrary waveform generator. **b**, Photograph of a superconducting microwave cavity with an enhanced neutron-irradiated type Ib synthetic diamond (black) on top, encased in a gold-plated copper sample box.

Our experiment is performed in a standard dilution refrigerator with the corresponding set-up being sketched in Fig. 1a and a photograph of the resonator with a synthetic diamond on top shown in Fig. 1b. To avoid thermal excitations we cool the entire set-up to a temperature of 25 mK, where the estimated thermal spin polarization is 99%. By applying an external magnetic field $|\mathbf{B}| = 9.4$ mT through a set of two superconducting Helmholtz coils we Zeeman tune the NV spin ensemble into resonance with the cavity. Our resonator has a fundamental resonance at $\omega_c/2\pi = 2.6899$ GHz with a quality factor of $Q = 3{,}060$. To excite and probe the coupled system we inject microwave pulses into the cavity and perform time-resolved transmission spectroscopy by a fast

---

[1]Vienna Center for Quantum Science and Technology, Atominstitut, Vienna University of Technology, Stadionallee 2, 1020 Vienna, Austria, [2]Zentrum für Mikro- und Nanostrukturen, Vienna University of Technology, Floragasse 7, 1040 Vienna, Austria, [3]Institute for Theoretical Physics, Vienna University of Technology, Wiedner Hauptstrasse 8-10/136, 1040 Vienna, Austria, [4]Research Institute of Molecular Pathology and Max F. Perutz Laboratories, University of Vienna, Dr.-Bohr-Gasse 7, 1030 Vienna, Austria. †These authors contributed equally to this work.
*e-mail: stefan.rotter@tuwien.ac.at; johannes@majer.ch

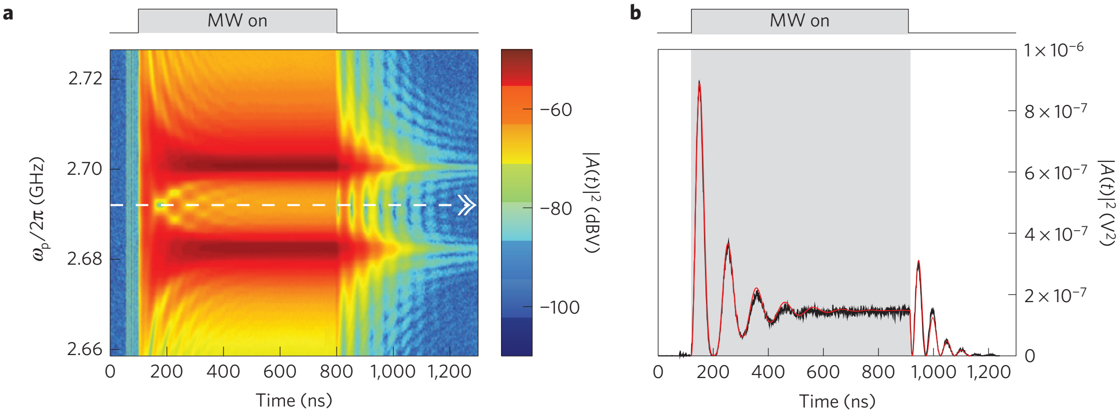

**Figure 2 | Time domain measurements of the cavity transmission.** **a**, Transmission of a rectangular microwave (MW) pulse through the cavity versus time and probe frequency $\omega_p$ (the spins are in resonance with the cavity, $\omega_s = \omega_c$). The observation of strong mode-splitting into the two hybridized modes $|\Psi_\pm\rangle \approx \frac{1}{\sqrt{2}}(|0\rangle_c|1\rangle_s \pm |1\rangle_c|0\rangle_s)$ (see dark red enhancements split by $\Omega_R/2\pi = 19.2$ MHz) confirms that the system is deep in the strong-coupling regime. **b**, The dynamics at the resonant probe frequency $\omega_p = \omega_s = \omega_c$ (white dashed line in **a**) is compared with the theoretical prediction for the cavity probability amplitude $|A(t)|^2$ (experiment: black: theory: red). Excellent agreement is achieved when incorporating the correct non-Lorentzian spectral spin distribution. After switching on the pulse, the system exhibits damped Rabi oscillations, with frequency $\Omega_R$, that equilibrate at a stationary state. After switching off the pulse, the cavity amplitude first decays from the stationary state and then features a pronounced overshoot corresponding to a strongly non-Markovian release of the energy stored in the spin ensemble back into the cavity.

homodyne detection set-up with subnanosecond time resolution. The number of microwave photons in the cavity remains at or below $\sim 10^6$, which is very low compared with the number of $\sim 10^{12}$ NV spins involved in the coupling, ensuring that the Holstein–Primakoff[20] approximation is valid for describing our experiments. As a result of this approximation, the excitations in the system can be treated as non-interacting quasiparticles[5] and the dynamics for the $\sim 10^6$ photons in our system is equivalent to that of a corresponding single-photon experiment as relevant for quantum information processing (see Supplementary Methods Section II).

Our starting point to account for the dynamics of a single-mode cavity coupled to a spin ensemble is the Tavis–Cummings Hamiltonian[21], which reads in the rotating wave approximation

$$H = \hbar\omega_c a^\dagger a + \frac{\hbar}{2}\sum_j^N \omega_j \sigma_j^z + i\hbar \sum_j^N \left[g_j \sigma_j^- a^\dagger - g_j^* \sigma_j^+ a\right]$$

$$- i\hbar\left[\eta(t) a^\dagger e^{-i\omega_p t} - \eta(t)^* a e^{i\omega_p t}\right]$$

where $a^\dagger$ and $a$ are standard creation and annihilation operators of the cavity mode and $\sigma_j^\pm$, $\sigma_j^z$ are the Pauli operators associated with each individual spin. The first and second terms stand for the uncoupled resonator with frequency $\omega_c$ and for the spin ensemble with frequencies $\omega_j$, centred around $\omega_s$, respectively. The third and the last terms describe the cavity–spin interaction with coupling strength $g_j$ as well as the driving electromagnetic field injected into the cavity with amplitude $\eta(t)$ and frequency $\omega_p$. The collective coupling to a large number of spins allows us to enter the strong-coupling regime of QED, for which the interaction term is commonly reduced to a collective term[22] $\Omega(S^- a^\dagger - S^+ a)$, where the collective spin operators read $S^\pm = \frac{1}{\sqrt{N}}\sum_j^N \sigma_j^\pm$. The prefactor $\Omega^2 = \sum_j^N g_j^2$ stands for an effective coupling strength, which scales up a single cavity–spin interaction, typically on the order of $g_j/2\pi \sim 12$ Hz, by a factor $\sqrt{N}$ (refs 3,4,23). In this formulation the effective spin waves that are excited by the cavity mode can be identified as superradiant collective Dicke states which are effectively damped by the coupling to subradiant states in the ensemble[13,24]. To accurately describe the corresponding dynamics we also need to take into account the specific profile of the spectral spin distribution[7] $\rho(\omega) = \sum_j g_j^2 \delta(\omega - \omega_j)/\Omega^2$. We achieve this by setting up a Volterra integral equation (see Supplementary Methods), $A(t) = \int_0^t \mathrm{d}\tau \int \mathrm{d}\omega\, \mathcal{K}(\rho(\omega); t - \tau) A(\tau) + \mathcal{F}(t)$, for the cavity amplitude $A(t) = \langle a(t)\rangle$. This includes a memory-kernel $\mathcal{K}(t - \tau)$, responsible for the non-Markovian feedback of the NV ensemble on the cavity, and the function $\mathcal{F}(t)$, which describes the contribution from an external drive and from the initial spin excitation. In the following, the cavity amplitude $|A(t)|^2$, calculated with this approach for stationary and pulsed driving fields, will be compared to its experimental counterpart—that is, the time-resolved microwave intensity measured in transmission through the cavity.

First, to demonstrate that our experiment is in the strong-coupling regime (having $\omega_s = \omega_c$) we apply a rectangular microwave pulse which is sufficiently long compared with the cavity decay rate $\kappa$, total decoherence rate $\Gamma$ and coupling strength $\Omega$ (800 ns $\gg 1/2\kappa = 199$ ns, $1/\Gamma = 53$ ns, $\pi/\Omega = 58$ ns) to drive the system into a steady state with varying probe frequency $\omega_p$. Figure 2a shows that two effective eigenstates (polaritons) of the coupled system emerge in the transmission, $|\Psi_\pm\rangle \approx \frac{1}{\sqrt{2}}(|0\rangle_c|1\rangle_s \pm |1\rangle_c|0\rangle_s)$, corresponding to the symmetric and antisymmetric superposition of the cavity and spin eigenstates, respectively. Strong coupling is secured because the Rabi splitting between these states $\Omega_R/2\pi = 19.2$ MHz is substantially larger than the total decay rate of the system $\Gamma/2\pi = 3.0$ MHz (full-width at half-maximum). The latter consists of a cavity decay rate, $\kappa/2\pi = 0.4$ MHz (half-width at half-maximum), as well as of a spin decay rate which contains a negligibly small spin dissipation $\gamma \to 0$ and a dominant contribution from the inhomogeneous broadening of the spin ensemble. Detailed spectroscopic measurements of the stationary transmission[6] reveal that the spectral function $\rho(\omega)$ which accurately captures the broadening is neither Lorentzian nor Gaussian, but has the intermediate form of a $q$-Gaussian[6] (see Supplementary Methods Section I). As shown in Fig. 2b, our explicitly time-dependent theoretical description yields excellent quantitative agreement with the experimental data, using such a $q$-Gaussian distribution function with a linewidth of $\gamma_q/2\pi = 9.4$ MHz (full-width at half-maximum), a shape parameter $q = 1.39$ and an effective coupling strength $2 \cdot \Omega/2\pi = 17.2$ MHz. After turning on and switching off the microwave pulse, coherent Rabi oscillations occur between the cavity and the spin ensemble, which we reproduce accurately, including their damping. Interestingly, the first Rabi

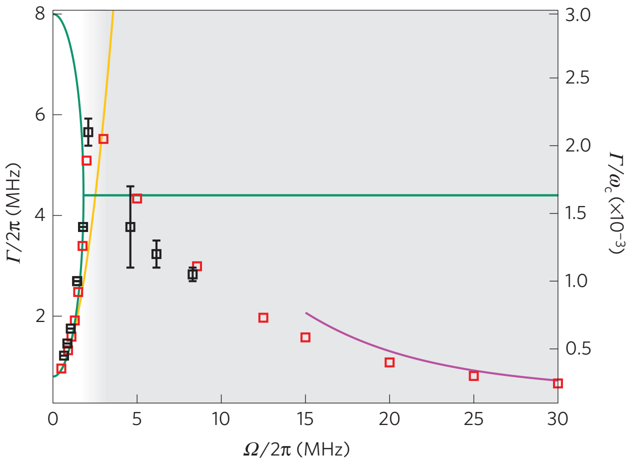

**Figure 3 | Characterization of the decay dynamics as a function of coupling strength.** For weak coupling, the decay rate $\Gamma$ of the cavity probability amplitude, $|A(t)|^2$, increases as a function of the coupling strength $\Omega$. For strong coupling, this trend reverses, showing a protection of the system against decoherence. Black symbols: experimentally observed decay rates from the steady state. Red symbols: decay rates extracted from the full numerical calculations. Orange curve: decay rate, $\Gamma = 2[\kappa + \pi\Omega^2\rho(\omega_s)]$, derived under the Markovian approximation. Green curve: characteristic decay rates, $\Gamma_{1,2} = \Delta + \kappa \pm \sqrt{(\Delta-\kappa)^2 - 4\Omega^2}$ under the assumption of a Lorentzian distribution of the spin density. Magenta curve: analytical estimate of $\Gamma = \kappa + \pi\Omega^2\rho(\omega_s \pm \Omega)$ in the very strong-coupling regime. The background colour indicates at which coupling strength the system undergoes a transition from the Markovian (white) to the non-Markovian (grey) regime. The error bars correspond to the minimal and maximal values of the estimated decay rates from the experimental data. As no Rabi oscillations occur in the Markovian regime, the values for the decay rate can be determined more accurately in this limit.

peak shows a pronounced overshoot after switching off the microwave drive, at which the energy stored in the spin ensemble is coherently released back into the cavity. These oscillations are a hallmark of the non-Markovian character of the system dynamics in the strong-coupling regime, for which an accurate knowledge of the memory-kernel $\mathcal{K}(t-\tau)$ in our Volterra equation is essential.

Our hybrid cavity–spin system can not be modelled by two coupled damped harmonic oscillators as in the case of a purely Lorentzian spin distribution. The spectral profile of a $q$-Gaussian has marked consequences on the dynamics in the strong-coupling regime: in particular, for spectral distributions $\rho(\omega)$ with tails that fall off faster than a Lorentzian lineshape ($\propto 1/\omega^2$), an increasing coupling strength was predicted to lead to a reduction of the decay rate $\Gamma$ and to protect the system against decoherence—hence the name 'cavity-protection effect'[5,7]. In a nutshell, 'cavity protection' can be understood as follows: in the strong-coupling regime, the cavity couples to a set of superradiant states forming hybridized energy levels split by $\hbar\Omega_R$. The resulting polariton states are coupled to subradiant spin-wave modes acting as the main source of decoherence, and the total decay rate depends on the energetic gap between the polaritons and the subradiant states. If the spectral profile of the inhomogeneous spin distribution decays sufficiently fast for increasing gap size, an energetic decoupling of the superradiant polaritons from the subradiant spin-wave modes occurs, leading to a suppressed damping of the polaritons. Although the origin of this intriguing effect can also be understood on the basis of an ensemble of coupled classical oscillators[5,7], the important point to note is that it also survives on the level of single-photon excitations (see Supplementary Methods Section II).

As the tails of our spin distribution satisfy the required fast decay, we now have the possibility to probe this exceptional behaviour in the experiment. We measure the decay rate $\Gamma(\Omega)$ of the cavity amplitude after driving the system for different coupling strengths $\Omega$ into steady state using a sufficiently long rectangular pulse (as in Fig. 2b, see Methods). The values of $\Gamma(\Omega)$, as determined by the slope of the temporal decay after switch off, are shown in Fig. 3. We find the decay rate to vary over almost one order of magnitude in a strongly non-monotonic fashion: in the weak-coupling regime the decay rate $\Gamma$ increases with growing coupling strength $\Omega$ as a result of the Purcell effect[25] as the cavity mode increasingly couples to the spin ensemble. Entering the strong-coupling regime, this trend reverses and $\Gamma$ decreases with growing $\Omega$. To highlight this remarkable phenomenon, we also plot in Fig. 3 the behaviour for a Lorentzian spin distribution, for which $\Gamma(\Omega)$ is constant in the strong-coupling limit. Performing a Laplace transform of our Volterra equation we find that in the limit of very strong coupling ($\Omega \to \infty$) the decay rate takes the following closed analytical form $\Gamma = \kappa + \pi\Omega^2\rho(\omega_s \pm \Omega)$ (in agreement with a stationary analysis[7]). Whereas the maximally reachable value of $\Omega/2\pi = 8.6$ MHz in our device already leads to a considerable reduction of $\Gamma$ by 50% below its maximum, our numerical results (Fig. 3) suggest a further reduction of the decay rate with increasing coupling strength by an order of magnitude. We predict that a three times higher $\Omega$ could be achieved by filling up the cavity with diamond and by further increasing the NV density. Having the mode volume entirely occupied with NV centres, a factor of two enhanced NV concentration would already bring us close to exploiting the full potential of the cavity-protection effect. We estimate that such an increased NV concentration would cause a mean NV–NV interaction strength of 120 kHz, which is still small enough to have only a negligible influence on the dynamics of our system.

In a next step, we demonstrate that the 'cavity-protection effect' can also be employed for the realization of coherent-control schemes. In particular, we address a central question when dealing with coherently driven spin ensembles—namely, how to achieve high excitation levels in the spin ensemble with limited driving powers[18,26]. In a simplified picture of two coupled harmonic oscillators this can be achieved by a drive modulated with the inverse of the effective coupling strength. To realize this for the non-Lorentzian spectral spin distribution of our ensemble a pulsed driving is required to match the Rabi frequency $\Omega_R$ rather than the effective coupling strength $2\,\Omega$, which quantities are here quite different from each other. We thus probe our set-up by a driving field with a carrier frequency $\omega_p = \omega_c = \omega_s$ and a periodic modulation with tunable period $\tau$. Realizing the latter with a simple periodic sign-change of the carrier signal, we find that this driving scheme produces giant oscillations in the transmission (Fig. 4a) corresponding to a coherent exchange of energy between the cavity and the spin ensemble. A maximum oscillation amplitude occurs exactly at the point where the modulation period $\tau$ coincides with the inverse of the Rabi splitting $2\pi/\Omega_R$. Note that at this resonant driving the steady-state oscillation amplitude in the transmission signal (Fig. 4b) exceeds the stationary amplitude (Fig. 2b) by two orders of magnitude, although the net power applied to the cavity is exactly the same in both cases. Our approach demonstrates how to sustain coherent oscillations and how to reach considerably high excitation amplitudes of the spin ensemble without using strong driving powers. For comparison, we also plot in Fig. 4b the results both for a $q$-Gaussian as well as for a Lorentzian spin density, which clearly shows the substantially lower excitation amplitudes for the Lorentzian case. This clear signature of the 'cavity-protection effect' paves the way for the realization of sophisticated coherent-control schemes in the strong-coupling regime of QED.

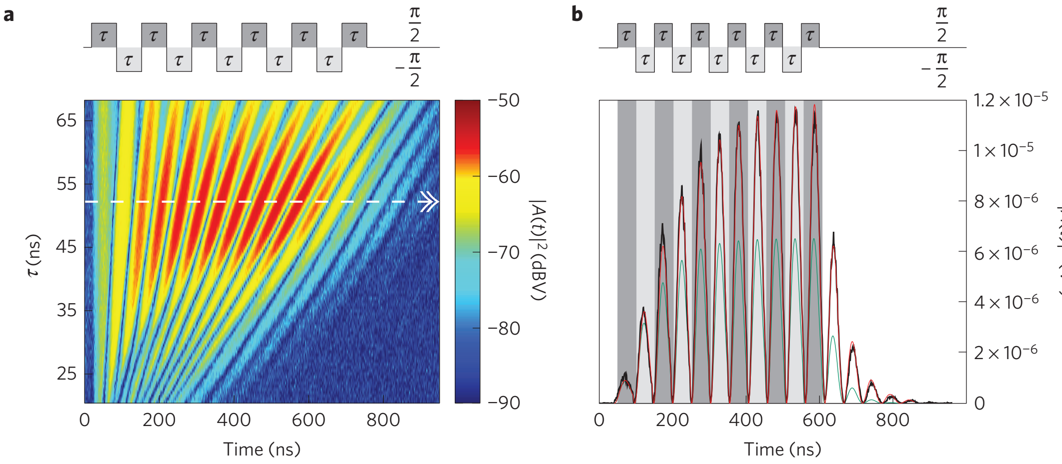

**Figure 4 | Enhancement of the cavity transmission intensity by pulsed driving. a**, The cavity transmission of eleven successive rectangular microwave pulses with carrier frequency $\omega_p = \omega_c = \omega_s$, phase-switched by $\pi$, as a function of time and pulse duration $\tau$ (see top panel for the pulse shape). **b**, Dynamics at the largest enhancement of the cavity transmission, corresponding to a pulse duration of $\tau = 52$ ns (indicated by the white dashed line in **a**) equal to the Rabi period $T_R = 2\pi/\Omega_R$. After switching off the probe signal the system settles back to the ground state through damped Rabi oscillations. Excellent agreement between experiment (black curve) and theory (red curve) is found, using the same system parameters as in Fig. 3. A Lorentzian spin distribution in the theoretical calculations (green curve) leads to a considerably smaller enhancement owing to the absence of the cavity-protection effect.

## Methods

The cavity is an overcoupled $\lambda/2$ resonator, made out of 200 nm thick sputtered niobium on a 330 μm thick sapphire substrate, structured by optical lithography and reactive ion etching. The diamond sample is a commercially available type Ib high-pressure high-temperature diamond (HPHT) with a size of $4.5 \times 2.25 \times 0.5$ mm$^3$ and two polished (100) surfaces. The crystal contains an initial concentration of 200 ppm nitrogen and has a natural abundance of $^{13}$C nuclear isotopes. We achieve a total density of ~6 ppm NV centres by 50 h of neutron irradiation with a fluence of $5 \times 10^{17}$ cm$^{-2}$ and by annealing the crystal for 3 h at 900 °C, resulting in a conversion efficiency from initial nitrogen to NV centres of 3%. The diamond sample has been characterized by means of a room-temperature confocal laser scanning microscope, allowing us to measure the NV density and the zero-field splitting parameters $D$ and $E$ by optically detected magnetic resonance[27]. Residual nitrogen is incorporated in the diamond mainly as substitutional single defect centres, which also act as paramagnetic impurities with $S = 1/2$ and thus form the main source of inhomogeneous broadening.

The NV centre is a paramagnetic impurity which consists of a substitutional nitrogen atom and an adjacent vacancy in the diamond lattice. The energy level structure features an electron spin triplet ($S = 1$) as its ground state[28]. Owing to negligible direct NV–NV interactions, it can be described, to lowest order, by the Hamiltonian[29], $H/h = DS_z^2 + E(S_x^2 - S_y^2) + \mu \mathbf{BS}$ with $\mathbf{S} = (S_x, S_y, S_z)$, $D = 2.877$ GHz, $E = 7.7$ MHz and $\mu = 28$ MHz mT$^{-1}$, providing us with an estimate for the mean spin transition frequency $\omega_s$. The zero-field splitting term $D = 2.877$ GHz corresponds to 138 mK, which is high compared with the temperature of 25 mK at which the experiments are performed and allows us to thermally polarize the NV spins up to 99%. In the diamond lattice four crystallographic orientations of the NV defect are possible. Our diamond sample has a (100) surface orientation. We apply a d.c. magnetic field of 9.4 mT to Zeeman tune the spins into resonance with the cavity, which is applied in the plane of the resonator and therefore in the (100) plane of the crystal. We rotate the magnetic field direction by 22.5° in the plane, at which only two subensembles are degenerate. The external magnetic field leads, on the one hand, to a Zeeman splitting of subensembles such that the maximal possible ensemble–cavity coupling strength is reduced by a factor of $\sqrt{2}$. On the other hand, it narrows the width of the spectral spin distribution induced by a misalignment of the applied external magnetic field with respect to the crystallographic frame.

For the application of short microwave pulses with adjustable phase and power we use a frequency mixer controlled by an arbitrary waveform generator (AWG). The microwave signal passes the cryostat and is attenuated by −60 dB when reaching the resonator. The transmitted signal is fed into a circulator and amplified on the 4 K stage. Using a homodyne detection scheme, the transmitted and amplified microwave signal is mixed with the reference signal and both quadrature signals I and Q are recorded by a fast analog-to-digital converter with 2 GS s$^{-1}$ sampling frequency. The AWG repeats the pulse sequence and $10^6$ single traces are averaged. From the two quadratures I and Q the transmitted microwave intensity $|A(t)|^2$ is calculated and plotted in Figs 2 and 4. Voltage fluctuations give a standard deviation of $\pm 1.02 \times 10^{-5}$ (V) on the quadratures I and Q. The squared steady-state amplitude of the cavity transmission (Fig. 2b) gives a mean signal of $|A|^2 = 1.44 \times 10^{-7} \pm 6.85 \times 10^{-9}$ (V$^2$). To reduce the coupling strength (Fig. 3) we repeatedly pump the resonator with high power and a long microwave pulse, corresponding to $\sim 2.5 \times 10^7$ microwave photons in the cavity. For this measurement power, a non-negligible number of NV spins gets excited, leading to a reduced number of ground-state spins coupled to the cavity.

Received 29 March 2014; accepted 30 June 2014;

## References

1. Zhu, X. *et al.* Coherent coupling of a superconducting flux qubit to an electron spin ensemble in diamond. *Nature* **478,** 221–224 (2011).
2. Xiang, Z-L., Ashhab, S., You, J. Q. & Nori, F. Hybrid quantum circuits: Superconducting circuits interacting with other quantum systems. *Rev. Mod. Phys.* **85,** 623–653 (2013).
3. Kubo, Y. *et al.* Hybrid quantum circuit with a superconducting qubit coupled to a spin ensemble. *Phys. Rev. Lett.* **107,** 220501 (2011).
4. Amsüss, R. *et al.* Cavity QED with magnetically coupled collective spin states. *Phys. Rev. Lett.* **107,** 060502 (2011).
5. Kurucz, Z., Wesenberg, J. H. & Mølmer, K. Spectroscopic properties of inhomogeneously broadened spin ensembles in a cavity. *Phys. Rev. A* **83,** 053852 (2011).
6. Sandner, K. *et al.* Strong magnetic coupling of an inhomogeneous nitrogen–vacancy ensemble to a cavity. *Phys. Rev. A* **85,** 053806 (2012).
7. Diniz, I. *et al.* Strongly coupling a cavity to inhomogeneous ensembles of emitters: Potential for long-lived solid-state quantum memories. *Phys. Rev. A* **84,** 063810 (2011).
8. Wallraff, A. *et al.* Strong coupling of a single photon to a superconducting qubit using circuit quantum electrodynamics. *Nature* **431,** 162–167 (2004).
9. Majer, J. Coupling superconducting qubits via a cavity bus. *Nature* **449,** 443–447 (2007).
10. Kubo, Y. *et al.* Strong coupling of a spin ensemble to a superconducting resonator. *Phys. Rev. Lett.* **105,** 140502 (2010).
11. Schuster, D. I. *et al.* High-cooperativity coupling of electron-spin ensembles to superconducting cavities. *Phys. Rev. Lett.* **105,** 140501 (2010).
12. Probst, S. *et al.* Anisotropic rare-earth spin ensemble strongly coupled to a superconducting resonator. *Phys. Rev. Lett.* **110,** 157001 (2013).
13. Kubo, Y. *et al.* Storage and retrieval of a microwave field in a spin ensemble. *Phys. Rev. A* **85,** 012333 (2012).
14. Saito, S. *et al.* Towards realizing a quantum memory for a superconducting qubit: Storage and retrieval of quantum states. *Phys. Rev. Lett.* **111,** 107008 (2013).
15. Bar-Gill, N., Pham, L., Jarmola, A., Budker, D. & Walsworth, R. Solid-state electronic spin coherence time approaching one second. *Nature Commun.* **4,** 456 (2013).

16. Childress, L. *et al.* Coherent dynamics of coupled electron and nuclear spin qubits in diamond. *Science* **314,** 281–285 (2006).
17. Stanwix, P. L. *et al.* Coherence of nitrogen–vacancy electronic spin ensembles in diamond. *Phys. Rev. B* **82,** 201201 (2010).
18. Grezes, C. *et al.* Multimode storage and retrieval of microwave fields in a spin ensemble. *Phys. Rev. X* **4,** 021049 (2014).
19. Wu, H. Storage of multiple coherent microwave excitations in an electron spin ensemble. *Phys. Rev. Lett.* **105,** 140503 (2010).
20. Primakoff, H. & Holstein, T. Many-body interactions in atomic and nuclear systems. *Phys. Rev.* **55,** 1218–1234 (1939).
21. Tavis, M. & Cummings, F. W. Exact solution for an $N$-molecule—radiation-field Hamiltonian. *Phys. Rev.* **170,** 379–384 (1968).
22. Emary, C. & Brandes, T. Chaos and the quantum phase transition in the Dicke model. *Phys. Rev. E* **67,** 066203 (2003).
23. Verdú, J. *et al.* Strong magnetic coupling of an ultracold gas to a superconducting waveguide cavity. *Phys. Rev. Lett.* **103,** 043603 (2009).
24. Dicke, R. H. Coherence in spontaneous radiation processes. *Phys. Rev.* **93,** 99–110 (1954).
25. Proceedings of the American Physical Society. *Phys. Rev.* **69,** 674 (1946).
26. Sigillito, A. J. *et al.* Fast, low-power manipulation of spin ensembles in superconducting microresonators. *Appl. Phys. Lett.* **104,** 222407 (2014).
27. Nöbauer, T. *et al.* Creation of ensembles of nitrogen–vacancy centers in diamond by neutron and electron irradiation. Preprint at http://arxiv.org/abs/1309.0453 (2013).
28. Redman, D. A., Brown, S., Sands, R. H. & Rand, S. C. Spin dynamics and electronic states of N-V centers in diamond by EPR and four-wave-mixing spectroscopy. *Phys. Rev. Lett.* **67,** 3420–3423 (1991).
29. Jelezko, F., Gaebel, T., Popa, I., Gruber, A. & Wrachtrup, J. Observation of coherent oscillations in a single electron spin. *Phys. Rev. Lett.* **92,** 076401 (2004).

## Acknowledgements

We would like to thank C. Koller, F. Mintert, P. Rabl, H. Ritsch, K. Sandner and M. Trupke for helpful discussions, and D. Brasch/Terra Mater Magazin for the image shown in Fig. 1b. The experimental effort has been supported by the TOP grant of TU Vienna. S.P. acknowledges support by the Austrian Science Fund (FWF) in the framework of the Doctoral School 'Building Solids for Function' (Project W1243). D.O.K. and S.R. acknowledge funding by the FWF through Projects No. F25-P14 (SFB IR-ON) and No. F49-P10 (SFB NextLite).

## Author contributions

S.P., R.A., A.V., T.N., J.S. and J.M. designed and set up the experiment. S.P., R.A. and A.V. carried out the measurements with supervision by J.M. D.O.K. and S.R. devised the theoretical framework and performed the calculations. S.P., D.O.K., S.R. and J.M. wrote the first manuscript draft, to which all authors suggested improvements.

## Additional information

Supplementary information is available in the online version of the paper. Reprints and permissions information is available online at www.nature.com/reprints. Correspondence and requests for materials should be addressed to S.R. or J.M.

## Competing financial interests

The authors declare no competing financial interests.

nature physics

SUPPLEMENTARY INFORMATION

DOI: 10.1038/NPHYS3050

# Protecting a spin ensemble against decoherence in the strong-coupling regime of cavity QED

S. Putz§,[1,2] D. O. Krimer§,[3] R. Amsüss,[1] A. Valookaran,[1]
T. Nöbauer,[1] J. Schmiedmayer,[1] S. Rotter,[3] and J. Majer[1,2]

[1] *Vienna Center for Quantum Science and Technology,*
*Atominstitut, Vienna University of Technology,*
*Stadionallee 2, 1020 Vienna, Austria*

[2] *Zentrum für Mikro- und Nanostrukturen,*
*Vienna University of Technology, Floragasse 7, 1040 Vienna, Austria*

[3] *Institute for Theoretical Physics, Vienna University of Technology,*
*Wiedner Hauptstrasse 8-10/136, 1040 Vienna, Austria*

(Dated: July 10, 2014)

---

§These authors contributed equally to this work (S.P. experiment, D.O.K. theory)

DOI: 10.1038/NPHYS3050

## I. VOLTERRA EQUATION FOR THE CAVITY AMPLITUDE

We start from the Hamiltonian of the main article and derive the Heisenberg operator equations for the cavity and spin operators ($\hbar = 1$), $\dot{a} = i[\mathcal{H}, a] - \kappa a$, $\dot{\sigma}_k^- = i[\mathcal{H}, \sigma_k^-] - \gamma\sigma_k^-$, respectively. Here $\kappa$ and $\gamma$ stand for the total cavity and spin losses, respectively. As was shown already in earlier work[1,2] the noise operators can be neglected when considering only expectation values, to which they do not contribute. We also note explicitly that in our calculations the influence of a finite temperature can be disregarded. At the minute temperatures at which the experiment is carried out ($\sim$ 25 mK) we have $k_B T \ll \hbar\omega_s$, resulting in an occupation probability of the ensemble ground state of 99%. Since the number of excited spins remains very small compared to the ensemble size, even with the weak external driving that we use for all the results reported in the main article, we are allowed to apply the commonly used Holstein-Primakoff-approximation, $\langle\sigma_k^z\rangle \approx -1$, when writing down the following set of equations for the operator expectation values in the frame rotating with the probe frequency $\omega_p$. Denoting $A(t) \equiv \langle a(t)\rangle$ and $B_k(t) \equiv \langle\sigma_k^-(t)\rangle$, we end up with the following set of first-order ODEs with respect to the cavity and spin amplitudes

$$\dot{A}(t) = -\left[\kappa + i(\omega_c - \omega_p)\right] A(t) + \sum_k g_k B_k(t) - \eta(t), \tag{1a}$$

$$\dot{B}_k(t) = -\left[\gamma + i(\omega_k - \omega_p)\right] B_k(t) - g_k A(t). \tag{1b}$$

Note, that the size of our spin ensemble is very large (typically $N \sim 10^{12}$) and individual spins are distributed around a certain mean frequency $\omega_s$. We can thus go to the continuum limit by introducing the continuous spectral density as $\rho(\omega) = \sum_k g_k^2 \delta(\omega - \omega_k)/\Omega^2$ (see, e.g. 1), where $\Omega$ is the collective coupling strength of the spin ensemble to the cavity and $\int d\omega\rho(\omega) = 1$. In what follows we will replace any discrete function $F(\omega_k)$ by its continuous counterpart, $F(\omega)$: $F(\omega_k) \rightarrow \Omega^2 \int d\omega\rho(\omega)F(\omega)$. By integrating Eq. (1b) in time, each individual spin amplitude, $B_k(t)$, can formally be expressed in terms of the cavity amplitude, $A(t)$. By plugging the resulting equation into Eq. (1a) and assuming that initially all spins are in the ground state, $B_k(t = 0) = 0$, we arrive at the following integro-differential Volterra equation for the cavity amplitude ($\omega_c = \omega_s$)

$$\dot{A}(t) = -\kappa A(t) - \Omega^2 \int d\omega\rho(\omega) \int_0^t d\tau e^{-i(\omega-\omega_c-i\gamma)(t-\tau)} A(\tau) - \eta(t), \tag{2}$$

Note that in the $\omega_p$-rotating frame the rapid oscillations presented in the original Hamiltonian (1) are absent, so that the time variation of $\eta(t)$ in Eq. (2) is much slower as compared to $1/\omega_p$.

For a proper description of the resulting dynamics, it is essential to capture the form of the spectral density $\rho(\omega)$ realized in the experiment as accurately as possible. Following 3, we take the $q$-Gaussian function for that purpose

$$\rho(\omega) = C \cdot \left[1 - (1-q)\frac{(\omega-\omega_s)^2}{\Delta^2}\right]^{\dfrac{1}{1-q}}, \tag{3}$$

characterized by the dimensionless shape parameter $1 < q < 3$ which yields the form of a Lorentzian and Gaussian distribution, for $q = 2$ and for $q \to 1$, respectively. Here $C$ is a normalization constant which is easily obtained numerically; the full-width at half-maximum (FWHM) of $\rho(\omega)$ is given by $\gamma_q = 2\Delta\sqrt{\dfrac{2^q-2}{2q-2}}$.

In a next step we formally integrate Eq. (2) in time to get rid of the time derivative of $A(t)$. The resulting double integral with respect to time on the right-hand side is simplified further by partial integration, so that we obtain again a single integral with respect to time. Assuming that the cavity is initially empty, $A(t=0) = 0$, we finally end up with the following equation for the cavity amplitude

$$A(t) = \int_0^t d\tau \mathcal{K}(t-\tau)A(\tau) + \mathcal{F}(t), \tag{4}$$

which contains the kernel function $\mathcal{K}(t-\tau)$,

$$\mathcal{K}(t-\tau) = \Omega^2 \int d\omega\, \frac{\rho(\omega)\left[e^{-i(\omega-\omega_c-i(\gamma-\kappa))(t-\tau)} - 1\right]}{i(\omega-\omega_c-i(\gamma-\kappa))} \cdot e^{-\kappa(t-\tau)}, \tag{5}$$

and the function $\mathcal{F}(t)$,

$$\mathcal{F}(t) = -\int_0^t d\tau\, \eta(\tau) \cdot e^{-\kappa(t-\tau)}. \tag{6}$$

Despite its seemingly simple form, Eq. (4) is not trivial to solve in practice, even numerically. The reasons are twofold: First, the result of the integration for $A(t)$ at time $t$ depends on the amplitude $A(\tau)$ calculated at all earlier times, $\tau < t$ (memory effect). Second, the kernel function $\mathcal{K}(t-\tau)$ contains the integration with respect to frequency, which is costly in terms of computational time. (Note that such an integration has to be performed for each $t$ and $\tau < t$.) The smallest possible time scale in our problem is given by $T = 2\pi/\omega_p \sim 0.4\,\mathrm{ns}$. To achieve a very good accuracy of the calculations for the results presented in Figs. 2,4 from the main article, we solve the equation on a mesh with uniform spacing, choosing a time step $dt \sim 0.05\,\mathrm{ns}$ (see e.g. 4 for more details about the method). The direct discretization of $\mathcal{K}(t-\tau)$ on the time interval of the order of µs (typical time of measurements) leads to a high-dimensional matrix (of a size typically exceeding $10^4 \times 10^4$), which, together with the integration with respect to frequency, makes the problem computationally intractable by way of a direct numerical solution. To overcome this problem and to speed up the calculations drastically, we divide the whole time integration into many successive subintervals, $T_n \le t \le T_{n+1}$, with $n = 1, 2, \ldots$. Such a time division might, in principle, be implemented arbitrarily but we choose it to be adapted to our experimental realization. Specifically, the driving amplitude is unchanged within each subinterval, so that in our case it is given by

$$\eta_n = \begin{cases} \eta & n = 1,3,5,\ldots \\ -\eta & n = 2,4,6,\ldots \end{cases} . \tag{7}$$

In this way the result of integration at the $n$-th time interval, $A^{(n)}(T_{n+1})$, enters as an initial condition for the integration during the $(n+1)$-th time interval, $A^{(n+1)}(T_{n+1})$. Finally, we end up with the following recurrence relation (time runs within $T_n \le t \le T_{n+1}$ for $n = 1, 2, 3, \ldots$)

$$A^{(n)}(t) = \int_{T_n}^{t} d\tau \mathcal{K}(t-\tau) A^{(n)}(\tau) + \mathcal{F}^{(n)}(t), \tag{8}$$

where the kernel function $\mathcal{K}(t-\tau)$ is defined by Eq. (5) and

$$\mathcal{F}^{(n)}(t) = A^{(n-1)}(T_n) e^{-\kappa(t-T_n)} + \Omega^2 e^{-\kappa(t-T_n)} \int d\omega \frac{\rho(\omega)\left[e^{-i(\omega-\omega_c-i(\gamma-\kappa))(t-T_n)} - 1\right]}{i(\omega-\omega_c-i(\gamma-\kappa))} \cdot \mathcal{I}_n(\omega) - \frac{\eta_n}{\kappa} \cdot \left[1 - e^{-\kappa(t-T_n)}\right] \tag{9}$$

Remarkably, the memory about previous events enters both through the amplitude $A^{(n-1)}(T_n)$ and through the function

$$\mathcal{I}_n(\omega) = e^{-i(\omega-\omega_p-i\gamma)(T_n-T_{n-1})} \mathcal{I}_{n-1}(\omega) + \int_{T_{n-1}}^{T_n} d\tau e^{-i(\omega-\omega_p-i\gamma)(T_n-\tau)} A^{(n-1)}(\tau). \tag{10}$$

In accordance with the above initial conditions ($t = T_1 = 0$), $A(T_1) = 0$ and $\mathcal{I}_1(\omega) = 0$.

The above technique allows us to solve Eq. (4) accurately while being very efficient in terms of computational time. We have tested the accuracy of our numerical results by varying the discretization both in time and frequency in a wide range obtaining excellent agreement with the experimental results shown in Figs. 2,4 of the main paper and thereby confirming the accuracy of our method.

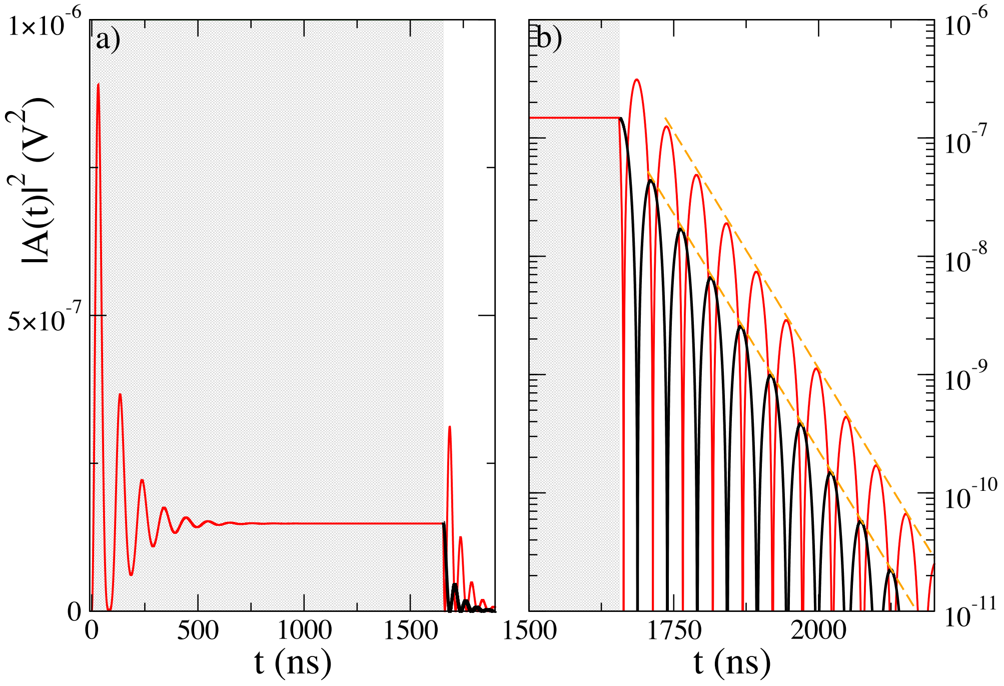

FIG. 1: a) Red curve: calculated cavity probability amplitude $|A(t)|^2$ versus time $t$ under the action of an incident long multi-photon pulse of duration 1.65 $\mu$s with the carrier frequency matching the resonance condition, $\omega_p = \omega_c = 2\pi \cdot 2.6915\,\mathrm{GHz}$, and the coupling strength $2\Omega = 17.2$ MHz (analogous to Fig. 2b from the main article). Gray (white) area indicates a time interval during which a pumping signal is on (off). Black curve: Decay from the initial state $|1, G\rangle$, for which a single photon with frequency $\omega_c$ is in the cavity and all spins are in the ground state. For the sake of visualisation, the initial probability is rescaled such as to coincide with the steady state value of the multi-photon signal. b) Same figure as a) with a zoom on the decaying part and with the ordinate plotted on a logarithmic scale. The asymptotic decay is well described, for both the red and the black curve, by the exponential function, $C\, e^{-\Gamma t}$, with $\Gamma/2\pi = 3.0\,\mathrm{MHz}$ taken from Fig. 3 of the main article (see orange dashed curves). This agreement illustrates the applicability of the cavity-protection effect also for single-photon processes.

## II. CAVITY PROTECTION EFFECT ON THE SINGLE PHOTON LEVEL

In the experiment presented in the main article the number of microwave photons in the cavity is typically of the order of $10^6$. Here we demonstrate that our main findings on the cavity protection effect also remain valid when only a single photon is populating the cavity. For this purpose we start from the Heisenberg equations for the cavity and spin operators, $a(t)$ and $\sigma_k^-(t)$, which have the same form as those described in Sec. I. We now assume that the cavity is fed with a single photon and all spins are in the ground state, $|1, G\rangle = a^\dagger(t = 0)|0\rangle$, where $|0\rangle$ stands for the vacuum state. We then let these operator equations act on the bra- and ket-vectors $\langle 0|$ and $a^\dagger(t = 0)|0\rangle$, respectively, and derive the corresponding equations for the expectation values. These equations perfectly coincide with Eqs. (1a,1b) from Sec. I where, however, the amplitudes $A(t), B(t)$ are now given as $A(t) \equiv \langle 0|a(t)a^\dagger(t = 0)|0\rangle$ and $B_k(t) \equiv \langle 0|\sigma_k^-(t)a^\dagger(t = 0)|0\rangle$. Note that the variable $A(t)$ stands here for the probability amplitude for a photon to be in the cavity at time $t$, if it was there initially, $A(t = 0) \equiv \langle 0|a(t = 0)a^\dagger(t = 0)|0\rangle = \langle 1, G|1, G\rangle = 1$.

We thus find for the single-photon regime the same Volterra equation for the cavity amplitude, $A(t)$, as we did before for the multi-photon decay process from the steady-state as considered in the main article (see Fig. 3 there). The only difference lies in the initial condition, which, in the single-photon case, takes on the simple form $A(t = 0) = 1$. However, the asymptotic decay rate $\Gamma$ is independent of the initial conditions and the cavity protection effect remains unaffected. To demonstrate this explicitly also numerically, we compare in Fig. 1 the multi-photon dynamics from the main text with the single-photon case considered here. At first sight, the decay dynamics look very different in these two cases, see Fig. 1a), even when the probability $|A(t)|^2$ is rescaled for both cases to coincide at $t = 0$. When plotting the decay logarithmically, see Fig. 1b), it becomes clear, however, that the asympotitic decay constants which are relevant for the cavity protection effect are, indeed, exactly the same. To conclude, the key insight on the reduction of the decay rate for increasing collective coupling strength $\Omega$ (as following from Fig. 3 of the main article), remains valid also on the single-photon level.

[1] Diniz, I. *et al.* Strongly coupling a cavity to inhomogeneous ensembles of emitters: Potential for long-lived solid-state quantum memories. *Phys. Rev. A* **84**, 063810 (2011). 2

[2] Kurucz, Z., Wesenberg, J. H. & Mølmer, K. Spectroscopic properties of inhomogeneously broadened spin ensembles in a cavity. *Phys. Rev. A* **83**, 053852 (2011). 2

[3] Sandner, K. *et al.* Strong magnetic coupling of an inhomogeneous nitrogen-vacancy ensemble to a cavity. *Phys. Rev. A* **85**, 053806 (2012). 3

[4] Press, W. H., Teukolsky, S. A., Vetterling, W. T. & Flannery, B. P. Numerical recipes: The art of scientific computing. *Cambridge University Press, New York* (2007). 4

# Hybrid Quantum Systems with Collectively Coupled Spin States: Suppression of Decoherence through Spectral Hole Burning

Dmitry O. Krimer,* Benedikt Hartl, and Stefan Rotter
*Institute for Theoretical Physics, Vienna University of Technology (TU Wien),*
*Wiedner Hauptstraße 8-10/136, A-1040 Vienna, Austria, European Union*

(Received 14 January 2015; published 14 July 2015)

Spin ensemble based hybrid quantum systems suffer from a significant degree of decoherence resulting from the inhomogeneous broadening of the spin transition frequencies in the ensemble. We demonstrate that this strongly restrictive drawback can be overcome simply by burning two narrow spectral holes in the spin spectral density at judiciously chosen frequencies. Using this procedure we find an increase of the coherence time by more than an order of magnitude as compared to the case without hole burning. Our findings pave the way for the practical use of these hybrid quantum systems for the processing of quantum information.

DOI: 10.1103/PhysRevLett.115.033601 PACS numbers: 42.50.Ct, 32.30.-r, 42.50.Gy, 42.50.Pq

Hybrid quantum circuits that conflate the advantages of different physical systems to achieve new device functionalities have recently shifted to the center of attention [1]. This is largely because a new generation of experiments [2–11] lends encouraging plausibility to the vision of using such hybrid device concepts to reliably store and manipulate quantum information [12–17]. In particular, the recent achievements in strongly coupling large spin ensembles to superconducting microwave cavities [2–6,11] hold promise for combining many of the advantageous features of microwave technology with the long spin coherence times found, e.g., in crystallographic defects of diamond.

Whereas the collective coupling to a whole ensemble of spins is the key to reach the strong-coupling limit, the ensemble generally comes with the downside of being inhomogeneously broadened; i.e., the transition frequencies between different spin levels are slightly different for each spin. As it turns out, the decoherence resultant from this broadening is currently the major bottleneck for the processing of quantum information in these hybrid quantum systems. First attempts at resolving this problem have meanwhile been put forward: On the one hand, it was shown that the decoherence is naturally suppressed for very strong coupling when the spectral spin distribution realized by the ensemble falls off sufficiently fast in its tails. Signatures of this so-called "cavity protection effect" [18,19] have meanwhile also been observed experimentally [11,20]. To fully bring to bear the potential of this effect requires, however, going to very high values of the coupling strength, which are presently difficult to reach experimentally. On the other hand, sophisticated concepts for the spectral engineering of the spin density profile have been proposed [21,22]. These concepts rely, however, on a strong modification of the intrinsically predefined density profile that is again very challenging to implement experimentally. In this Letter, we present a method that circumvents the problems of both approaches by building on a very elementary concept that requires only a considerably reduced experimental effort. Specifically, we demonstrate that the burning of two judiciously placed spectral holes in the spin distribution suffices to drastically increase the coherence properties of the hybrid spin-cavity system. From the viewpoint of quantum control, our approach constitutes a new and efficient strategy to stabilize Rabi oscillations in the strong-coupling limit of cavity QED [23–25]. Suppressing the detrimental influence of inhomogeneous broadening, as suggested in our work, could also prove to be a key element for the realization of ultranarrow linewidth lasers [26,27].

To connect our theoretical work directly with the experiment we will study in the following the recently implemented case of a superconducting microwave resonator strongly coupled to an ensemble of negatively charged nitrogen-vacancy centers in a diamond (see Fig. 1) [2,3,11,20]. Our starting point is the Tavis-Cummings Hamiltonian ($\hbar = 1$) [28], which describes the dynamics of a single-mode cavity coupled to a spin ensemble in the dipole and rotating-wave approximation,

$$\mathcal{H} = \omega_c a^\dagger a + \frac{1}{2}\sum_j^N \omega_j \sigma_j^z + i\sum_j^N [g_j\sigma_j^- a^\dagger - g_j^*\sigma_j^+ a] - i[\eta(t)a^\dagger e^{-i\omega t} - \eta(t)^* a e^{i\omega t}]. \quad (1)$$

Here $\sigma_j^+, \sigma_j^-, \sigma_j^z$ are the Pauli operators associated with the individual spins of frequency $\omega_j$. Each spin is coupled with a

---

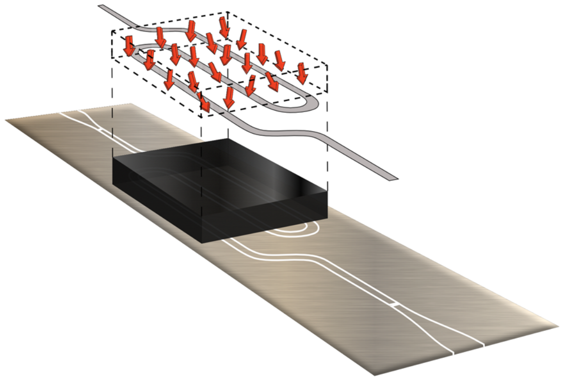

FIG. 1 (color online). Sketch of the studied hybrid quantum system: a synthetic diamond (black) containing a spin ensemble (red arrows) coupled to a transmission-line resonator (curved gray line) confining the electromagnetic field to a small volume.

strength $g_j$ to the single cavity mode of frequency $\omega_c$, in which photons are created and annihilated through the operators $a^\dagger$ and $a$. The probing electromagnetic field injected into the cavity is characterized by its carrier frequency $\omega$ and by the amplitude $\eta(t)$.

Next, we derive the semiclassical equations of motion using the Holstein-Primakoff approximation [29] (implying that the condition $\langle\sigma_k^z\rangle \approx -1$ always holds), the rotating-wave approximation and neglecting the dipole-dipole interaction between spins. With these simplifications, which are well justified for the experiments [11,20] operating at low input powers of an incoming signal, the equations for $A(t) \equiv \langle a(t)\rangle$ and $B_j(t) \equiv \langle\sigma_j^-(t)\rangle$ acquire the following form (in the $\omega$-rotating frame):

$$\dot{A}(t) = -[\kappa + i(\omega_c - \omega)]A(t) + \sum_j g_j B_j(t) - \eta(t), \tag{2a}$$

$$\dot{B}_j(t) = -[\gamma + i(\omega_j - \omega)]B_j(t) - g_j A(t), \tag{2b}$$

where $\kappa$, $\gamma$ are the dissipative cavity and spin losses, respectively.

Large spin ensembles ($N \sim 10^{12}$ in [11,20]) are best described by the continuum limit of the normalized spectral density $\rho(\omega) = \sum_j^N g_j^2 \delta(\omega - \omega_j)/\Omega^2$. Here $\Omega = (\sum_j^N g_j^2)^{1/2}$ is an effective coupling strength which is enhanced by a factor of $\sqrt{N}$ as compared to a single coupling strength, $g_j$, so that $\Omega$ can reach the values necessary for the realization of the strong-coupling regime. The inhomogeneous broadening of the spin frequencies $\omega_j$ and coupling strengths $g_j$ then lead to a finite-width distribution $\rho(\omega)$ centered around a certain mean frequency $\omega_s$. The specific shape of this spectral density $\rho(\omega)$ can typically be determined by a careful comparison with the experiment based on stationary [3] or dynamical [11] transmission measurements. In the following, we will use the same parameters as in [11,20], taking a $q$-Gaussian distribution [3] for $\rho(\omega)$ centered around $\omega_s/2\pi = 2.6915$ GHz, a full-width at half-maximum of $\gamma_q/2\pi = 9.44$ MHz and a $q$ parameter of 1.39. The cavity decay rate $\kappa/2\pi = 0.4$ MHz (half-width at half-maximum) and the coupling strength $\Omega/2\pi = 8.56$ MHz.

The starting point for our strategy is the insight that the non-Markovian dynamics of the spin system, which is described by $\rho(\omega)$ and strongly coupled to the cavity mode, can be accurately modeled by an integral Volterra equation for the cavity amplitude $A(t)$ [see Eq. (5) below and [11,20]]. The latter includes a memory kernel, which is responsible for the non-Markovian feedback of the spin ensemble on the cavity, so that the cavity amplitude at time $t$ depends on all previous events $\tau < t$. By performing a Laplace transform of this Volterra equation [20] or by carrying out a stationary transmission analysis [18,19], the total rate of decoherence turns out to be $\Gamma \approx \kappa + \pi\Omega^2\rho(\omega_s \pm \Omega)$ in the limit of large coupling strengths, $\Omega > \Gamma$ and $\gamma \to 0$. The value of $\Gamma$ is thus determined by the spin density $\rho(\omega)$, evaluated close to the maxima of the two polaritonic peaks, $\omega = \omega_s \pm \Omega$, split by the Rabi frequency $\Omega_R \approx 2\Omega$ due to strong coupling. Our approach is now to take this relation literally, which is tantamount to saying that the decoherence rate $\Gamma$ can be strongly suppressed by burning two spectral holes into the spin distribution $\rho(\omega)$ right at these two positions, $\omega_h = \omega_s \pm \Omega$, such that $\rho(\omega_h) = 0$. The width of the holes $\Delta_h$ should be very small, such as to remove only a negligible fraction of the spins by the hole burning. On the other hand, $\Delta_h$ is limited from below by the spin dissipation rate, $\Delta_h > \gamma$.

To demonstrate the efficiency of our approach explicitly, we first perform a stationary analysis $[\dot{A}(t) = \dot{B}_k(t) = 0]$ of the transmission $T(\omega)$ through the microwave resonator as a function of the probing frequency $\omega$. This quantity, which is directly accessible in the experiment [11,20], provides direct access to the occupation amplitude of the cavity $[T(\omega) \propto A(\omega)]$. Assuming $\gamma \to 0$, the transmission $T(\omega)$ acquires the following form:

$$T(\omega) = \frac{i\kappa}{\omega - \omega_c - \Omega^2\delta(\omega) + i[\kappa + \pi\Omega^2\rho(\omega)]}. \tag{3}$$

This expression is normalized such as to reach the maximum possible value $\max(|T(\omega)|) = 1$ for suitably chosen $\omega$, $\kappa$, and $\rho(\omega)$. The real function $\delta(\omega)$ is the nonlinear Lamb shift [30] defined as

$$\delta(\omega) = \mathcal{P}\int_0^\infty \frac{d\tilde{\omega}\,\rho(\tilde{\omega})}{\omega - \tilde{\omega}}, \tag{4}$$

where $\mathcal{P}$ stands for the Cauchy principal value. In the reference case taken from the experiment [11,20], $\rho(\omega)$ has no holes, see Fig. 2(a), and the transmission $|T(\omega)|^2$ displays the well-resolved double-peak structure typical for the strong-coupling regime; see Fig. 2(b). If we now

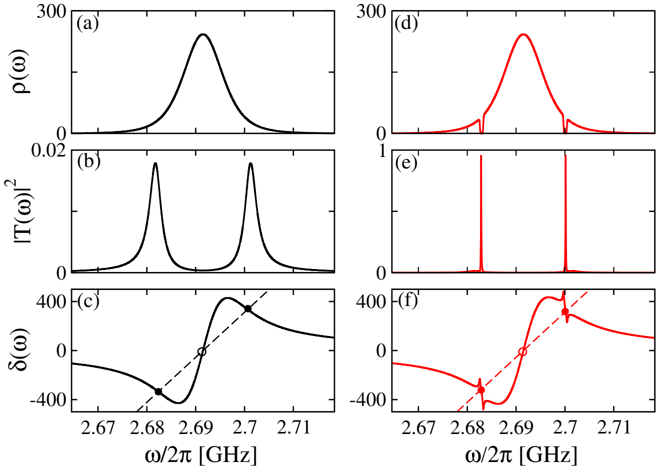

FIG. 2 (color online). Comparison of the cavity coupled to the inhomogeneously broadened spin ensemble without and with hole burning in the spin density profile (left and right panels, respectively). (a),(d): The $q$-Gaussian spin density distribution, $\rho(\omega)$, without and with hole burning at $\omega_h = \omega_s \pm \Omega$. Both holes are of equal width, $\Delta_h/2\pi = 0.7$ MHz, and have a Fermi-Dirac profile. (b),(e): Transmission $T(\omega)$ without and with hole burning in $\rho(\omega)$ (note different $y$ axes scale). (c),(f): The corresponding nonlinear Lamb shift $\delta(\omega)$. Filled circles label resonance values $\omega_r$ of the transmission $T(\omega)$ occurring at the intersections between the Lamb shift $\delta(\omega)$ and the dashed line $(\omega - \omega_c)/\Omega^2$. At empty circles such intersections are nonresonant (see text).

burn two narrow holes into the spin density at the relevant positions $\omega_h = \omega_s \pm \Omega$, see Fig. 2(d), and reevaluate $|T(\omega)|^2$, we observe a more than 50-fold increase in the corresponding transmission peak values; see Fig. 2(e). This dramatic change is all the more surprising considering that the relative number of spins removed from $\rho(\omega)$ through the hole burning is less than 3%.

To understand this behavior it is best to analyze the real and imaginary parts of the denominator of $T(\omega)$; see Eq. (3). For the observed transmission resonances at $\omega = \omega_r$ with a maximum value of $T(\omega_r) = 1$ to occur, two conditions are satisfied simultaneously: (i) $(\omega_r - \omega_c)/\Omega^2 = \delta(\omega_r)$ and (ii) $\rho(\omega_r) = 0$. Consider condition (i): In the reference case without holes, see Fig. 2(c), the nonlinear Lamb shift $\delta(\omega)$ displays rather smooth variations in the vicinity of the resonant frequencies $\omega_r$, determined by the intersection of $\delta(\omega)$ and a straight line $(\omega - \omega_c)/\Omega^2$. In contrast, for the case with hole burning, see Fig. 2(f), $\delta(\omega)$ exhibits rapid variations around the two resonance points within a very narrow spectral interval. As a consequence, the resultant transmission peaks become substantially sharper. Because of condition (ii) they also dramatically increase in height. Note that no resonance occurs at $\omega = \omega_c$ because $\rho(\omega)$ has a maximum at this point and condition (ii) is strongly violated; see Figs. 2(c) and 2(f). A close examination of the structure of $T(\omega)$ shows, furthermore, that the narrow transmission peaks resultant from the hole burning do not replace the broad polaritonic peaks present in the reference case, but rather get to sit on top of them; see Fig. 3(a). As will be seen below, the different resonance widths in $T(\omega)$ set two different time scales in the dynamics with, in particular, the sharp peaks in the transmission giving rise to an asymptotically slowly decaying dynamics with a strongly suppressed decoherence.

To explore whether the narrow holes we burnt into the spectral spin distribution at $\omega_h = \omega_s \pm \Omega$ have, indeed, the optimal location, we now also test all possible other hole positions symmetrically placed around the maximum of $\rho(\omega)$ at $\omega = \omega_s$. In Fig. 3(b) we present the numerical results for $T(\omega)$ as a function of the probe frequency $\omega$ and

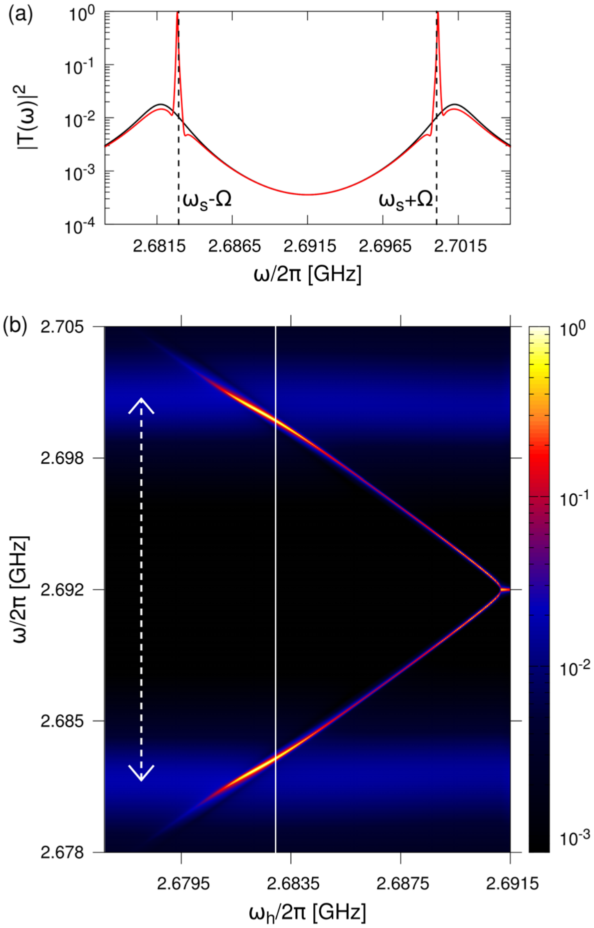

FIG. 3 (color online). Transmission through the cavity $T(\omega)$ versus probe frequency $\omega$ for different locations of the holes, $\omega_h$, in the spin density profile, $\rho(\omega)$ (the width of the holes is $\Delta_h/2\pi = 0.7$ MHz). (a) Red (gray) curve: $|T(\omega)|^2$ in lin-log scale versus $\omega$ for $\omega_h = \omega_s \pm \Omega$. Black curve: Transmission in the absence of hole burning. (b) Yellow (light gray) areas mark the most pronounced peaks in $|T(\omega)|^2$ in the presence of hole burning. Blue (gray) areas stand for the secondary polaritonic peaks which stem from the case without hole burning. Dashed arrows designate the distance $\Omega_R$ between polaritonic peaks. The white vertical cut corresponds to the transmission shown in (a).

of different hole locations $\omega_h = \omega_s \pm \bar{\omega}$ scanned between $\bar{\omega} = 0$ and $\bar{\omega} = 16$ MHz: While for large hole spacings ($\bar{\omega} \gtrsim 11.5$ MHz) the effect of holes is negligible, in the interval $0.8 \text{ MHz} \lesssim \bar{\omega} \lesssim 11.5$ MHz we always find two sharp peaks superimposed on the two polaritonic peaks approximately at the hole positions. Close to $\omega_h = \omega_s \pm \Omega$, these peaks are most pronounced and reach unity. In the limit when the holes are burnt very close together ($\bar{\omega} \lesssim 0.8$ MHz) the sharp peaks merge into a single one, located directly at the central frequency $\omega_s$ with a transmission maximum reaching again unity in the limit of $\omega_h \to \omega_s$ [see the yellow cusp in Fig. 3(b)]. Using the symmetry of $\rho(\omega)$ with respect to $\omega_s$, this behavior can also be proven analytically (not shown). To check the robustness of our method we also tested different functional forms for the hole profiles (Fermi-Dirac, $q$-Gaussian, and rectangular distributions) and found qualitatively similar results to the Fermi-Dirac form employed for all of the above figures.

To reach our ultimate goal of understanding the influence of the spectral hole burning on the resultant dynamics, we now study the time evolution of $A(t)$ explicitly for the resonant case $\omega = \omega_c = \omega_s$. The expression for the corresponding Volterra equation can be derived from Eqs. (2a) and (2b) (see [20] for details),

$$\dot{A}(t) = -\kappa A(t) - \Omega^2 \int d\omega \rho(\omega) \int_0^t d\tau e^{-i(\omega-\omega_c-i\gamma)(t-\tau)} A(\tau) - \eta(t). \qquad (5)$$

To prove that our predictions are valid not only in the semiclassical but also in the quantum case, we consider the case when all spins are initially in the ground state and the cavity mode $a$ contains initially a single photon, $|1,\downarrow\rangle$. It can be shown that the probability for a photon to reside in the cavity at time $t > 0$, $N(t) = \langle 1,\downarrow| a^\dagger(t) a(t) |1,\downarrow\rangle$, reduces to $N(t) = |\langle 0,\downarrow| a(t) |1,\downarrow\rangle|^2 = |A(t)|^2$, where $A(t)$ is the solution of Eq. (5) with the initial condition $A(t=0) = 1$ [external drive $\eta(t) = 0$]. For the case without hole burning, this solution is represented by the damped Rabi oscillations [see Fig. 4(a)] found already previously [11,20]. By burning narrow holes in $\rho(\omega)$ at $\omega_h = \omega_s \pm \Omega$ (immediately before $t = 0$), we observe very similar transient dynamics, which is followed, however, by a crossover to Rabi oscillations with a much slower asymptotic decay [see Fig. 4(b)]. Quite remarkably, the total decay rate $\Gamma$ in this asymptotic time limit can even be substantially smaller than the cavity decay rate $\kappa$ alone. This is all the more surprising since $\kappa$ was identified as the minimally reachable value for $\Gamma$ in recent studies on the cavity protection effect [11,19,20]. Apparently a new type of physics is at work here: Although the system is in the strong-coupling regime, the two spectral holes slow down the leakage of the energy stored in the spin ensemble back into the cavity. In particular, when being even slower than the inverse of the cavity decay rate $\kappa$, this sets a new global time scale for $\Gamma$, corresponding to the width of the sharp resonance peaks which we identified before in Fig. 3(a). From the mathematical point of view such a slow asymptotic behavior is associated with the contribution of two poles in the Laplace transform of Eq. (5) [20], which appear when the holes in $\rho(\omega)$ reach a critical depth. The pole contributions also stabilize the long-time behavior when the holes are shifted away from the polaritonic peaks [see Fig. 3(b)], but the optimal hole positions remain close to the polaritonic peaks. Note that despite the considerable photon loss [$N(t) \ll 1$] for long times, the phase coherence is very well preserved here, a clear signature of which is the stable form of the Rabi oscillations. In this way a high "visibility" can be achieved, as required for the efficient processing of quantum information [31].

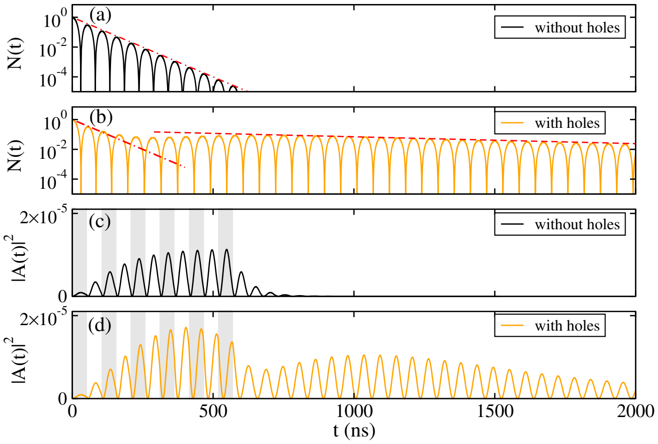

FIG. 4 (color online). (a),(b): Decay of the cavity occupation $N(t) = \langle 1,\downarrow| a^\dagger(t) a(t) |1,\downarrow\rangle$ from the initial state, for which a single photon with frequency $\omega_c$ resides in the cavity and all spins are unexcited. The asymptotic decay $Ce^{-\Gamma t}$ with and without hole burning (see red lines) is determined by the constants $\Gamma/2\pi = 3$ MHz in (a) and a drastically reduced $\Gamma = 0.42\kappa = 2\pi 0.17$ MHz in (b). (c),(d): Dynamics of $|A(t)|^2$ under the action of 11 successive rectangular microwave pulses of duration corresponding to the Rabi period, $\tau = 2\pi/\Omega_R = 52$ ns, phase switched by $\pi$ (every second pulse is shown as a vertical gray bar). Also here the asymptotic decay is much slower due to the presence of the holes. In all panels the holes in $\rho(\omega)$ have a width $\Delta_h/2\pi = 1.4$ MHz and are burnt at $t = 0$ at $\omega_h = \omega_s \pm \Omega$.

To demonstrate the efficiency of the hole burning effect also for quantum control schemes, we pump the cavity by a sequence of $\pi$ phase-switched rectangular pulses, each with a duration corresponding to the Rabi period, $\tau = 2\pi/\Omega_R$ and a carrier frequency $\omega = \omega_c = \omega_s$. As shown in [11], this procedure is very well suited to feed energy into the strongly coupled cavity-spin system, leading to giant oscillations of both spin and cavity amplitude [see left parts of Figs. 4(c) and 4(d)]. Not only do we observe that these driven oscillations are more pronounced when burning holes at $\omega_h = \omega_s \pm \Omega$, but we find, in particular, that the Rabi relaxation oscillations setting in after switching off the driving field are dramatically more long lived than in the case without holes [compare right parts of Figs. 4(c) and 4(d)]. These results confirm the robustness as well as the general applicability of our approach for various coherent-control schemes in the strong-coupling regime of cavity QED.

In summary, we present an efficient method to suppress the decoherence in a single-mode cavity strongly coupled to an inhomogeneously broadened spin ensemble. By burning narrow spectral holes in the spin density at judiciously chosen positions, the total decay rate is dramatically decreased to values that may even lie below the dissipation rate of the bare cavity. Experimentally, our approach can be implemented by exposing the cavity to high-intensity microwave signals with spectral components near the desired hole positions. Because of the strong driving the spins at these frequencies will equally populate their ground and excited state and will thus be effectively removed from the coupling process with the cavity.

We thank S. Putz, R. Amsüss and J. Majer for suggesting us to work on this topic and for pointing out other spectral hole burning technique as studied in [21]. Support by the Austrian Science Fund (FWF) through Project No. F49-P10 (SFB NextLite) is gratefully acknowledged.

---

[*] dmitry.krimer@gmail.com

[1] Z.-L. Xiang, S. Ashhab, J. Q. You, and F. Nori, Rev. Mod. Phys. **85**, 623 (2013).
[2] R. Amsüss, Ch. Koller, T. Nöbauer, S. Putz, S. Rotter, K. Sandner, S. Schneider, M. Schramböck, G. Steinhauser, H. Ritsch, J. Schmiedmayer, and J. Majer, Phys. Rev. Lett. **107**, 060502 (2011).
[3] K. Sandner, H. Ritsch, R. Amsüss, Ch. Koller, T. Nöbauer, S. Putz, J. Schmiedmayer, and J. Majer, Phys. Rev. A **85**, 053806 (2012).
[4] Y. Kubo, F. R. Ong, P. Bertet, D. Vion, V. Jacques, D. Zheng, A. Dréau, J.-F. Roch, A. Auffeves, F. Jelezko, J. Wrachtrup, M. F. Barthe, P. Bergonzo, and D. Esteve, Phys. Rev. Lett. **105**, 140502 (2010).
[5] Y. Kubo, C. Grezes, A. Dewes, T. Umeda, J. Isoya, H. Sumiya, N. Morishita, H. Abe, S. Onoda, T. Ohshima, V. Jacques, A. Dréau, J.-F. Roch, I. Diniz, A. Auffeves, D. Vion, D. Esteve, and P. Bertet, Phys. Rev. Lett. **107**, 220501 (2011).
[6] Y. Kubo, I. Diniz, A. Dewes, V. Jacques, A. Dréau, J.-F. Roch, A. Auffeves, D. Vion, D. Esteve, and P. Bertet, Phys. Rev. A **85**, 012333 (2012).
[7] D. I. Schuster, A. P. Sears, E. Ginossar, L. DiCarlo, L. Frunzio, J. J. L. Morton, H. Wu, G. A. D. Briggs, B. B. Buckley, D. D. Awschalom, and R. J. Schoelkopf, Phys. Rev. Lett. **105**, 140501 (2010).
[8] P. Bushev, A. K. Feofanov, H. Rotzinger, I. Protopopov, J. H. Cole, C. M. Wilson, G. Fischer, A. Lukashenko, and A. V. Ustinov, Phys. Rev. B **84**, 060501(R) (2011).
[9] X. Zhu, S.Saito, A. Kemp, K. Kakuyanagi, S. Karimoto, H. Nakano, W. J. Munro, Y. Tokura, M. S. Everitt, K. Nemoto, M. Kasu, N. Mizuochi, and K. Semba, Nature (London) **478**, 221 (2011).
[10] S. Probst, H. Rotzinger, S. Wünsch, P. Jung, M. Jerger, M. Siegel, A. V. Ustinov, and P. A. Bushev, Phys. Rev. Lett. **110**, 157001 (2013).
[11] S. Putz, D. O. Krimer, R. Amsüss, A. Valookaran, T. Nöbauer, J. Schmiedmayer, S. Rotter, and J. Majer, Nat. Phys. **10**, 720 (2014).
[12] P. Rabl, D. DeMille, J. M. Doyle, M. D. Lukin, R. J. Schoelkopf, and P. Zoller, Phys. Rev. Lett. **97**, 033003 (2006).
[13] K. Tordrup, A. Negretti, and K. Mølmer, Phys. Rev. Lett. **101**, 040501 (2008).
[14] J. Verdú, H. Zoubi, Ch. Koller, J. Majer, H. Ritsch, and J. Schmiedmayer, Phys. Rev. Lett. **103**, 043603 (2009).
[15] D. Petrosyan, G. Bensky, G. Kurizki, I. Mazets, J. Majer, and J. Schmiedmayer, Phys. Rev. A **79**, 040304(R) (2009).
[16] A. Imamoglu, D. D. Awschalom, G. Burkard, D. P. DiVincenzo, D. Loss, M. Sherwin, and A. Small, Phys. Rev. Lett. **83**, 4204 (1999).
[17] J. H. Wesenberg, A. Ardavan, G. A. D. Briggs, J. J. L. Morton, R. J. Schoelkopf, D. I. Schuster, and K. Mølmer, Phys. Rev. Lett. **103**, 070502 (2009).
[18] Z. Kurucz, J. H. Wesenberg, and K. Mølmer, Phys. Rev. A **83**, 053852 (2011).
[19] I. Diniz, S. Portolan, R. Ferreira, J. M. Gerard, P. Bertet, and A. Auffeves, Phys. Rev. A **84**, 063810 (2011).
[20] D. O. Krimer, S. Putz, J. Majer, and S. Rotter, Phys. Rev. A **90**, 043852 (2014).
[21] G. Bensky, D. Petrosyan, J. Majer, J. Schmiedmayer, and G. Kurizki, Phys. Rev. A **86**, 012310 (2012).
[22] J. Cai, F. Jelezko, N. Katz, A. Retzker, and M. B Plenio, New J. Phys. **14**, 093030 (2012).
[23] R. Vijay, C. Macklin, D. H. Slichter, S. J. Weber, K. W. Murch, R. Naik, A. N. Korotkov, and I. Siddiqi, Nature (London) **490**, 77 (2012).
[24] A. Carmele, J. Kabuss, F. Schulze, S. Reitzenstein, and A. Knorr, Phys. Rev. Lett. **110**, 013601 (2013).
[25] J. Kabuss, D. O. Krimer, S. Rotter, K. Stannigel, A. Knorr, and A. Carmele, arXiv:1503.05722.
[26] D. Meiser, J. Ye, D. R. Carlson, and M. J. Holland, Phys. Rev. Lett. **102**, 163601 (2009).
[27] J. G. Bohnet, Z. Chen, J. M. Weiner, D. Meiser, M. J. Holland, and J. K. Thompson, Nature (London) **484**, 78 (2012).
[28] M. Tavis and F. W. Cummings, Phys. Rev. **170**, 379 (1968).
[29] H. Primakoff and T. Holstein, Phys. Rev. **55**, 1218 (1939).
[30] D. O. Krimer, M. Liertzer, S. Rotter, and H. E. Türeci, Phys. Rev. A **89**, 033820 (2014).
[31] H. de Riedmatten, M. Afzelius, M. U. Staudt, C. Simon, and N. Gisin, Nature (London) **456**, 773 (2008).

LETTERS
PUBLISHED ONLINE: 21 NOVEMBER 2016 | DOI: 10.1038/NPHOTON.2016.225
nature photonics

# Spectral hole burning and its application in microwave photonics

**Stefan Putz[1,2,3★†], Andreas Angerer[1,2†], Dmitry O. Krimer[4], Ralph Glattauer[1], William J. Munro[5,6], Stefan Rotter[4], Jörg Schmiedmayer[1,2] and Johannes Majer[1,2★]**

**Spectral hole burning, used in inhomogeneously broadened emitters, is a well-established optical[1] technique, with applications from spectroscopy to slow light[2] and frequency combs[3]. In microwave photonics[4], electron spin ensembles[5,6] are candidates for use as quantum memories[7] with potentially long storage times[8]. Here, we demonstrate long-lived collective dark states[9] by spectral hole burning in the microwave regime[10]. The coherence time in our hybrid quantum system (nitrogen–vacancy centres strongly coupled to a superconducting microwave cavity) becomes longer than both the ensemble's free-induction decay and the bare cavity dissipation rate. The hybrid quantum system thus performs better than its individual subcomponents. This opens the way for long-lived quantum multimode memories, solid-state microwave frequency combs, spin squeezed states[11], optical-to-microwave quantum transducers[12] and novel metamaterials[13]. Beyond these, new cavity quantum electrodynamics experiments will be possible where spin–spin interactions and many-body phenomena[14] are directly accessible.**

Quantum information science and metrology rely on the coherent manipulation of two-level systems, which allow the storage of single excitations in high-capacity multimode memories[15]. The manipulation of information within those memories has proven to be difficult, and so the hybridization of distinct quantum systems to form quantum metamaterials offers a realistic way forward. Such 'hybrid' quantum systems have become a key strategy in microwave circuit cavity quantum electrodynamics (cQED)[4,16]. As an example we discuss the hybridization of superconducting devices with electron spin ensembles[5,6,17] and show their potential to bypass individual weaknesses while harnessing their strengths. Electrical circuits offer easy manipulation and processing[18,19], yet have limited coherence properties, while single electron spins in semiconductor crystals can have coherence times of up to almost one hour[20] but are hard to manipulate. In early experiments, coherent energy exchange on the single-photon level and basic memory operations[7] were demonstrated in this context[21].

An outstanding challenge in solid-state-based hybrid systems is the suppression of spin dephasing induced by the host material[5,6,17]. However, the realization of true multimode memories is only possible in the presence of inhomogeneous spectral broadening and so their short memory times have to be actively recovered by echo refocusing techniques[21] or improved by the cavity protection effect[22]. In this Letter, we present an alternative approach based on collective dark states[9,23] that circumvents the necessity for recovery protocols and substantially improves the coherence times beyond the limit given by the cavity and spin ensemble.

Our hybrid system consists of a superconducting resonator with a diamond crystal containing an ensemble of negatively charged nitrogen–vacancy (NV) centre electron spins magnetically coupled to it (Fig. 1a,b). The device was placed in a dilution refrigerator operating at temperatures <25 mK. The resonator was characterized at zero external magnetic field by transmission spectroscopy and was determined to have a fundamental resonance at $\omega_c/2\pi = 2.691$ GHz with a cavity linewidth of $\kappa/2\pi = 440 \pm 10$ kHz and quality factor of $Q = 3{,}130$. The diamond crystal has a NV concentration of $\sim 4 \times 10^{17}$ cm$^{-3}$, meaning that the macroscopic spin ensemble in the cavity mode volume consists of $N \approx 1 \times 10^{12}$ NV spins thermally polarized (≥99%) at our refrigerator's base temperature. These electron spins were Zeeman-shifted into resonance with the cavity by applying an external d.c. magnetic field (Fig. 1c).

We observed a mode splitting and Rabi oscillations with frequency $\Omega_R/2\pi = 21.3 \pm 0.1$ MHz and linewidth/decay rate of $\Gamma/2\pi = 1.45 \pm 0.05$ MHz on probing the system with low intensities of $<1 \times 10^{-6}$ photons per spin in the cavity (Supplementary Fig. 1). Although the single spin–cavity coupling strength, $g_j$, is rather small ($\lesssim 10$ Hz) (ref. 6), the large number $N$ of weakly dipole–dipole interacting spins allows us to deeply enter the strong coupling regime ($\Omega_R \gg \Gamma \gg \kappa$) with cooperativity $C \approx 26$. Such an ensemble of individual two-level systems coupled to a single-mode cavity is described by the Tavis–Cummings model, which in the rotating wave approximation can be written as

$$\mathcal{H} = \hbar\omega_c a^\dagger a + \frac{\hbar}{2}\sum_{j=1}^{N}\omega_j\sigma_j^z + \hbar\sum_{j=1}^{N} g_j\left[\sigma_j^- a^\dagger + \sigma_j^+ a\right] \qquad (1)$$

with the cavity modes' bosonic creation (annihilation) operators $a^\dagger$ ($a$) operating at frequency $\omega_c$. The Pauli spin operators $\sigma_j^{\pm,z}$ are associated with the $j$th spin at frequency $\omega_j$. In such an ensemble of $N$ spins that share a single excitation, we find one super-radiant state[24] $|B\rangle = J^+|G\rangle$ and $N-1$ subradiant states $|S\rangle$, where $J^\pm = (1/\sqrt{\Sigma_i^N g_i^2})\Sigma_j^N g_j\sigma_j^\pm$ is the collective spin operator and $|G\rangle$ the collective spin ground state.

The hybridized polariton modes $|\pm\rangle = (|1\rangle_c|G\rangle_s \pm |0\rangle_c|B\rangle_s)/\sqrt{2}$ are entangled states between the cavity and the super-radiant spin state. The vacuum Rabi splitting[25] is due to a collectively enhanced interaction $\Omega_R/2 \approx \Omega = \sqrt{\Sigma_i^N g_i^2}$ scaling approximately as $\sqrt{N}$. Subradiant states remain uncoupled and degenerate in the absence of spin broadening. In the presence of inhomogeneous spin broadening, corresponding to a variation of $\omega_j$ centred around a central spin frequency $\omega_s$ (Fig. 2a(i),b(i) and c(i)), the polariton modes and subradiant states are not entirely decoupled. The inhomogeneous spin broadening of $\gamma_{\text{inh}}/2\pi = 4.55$ MHz is the main source

---

[1]Vienna Center for Quantum Science and Technology (VCQ), Atominstitut, TU Wien, Stadionallee 2, 1020 Vienna, Austria. [2]Zentrum für Mikro- und Nanostrukturen, TU Wien, Floragasse 7, 1040 Vienna, Austria. [3]Department of Physics, Princeton University, Princeton, New Jersey 08544, USA. [4]Institute for Theoretical Physics, TU Wien, Wiedner Hauptstraße 8-10/136, 1040 Vienna, Austria. [5]NTT Basic Research Laboratories, 3-1 Morinosato-Wakamiya, Atsugi, Kanagawa 243-0198, Japan. [6]National Institute of Informatics, 2-1-2 Hitotsubashi, Chiyoda-ku, Tokyo 101-8430, Japan. †These authors contributed equally to this work. *e-mail: stef.putz@gmail.com; jmajer@ati.ac.at

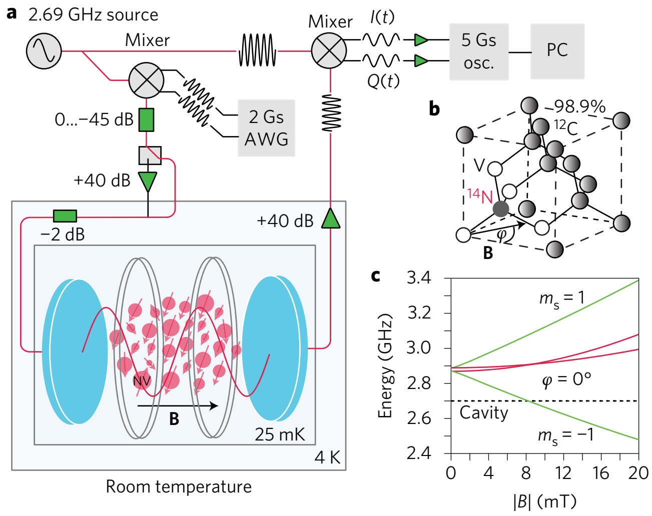

**Figure 1 | Experimental set-up. a**, A superconducting cavity loaded with an enhanced synthetic diamond crystal and surrounded by a three-dimensional d.c. Helmholtz coil cage is placed in a dilution refrigerator operating at temperatures below 25 mK. Further details about the measurement scheme can be found in the Methods. **b**, Structure of the NV defect centre ($S = 1$) in diamond consisting of a substitutional nitrogen atom and an adjacent lattice vacancy. **c**, Zeeman tuning of the NV central spin transition frequencies. Red and green indicate the two degenerate NV subensembles.

of decoherence here, accelerating the evolution of an excitation stored in the super-radiant mode into the bath of subradiant states.

The polariton modes $|\pm\rangle$ can be decoupled from the bath of subradiant states by the 'cavity protection effect'[26,27]. Only in the limit of $\Omega \to \infty$ is the decay rate ultimately bound by the mean of both dissipation rates $\Gamma_{\min} = (\kappa + \gamma)/2$. As suggested in ref. 10, it is possible to break this limit of $\Gamma_{\min}$ by engineering polariton modes that live mostly in the spins, for which the decay rate is much smaller than that of our cavity interface, $\gamma \ll \kappa$. In traditional hole burning, such a long-lived spin population is pumped back into the created hole. Here, however, the strong cavity spin interaction automatically hybridizes a narrow state in the centre of the created spectral hole. We identify the resulting long-lived spin states as 'collective dark states'[9,27], which allows us to improve the total coherence times by over more than one order of magnitude.

If a hole is burnt at the positions of the polariton modes $\omega_s \pm \Omega_R/2$ (Fig. 2a(ii),b(ii) and c(ii)) two new spin distributions are effectively created left ($|L\rangle$) and right ($|R\rangle$) detuned of the spectral hole. These spin packets share a common ground state $|G\rangle$, meaning that the cavity sees a V level system[28] that naturally features a dark state $|D\rangle$. Both transitions $|G\rangle \to |L\rangle$ and $|G\rangle \to |R\rangle$ are coupled to the cavity field, and so a small cavity $|1\rangle_c$ component is added to the emerging dark state. If the spectral hole is created in the centre of the polariton mode this dark state

$$|D\rangle \approx \frac{1}{\sqrt{\Delta^2 + 2g_\mu^2}}\left[g_\mu(|R\rangle - |L\rangle)|0\rangle_c + \Delta|G\rangle|1\rangle_c\right]$$

lies right in the middle of the spectral hole and is isolated from the bath of subradiant states, with the spectral hole having width $\Delta$ and an effective cavity spin coupling strength $g_\mu$. This anti-symmetric long-lived spin state $|D\rangle$ has a linewidth $\Gamma_D \geq \gamma$, which is governed by the width of the spectral hole $\Delta$ and can be substantially narrower than the cavity linewidth $\kappa$, as we show in the following.

We created dark states, as shown in Fig. 2a(ii), b(ii) and c(ii), by burning two spectral holes at $\omega_s \pm \Omega_R/2$ with a bandwidth of $\Delta/2\pi = 235$ kHz (see Methods). This bleaching thermalizes spins into an equal mixture of their ground and excited states and so cancels out their collective spin–cavity interaction. Saturated spins will decay slowly towards their ground state on a timescale of ≥10 ms, given by their spin lifetime[6] of $T_1 = 45$ s, which is shortened due to the Purcell effect[29] and spin diffusion resulting from spin–spin interactions. When the hole burning pulse intensity is above a certain power threshold, long-lived dark states are created (Fig. 3a, inset). This shows through long-lived coherent Rabi oscillations after we switch off a strong hole burning pulse (shown in Fig. 3a,b). In Fig. 3c we demonstrate that the hole burning procedure not only suppresses the decoherence but also allows us to control the Rabi flopping frequency when varying the position of the spectral holes.

The achieved decay rates of the engineered collective dark states $\Gamma_D/2\pi = 125 \pm 10$ kHz (Fig. 3a) are significantly below the fundamental limit ($\Gamma_{\min} = (\kappa + \gamma)/2 > 2\pi \times 220$ kHz) reachable by the 'cavity protection effect'[22]. As a result of the created spectral holes, two narrow peaks emerge directly on top of the polariton modes. To observe this directly, we compared the spectrally transmitted steady-state intensity $|A(\omega_p)|^2$, as depicted in Fig. 3d, before and

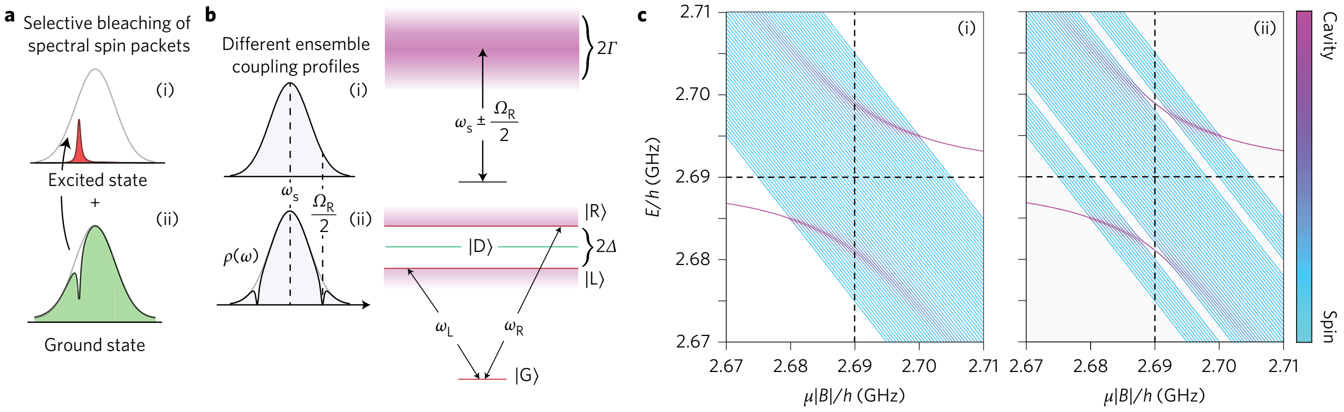

**Figure 2 | Visualization of engineered collective dark states. a**, Spectral hole burning in narrow frequency windows bleaches spin components by bringing them into a mixture between their ground and excited states. The spin density $\rho(\omega)$ (i) is modified (ii). **b**, Two polariton modes of width $2\Gamma$ are created in the strong coupling regime ($\Omega_R > 2\Gamma$) (i). If a spin population is removed in a window $\Delta < \Gamma$, the cavity sees a V level system with states $|G\rangle$, $|R\rangle$ and $|L\rangle$ featuring a dark state $|D\rangle$ (ii). **c**, The eigenenergy spectra of the cavity strongly coupled to a broadened spin ensemble with cavity and spin contributions indicated by the colour gradient (colour bar on the right). (i) Two polariton modes in a bath of subradiant states are visible. (ii) Spectral hole burning at $\omega_s \pm \Omega_R/2$ creates long-lived dark states $|D\rangle$, which lie within the created holes and decouple from the remaining bath of subradiant states.

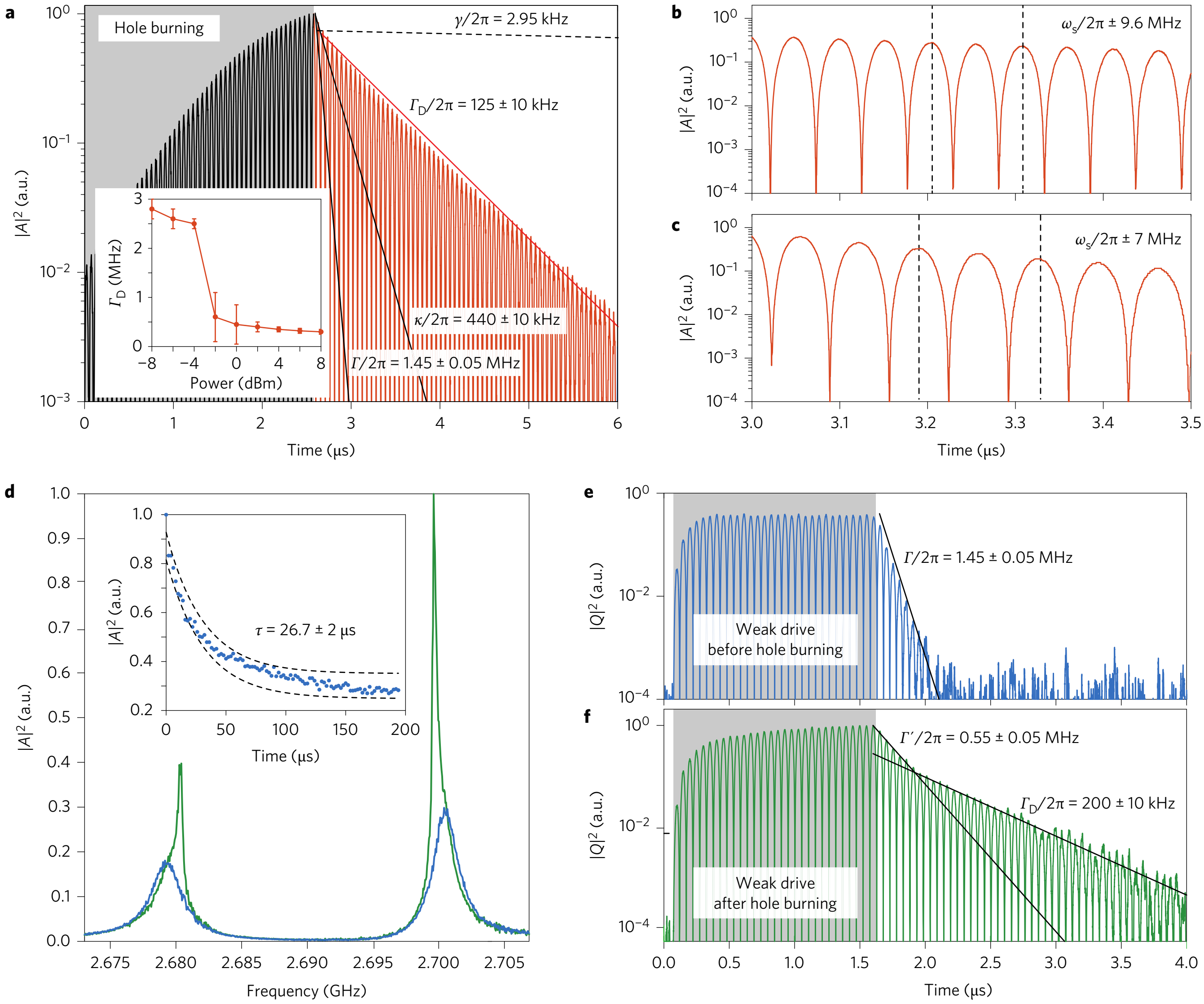

**Figure 3 | Spectral hole burning, dark state spectroscopy and dark state dynamics.** **a**, Two spectral holes are burned at $\omega_s/2\pi \pm 9.6$ MHz with a bandwidth $\Delta/2\pi = 235$ kHz. When the hole burning pulse intensity reaches a critical threshold (inset), the decay rate is slowed after the drive is switched off (red). **b**, Close-up of the damped Rabi oscillations shown in **a**. **c**, The Rabi frequency is controlled by changing the position of the spectral holes. **d**, The spectral transmitted steady-state intensity through the cavity is scanned with weak probe powers: before (blue) and >5 μs after (green) a hole burning pulse has decayed. Two narrow peaks emerge directly on top of the polariton modes, identified as the created dark states. The unequal peak amplitudes are caused by an additional Fano resonance, although spins and cavity are in resonance ($\omega_c = \omega_s$). The lifetime of the holes is measured by repeatedly probing the system with low intensities and monitoring the decaying dark-state amplitude (inset). **e**, Linear dynamical response for a sinusoidally modulated weak pulse (grey area, see Methods). **f**, The substantially improved coherence time is shown by probing the system as in **e**, but 5 μs after spectral holes were burnt and the cavity was emptied. Errors in **a**–**f** correspond to the minimum and maximum values of the estimated decay rates and in the inset of **d** to the $1\sigma$ deviation.

after spectral holes were burnt at positions equal to $\omega_s \pm \Omega_R/2$. The created holes and engineered dark states in Fig. 3d decay with a time constant $\tau = 26.7 \pm 2$ μs due to spin diffusion, which limits the spectral hole lifetime. In our experiment this is more than four times longer than the best achievable spin echo time $T_2 = 4.8 \pm 1.6$ μs. We conclude that $\tau \sim 1/2\gamma$, as both rates are limited by spin diffusion in our experiment (see Methods).

It is possible to use this procedure to store and retrieve a weak intensity excitation from the spin ensemble. We drove our system with a weak ($<1 \times 10^{-5}$ photons per spin) sinusoidally modulated pulse. In the absence of spectral holes we observed the unchanged system decay rate $\Gamma/2\pi = 1.45 \pm 0.05$ MHz after switching off the driving tone (Fig. 3e). We then applied a hole burning pulse and, 5 μs after the signal has decayed, the system was probed again. After the weak probe pulse was switched off, different decay rates were clearly distinguishable in the Rabi oscillations (Fig. 3f). We first observed a reduced decay rate, $\Gamma'/2\pi = 550 \pm 50$ kHz, due to the created spectral holes and reduced damping of the bright polariton modes. This first decay was followed by a crossover to a second much slower decay, $\Gamma_D/2\pi = 200 \pm 10$ kHz, featuring long-lived Rabi oscillations as the hallmark of the created dark states.

To show the potential of this hole burning we created multiple pairs of dark states. Four spectral holes were created in the polariton modes with $\Delta/2\pi = 150$ kHz bandwidth at positions $\nu_1^{\pm} = \omega_s/2\pi \pm 9$ MHz and $\nu_2^{\pm} = \omega_s/2\pi \pm 10.8$ MHz. In Fig. 4 we probe the dynamical response after the hole burning with a weak sinusoidally modulated microwave pulse and observe a clear beating in the Rabi oscillations with a mean dark state decay rate of $\Gamma_D/2\pi = 280 \pm 20$ kHz. The beat frequency of ~1.8 MHz corresponds to the frequency difference of both spectral holes in each polariton mode. The two revivals in the Rabi oscillations

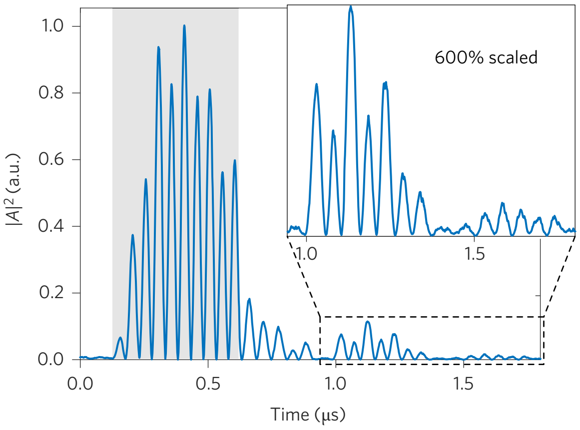

**Figure 4 | Engineering of multiple dark states.** We create four spectral holes and dark states at frequencies $\nu_1^\pm = \omega_s/2\pi \pm 9$ MHz and $\nu_2^\pm = \omega_s/2\pi \pm 10.8$ MHz close to the polariton modes. The response is probed with weak pulse intensities of $\sim 1 \times 10^{-5}$ photons per spin in the cavity. After the sinusoidally modulated drive with frequency $\Omega_R/2$ and carrier frequency $\omega_p = \omega_c = \omega_s$ (grey area) is switched off, we observe a clear beating with $\Delta_{\nu_{21}} \approx 1.8$ MHz characterized by revivals of the damped Rabi oscillations decaying with a rate $\Gamma_D/2\pi = 280 \pm 20$ kHz. Error corresponds to the minimum and maximum values of the estimated decay rate.

are a clear signature of the coherent dark states beating against each other. This is a first step towards the realization of a solid-state microwave frequency comb, in which one could ideally address up to approximately $\Gamma/\Delta$ long-lived dark states in one polariton mode.

To conclude, we have demonstrated how spectral hole burning can be used to selectively bleach the ensemble's absorption spectrum in the microwave domain. The created holes allow the engineering of coherent collective long-lived dark states that decay significantly more slowly than the constituent subsystems. This hybridizes the system in such a way that the overall coherence time is no longer bound by the cavity and spin ensemble linewidth. Our work can be seen as a first proof-of-principle experiment for the great potential of hybrid systems. The reported technique opens new possibilities in quantum devices and a new class of cavity QED experiments beyond the standard Dicke[24] and Tavis–Cummings model.

## Methods

Methods and any associated references are available in the online version of the paper.

Received 28 May 2016; accepted 10 October 2016;
published online 21 November 2016

## References

1. Moerner, W. E. *Persistent Spectral Hole-Burning: Science and Applications* (Springer Science & Business Media, 2012).
2. Turukhin, A. V. *et al.* Observation of ultraslow and stored light pulses in a solid. *Phys. Rev. Lett.* **88,** 023602 (2001).
3. de Riedmatten, H., Afzelius, M., Staudt, M. U., Simon, C. & Gisin, N. A solid-state light–matter interface at the single-photon level. *Nature* **456,** 773–777 (2008).
4. Xiang, Z.-L., Ashhab, S., You, J. Q. & Nori, F. Hybrid quantum circuits: superconducting circuits interacting with other quantum systems. *Rev. Mod. Phys.* **85,** 623–653 (2013).
5. Kubo, Y. *et al.* Strong coupling of a spin ensemble to a superconducting resonator. *Phys. Rev. Lett.* **105,** 140502 (2010).
6. Amsüss, R. *et al.* Cavity QED with magnetically coupled collective spin states. *Phys. Rev. Lett.* **107,** 060502 (2011).
7. Nunn, J. *et al.* Multimode memories in atomic ensembles. *Phys. Rev. Lett.* **101,** 260502 (2008).
8. Plankensteiner, D., Ostermann, L., Ritsch, H. & Genes, C. Selective protected state preparation of coupled dissipative quantum emitters. *Sci. Rep.* **5,** 16231 (2015).
9. Zhu, X. *et al.* Observation of dark states in a superconductor diamond quantum hybrid system. *Nat. Commun.* **5,** 3424 (2014).
10. Krimer, D. O., Hartl, B. & Rotter, S. Hybrid quantum systems with collectively coupled spin states: suppression of decoherence through spectral hole burning. *Phys. Rev. Lett.* **115,** 033601 (2015).
11. Wineland, D. J., Bollinger, J. J., Itano, W. M. & Heinzen, D. J. Squeezed atomic states and projection noise in spectroscopy. *Phys. Rev. A* **50,** 67–88 (1994).
12. Stannigel, K., Rabl, P., Sørensen, A. S., Zoller, P. & Lukin, M. D. Optomechanical transducers for long-distance quantum communication. *Phys. Rev. Lett.* **105,** 220501 (2010).
13. Rakhmanov, A. L., Zagoskin, A. M., Savel'ev, S. & Nori, F. Quantum metamaterials: electromagnetic waves in a Josephson qubit line. *Phys. Rev. B* **77,** 144507 (2008).
14. Ma, W.-L. *et al.* Uncovering many-body correlations in nanoscale nuclear spin baths by central spin decoherence. *Nat. Commun.* **5,** 4822 (2014).
15. Lvovsky, A. I., Sanders, B. C. & Tittel, W. Optical quantum memory. *Nat. Photon.* **3,** 706–714 (2009).
16. İmamoğlu, A. Cavity QED based on collective magnetic dipole coupling: spin ensembles as hybrid two-level systems. *Phys. Rev. Lett.* **102,** 083602 (2009).
17. Schuster, D. I. *et al.* High-cooperativity coupling of electron–spin ensembles to superconducting cavities. *Phys. Rev. Lett.* **105,** 140501 (2010).
18. Nakamura, Y., Pashkin, Y. A. & Tsai, J. S. Coherent control of macroscopic quantum states in a single-Cooper-pair box. *Nature* **398,** 786–788 (1999).
19. Wallraff, A. *et al.* Strong coupling of a single photon to a superconducting qubit using circuit quantum electrodynamics. *Nature* **431,** 162–167 (2004).
20. Saeedi, K. *et al.* Room-temperature quantum bit storage exceeding 39 minutes using ionized donors in silicon-28. *Science* **342,** 830–833 (2013).
21. Wu, H. *et al.* Storage of multiple coherent microwave excitations in an electron spin ensemble. *Phys. Rev. Lett.* **105,** 140503 (2010).
22. Putz, S. *et al.* Protecting a spin ensemble against decoherence in the strong-coupling regime of cavity QED. *Nat. Phys.* **10,** 720–724 (2014).
23. Zhang, X. *et al.* Magnon dark modes and gradient memory. *Nat. Commun.* **6,** 8914 (2015).
24. Dicke, R. H. Coherence in spontaneous radiation processes. *Phys. Rev.* **93,** 99–110 (1954).
25. Thompson, R. J., Rempe, G. & Kimble, H. J. Observation of normal-mode splitting for an atom in an optical cavity. *Phys. Rev. Lett.* **68,** 1132–1135 (1992).
26. Kurucz, Z., Wesenberg, J. H. & Mølmer, K. Spectroscopic properties of inhomogeneously broadened spin ensembles in a cavity. *Phys. Rev. A* **83,** 053852 (2011).
27. Diniz, I. *et al.* Strongly coupling a cavity to inhomogeneous ensembles of emitters: potential for long-lived solid-state quantum memories. *Phys. Rev. A* **84,** 063810 (2011).
28. Fleischhauer, M., İmamoğlu, A. & Marangos, J. P. Electromagnetically induced transparency: optics in coherent media. *Rev. Mod. Phys.* **77,** 633–673 (2005).
29. Purcell, E. M. Spontaneous emission probabilities at radio frequencies. *Phys. Rev.* **69,** 681 (1946).

## Acknowledgements

The authors thank A. Ardavan, B. Hartl, G. Kirchmair, K. Nemoto, H. Ritsch and M. Trupke for helpful discussions. The experimental effort led by J.M. was supported by the Top-/Anschubfinanzierung grant of TU Wien. S.P. and A.A. acknowledge support from the Austrian Science Fund (FWF) in the framework of the Doctoral School 'Building Solids for Function' Project W1243. D.O.K. and S.R. acknowledge funding by the Austrian Science Fund (FWF) through the Spezialforschungsbereich (SFB) NextLite Project No. F49-P10.

## Author contributions

S.P., A.A., J.S. and J.M. designed and set up the experiment. A.A. and R.G. carried out the measurements under the supervision of S.P. and J.M. D.O.K. and S.R. devised the theoretical framework and, together with W.J.M., provided the theoretical support for modelling the experiment. S.P. wrote the manuscript and all authors suggested improvements.

## Additional information

Supplementary information is available in the online version of the paper. Reprints and permissions information is available online at www.nature.com/reprints. Correspondence and requests for materials should be addressed to S.P. and J.M.

## Competing financial interests

The authors declare no competing financial interests.

## Methods

The microwave cavity was loaded by placing the diamond sample on top of a $\lambda/2$ transmission line resonator. The superconducting microwave cavity was fabricated by optical lithography and reactive-ion etching of a 200-nm-thick niobium film sputtered on a 330-μm-thick sapphire substrate. The loaded chip was hosted and bonded to a printed circuit board enclosed in a copper sarcophagus and connected to microwave transmission lines.

The spin ensemble was realized by enhancing a type Ib high-pressure high-temperature diamond (HPHT) crystal containing an initial concentration of 200 ppm nitrogen with a natural abundance of $^{13}$C nuclear isotopes. We achieved a total density of ~6 ppm negatively charged NV centres by 50 h of neutron irradiation with a fluence of $5 \times 10^{17}$ cm$^{-2}$ and annealing the crystal for 3 h at 900 °C. In our system, excess nitrogen P1 centres ($S = 1/2$), uncharged NV$^0$ centres, plus additional lattice stress served as the main sources of decoherence and caused spectral line broadening, which by far exceeded dephasing due to the naturally abundant 1.1% $^{13}$C spin bath. The characteristics of the diamond crystal and NV ensemble were initially determined at room temperature using an optical laser scanning microscope[30]. In the present experiment, the broadened spin ensemble was characterized by a $q$-Gaussian spectral line shape $\rho(\omega)$ with a linewidth of $\gamma_{\mathrm{inh}}/2\pi = 4.55$ MHz (ref. 22).

The negatively charged NV centre is a paramagnetic impurity with electron spin $S = 1$ that consists of a substitutional nitrogen atom and an adjacent vacancy in the diamond lattice. The electron spin triplet can be described by the Hamiltonian, $\mathcal{H}/h = DS_z^2 + \mu BS$, with $\mu = 28$ MHz mT$^{-1}$ and a large zero-field splitting of $D = 2.877$ GHz corresponding to $hD/k_{\mathrm{B}} \approx 138$ mK. This allowed us to thermally polarize the NV spin (at finite temperatures of 25 mK) up to 99%. Due to the diamond lattice structure, four different orientations of the adjacent vacancy were possible, resulting in four NV sub-ensembles. Magnetic field strengths on the order of $|\mathrm{B}| = 8$ mT, applied in the (100) crystallographic plane and parallel to the transmission line resonator, were sufficient to bring the cavity and spins into resonance. In the experiments presented in the main text the magnetic field was rotated by 45° in this plane, at which only two sub-ensembles were degenerate, being in resonance with the cavity.

The measurement scheme was an autodyne detection scheme for spectral hole burning and for measuring the transmitted intensity $|A(t)|^2$ through the cavity. The signal of a microwave source was split into two paths: one serving as cavity probe tone and the other as a local oscillator, both with frequency $\omega_{\mathrm{p}}$. The cavity probe tone was modulated by a frequency mixer and an arbitrary waveform generator (AWG) with 2 GS s$^{-1}$ sampling frequency. The pulsed microwave probe tone could be attenuated up to −45 dB and routed through a high-power amplifier with +40 dB gain by a fast microwave switch. The microwave drive was then fed into the cryostat and attenuated by −2 dB on the 4 K stage, allowing the application of up to 500 mW power at the cavity input. The transmitted signal was fed into a low-noise amplifier with +40 dB gain on the 4 K stage and mixed with the reference signal, and both quadrature signals were recorded by an oscilloscope with 5 GS s$^{-1}$ sampling frequency. From the measured quadratures $I(t)$ and $Q(t)$, the transmitted microwave intensity $|A(t)|^2$ was calculated (and plotted in Figs 3 and 4 and Supplementary Fig. 2). The transmitted intensity through the cavity resulted in a steady-state signal of $|A|^2 = 5 \times 10^{-4} \pm 2.5 \times 10^{-7}$ (V$^2$) for a single shot, which was then averaged 100 times for the measurements shown in Fig. 3e,f (where only one quadrature $|Q|^2$ is plotted) and Fig. 4. All line- and bandwidths and associated decay rates are given as half-width at half-maximum (HWHM).

Hole burning was experimentally achieved by quadrature amplitude modulation of a high-intensity hole burning pulse. The carrier frequency $\omega_{\mathrm{p}} = \omega_{\mathrm{c}} = \omega_{\mathrm{s}}$ was modulated by a sinusoidal signal $\eta_0 \sin(\Omega_{\mathrm{R}} t/2)\mathrm{e}^{-i\omega_{\mathrm{p}} t}$ with a Gaussian envelope and bandwidth $\Delta$. Power values of up to $|\eta_0|^2 \propto 20$ mW were obtained, corresponding to a steady state with ~$1 \times 10^4$ photons per spin in the cavity. This intensity is strong enough to bleach spin components selectively at the frequencies of the modulated drive signal. Such a pulse creates two frequency components and spectral holes at $\omega_{\mathrm{p}} \pm \Omega_{\mathrm{R}}/2$ with $\Delta$ bandwidth. However, the large number of spins in the experiment makes it necessary to use even larger input powers to burn multiple spectral holes in one shot. We therefore used two consecutive ~5-μs-long sequences to create two pairs of holes close to the polaritonic modes. After the creation of single and multiple pairs of dark states we probed the system again with a weak pulse $\eta_0 \sin(\Omega_{\mathrm{R}} t/2)\mathrm{e}^{-i\omega_{\mathrm{p}} t}$ ($\omega_{\mathrm{p}} = \omega_{\mathrm{c}} = \omega_{\mathrm{s}}$) corresponding to $<1 \times 10^{-5}$ photons per spin in the cavity after the hole burning pulse had decayed.

Spin echo spectroscopy measurements were used to quantify the spectral hole lifetime. A Car–Purcell–Meiboom–Gill (CPMG) sequence was used to estimate the spin–spin relaxation time ($T_2$), and stimulated echo spectroscopy techniques were used to measure the spin-lattice relaxation time in the rotating frame ($T_{1\rho}$). The best achievable echo times in our experiment were $T_2 = 4.8 \pm 1.6$ μs and $T_{1\rho} = 6.4 \pm 0.59$ μs, measured by CPMG and stimulated echo, respectively. We therefore conclude that the spin dissipation rate $\gamma \equiv 1/\tau = 2\pi \times 5.9$ kHz is dominated by spin diffusion in our experiment, given that $T_2 \approx T_{1\rho}$. Although limited by the same process, the spectral hole lifetime is more than a factor of four longer than $T_2$ and $T_{1\rho}$. This can be explained by the misalignment of the external d.c. magnetic field with respect to the NV axis and a bath of excess electron and nuclear spins in the host material.

## References

30. Nöbauer, T. *et al.* Creation of ensembles of nitrogen-vacancy centers in diamond by neutron and electron irradiation. Preprint at http://lanl.arxiv.org/abs/1309.0453v1 (2013).

nature photonics
SUPPLEMENTARY INFORMATION
DOI: 10.1038/NPHOTON.2016.225

# Spectral hole burning and its application in microwave photonics

Stefan Putz§,[1,2,3,*] Andreas Angerer§,[1,2] Dmitry O. Krimer,[4] Ralph Glattauer,[1]
William J. Munro,[5,6] Stefan Rotter,[4] Jörg Schmiedmayer,[1,2] and Johannes Majer[1,2]

[1] *Vienna Center for Quantum Science and Technology,*
*Atominstitut, TU Wien, Stadionallee 2, 1020 Vienna, Austria*
[2] *Zentrum für Mikro- und Nanostrukturen,*
*TU Wien, Floragasse 7, 1040 Vienna, Austria*
[3] *Department of Physics, Princeton University, Princeton, NJ 08544, USA*
[4] *Institute for Theoretical Physics, TU Wien,*
*Wiedner Hauptstraße 8-10/136, 1040 Vienna, Austria*
[5] *NTT Basic Research Laboratories, 3-1 Morinosato-Wakamiya,*
*Atsugi, Kanagawa 243-0198, Japan*
[6] *National Institute of Informatics, 2-1-2 Hitotsubashi,*
*Chiyoda-ku, Tokyo 101-8430, Japan*

(Dated: September 26, 2016)

---

§These authors contributed equally to this work.

## I. RABI SPLITTING & RABI OSCILLATIONS

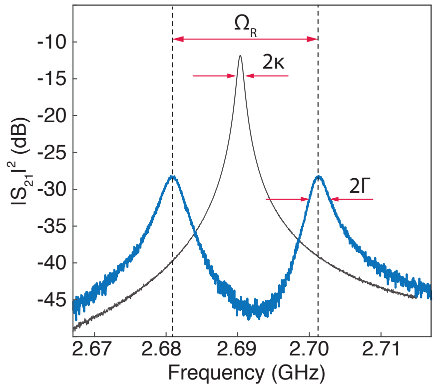

FIG. S1: **Transmission spectroscopy measurements.** The probe frequency $\omega_p$ is scanned and the cavity scattering parameter $|S_{21}|^2$ is measured by a vector network analyser. At zero external magnetic field *(black)* the cavity is largely detuned from the NV spin ensemble ($\omega_s \neq \omega_c$) and the bare cavity with a linewidth $\kappa/2\pi = 440 \pm 10$ kHz (HWHM) with a fundamental resonance at $\omega_c/2\pi$=2.691 GHz and a quality factor of $Q = 3,130$ is observed. A d.c. magnetic field of $|B| \approx 8$ mT is applied and a normal mode splitting *(blue)* $\Omega_R/2\pi = 21.3 \pm 0.1$ MHz is observed with a linewidth $\Gamma/2\pi = 1.45 \pm 0.05$ MHz (HWHM) when the spin ensemble is in resonance with the cavity ($\omega_s = \omega_c$).

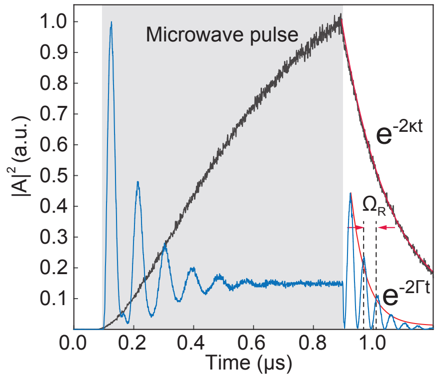

FIG. S2: **Time dependent cavity transmission.** A rectangular 800 ns long microwave pulse *(gray area)* with carrier frequency $\omega_p = \omega_c = \omega_s$ is applied. The transmitted intensity $|A|^2$ is measured by an auto-dyne measurement scheme and the down converted signal is displayed. At zero external magnetic field ($\omega_p = \omega_c \neq \omega_s$) the bare and resonant cavity transmission *(black)* is observed. After the drive is switched off the intensity decays with $\kappa = 440 \pm 10$ kHz. The NV ensemble is brought into resonance with the cavity ($\omega_p = \omega_c = \omega_s$) by a Zeeman shift and the system hybridises. We observe Rabi oscillations *(blue)* in the transmission signal with $\Omega_R/2\pi = 21.3 \pm 0.1$ MHz and a decay rate $\Gamma/2\pi = 1.45 \pm 0.05$ MHz. Both signals have been normalised with respect to their maximal transmitted intensity.

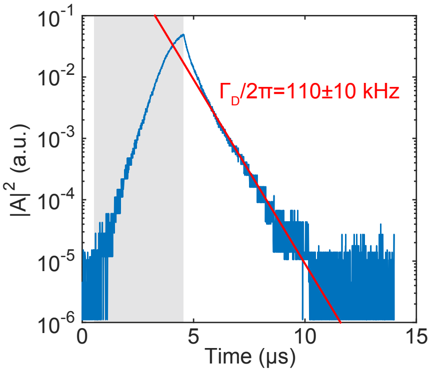

FIG. S3: **Decay of a single dark state.** A strong microwave pulse *(grey area)* creates a single spectral hole in the center of one of the polariton modes. The decay of the cavity field shows a fast initial decay which is followed by a crossover to a much slower decay rate. This slowed down exponential decay with a rate $\Gamma_D = 110 \pm 10$ kHz of the cavity field is associated with a single dark state. This procedure is used to optimise the experimental hole burning technique.

## II. THEORETICAL ANALYSIS

The modelling of the dynamics after the hole burning process is done by deriving the Heisenberg operator equations for the cavity and spin operators, $\dot{a} = \frac{\mathrm{i}}{\hbar}[\mathcal{H}, a] - \kappa a$, $\dot{\sigma}_j^- = \frac{\mathrm{i}}{\hbar}[\mathcal{H}, \sigma_j^-] - \gamma\sigma_j^-$, respectively, where $\mathcal{H}$ stands for the Tavis-Cummings Hamiltonian[1] given by Eq. (1) of the main article. Although the hole burning is a nonlinear process, our primary aim here is a theoretical model which is capable of capturing the linear non-Markovian dynamics in the limit of weak driving powers after the holes in the spin density have been burnt. This allows us to simplify the equations by setting $\langle\sigma_j^z\rangle \approx -1$ (Holstein-Primakoff-approximation[2]) and we derive the following linear set of first-order ODEs with respect to the cavity and spin amplitudes (in the $\omega_p$-rotating frame)

$$\begin{aligned} \dot{A}(t) &= -\left[\kappa + i(\omega_c - \omega_p)\right] A(t) + \sum_j g_j B_j(t) - \eta(t), \\ \dot{B}_j(t) &= -\left[\gamma + i(\omega_j - \omega_p)\right] B_j(t) - g_j A(t), \end{aligned} \tag{1}$$

where $A(t) = \langle a(t)\rangle$ and $B_j(t) = \langle\sigma_j^-(t)\rangle$ with $\eta(t)$ being a time dependent drive term with a carrier frequency $\omega_p$.

Owing to the large number of spins within the ensemble, the continuous spectral density can be modeled as $\rho(\omega) = \sum_j^N g_j^2\delta(\omega - \omega_j)/\Omega^2$, where $\Omega^2 = \sum_j^N g_j^2$ is the collective coupling strength of the spin ensemble to the cavity. Finally, we set up a Volterra equation for the cavity amplitude, $A(t) = \int_0^t d\tau \mathcal{K}(t-\tau)A(\tau) + \mathcal{F}(t)$, with the memory kernel function, $\mathcal{K}(t-\tau) = \int d\omega \rho(\omega)\mathcal{S}(\omega, t, \tau)$ (see[3,4] for details). The latter has a nontrivial structure and strongly depends on the exact shape of the spectral spin density $\rho(\omega)$. The system dynamics is then calculated by assuming a weak sinusoidal driving pulse, $\eta(t) = \eta_0 \sin(\Omega_R\, t/2)\, \mathrm{e}^{-i\omega_p t}$, with the carrier frequency matching the resonance condition $\omega_p = \omega_s = \omega_c$, similarly to what is done in the experiment (see Figs. 3 (e),(f) in the main text). The resulting dynamics is displayed in Figs. S4 (b),(d) for the case without and with hole burning. Note that we achieve very good agreement with the experimental data.

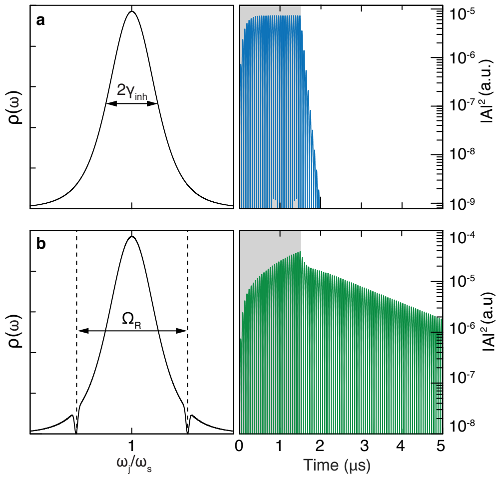

FIG. S4: *(Left panel)*: spectral spin density modeled by a $q$-Gaussian distribution[3–5] without **a** and with two spectral holes **b** burned at $\omega_s \pm \Omega_R/2$. *(Right panel)*: the corresponding dynamics under the action of a sinusoidal driving signal with small intensity, $\sin(\Omega_R\, t/2)\, \mathrm{e}^{-\mathrm{i}\omega_p t}$, with $\omega_p = \omega_s = \omega_c$. Gray (white) area indicates the time interval during which the driving signal is on (off).

The connection between the physics of spectral hole burning and the collective dark states shown in Fig. 2 of the main article is made by solving the eigenvalue problem of our spin-cavity system and analyzing the resulting spectra. After substituting $A(t) = A\exp(\lambda t)$, $B_j(t) = B_j \exp(\lambda t)$ and $\eta = 0$ into Eqs. (1), we derive the complex eigenvalue problem for $\lambda$, which can be represented schematically as, $\mathcal{L}\psi = \lambda\psi$, with $\psi = (A, B_k)^T$. Note that in Fig. 2 of the main article, the value of $E = Re(\lambda)$ is depicted. We take advantage of the previously established continuous form for the spin density $\rho(\omega)$[4,5] and discretise our problem by performing the following transformation, $g_\mu = \Omega\sqrt{\rho(\omega_\mu)/\sum_l \rho(\omega_l)}$. Since in total we deal with a sizeable number of spins ($N \approx 10^{12}$), we make our problem numerically tractable by dividing spins into many spin packets, so that $g_\mu$ represent a coupling strength within each spin packet rather than an individual spin coupling strength $g_j$. To provide an intuitive understanding how spectral hole burning reduces the decay rate we discuss here the case when spins are uncoupled within narrow spectral intervals at frequencies corresponding (approximately) to the location of two polaritonic peaks, $\omega_s \pm \Omega_R/2$.

---

[*] Electronic address: stef.putz@gmail.com

[1] Tavis, M. & Cummings, F. W. Exact Solution for an N-Molecule—Radiation-Field Hamiltonian. *Phys. Rev.* **170**, 379–384 (1968). 3

[2] Primakoff, H. & Holstein, T. Many-Body Interactions in Atomic and Nuclear Systems. *Phys. Rev.* **55**, 1218–1234 (1939). 3

[3] Putz, S. *et al.* Protecting a spin ensemble against decoherence in the strong-coupling regime of cavity QED. *Nat. Phys.* **10**, 720–724 (2014). 4, 5

[4] Krimer, D. O., Putz, S., Majer, J. & Rotter, S. Non-Markovian dynamics of a single-mode cavity strongly coupled to an inhomogeneously broadened spin ensemble. *Phys. Rev. A* **90**, 043852 (2014). 4

[5] Sandner, K. *et al.* Strong magnetic coupling of an inhomogeneous nitrogen-vacancy ensemble to a cavity. *Phys. Rev. A* **85**, 053806 (2012). 4, 5

LASER
& PHOTONICS
REVIEWS

Laser Photonics Rev. **10,** No. 6, 1023–1030 (2016) / **DOI** 10.1002/lpor.201600189

**Abstract** A very promising recent trend in applied quantum physics is to combine the advantageous features of different quantum systems into what is called "hybrid quantum technology". One of the key elements in this new field will have to be a quantum memory enabling to store quanta over extended periods of time. Systems that may fulfill the demands of such applications are comb-shaped spin ensembles coupled to a cavity. Due to the decoherence induced by the inhomogeneous ensemble broadening, the storage time of these quantum memories is, however, still rather limited. Here we demonstrate how to overcome this problem by burning well-placed holes into the spectral spin density leading to spectacular performance in the multimode regime. Specifically, we show how an initial excitation of the ensemble leads to the emission of more than a hundred well-separated photon pulses with a decay rate significantly below the fundamental limit of the recently proposed "cavity protection effect".

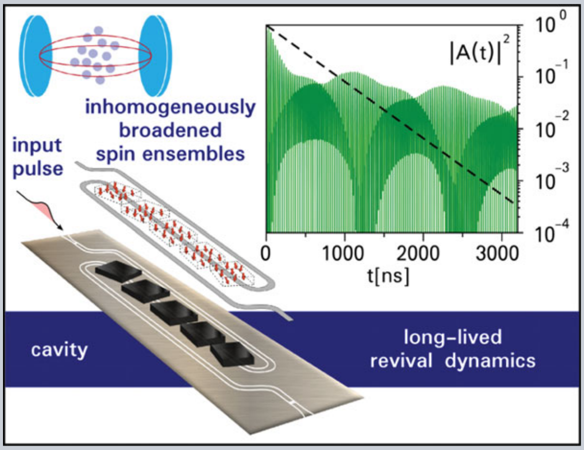

# Sustained photon pulse revivals from inhomogeneously broadened spin ensembles

**Dmitry O. Krimer[1],*, Matthias Zens[1], Stefan Putz[2,3], and Stefan Rotter[1]**

## 1. Introduction

Various setups in cavity quantum electrodynamics (QED) have been intensively studied during the last decade with regard to their potential for enabling the storage and processing of quantum information. Particularly attractive in this context are so-called "hybrid quantum systems" (HQS) [1,2], which combine the individual advantages of different quantum technologies. A major challenge for the realization of quantum information processing consists in ensuring coherent and reversible mapping of an encoded information between different elements in such systems [3–8]. A particularly attractive scenario in this context is realized based on atomic frequency combs or gradient memories in cavity or cavity-less setups [9–18] for which the information that one intends to store is emitted by the memory after the writing process in pulsed revivals at equidistant times. One of the major bottlenecks of this technology is, however, that an inhomogeneous broadening of the atomic or spin ensemble, which plays the role of a quantum memory [19,20], typically leads to a relatively fast decoherence of the stored information [21–23]. To counteract this detrimental effect on the storage time, various techniques have been developed based, e.g., on refocusing pulses [24], gradient inversion methods [25], or preselecting the optimal spectral portion of the inhomogeneously broadened ensemble [26]. Other very recent studies propose to access long-lived dark or subradiant states in atomic or spin ensembles for efficient information storage [27–31]. Also new setup designs without any inhomogeneous broadening such as those based on magnon modes strongly coupled to a cavity have recently been realized [17,18]. In this case, however, the gradient memory is characterized by relatively large intrinsic losses which impose limitations on the achievable time span of the revival dynamics. From these state-of-the-art experiments it is clear that new ideas and concepts will be needed to make these quantum memories viable for practical implementations, in particular in terms of the achievable storage time and the associated information retrieval efficiency.

In this work, we propose a novel approach to obtain a sustained emission of photon pulses from spin-ensembles in spite of a significant inhomogeneous broadening of the spin transition frequencies. Our concept is not restricted to a particular experimental realization of a spin ensemble, but can instead be generally applied to different physical realizations based, for instance, on negatively charged nitrogen-vacancy (NV) defects in diamond [21–23,32], or rare-earth spin ensembles [13,33,34]. The main requirement for our theory to be applied is that the losses exhibited by each individual constituent in the ensemble, $\gamma$, are substantially smaller as compared to the bare cavity decay rate, $\kappa$. Our key insight is that the decoherence in such hybrid quantum systems can be all but suppressed by a very non-invasive preparatory step involving the burning of a certain number

---

[1] Institute for Theoretical Physics, Vienna University of Technology (TU Wien), Wiedner Hauptstraße 8-10/136, 1040, Vienna, Austria
[2] Vienna Center for Quantum Science and Technology, Atominstitut, Vienna University of Technology (TU Wien), Stadionallee 2, 1020, Vienna, Austria
[3] Department of Physics, Princeton University, Princeton, NJ 08544, USA
*Corresponding author: e-mail: dmitry.krimer@gmail.com

of narrow holes in the comb-shaped spectral spin distribution at well-defined frequencies. Such a procedure allows us to access the corresponding collective dark state to align the system with the lowest decay scale $\gamma$, and as a result, to go beyond the fundamental limit of half the bare cavity decay rate $\kappa$ set by the recently proposed “cavity protection effect” [35–38]. In this way we demonstrate how to sustain the pulsed emission from the ensemble during very long time intervals up to a few microseconds, achieving more than a hundred well-separated pulses.

## 2. Results

Starting point of our analysis is an arrangement of several inhomogeneously broadened spin ensembles coupled to a single cavity mode with frequency $\omega_c$. We assume that the spin ensembles have been prepared with mean frequencies $\omega_s^{(\mu)}$ that are equidistantly spaced at intervals of $\Delta\omega$, such that $\omega_s^{(\mu)} = \omega_c \pm n_\mu \Delta\omega$, resulting in a comb-shaped spectral density (see Fig. 1(a)). While our approach is general we will be referring in the following to one particular experimental realization based on magnetic coupling of NV-ensembles residing in several diamonds coupled to a superconducting microwave resonator. Note that by an appropriate alignment of the diamonds with respect to an external magnetic field and by exploiting the Zeeman effect, the mean frequencies of the spin ensembles, $\omega_s^{(\mu)}$, can be efficiently tuned in a rather wide spectral interval [22, 23]. To be concrete, we used in our calculations the specific parameter values from recent studies, where the non-Markovian dynamics and the cavity protection effect in a single-mode cavity strongly coupled to a single inhomogeneously broadened NV-ensemble have been studied (without holes in the spectral spin density) [37, 38].

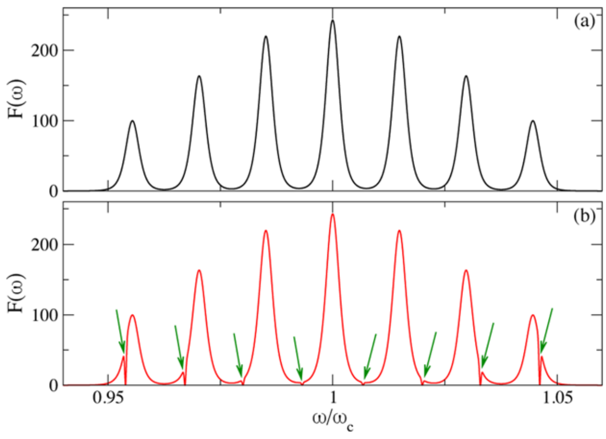

**Figure 1** (a) Spectral spin distribution, $F(\omega) = \sum_{\mu=1}^{M} \Omega_\mu^2/\Omega^2 \cdot \rho_\mu(\omega)$, consisting of seven equally spaced $q$-Gaussians of equal width, $\gamma_q/2\pi = 9.4$ MHz. $F(\omega)$ has peaks at frequencies $\omega_s^{(\mu)} = \omega_c \pm n_\mu \Delta\omega$ with the spacing, $\Delta\omega/2\pi = 40$ MHz. The cavity frequency $\omega_c$ coincides with the mean frequency of the central $q$-Gaussian, $\omega_s = \omega_c = 2\pi \cdot 2.6915$ GHz. Spin ensembles have coupling strengths distributed as $\Omega_\mu^2/\Omega^2 = \exp[-(\omega_c - \omega_s^{(\mu)})^2/2\sigma_G^2]$, with $\sigma_G/2\pi = 150$ MHz. (b) Spectral function from (a) with eight spectral holes (see arrows) at the maxima of the cavity content $|A_\mu|^2$ shown in Fig. 3(e) for $\Omega/2\pi = 26$ MHz. All holes are of equal width, $\Delta_h/2\pi = 0.47$ MHz, and are modelled by a Gaussian lineshape.

### 2.1. Theoretical model

To account for the spin-cavity dynamics, we start from the Tavis-Cummings Hamiltonian ($\hbar = 1$) [40]

$$\mathcal{H} = \omega_c a^\dagger a + \frac{1}{2}\sum_{\mu=1}^{M}\sum_{k=1}^{N_\mu} \omega_k^{(\mu)} \sigma_k^{(\mu)(z)} + \mathrm{i}\sum_{\mu=1}^{M}\sum_{k=1}^{N_\mu}\left[g_k^{(\mu)}\sigma_k^{(\mu)(-)}a^\dagger - g_k^{(\mu)*}\sigma_k^{(\mu)(+)}a\right] - \mathrm{i}\left[\eta(t)a^\dagger \mathrm{e}^{-\mathrm{i}\omega_p t} - \eta(t)^* a \mathrm{e}^{\mathrm{i}\omega_p t}\right], \quad (1)$$

where $M$ and $N_\mu$ in the summations above stand for the number of spin ensembles coupled to the single cavity mode and the number of spins in the $\mu$-th ensemble, respectively. Here $a^\dagger$ and $a$ are standard cavity creation and annihilation operators and $\sigma_k^{(\mu)(\pm,z)}$ are the Pauli operators associated with each individual spin of frequency $\omega_k^{(\mu)}$, which obey the usual fermionic commutation relations. (The subscript $k$ enumerates an individual spin which resides in the $\mu$-th ensemble.) The interaction part of the Hamiltonian is written in the rotating-wave and dipole approximation, with $g_k^{(\mu)}$ being the coupling strength of the $k$-th spin located in the $\mu$-th ensemble. The absence of dipole-dipole interaction terms in Eq. (1) implies that the concentration of spins in each ensemble is sufficiently low and the distance between them is large enough. The last term in Eq. (1) describes an incoming signal with carrier frequency $\omega_p$ and amplitude $\eta(t)$ whose time variation is much slower as compared to $1/\omega_p$.

Although the individual spin coupling strengths $g_k^{(\mu)}$ are very small, the effective collective coupling strength of each spin ensemble to the cavity mode, $\Omega_\mu = (\sum_{k=1}^{N_\mu} g_k^{(\mu)2})^{1/2}$, is enhanced by a factor of $\sim \sqrt{N_\mu}$. Thus, thanks to this collective coupling it becomes possible to reach the strong coupling regime for sufficiently large ensembles (see, e.g., [7, 22, 32] for NV spin ensembles). In a number of previous studies [23, 35–38] it was demonstrated that it is very convenient to phenomenologically introduce a continuous distribution $\rho(\omega)$ which describes the shape of the single spin spectral density. In a similar manner, we define here $M$ distributions, $\rho_\mu(\omega) = \sum_{k=1}^{N_\mu} g_k^{(\mu)2}\delta(\omega - \omega_k^{(\mu)})/\Omega_\mu^2$, which stand for the shape of the $\mu$-th spin spectral density, each satisfying the normalization condition $\int d\omega \rho_\mu(\omega) = 1$. Note that the coupling strengths $\Omega_\mu$ are not equal in general, so that the total spectral distribution acquires the following form, $F(\omega) = \sum_{\mu=1}^{M} \Omega_\mu^2/\Omega^2 \cdot \rho_\mu(\omega)$, where $\Omega$

stands for the collective coupling strength of the central ensemble [see Fig. 1(a)]. In agreement with our previous studies [23,37,38], we assume that the spectral spin density of each ensemble, $\rho_\mu(\omega)$, can be modelled by a $q$-Gaussian distribution of the following form

$$\rho_\mu(\omega) = C \cdot \left[1-(1-q)(\omega-\omega_s^{(\mu)})^2/\Delta^2\right]^{\frac{1}{1-q}},$$

where $q$ is the dimensionless shape parameter, $1 < q < 3$, $\gamma_q = 2\Delta\sqrt{(2^q-2)/(2q-2)}$ is the full-width at half maximum (FWHM) and $C$ is the normalization constant.

Next, we derive the Heisenberg operator equations for the cavity and spin operators and write a set of equations for the expectation values (semiclassical approach). We consider the limit of weak driving powers and therefore the number of the excited spins is always small compared to the ensemble size. This allows us to simplify these equations by setting $\langle\sigma_k^{(\mu)(z)}\rangle \approx -1$ (Holstein-Primakoff-approximation [41]) which results in a closed set of linear first-order ordinary differential equations (ODEs) for the cavity and spin expectation values, $A(t) = \langle a(t)\rangle$ and $B_k^{(\mu)}(t) = \langle\sigma_k^{(\mu)(-)}(t)\rangle$. Finally, by going to the continuous limit and performing rather cumbersome but straightforward calculations, we end up with a Volterra integral equation for the cavity amplitude, $A(t) = \Omega^2 \int_0^t d\tau \mathcal{K}(t-\tau)A(\tau) + \mathcal{D}(t)$ [38], where $\mathcal{D}(t)$ depends on the driving signal and initial conditions. Here the memory kernel function, $\mathcal{K}(t-\tau) = \int d\omega F(\omega)\mathcal{S}(\omega, t, \tau)$ (see Supplementary Note 1), strongly depends on the exact shape of the spectral distribution, $F(\omega)$, and is responsible for the non-Markovian feedback of the spin ensembles on the cavity, so that the cavity amplitude at time $t$ depends on all previous events $\tau < t$. ($\mathcal{S}(\omega, t, \tau)$ depends on the time delay, $t-\tau$, frequency, $\omega$, but is independent from the spectral distribution.)

The Volterra equation turns out to be the governing equation not only for the semiclassical but also for the quantum case, when at $t = 0$ the cavity is fed with a single photon and all spins in the ensembles are unexcited, $|1, \downarrow^{(i)}\rangle$. In Supplementary Note 2 we show in detail that the probability for a photon to stay inside the cavity at time $t > 0$, $N(t) = \langle 1, \downarrow|a^\dagger(t)a(t)|1, \downarrow\rangle$, reduces to $N(t) = |A(t)|^2$ in this case, where $A(t)$ is the solution of the aforementioned Volterra equation with the initial condition $A(t=0) = 1$. Note that in the context of spontaneous emission inhibition using the Zeno effect also analytical solutions of the Volterra equation have been explored [39].

## *2.2. Multimode strong coupling dynamics*

We first apply the Volterra equation to the spectral function $F(\omega)$ displayed in Fig. 1(a), for the case when the coupling strength is in the regime, where only the central spin ensemble is strongly coupled to the cavity mode (at the resonance condition $\omega_s = \omega_c$). In Fig. 2(a) we plot the decay of the cavity occupation $N(t) = \langle 1, \downarrow|a^\dagger(t)a(t)|1, \downarrow\rangle$ from the initial state, for which a single photon with frequency $\omega_c$ resides in the cavity and all spins are unexcited (the model is given in Supplementary Note 2). The resulting dynamics displays damped Rabi oscillations, which feature, however, a slightly distorted shape arising from the dispersive contribution of neighbouring spin ensembles. We observe very similar dynamics also in the semiclassical case shown in Fig. 2(b), when the cavity is pumped by a short rectangular microwave pulse with a carrier frequency matching the resonance condition, $\omega_p = \omega_s = \omega_c$ (see Supplementary Note 1 for the derivation of governing equations).

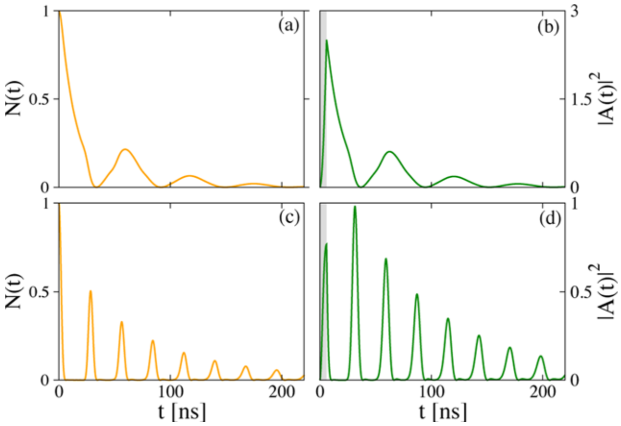

**Figure 2** *Left column*: Decay of the cavity occupation $N(t) = \langle 1, \downarrow|a^\dagger(t)a(t)|1, \downarrow\rangle$, when at $t = 0$ the cavity is fed with a single photon of frequency $\omega_c$ and all spins are in the ground state, $|1, \downarrow\rangle$. *Right column*: Cavity probability amplitude $|A(t)|^2$ versus time $t$ under the action of an incident short rectangular pulse of duration 6 ns. The carrier frequency, $\omega_p = \omega_c = 2\pi \cdot 2.6915$ GHz. Gray (white) area indicates the time interval during which the pumping signal is on (off). (a,b) Strong coupling regime ($\Omega/2\pi = 8$ MHz) with damped Rabi oscillations. (c,d) Multimode strong coupling regime ($\Omega/2\pi = 26$ MHz) featuring pulsed revivals. The spectral function $F(\omega)$ is taken from Fig. 1(a) when the mean spin frequency of the central $q$-Gaussian, $\omega_s = \omega_c$ [resonant case designated by vertical cuts in Fig. 3(a,d)].

In a next step, we repeat the calculations for both the quantum and the semiclassical case keeping all parameters unchanged except for the coupling strength, which we increase from $\Omega/2\pi = 8$ MHz to $\Omega/2\pi = 26$ MHz. In this limit we already entered the multimode strong coupling regime (see [42], where the reverse situation was explored, when a single emitter is coupled to many cavity modes). Correspondingly, we now observe the desired pulsed revivals of the cavity occupation $N(t)$ and the periodic emission of excitations from the spin-ensembles into the cavity amplitude $A(t)$. This type of dynamics can be attributed to a constructive rephasing of spins in the ensembles at time intervals that are approximately equal to the inverse of the spectral distance between adjacent spin-ensembles, $2\pi/\Delta\omega$, shown in Fig. 1(a). It is worth noting that we intentionally chose the duration of the initial driving pulse in Fig. 2(d) to be much smaller as compared to the characteristic dephasing time in our system. Such a choice ensures that the dephasing, caused by the effect of inhomogeneous broadening, only has a negligible influence up to the moment of time when the driving pulse is turned off. As a result, we obtain very regularly spaced and well-separated pulses similar to the single-photon case. As the duration of the driving pulse increases, the dephasing effect gradually sets in, and as a consequence, the dynamics becomes more and more irregular (not shown). While these results already demonstrate that the pulsed emission from collectively coupled and inhomogeneously broadened spin ensembles is achievable for realistic parameter values, the number of pulses that we observe in our solutions is rather limited (see Fig. 2). The crucial question to ask at this point is thus, whether a simple and efficient procedure can resolve this major bottleneck in the system performance.

## 2.3. Eigenvalue analysis

As we will show below, such a procedure can, indeed, be worked out based on a delicate modification of the spin spectral density. To arrive at this result, we need to investigate first how the eigenvalues and the corresponding eigenstates of this hybrid cavity-spin system look like. For this purpose we discretise the spectral distribution $F(\omega)$ in the frequency domain and substitute $A(t) = A \cdot \exp(-\lambda t)$ as well as $B_k^{(\mu)}(t) = B^k \cdot \exp(-\lambda t)$ into the above set of ODEs for the cavity and spin expectation values. This allows us to derive and solve numerically for each value of $\omega_s$ the non-Hermitian eigenvalue problem $\mathcal{L}\psi_l = \lambda_l \psi_l$, with $\psi_l = (A_l, B_l^k)^T$ being the eigenvector which represents the collective spin-cavity excitation belonging to the eigenvalue $\lambda_l$ (see Supplementary Note 4 for details). Note that $\mathrm{Im}(\lambda_l)$ plays the role of the collective eigenfrequency and $\mathrm{Re}(\lambda_l) > 0$ is the rate at which $\psi_l$ decays. When solving this eigenvalue problem we always keep the same shape for the spectral function $F(\omega)$ depicted in Fig. 1(a) but shift the whole structure in the frequency domain by detuning the mean spin frequency $\omega_s$ of the central ensemble with respect to the cavity $\omega_c$. [Fig. 1(a) corresponds to the resonant case, $\omega_s = \omega_c$.] The only other parameter that we vary is again the value of the coupling strength $\Omega$, that we tune from the limit where the cavity mode is strongly coupled solely to the central spin subensemble to the regime of "multimode strong coupling".

The results of these calculations are presented in Fig. 3, where we plot the cavity content, $|A_l|^2$, of the normalised eigenvector $\psi_l$ as a function of $\omega_s$ and the calculated collective eigenfrequency $\mathrm{Im}(\lambda_l)$ [(a),(d)] or decay rate $\mathrm{Re}(\lambda_l)$ [(c),(f)]. Let us consider first the regime where the value for the coupling strength $\Omega_\mu$ of each spin ensemble separately is large enough to ensure strong coupling to the cavity. In this "single-mode strong coupling limit" we observe an avoided crossing in Fig. 3(a) whenever the resonance condition with the $\mu$-th ensemble is met, $\omega_s^{(\mu)} = \omega_c$. The other off-resonant spin ensembles in turn give rise to small dispersive contribution only. The most pronounced avoided crossing is observed when the cavity is at resonance with the central spin ensemble, $\omega_s = \omega_c$, where two symmetric polaritonic peaks in the structure of $|A_l|^2$ occur, see Fig. 3(b). It is also seen from Fig. 3(c) [yellow symbols] that a large fraction of eigenstates, $\psi_l$, decays with some intermediate values of the decay rate which lie within the interval $\gamma < \mathrm{Re}\lambda_l < \kappa$. (Here $\kappa$ and $\gamma \ll \kappa$ are the dissipative cavity and spin losses, respectively.) This can be explained by the fact that such eigenvectors represent an entangled spin-cavity state, where both the cavity and spin contents are essentially nonzero.

With a further increase of the coupling strength, the distance between the two polaritonic peaks depicted in Fig. 3(b), which is approximately as large as $2\Omega$, increases and the peak line shapes become substantially sharper (not shown). Such a peak narrowing can be attributed to the so-called "cavity protection effect" [35–38] that appears in the strong coupling regime provided that the spin density has a spectral distribution with tails that decay sufficiently fast. The latter requirement is indeed satisfied in our case because the spectral function $F(\omega)$ in Fig. 1(a) consists of seven $q$-Gaussian distributions.

At even larger values of $\Omega$ the avoided crossings eventually disappear, being replaced instead by a comb-shaped structure with parallel stripes characterised by a large cavity content, see yellow curves in Fig. 3(d). Such a picture is, however, valid only for moderate values of detuning of $\omega_s$ from $\omega_c$, whereas for large detuning we are in the dispersive regime [see Fig. 3(d,f)]. A comb-shaped structure of $|A_l|^2$ with almost equally spaced polaritonic peaks is clearly seen at resonance, $\omega_s = \omega_c$, indicating the multimode strong coupling between all spin ensembles and the cavity mode [see Fig. 3(e)]. It is worth noting that the peaks become substantially sharper as compared to the case of the single-mode strong coupling regime [compare Fig. 3(e) with Fig. 3(b)] due to the aforementioned "cavity protection effect". These narrow peaks in the frequency domain are exactly those that are responsible for the pulsed emission in the time domain as observed in Fig. 2(d).

The shapes of $|A_l|^2$ versus $\mathrm{Im}(\lambda_l)$ at $\omega_s = \omega_c$ for both the multimode and the single-mode strong coupling regime reproduce exactly the corresponding shapes of the kernel function $U(\omega)$ obtained in the framework of the Laplace transform technique sketched in Supplementary Note 3 [compare Fig. 3(b,e) in the main text with Fig. 2(a,b) in Supplementary Material]. The connection between these two complementary concepts provides instructive insights into the physics underlying the multimode strong coupling regime.

## 2.4. Suppression of decoherence

Specifically, we want to apply these findings now to the suppression of decoherence in the multimode strong-coupling regime [17, 42]. For this purpose we will make use of the recent insight [30], that for single-mode strong-coupling the decoherence induced by the spin broadening can be strongly suppressed simply by burning two narrow spectral holes in the spin spectral density close to the maxima of

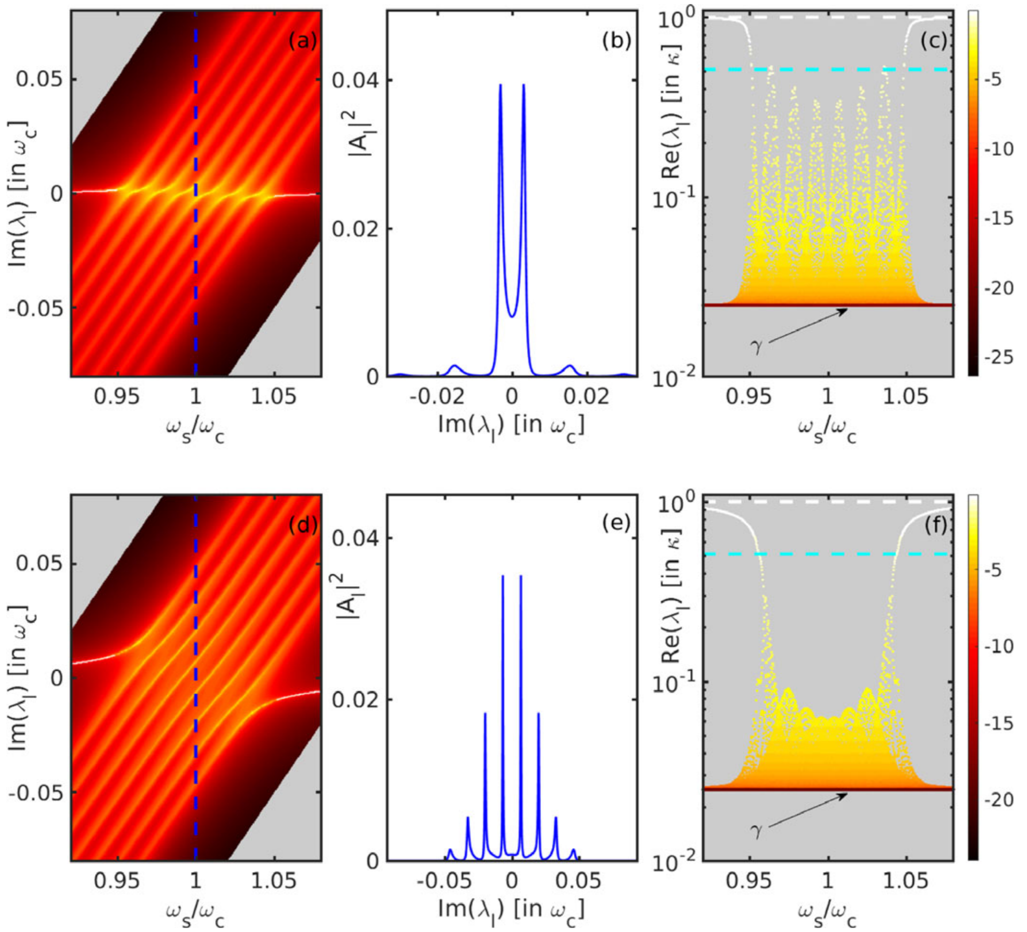

**Figure 3** *Upper row*: **Single-mode strong coupling regime**. Solution of the eigenvalue problem (see the main text for details) at $\Omega/2\pi = 8$ MHz as a function of the mean spin frequency $\omega_s$ of the spectral function $F(\omega)$ shown in Fig. 1(a). (a) The cavity content, $|A_l|^2$, of the normalised eigenvector, $\psi_l = (A_l, B_l^k)$, versus eigenfrequencies $\mathrm{Im}(\lambda_l)$ and $\omega_s$ is represented by the color gradient (color bar on the right in log scale): two prominent polariton modes are clearly distinguishable from a bath of dark states at fixed value of $\omega_s$. (b) the cavity content $|A_l|^2$ versus $\mathrm{Im}(\lambda_l)$ for the resonant case, $\omega_s = \omega_c$, along the vertical cut shown in (a) (dashed blued line). (c) $|A_l|^2$ versus decay rates, $\mathrm{Re}(\lambda_l)$, and $\omega_s$ with the same coloring as in (a). Cyan dashed line: the minimally reachable decay rate achieved due to the cavity protection effect, $\Gamma/2 \approx \kappa/2$ (limit of $\gamma \ll \kappa$), with $\kappa = 2\pi \cdot 0.4$ MHz (HWHM of the cavity decay) and $\gamma = 2\pi \cdot 0.01$ MHz $\ll \kappa$ (HWHM of the spin decay). White dashed line: decay rate of a bare cavity mode, $\kappa$.
*Lower row*: **Multimode strong coupling regime**. Solution of the same eigenvalue problem as above, but for an increased coupling strength $\Omega/2\pi = 26$ MHz (notation and colors are the same as in the upper row). Eight polariton modes are clearly distinguishable with an almost equidistant spacing, see (e) for the resonant case, $\omega_s = \omega_c$. In all calculations $N = 1200$ spins were used.

the two polaritonic peaks as shown here in Fig. 3(b). The working principle of this effect is based on the creation of long-lived collective dark states [27, 31, 35, 36] in the spin ensemble that only have very little cavity content and may thus even outperform the ultimate limit for the decoherence rate of the cavity protection effect given by $\Gamma = \kappa$ for $\gamma \ll \kappa$ [30]. (Note that the decay rate for a bare cavity without spin ensembles coupled to it is $2\kappa$.) Mathematically, this effect can be associated with rapid variations of the nonlinear Lamb shift around the holes' positions and with contribution of poles in the Laplace transform of the Volterra equation derived above [30]. Since this theoretical concept has meanwhile also been successfully implemented in a corresponding experiment [31], we will try to generalize it here to the case where not just two polaritonic peaks appear (as for single-mode strong coupling), but instead many of them (as for multimode strong coupling).

The most natural extension of this hole-burning approach to the multimode regime would demand that the positions of the burned spectral holes remain close to the polaritonic peaks of which we observe altogether eight in Fig. 3(e), corresponding to the seven spin-subensembles shown in Fig. 1(a). As illustrated in Fig. 1(b), we therefore propose to burn eight narrow spectral holes into the spin distribution at frequencies which correspond to the maxima of the cavity content, $|A_l|^2$, shown in Fig. 3(e) (or,

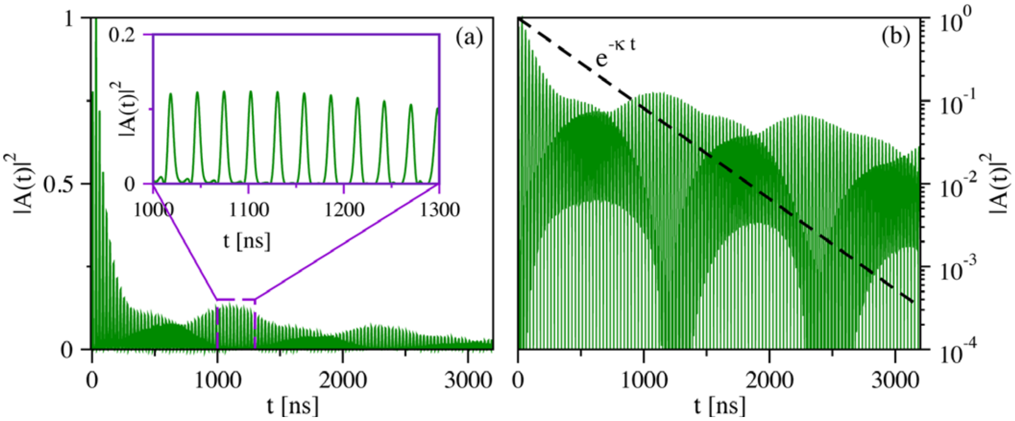

**Figure 4** (a) Cavity probability amplitude $|A(t)|^2$ versus time $t$ under the action of an incident short rectangular pulse of duration 6 ns after eight holes are burnt at $t = 0$, see Fig. 1(b). All other parameters are the same as for the case without hole burning presented in Fig. 2(d). (b) Same as (a) with the ordinate plotted on a logarithmic scale. The decay process with the minimal decay rate reachable by the cavity protection effect, $e^{-\kappa t}$, with $\kappa/2\pi = 0.4$ MHz is depicted by the dashed line (limit of $\gamma \ll \kappa$). The decay rate of $|A(t)|^2$ for a bare cavity without spin ensembles coupled to it is given by $e^{-2\kappa t}$ (not shown).

equivalently, to the maxima of the kernel function $U(\omega)$ depicted in Fig. 2(b) of the Supplementary material). The hole burning itself can be straightforwardly implemented in the experiment by exposing the cavity to very high intensity tones that feature frequency components exactly at the desired holes positions. In this way the spins at these frequency values will be shuffled into an equal population of ground and excited states, where they can no longer couple to the cavity and thus effectively form a hole in the spin distribution. This hole burning is essentially a nonlinear process, which can not be captured by the Volterra equation, but we may very well describe the system dynamics right after the holes have been burned. For this purpose we directly integrate the Volterra equation numerically in time, resulting in the time evolution for both the quantum and the semiclassical case, which looks qualitatively very similar for both cases (see Fig. 4, where the results for the semiclassical case are presented only). For these results we assume that the holes are burned at $t = 0$ and that they keep their shape during the whole time interval shown in Fig. 4, a property which is well-fulfilled in recent experiments where the hole lifetime was estimated to be as large as 27 $\mu$s [31]. Most importantly, we can see very clearly in Fig. 4 that the pulsed emission from the spin ensemble persists over a drastically increased time interval as compared to the corresponding case without hole burning represented in Fig. 2(d). This suppression of decoherence is not only a quantitative improvement, but it breaks the barrier achievable when making maximal use of the "cavity protection effect". To illustrate this explicitly, we replot in Fig. 4(b) our results from Fig. 4(a) on a logarithmic scale and compare them with this minimal exponential decay $e^{-\kappa t}$ of the fully cavity-protected ensemble. We find that the probabilities $|A(t)|^2$ for the photon pulse revivals significantly exceed this barrier such that, e.g., at $t \sim 3\,\mu s$ after the driving pulse, the values for $|A(t)|^2$ are two orders of magnitude above those achievable through cavity-protection. For longer time-scales this outperformance ratio continues to grow. To check if the holes we burned in the ensemble are, indeed, located at the optimal positions, we also performed additional calculations in which we varied the hole positions by only a few percent away from the maxima of $|A_l|^2$. We find that such a shift leads to a substantial decrease in the revival amplitudes as compared to those in Fig. 4 (not shown), thereby confirming our initial choice of positioning the holes right at the frequencies of the polaritonic peaks to secure the long-lived photon pulse revivals.

## 3. Conclusions and outlook

In conclusion, our study provides a novel approach to suppress the decoherence in quantum memories based on inhomogeneously broadened spin ensembles coupled to a cavity. Specifically, when the ensembles feature a comb-shape structure to give rise to repetitive photon pulse revivals, we show how the burning of narrow holes in this atomic frequency comb leads to a dramatic prolongation of the revival dynamics. We emphasize that the positions of the holes are generally incommensurate with the positions of the peaks in the frequency comb - a result that follows directly from our theory for the multimode strong coupling regime. Since our protocol successfully manages to overcome the decoherence both from the inhomogeneous spin broadening as well as from the cavity dissipation, we expect our protocol to be an important step towards future possible realizations of quantum memories based on spin ensembles.

The challenges we anticipate on the experimental side are the preparation of a comb-shaped spectral spin distribution (e.g., by detuning several sub-ensembles from each other) as well as the strong coupling to a single-mode cavity. Following our proposal, several narrow spectral holes then need to be burned into this spin ensemble (through the cavity or from the outside). After such a preparatory step, the quantum information (as stored, e.g., in a qubit [32]) may be transferred through the cavity bus to the spins from where it is reemitted back into the cavity at periodic time intervals without requiring any further control or refocusing techniques.

## Supporting Information

Additional supporting information may be found in the online version of this article at the publisher's website.

**Acknowledgements.** We would like to thank A. Angerer, R. Glattauer, B. Hartl, M. Liertzer, J. Majer, W. J. Munro and J. Schmiedmayer for helpful discussions and acknowledge support by the Austrian Science Fund (FWF) through Project No. F49-P10 (SFB NextLite). S.P. acknowledges support by the Austrian Science Fund (FWF) in the framework of the Doctoral School "Building Solids for Function" (Project W1243).

**Received:** 13 July 2016, **Revised:** 24 September 2016, **Accepted:** 26 September 2016

**Key words:** Cavity QED, quantum emitters, collective dynamics, strong coupling regime, quantum interference, microwave.

## References

[1] Z.-L. Xiang, S. Ashhab, J. Q. You, and F. Nori, Rev. Mod. Phys. **85**, 623 (2013).

[2] G. Kurizki, P. Bertet, Y. Kubo, K. Mølmer, D. Petrosyan, P. Rabl, and J. Schmiedmayer, Proceedings of the National Academy of Sciences **112**, 3866 (2015).

[3] A. Imamoglu, D. D. Awschalom, G. Burkard, D. P. DiVincenzo, D. Loss, M. Sherwin, and A. Small, Phys. Rev. Lett. **83**, 4204 (1999).

[4] P. Rabl, D. DeMille, J. M. Doyle, M. D. Lukin, R. J. Schoelkopf, and P. Zoller, Phys. Rev. Lett. **97**, 033003 (2006).

[5] K. Tordrup, A. Negretti, and K. Mølmer, Phys. Rev. Lett. **101**, 040501 (2008).

[6] D. Petrosyan, G. Bensky, G. Kurizki, I. Mazets, J. Majer, and J. Schmiedmayer, Phys. Rev. A **79**, 040304(R) (2009).

[7] J. Verdú, H. Zoubi, Ch. Koller, J. Majer, H. Ritsch, and J. Schmiedmayer, Phys. Rev. Lett. **103**, 043603 (2009).

[8] J. H. Wesenberg, A. Ardavan, G. A. D. Briggs, J. J. L. Morton, R. J. Schoelkopf, D. I. Schuster, and K. Mølmer, Phys. Rev. Lett. **103**, 070502 (2009).

[9] H. de Riedmatten, M. Afzelius, M. U. Staudt, C. Simon, and N. Gisin, Nature **456**, 773 (2008).

[10] M. Afzelius, C. Simon, H. de Riedmatten, and N. Gisin, Phys. Rev. A **79**, 052329 (2009).

[11] I. Usmani, M. Afzelius, H. de Riedmatten, and N. Gisin, Nat. Commun. **1**, 12 (2010).

[12] K. I. Gerasimov, S. A. Moiseev, V. I. Morosov, and R. B. Zaripov, Phys. Rev. A **90**, 042306 (2014).

[13] P. Jobez, I. Usmani, N. Timoney, C. Laplane, N. Gisin, and M. Afzelius, New J. of Phys. **16**, 083005 (2014).

[14] S. A. Moiseev and S. Kröll, Phys. Rev. Lett. **87**, 173601 (2001).

[15] B. Kraus, W. Tittel, N. Gisin, M. Nilsson, S. Kröll, and J. I. Cirac, Phys. Rev. A **73**, 020302 (2006).

[16] V. Damon, M. Bonarota, A. Louchet-Chauvet, T. Chanelière, and J.-L. L. Gouët, New J. of Phys. **13**, 093031 (2011).

[17] X. Zhang, C.-L. Zou, N. Zhu, F. Marquardt, L. Jiang, and H. X. Tang, Nat. Commun. **6**, 8914 (2015).

[18] X. Zhang, C. Zou, L. Jiang, and H. X. Tang, J. Appl. Phys. **119**, 023905 (2016).

[19] L. M. Duan, M. D. Lukin, J. I. Cirac, and P. Zoller, Nature **414**, 413 (2001).

[20] C. Simon, M. Afzelius, J. Appel, A. Boyer de la Giroday, S. J. Dewhurst, N. Gisin, C. Y. Hu, F. Jelezko, S. Kröll, J.H. Müller, J. Nunn, E. S. Polzik, J. G. Rarity, H. De Riedmatten, W. Rosenfeld, A.J. Shields, N. Sköld, R. M. Stevenson, R. Thew, I. A. Walmsley, M. C. Weber, H. Weinfurter, J. Wrachtrup, and R. J. Young, Eur. Phys. J. D **58**, 1 (2010).

[21] Y. Kubo, F. R. Ong, P. Bertet, D. Vion, V. Jacques, D. Zheng, A. Dréau, J.-F. Roch, A. Aueves, F. Jelezko, J. Wrachtrup, M. F. Barthe, P. Bergonzo, and D. Esteve, Phys. Rev. Lett. **105**, 140502 (2010).

[22] R. Amsüss, C. Koller, T. Nöbauer, S. Putz, S. Rotter, K. Sandner, S. Schneider, M. Schramböck, G. Steinhauser, H. Ritsch, J. Schmiedmayer, and J. Majer, Phys. Rev. Lett. **107**, 060502 (2011).

[23] K. Sandner, H. Ritsch, R. Amsüss, C. Koller, T. Nöbauer, S. Putz, J. Schmiedmayer, and J. Majer, Phys. Rev. A **85**, 053806 (2012).

[24] M. U. Staudt, S. R. Hastings-Simon, M. Nilsson, M. Afzelius, V. Scarani, R. Ricken, H. Suche, W. Sohler, W. Tittel, and N. Gisin, Phys. Rev. Lett. **98**, 113601 (2007).

[25] M. P. Hedges, J. J. Longdell, Y. Li, and M. J. Sellars, Nature **465**, 1052 (2010).

[26] G. Bensky, D. Petrosyan, J. Majer, J. Schmiedmayer, and G. Kurizki, Phys. Rev. A **86**, 012310 (2012).

[27] X. Zhu, Y. Matsuzaki, R. Amsüss, K. Kakuyanagi, T. Shimo-Oka, N. Mizuochi, K. Nemoto, K. Semba, W. J. Munro, and S. Saito, Nat Commun **5**, 3424 (2014).

[28] M. O. Scully, Phys. Rev. Lett. **115**, 243602 (2015).

[29] W. Guerin, M. O. Araújo, and R. Kaiser, Phys. Rev. Lett. **116**, 083601 (2016).

[30] D. O. Krimer, B. Hartl, and S. Rotter, Phys. Rev. Lett. **115**, 033601 (2015).

[31] S. Putz, A. Angerer, D. O. Krimer, R. Glattauer, W. J. Munro, S. Rotter, J. Schmiedmayer, and J. Majer, arXiv:1512.00248.

[32] Y. Kubo, C. Grezes, A. Dewes, T. Umeda, J. Isoya, H. Sumiya, N. Morishita, H. Abe, S. Onoda, T. Ohshima, V. Jacques, A. Dréau, J.-F. Roch, I. Diniz, A. Aufféves, D. Vion, D. Esteve, and P. Bertet, Phys. Rev. Lett. **107**, 220501 (2011).

[33] S. Probst, H. Rotzinger, S. Wünsch, P. Jung, M. Jerger, M. Siegel, A. V. Ustinov, and P. A. Bushev, Phys. Rev. Lett. **110**, 157001 (2013).

[34] T. Zhong, J. M. Kindem, E. Miyazono, and A. Faraon, Nat. Commun. **6**, 8206 (2015).

[35] I. Diniz, S. Portolan, R. Ferreira, J. M. Gérard, P. Bertet, and A. Aufféves, Phys. Rev. A **84**, 063810 (2011).

[36] Z. Kurucz, J. H. Wesenberg, and K. Mølmer, Phys. Rev. A **83**, 053852 (2011).

[37] S. Putz, D. O. Krimer, R. Amsüss, A. Valookaran, T. Nöbauer, J. Schmiedmayer, S. Rotter, and J. Majer, Nat. Phys. **10**, 720 (2014).

[38] D. O. Krimer, S. Putz, J. Majer, and S. Rotter, Phys. Rev. A **90**, 043852 (2014).

[39] A. G. Kofman and G. Kurizki, Phys. Rev. A **54**, R3750 (1996).

[40] M. Tavis and F. W. Cummings, Phys. Rev. **170**, 379 (1968).

[41] H. Primakoff and T. Holstein, Phys. Rev. **55**, 1218 (1939).

[42] D. O. Krimer, M. Liertzer, S. Rotter, and H. E. Türeci, Phys. Rev. A **89**, 033820 (2014).

# *Supporting Information*: Sustained photon pulse revivals from inhomogeneously broadened spin ensembles

**Dmitry O. Krimer[1,*], Matthias Zens[1], Stefan Putz[2,3], and Stefan Rotter[1]**

### Supplementary Note 1. Volterra equation for the cavity amplitude

Our starting point is the Hamiltonian (1) of the main article from which we derive the equations for the cavity and spin operators, $\dot{a} = i[\mathscr{H}, a]$, $\dot{\sigma}_k^{(\mu)(-)} = i[\mathscr{H}, \dot{\sigma}_k^{(\mu)(-)}]$, respectively. Here $a$ stands for the cavity operator and $\sigma_k^{(\mu)(-)}$ are standard Pauli operators associated with the $k$-th spin residing in the $\mu$-th ensemble. (All notations are in tact with those introduced in the main article.) During the derivations we use the following simplifications and approximations valid for various experimental realizations: (i) $kT \ll \hbar\omega_c$ (the energy of photons of the external bath is substantially smaller than that of cavity photons); (ii) the number of microwave photons in the cavity remains small as compared to the total number of spins participating in the coupling (limit of low input powers of an incoming signal), so that the Holstein-Primakoff-approximation, $\langle \sigma_k^{(\mu)(z)} \rangle \approx -1$, always holds; (iii) the effective collective coupling strength of each spin ensemble, $\Omega_\mu^2 = \sum_{k=1}^{N_\mu} g_k^{(\mu)2}$, satisfies to the inequality $\Omega_\mu \ll \omega_c$, justifying the rotating-wave approximation; (iv) the spatial size of the spin ensembles is sufficiently smaller than the wavelength of a cavity mode. Having introduced all these assumptions, we derive the following system of coupled first-order linear ordinary operator equations for the cavity and spin operators in $\omega_p = \omega_c$-rotating frame

$$\dot{a}(t) = -\kappa \cdot a(t) + \sum_{\mu=1}^{M} \sum_{k=1}^{N_\mu} g_k^{(\mu)} \sigma_k^{(\mu)(-)}(t) - \eta(t), \tag{1a}$$

$$\dot{\sigma}_k^{(\mu)(-)}(t) = -\left[\gamma + i(\omega_k^{(\mu)} - \omega_c)\right] \sigma_k^{(\mu)(-)}(t) - g_k^{(\mu)} a(t), \tag{1b}$$

where $\kappa$ and $\gamma$ are the total dissipative cavity and individual spin losses. By formally integrating the equations (1b) for the spin operators and inserting them into Eq. (1a) for the cavity operator, we get

$$\dot{a}(t) = -\kappa \cdot a(t) + \sum_{\mu=1}^{M} \sum_{k=1}^{N_\mu} g_k^{(\mu)} \sigma_k^{(\mu)(-)}(0) e^{-i\left(\omega_k^{(\mu)} - \omega_c - i\gamma\right)t} - \Omega^2 \int_0^\infty d\omega F(\omega) \int\limits_0^t d\tau e^{-i(\omega - \omega_c - i\gamma)(t-\tau)} a(\tau) - \eta(t),$$

---

[1] Institute for Theoretical Physics, Vienna University of Technology (TU Wien), Wiedner Hauptstraße 8-10/136, 1040 Vienna, Austria

[2] Vienna Center for Quantum Science and Technology, Atominstitut, Vienna University of Technology (TU Wien), Stadionallee 2, 1020 Vienna, Austria

[3] Department of Physics, Princeton University, Princeton, NJ 08544, USA

[*] Corresponding author: e-mail: dmitry.krimer@gmail.com

where $\sigma_k^{(\mu)(-)}(0)$ is the initial spin operator and $F(\omega)$ stands for the total spectral function which is defined as a sum over the spectral densities of each spin ensemble, $F(\omega) = \sum_{\mu=1}^{M} \Omega_\mu^2/\Omega^2 \cdot \rho_\mu(\omega)$. Here $\rho_\mu(\omega) = \sum_{k=1}^{N_\mu} g_k^{(\mu)2}\delta(\omega-\omega_k^{(i)})/\Omega_i^2$ describes the spin spectral density of the $\mu$-th ensemble, $\Omega_\mu = (\sum_{k=1}^{N_\mu} g_k^{(\mu)2})^{1/2}$ is its effective collective coupling strength to the cavity mode and $\Omega$ stands for the coupling strength of the central ensemble.

We then treat the problem semiclassically by introducing the cavity and spin expectation values, $A(t) = \langle a(t)\rangle$ and $B_k^{(\mu)}(t) = \langle \sigma_k^{(\mu)(-)}(t)\rangle$. For the sake of simplicity we consider the case when all spins are initially in the ground state, $B_k^{(\mu)}(0) = 0$, so that Eq. (2) reduces to the closed Volterra integro-differential equation for the cavity amplitude

$$\dot{A}(t) = -\kappa\cdot A(t) - \Omega^2\int_0^\infty d\omega F(\omega)\int_0^t d\tau e^{-i(\omega-\omega_c-i\gamma)(t-\tau)}A(\tau) - \eta(t). \tag{2}$$

Next we formally integrate Eq. (2) in time and simplify the resulting double integral on the right-hand side by means of the partial integration method. Assuming that the cavity is initially empty, $A(0) = 0$, we finally derive the following Volterra integral equation for the cavity amplitude

$$A(t) = \int_0^t d\tau \mathscr{K}(t-\tau)A(\tau) + \mathscr{D}(t), \tag{3}$$

where $\mathscr{K}(t-\tau)$ is the kernel function

$$\mathscr{K}(t-\tau) = \Omega^2 \int d\omega \frac{F(\omega)\left[e^{-i(\omega-\omega_c-i(\gamma-\kappa))(t-\tau)}-1\right]}{i(\omega-\omega_c-i(\gamma-\kappa))}\cdot e^{-\kappa(t-\tau)}, \tag{4}$$

and the function $\mathscr{D}(t)$ is given by

$$\mathscr{D}(t) = \int_0^t d\tau\, \eta(\tau)\cdot e^{-\kappa(t-\tau)}. \tag{5}$$

We solve then Eq. (3) numerically using the methods described in details in our recent publications [1,2].

### Supplementary Note 2. Single-photon dynamics

Here we prove that the probability for a single photon, which is populating the cavity at time $t = 0$, to stay inside the cavity at $t > 0$, reduces to $N(t) = |A(t)|^2$, where $A(t)$ is the solution of the Volterra equation (2) with the initial condition $A(0) = 1$ and $\eta(t) = 0$. By definition, this probability is nothing more than the expectation value of the number operator $\mathscr{N} = a^\dagger(t)a(t)$, i.e. $N(t) = \langle 1,\downarrow|a^\dagger(t)a(t)|1,\downarrow\rangle$. Taking into account that we deal with a single excitation in the system, we make use of the following closure relation,

$$\mathbb{1} = |0,\downarrow\rangle\langle 0,\downarrow| + \sum_l |0,\uparrow_l\rangle\langle 0,\uparrow_l| + |1,\downarrow\rangle\langle 1,\downarrow| + \sum_l |1,\uparrow_l\rangle\langle 1,\uparrow_l|, \tag{6}$$

where for the sake of notational simplicity the index $l$ enumerates all spins independently of the spin ensemble to which they belong to. We derive the following expression for $N(t)$

$$N(t) \equiv \langle 1,\downarrow|a^\dagger(t)\mathbb{1}a(t)|1,\downarrow\rangle = \tag{7}$$

$$|\langle 0,\downarrow|a(t)|1,\downarrow\rangle|^2 + |\langle 1,\downarrow|a(t)|1,\downarrow\rangle|^2 + \sum_l |\langle 0,\uparrow_l|a(t)|1,\downarrow\rangle|^2 + \sum_l |\langle 1,\uparrow_l|a(t)|1,\downarrow\rangle|^2.$$

We then let the operator equations (1a, 1b) from Supplementary Note 1 act on the bra- and ket-vectors which show up in Eq. (7) and derive four independent sets of coupled ODEs for the corresponding expectation values $\langle a(t)\rangle$ and $\langle\sigma_j^-(t)\rangle$.

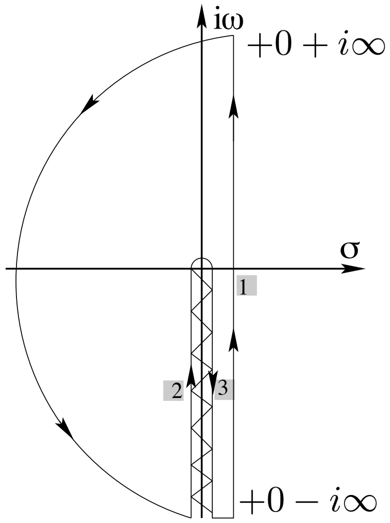

**S 1** Contour completion in the complex plane $s=\sigma+i\omega$ for the calculation of the inverse Laplace transform. Those contours which give nonzero contribution are designated by numbers. The zig-zag line corresponds to the branch cut along the negative part of the imaginary axis.

Remarkably, these sets of equations look formally the same being independent of the specific bra- or ket-vector appearing on the left or right side in these operator equations i.e. they evolve in the same fashion as the corresponding operators themselves. The only difference between the resulting solutions for the expectation values appearing in Eq. (7) stems from the initial conditions which are nonzero only for the first term in the r.h.s. of Eq. (7), namely $A(0)=\langle 0,\downarrow|a(0)|1,\downarrow\rangle=1$. For all other terms the resulting expectation values are zero at $t=0$, and as a consequence, they remain zero at $t>0$ as well. Therefore, the probability for a photon to reside in the cavity at $t>0$ reduces to $N(t)=|\langle 0,\downarrow|a(t)|1,\downarrow\rangle|^2=|A(t)|^2$, where $A(t)$ is exactly given as the solution of the Volterra equation (2) in Supplementary Note 1 with the initial conditions $A(0)=1$ and $B_l(0)=0$.

### Supplementary Note 3. Laplace transform of the Volterra equation

Here we sketch the derivation of the Laplace transformation of the Volterra equation (2) from Supplementary Note 1 assuming that all spins are initially in the ground state and the cavity mode $a$ contains initially a single photon, $A(0)=1$ (the case considered in Supplementary Note 2). For that purpose we multiply Eq. (2) by $e^{-st}$ ($s=\sigma+i\omega$ is the complex variable), integrate both sides of the equation with respect to time and finally obtain the following expression for the Laplace transform:

$$\tilde{A}(s)=\frac{1}{s+\kappa-\gamma+\Omega^2\int_0^\infty \dfrac{d\omega F(\omega)}{s+i(\omega-\omega_c)}}. \tag{8}$$

By performing the inverse Laplace transformation, $A(t)=(2\pi i)^{-1}\int_{\sigma-i\infty}^{\sigma+i\infty} ds\, e^{st}\tilde{A}(s)$ (see e.g. [3] for more details), we get the formal solution for the cavity amplitude $A(t)$ which is as follows

$$A(t)=\frac{e^{i(\omega_c-i\gamma)t}}{2\pi i}\int_{\sigma-i\infty}^{\sigma+i\infty}\frac{e^{st}ds}{s+\kappa-\gamma+i\omega_c+\Omega^2\int_0^\infty \dfrac{d\omega F(\omega)}{s+i\omega}}, \tag{9}$$

where $\sigma>0$ is chosen such that the real parts of all singularities of $\tilde{A}(s)$ are smaller than $\sigma$. It turned out that the integral in the denominator of Eq. (9) has a jump when passing across the negative part of the imaginary axis leading to the branch cut in the complex plane of $s$ (see Fig. 1). By setting the denominator of the integrand in Eq. (9) to zero, one can derive the

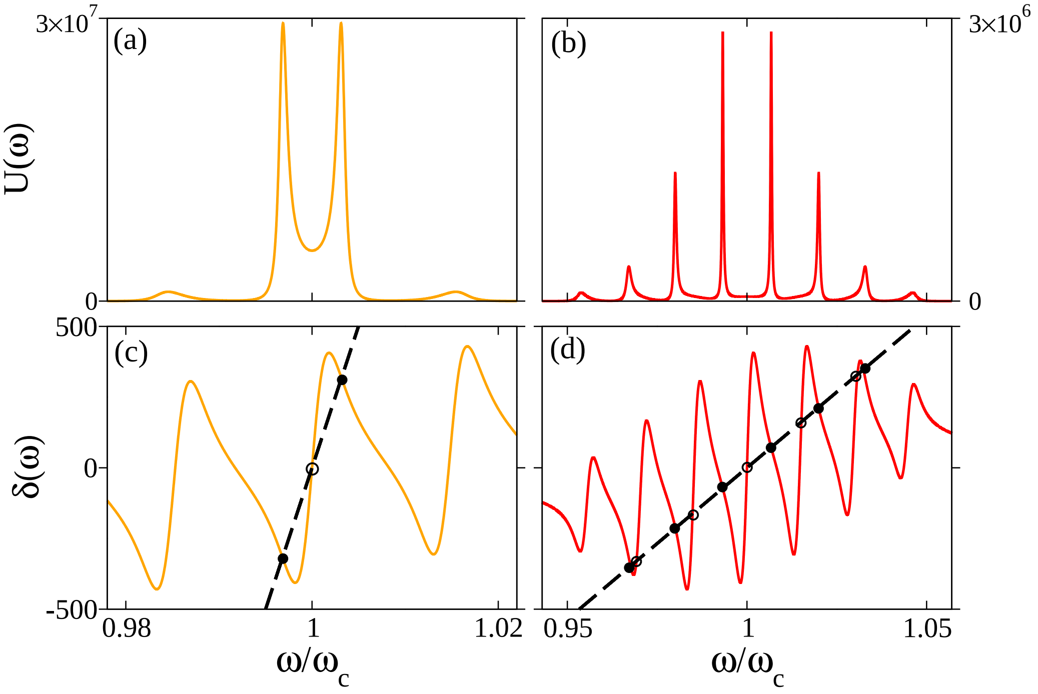

**S 2** Route from strong coupling to multimode strong coupling regime for two different coupling strengths, $\Omega/2\pi = 8\,\mathrm{MHz}$ (left column) and $\Omega/2\pi = 26\,\mathrm{MHz}$ (right column). *Upper row*: Kernel function $U(\omega)$. *Lower row*: Nonlinear Lamb shift $\delta(\omega)$ for the same $\omega$-interval as above (note the different zooms for the two columns). *Left column*: Strong coupling regime with a well-resolved Rabi splitting in $U(\omega)$ (regime of damped Rabi oscillations). *Right column*: Multimode strong coupling regime with a multi-peak structure in $U(\omega)$ when all seven spin ensembles are effectively coupled to the cavity (regime of revivals). Filled circles label resonance values $\omega_r$ of the kernel $U(\omega)$ occurring at the intersections between the Lamb shift $\delta(\omega)$ and the dashed line $(\omega-\omega_c)/\Omega^2$. At empty circles such intersections are non-resonant and do not lead to a corresponding peak in $U(\omega)$. The cavity frequency $\omega_c$ coincides with the mean frequency of the central $q$-Gaussian, $\omega_s = \omega_c$, shown in Fig. 1(a) of the main article.

equations for simple poles, $s_j = \sigma_j + i\omega_j$, which, however, do not appear for the spectral function shown in Fig. 1(a) of the main paper and will not be discussed here (see [2] for more details about poles' contribution).

Next, we apply Cauchy's theorem to a closed contour to evaluate the formal integral (9) taking into account that only a few paths of those shown in Fig. S1 contribute. Finally, we end up with the following expression for the cavity amplitude

$$A(t) = \Omega^2 \int_0^\infty d\omega e^{-i(\omega-\omega_c-i\gamma)t} U(\omega), \tag{10}$$

where

$$U(\omega) = \lim_{\sigma\to 0^+} \left\{ \frac{F(\omega)}{(\omega-\omega_c-\Omega^2\delta(\omega)+i(\kappa-\gamma))^2+(\pi\Omega^2F(\omega)+\sigma)^2} \right\}. \tag{11}$$

is the kernel function and

$$\delta(\omega) = \mathscr{P}\int_0^\infty \frac{d\tilde{\omega}F(\tilde{\omega})}{\omega-\tilde{\omega}} \tag{12}$$

has the meaning of the nonlinear Lamb shift of the cavity frequency $\omega_c$, which depends on the total spectral distribution, $F(\omega)$.

Obviously, the relevant frequency components contributing to the dynamics of $A(t)$ are those which are resonant in the kernel function $U(\omega)$. As it can be deduced from the structure of $U(\omega)$ given by Eq. (11), a necessary condition for such resonances to show up strongly depends on the structure of the Lamb shift and the value of the coupling strength. Namely, it is given by the following approximate formula, $(\omega_r - \omega_c)/\Omega^2 \approx \delta(\omega_r)$. At small values for the coupling strength $\Omega$ the straight line $(\omega_r - \omega_c)/\Omega^2$ becomes very steep and thus leads just to a single intersection with $\delta(\omega_r)$. As a result, a single resonance occurs at $\omega_r \approx \omega_c$, so that only the central spin ensemble contributes to the coupling with the cavity, whereas the others yield a negligible contribution. In this case the kernel function $U(\omega)$ can be well approximated by a Lorentzian centered around the slightly shifted cavity frequency $\omega_c + \Omega^2\delta(\omega_c)$. We will thus deal with the exponential decay of the cavity amplitude $A(t)$ in the time domain with a decay rate depending on $\Omega$. Actually this regime is very similar to the Purcell enhancement of the spontaneous emission rate of a single emitter inside a cavity [4]. As the coupling strength reaches a certain critical value, the straight line intersects the nonlinear Lamb shift at three points from which only two give rise to the resonances in $U(\omega)$. As a consequence, the kernel function $U(\omega)$ consists of two well-separated polaritonic peaks, which is the hallmark of the strong coupling regime of cavity QED (see the left column in Fig. S2). Note that these two resonances still reside in the vicinity of the cavity frequency and the contribution of all but the central ensemble is rather small.

The situation changes qualitatively at higher values of the coupling strength $\Omega$, when the straight line also intersects the other distant resonances of the Lamb shift, as is seen from the right column in Fig. S2. As a result, the kernel function $U(\omega)$ forms a comb-shaped structure with almost equally spaced polaritonic peaks at frequencies which are shifted with respect to the resonances of the spectral function $F(\omega)$. It is worth noting, that such a communication of the cavity mode with distant resonances of $F(\omega)$ would never take place if the Lamb shift were approximated by its value at the cavity frequency, $\delta(\omega_c)$.

### Supplementary Note 4. Eigenvalue problem

To solve the eigenvalue problem we first discretize the spectral function $F(\omega)$ (see Fig. 1 in the main article) by performing the following transformation:

$$g_l = \left[ F(\omega_l) \cdot (\sum_{\mu=1}^{M} \Omega_\mu^2) / \sum_m F(\omega_m) \right]^{1/2}. \tag{13}$$

Since in total we deal with a sizeable number of spins, we make our problem numerically tractable by dividing spins into many subgroups with approximately the same coupling strengths, so that $g_l$ in Eq. (13) represents a coupling strength within each subgroup rather than an individual coupling strength. Note also that once a shape of the spectral function $F(\omega)$ is defined, it is not relevant anymore to which ensemble an individual spin belongs to. By doing so we get the following linear set of first-order ODEs with respect to the cavity and spin amplitudes from Eqs. (1a,1b) ($\eta(t) = 0$)

$$\dot{A}(t) = -\kappa \cdot A(t) + \sum_l g_l B_l(t) \tag{14a}$$

$$\dot{B}_l(t) = -\left[\gamma + i(\omega_l - \omega_c)\right] B_l(t) - g_l A(t), \tag{14b}$$

where $A(t) \equiv \langle a(t) \rangle$ and $B_l(t) \equiv \langle \sigma_l^-(t) \rangle$. After substituting $A(t) = A \cdot \exp(-\lambda t)$ and $B_l(t) = B_l \cdot \exp(-\lambda t)$ into Eqs. (14a, 14b), we derive the complex eigenvalue problem for $\lambda$, which can be represented as, $\mathscr{L}\psi = \lambda\psi$, where

$$\mathscr{L} = \begin{pmatrix} \kappa & -g_1 & -g_2 & ... & -g_N \\ g_1 & \gamma + i(\omega_1 - \omega_c) & 0 & ... & 0 \\ g_2 & 0 & \gamma + i(\omega_2 - \omega_c) & ... & 0 \\ ... & ... & ... & ... & ... \\ g_N & 0 & 0 & ... & \gamma + i(\omega_N - \omega_c) \end{pmatrix},$$

and $\psi = (A \;\; B_1 \;\; B_2 \, ... \, B_N)^T$.

## References

[1] S. Putz, D. O. Krimer, R. Amsüss, A. Valookaran, T. Nöbauer, J. Schmiedmayer, S. Rotter, and J. Majer, Nature Physics **10**, 720 (2014).

[2] D. O. Krimer, S. Putz, J. Majer, and S. Rotter, Phys. Rev. A **90**, 043852 (2014).

[3] K. F. Riley, M. P. Hobson and S. J. Bence, *Mathematical methods for physics and engineering*, Cambridge University Press (2006).

[4] E. M. Purcell, Phys. Rev. **69**, 681 (1946).

PHYSICAL REVIEW A **96**, 043837 (2017)

# Optimal control of non-Markovian dynamics in a single-mode cavity strongly coupled to an inhomogeneously broadened spin ensemble

Dmitry O. Krimer,[1,*] Benedikt Hartl,[1] Florian Mintert,[2] and Stefan Rotter[1]

[1] *Institute for Theoretical Physics, Vienna University of Technology (TU Wien), 1040 Vienna, Austria, EU*

[2] *Department of Physics, Imperial College, SW7 2AZ London, United Kingdom, EU*

(Received 22 January 2017; published 16 October 2017)

Ensembles of quantum-mechanical spins offer a promising platform for quantum memories, but proper functionality requires accurate control of unavoidable system imperfections. We present an efficient control scheme for a spin ensemble strongly coupled to a single-mode cavity based on a set of Volterra equations relying solely on weak classical control pulses. The viability of our approach is demonstrated in terms of explicit storage and readout sequences that will serve as a starting point towards the realization of more demanding full quantum-mechanical optimal control schemes.

DOI: 10.1103/PhysRevA.96.043837

## I. INTRODUCTION

In the past decade we have witnessed tremendous progress in the implementation of elementary operations for quantum information processing. Single-qubit gates can be realized with fidelities reaching 1–$10^{-6}$ [1] and also two-qubit gates can be implemented in a variety of systems [2,3]. With all these elements at hand, it is nowadays possible to implement quantum algorithms on architectures with a few qubits (on the order of five) [4] and to engineer quantum metamaterials based on an ensemble of superconducting qubits coupled to a microwave cavity [5,6]. Implementing quantum logics on larger architectures, however, will most likely require a separation between quantum processing units and quantum memory units, where qubits in the former units admit fast gate operations and the qubits in the latter units offer long coherence times.

Since extended coherence times naturally imply weak interactions with other degrees of freedom, the sufficiently fast swapping of quantum information between processing and memory units is a challenging task. The most promising route to overcome slow swapping is the encoding of quantum information as a collective excitation in a large ensemble composed of many ($N$) constituents, since this increases the swapping speed by a factor of $\sqrt{N}$. Among promising realizations of such ensembles, those based on spins, atoms, ions, or molecules are of particular interest [7–13]. In many cases, however, system imperfections result in broadening effects giving rise to rapid dephasing of ensemble constituents, a restriction that limits the coherence times of such collective quantum memories.

As a result, various protocols to ensure the controlled and reversible temporal dynamics in the presence of inhomogeneous broadening were recently the subject of many studies. One of the proposed techniques in this context is the so-called controlled reversible inhomogeneous broadening approach [14–16], which is based on a rather subtle preparation method and on the inversion of atomic detunings during the temporal evolution. Most of the techniques developed for this purpose are based on photon-echo-type approaches in cavity or cavityless setups, such as those dealing with spin refocusing [17,18], with atomic frequency combs [19–24], or with electromagnetically induced transparency [25]. Traditionally, these architectures operate in the optical region and require additional high-intensity control fields. The resulting large number of excitations is prone to spoil the delicate quantum information that is encoded in states with extremely low numbers of excitations. It would therefore be much better to work with low-intensity control fields, which, however, have the other problem to become easily correlated with the quantum memory. For the identification of control strategies, this implies that one may no longer treat the many different memory spins as independent objects, but that the (macroscopically) large ensemble needs to be described by a quantum many-body state. This makes any description of dynamics and an identification of control strategies a seemingly hopeless task.

In this paper we develop a very efficient semiclassical optimization technique based on a set of Volterra integral equations, which allows us to write information into a large, inhomogeneously broadened spin ensemble coupled to a single-cavity mode by means of optimized classical microwave pulses and to retrieve it at some later time in the form of well-separated cavity responses. In contrast to established echo techniques, our scheme only involves low-intensity signals and therefore diminishes the influence of noise caused by writing and reading pulses. The applicability of our approach is also demonstrated in conjunction with a spectral hole-burning technique [26–28] that allows us to reach storage times going far beyond the dephasing time of the inhomogeneously broadened ensemble. Importantly, the Volterra equation exactly governs the resulting linear non-Markovian dynamics not only in the semiclassical but also in the pure quantum case for the particular situation without external drive, when all spins are initially in the ground state and the cavity contains initially a single photon [26,28,29]. Furthermore, the system's density function or nonequilibirum Green's functions, which show up in the framework of a full quantum-mechanical description, also satisfy mathematically similar integro-differential Volterra equations [30,31]. Hence, although the problem is treated semiclassically in what follows, we believe that our approach can be generalized to pure quantum regimes as well in which case the inclusion of the

---

[*] dmitry.krimer@gmail.com

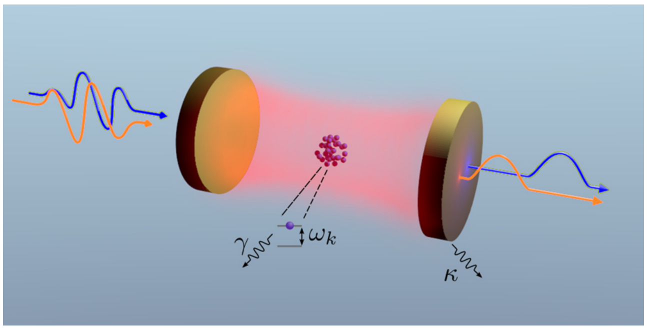

FIG. 1. Schematics of a single-mode cavity characterized by a frequency $\omega_c$ and a loss rate $\kappa$, coupled to an ensemble of two-level atoms (spheres) with transition frequencies $\omega_k$ and a loss rate $\gamma \ll \kappa$. Curves designate optimized input and (nonoverlapping) output signals.

transient two-time correlation function of the cavity operator between the write and the readout may be needed, an issue that will be postponed for future studies.

## II. THEORETICAL MODEL

To be specific, we consider an ensemble of spins strongly coupled to a single-mode cavity via magnetic or electric dipole interaction as sketched in Fig. 1. All typical parameter values are chosen here in accordance with the recent experiment [29], the dynamics of which can be excellently described by the Tavis-Cummings Hamiltonian [32] (in units of $\hbar$)

$$\mathcal{H} = \omega_c a^\dagger a + \frac{1}{2}\sum\nolimits_j^N \omega_j \sigma_j^z + i\sum\nolimits_j^N [g_j \sigma_j^- a^\dagger - g_j^* \sigma_j^+ a] \\ - i[\eta(t) a^\dagger e^{-i\omega_p t} - \eta(t)^* a e^{i\omega_p t}]. \quad (1)$$

Here $\sigma_j^\pm$ and $\sigma_j^z$ are the Pauli operators associated with each individual spin of frequency $\omega_j$ and $a^\dagger$ and $a$ are creation and annihilation operators of the single cavity mode with frequency $\omega_c$. An incoming signal is characterized by the carrier frequency $\omega_p$ and by the envelope $\eta(t)$. The interaction part of $\mathcal{H}$ is written in the dipole and rotating-wave approximation (terms proportional to $a\sigma_j^-$ and $a^\dagger\sigma_j^+$ are neglected), where $g_j$ is the coupling strength of the $j$th spin. The distance between spins is assumed to be large enough such that the direct dipole-dipole interactions between spins can be neglected. Furthermore, the large number of spins allows us to enter the strong-coupling regime of cavity QED with the collective coupling strength $\Omega = (\sum_j^N g_j^2)^{1/2}$ [33], which leads to the enhancement of a single coupling strength $g_j$ by a factor of $\sqrt{N}$ ($N \approx 10^{12}$ in [29]).

We are aiming at the transfer of information from the cavity to the spin ensemble, its storage over a well-defined period of time, and its transfer back to the cavity. Our control scheme thus consists of a write and readout section, with a variable delay section in between. Starting from a polarized state with all spins in their ground state, we construct (i) two write pulses $\eta_{|0\rangle}^{(W)}(t)$ and $\eta_{|1\rangle}^{(W)}(t)$ that encode the respective logical states $|0\rangle$ and $|1\rangle$ in the spin ensemble. During the delay section (ii) the information is subject to dephasing by the inhomogeneous ensemble broadening and the external drive is optimized here to reduce the cavity amplitude $A(t) \equiv \langle a(t)\rangle$ (to prevent the information in the spin ensemble from leaking back to the cavity prematurely). In the readout section (iii) we switch on the readout pulse $\eta^{(R)}(t)$ [with substantially lower power than $\eta_{|0/1\rangle}^{(W)}(t)$] that maps the two logical states of the spin ensemble on two mutually orthogonal states of the cavity field, expressed by the cavity amplitude $A_{|0\rangle}^{(R)}(t)$ or $A_{|1\rangle}^{(R)}(t)$, respectively. Note that the write pulses (i) are specific for the input states $|0\rangle$ and $|1\rangle$, but pulses (ii) and (iii) are generic as they are designed without prior knowledge of the information stored in the ensemble. [For the sake of simplicity we formally absorb the delay pulse into $\eta^{(R)}(t)$.] The goal of our work is to find optimal time-dependent choices for $\eta_{|0\rangle}^{(W)}(t)$, $\eta_{|1\rangle}^{(W)}(t)$, and $\eta^{(R)}(t)$ such that $A_{|0\rangle}^{(R)}(t)$ and $A_{|1\rangle}^{(R)}(t)$ have minimal temporal overlap in analogy to time-binned qubits where information is stored in the occupation amplitudes of two well-distinguishable time bins [20,34].

We describe the dynamics by deriving the equations for the spin and cavity expectation values $\langle\sigma_k^-(t)\rangle$ and $A(t)$ under the Holstein-Primakoff-approximation [35] ($\langle\sigma_k^{(z)}\rangle \approx -1$) valid in the regime of weak driving powers (the number of the excited spins is always small compared to the ensemble size). This allows us to formally express $\langle\sigma_k^-(t)\rangle$ as a time integral with respect to $A(t)$ and to develop an efficient framework in terms of Volterra equations that relate cavity amplitudes $A(t)$ and pump profiles $\eta(t)$ [36],

$$A(t) = \int_0^t d\tau\, \mathcal{K}(t-\tau)A(\tau) + \mathcal{D}(t), \quad (2)$$

where $\mathcal{D}(t)$ depends on the time integral of the driving signal and on the initial conditions for the cavity amplitude as well as of the spin ensemble. The memory kernel function $\mathcal{K}(t-\tau)$, which is responsible for the non-Markovian feedback of the spin ensemble on the cavity, is proportional to the collective coupling strength $\Omega^2$ and explicitly depends on a spectral spin distribution characterized by a function $\rho(\omega)$ (see Appendix A). When switching on a constant drive, the system exhibits damped oscillations characterized by the Rabi frequency $\Omega_R \approx 2\Omega$ and the total decoherence rate $\Gamma$ mostly determined by the dephasing caused by the inhomogeneous broadening of the spin ensemble [36].

A consequence of the linearity of the governing Volterra equations is that for two pump profiles $\eta_{1/2}(t)$, resulting in the two cavity amplitudes $A_{1/2}(t)$, any coherent superposition of these pulses $c_1\eta_1(t) + c_2\eta_2(t)$ will result in the corresponding cavity amplitudes $c_1 A_1(t) + c_2 A_2(t)$.

The Volterra equation for the cavity amplitude is physically the classical correspondence of the Heisenberg cavity spin equations on the level of expectation averages after elimination of the spin ensemble variables (see Appendix A). However, as was demonstrated in [26,29,37], the Volterra equation also governs quantum spin–cavity dynamics for the particular case when all spins are initially in the ground state and the cavity contains initially a single photon. Therefore, we take the amplitude of the write pulses $\eta_{|0/1\rangle}^{(W)}(t)$ such that the net power injected into the cavity corresponds to the power of a coherent driving signal with an amplitude equal to the cavity decay rate $\kappa$. The latter prepares on average a single photon in the empty cavity for stationary transmission experiments (see

Appendix D for details). Due to the linearity of the Volterra equations, also rescaling their solutions by a global prefactor leaves them perfectly valid.

## III. OPTIMAL CONTROL SCHEME

As a first step we need to find optimal write and readout pulses that prepare the logical spin ensemble configurations $|0\rangle$ and $|1\rangle$ and map them onto well-distinguishable cavity responses. We do this through the optimization of a functional, which ensures the minimal overlap between the cavity amplitudes $A^{(R)}_{|0\rangle}(t)$ and $A^{(R)}_{|1\rangle}(t)$ of the logical states $|0\rangle$ and $|1\rangle$ in the readout section by exploring various temporal shapes of both the write pulses $\eta^{(W)}_{|0/1\rangle}(t)$ and of the readout pulse $\eta^{(R)}(t)$. In practice we expand all involved driving pulses in a basis of trial functions $\sin(n\omega_f t)$ $(n = 1,2,\ldots)$ with the fundamental frequency $\omega_f$ defined as the inverse of the time duration of the write or readout section counted in multiples of half the Rabi period $\pi/\Omega_R$. Next we construct the functional defined as the time-overlap integral between $A^{(R)}_{|0\rangle}(t)$ and $A^{(R)}_{|1\rangle}(t)$ in the readout section. We then search the functional's minima under several constraints considering the expansion coefficients as unknown variables using the standard method of Lagrange multipliers (see Appendixes A and B). Due to the linearity of governing equations with respect to the control pulses this procedure, as shown in Appendix B, is numerically highly efficient since the time integration of the Volterra equations can be performed independently of the subsequent optimization of the expansion coefficients of the control pulses.

A typical result of this optimization (first without a delay section) is depicted in Fig. 2 (left column), where the amplitudes of all optimized pulses as well as those of the resulting cavity responses are depicted. One can indeed see that the two different configurations stored in the spin ensemble, $|0\rangle$ and $|1\rangle$, are retrieved by the same readout pulse in the form of two well-separated cavity responses. The storage efficiency can be quantified in terms of the ratio of integrated cavity amplitudes during the readout and write section, which turns out to be $\approx 40\%$ for the configurations $|0\rangle$ and $|1\rangle$ shown in Fig. 2 (left column).

The bottleneck for extended information storage times in the ensemble is its inhomogeneous broadening, as determined by the continuous spectral density $\rho(\omega)$ appearing in our theoretical description. Specifically, the total decoherence rate in the limit of strong coupling (when $\Omega > \Gamma$) can be estimated as $\Gamma \approx \kappa + \pi\Omega^2\rho(\omega_s \pm \Omega)$ [36,37], indicating that the dominant contribution to $\Gamma$ stems from the spectral density $\rho(\omega)$ at frequencies close to the maxima of the two polaritonic peaks $\omega = \omega_s \pm \Omega$. To suppress this decoherence rate $\Gamma$ it is thus advisable to work with spin ensembles having a spectral density that falls off faster than $1/\Omega^2$ in its tails such that $\Gamma \to \kappa$ for large $\Omega$. The corresponding cavity protection effect [36–38] has meanwhile been demonstrated also experimentally [29], but has the drawback of requiring prohibitively large coupling strengths to take full effect. Alternatively, one can burn two narrow spectral holes at frequencies close to $\omega_s \pm \Omega$, during a preparatory step for $t \leqslant 0$. This technique [26–28] was recently shown to be both easily implementable and very efficient in suppressing the decoherence rate $\Gamma$ even below the bare cavity decay rate $\kappa$ [27]. Incorporating this hole-burning protocol in the present analysis allows us to increase the dephasing time from $1/\Gamma \sim 75$ ns [the case shown in Fig. 2 (left column)] to microsecond time scales [see Fig. 2 (right column)] for which we can now meaningfully introduce a delay section in between the write and the readout section. In Fig. 2 (right column) we show that with parameters taken from recent experiments [27] we can extend the storage time and thereby our method's temporal range of control beyond 1 $\mu$s. Evidently, such an extension of the storage time comes with a reduced efficiency, which is here as large as 5%.

With these long coherence times we can now proceed to the main goal of storing coherent superpositions of the two spin configurations $|0/1\rangle$. Those can be created by the corresponding superposition $\eta^{(W)}(t) = \alpha\eta^{(W)}_{|0\rangle}(t) + \beta\eta^{(W)}_{|1\rangle}(t)$ of the respective write pulses and, ideally, the corresponding superposition of time-binned cavity responses would be observed under the application of the readout pulse $\eta^{(R)}(t)$. Since the cavity response is of the form $A^{(R)}(t;\alpha,\beta) = \alpha\tilde{A}^{(R)}_{|0\rangle}(t) + \beta\tilde{A}^{(R)}_{|1\rangle}(t) + \tilde{A}^{(R)}(t)$, where the two cavity responses $\tilde{A}^{(R)}_{|0/1\rangle}(t)$ only depend on the stored spin configurations $|0/1\rangle$ and $\tilde{A}^{(R)}(t)$ is the response induced by the readout pulse, the desired superposition of cavity outputs is obtained if the readout pulse satisfies $(\alpha + \beta)\eta^{(R)}(t) = \eta^{(R)}(t)$ (see Appendix B). Together with the normalization $|\alpha|^2 + |\beta|^2 = 1$, this implies that for the amplitudes $\alpha_x = 1 - x \pm i\sqrt{x(1-x)}$ and $\beta_x = x \mp i\sqrt{x(1-x)}$ with $x \in [0,1]$ the desired cavity response will be obtained. As a result, the proposed storage sequence works not only for the two logical basis states $|0/1\rangle$, but, indeed for a one-dimensional set of coherent superpositions, such as for a rebit [34,39].

Note that when being only interested in reading out the parameters $\alpha$ and $\beta$ (and not in further processing the resulting cavity response) one is not restricted by the above rebit parametrization, but has the full qubit parameter space at one's disposal. As we show in Appendix B, $\alpha$ and $\beta$ can be unambiguously determined through the time-overlap integrals defined only in the readout section $[\tau_a,\tau_c]$ as $\mathcal{O}_{0/1} = \int_{\tau_a}^{\tau_c} dt\, A^{(R)}(t;\alpha,\beta)A^{(R)*}_{|0/1\rangle}(t)$, where $A^{(R)}_{|0/1\rangle}(t) = \tilde{A}^{(R)}_{|0/1\rangle}(t) + \tilde{A}^{(R)}(t)$.

In principle, this information retrieval is exact, but noise (which is not included in the previous theoretical modeling) affects the readout if it reaches values comparable to the cavity amplitudes. Therefore, in the next line of our study we examine the robustness of our optimal control scheme against possible noise. For that purpose, we subject the previously established optimized pulses $\eta^{(W)}_{|0/1\rangle}(t)$ and $\eta^{(R)}(t)$ to a small perturbation by adding Gaussian white noise as an additional driving term in our Volterra equations (see Appendix C). We treat the problem numerically using well-established methods for integrating stochastic differential equations (see, e.g., [40]) and accumulate statistics by evaluating many trajectories for different noise realizations. We then average the resulting retrieved values with respect to noise realizations and calculate the absolute retrieval errors as the deviation from the input configuration, $\epsilon_\alpha = |\alpha - \langle\alpha_{\mathcal{R}}\rangle|$ and $\epsilon_\beta = |\beta - \langle\beta_{\mathcal{R}}\rangle|$. The typical results of our calculations are displayed in Fig. 3. It turns out that $\epsilon_\alpha$ and $\epsilon_\beta$ scale approximately linearly with the noise amplitude and, e.g., the maximal absolute error

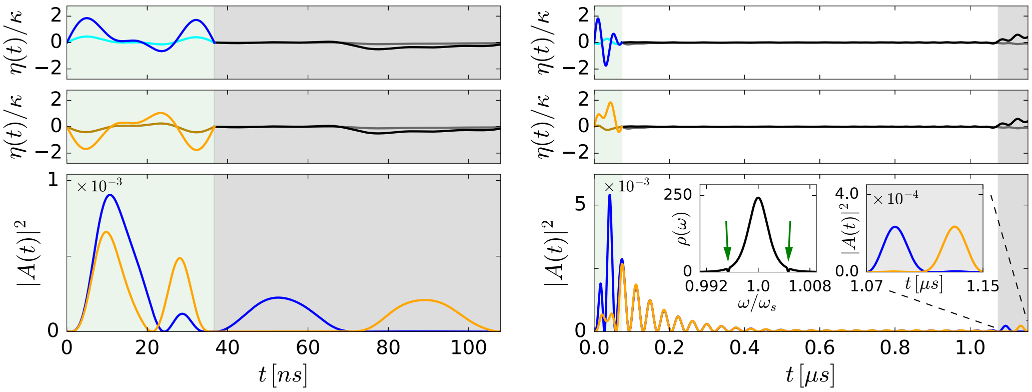

FIG. 2. Preparation of the spin ensemble configurations $|0\rangle$ and $|1\rangle$ for a spin density $\rho(\omega) = C[1-(1-q)(\omega-\omega_s)^2/\Delta^2]^{1/(1-q)}$ following a $q$-Gaussian distribution with $q = 1.39$ centered around the cavity frequency $\omega_s = \omega_c$ and a full width at half maximum $\gamma_q = 2\Delta\sqrt{(2^q-2)/(2q-2)} = 2\pi \times 9.4$ MHz. This form for $\rho(\omega)$ was established in our previous studies by a careful comparison with the experiment [29,36]. The right column shows that two holes were burnt into $\rho(\omega)$ at frequencies $\omega_s \pm \Omega$ (two arrows in the inset) to suppress decoherence [26,27] and to make room for a delay section (white area) between the write [green area (light gray)] and readout (gray area) sections. [In the inset $\rho(\omega)$ is plotted in units of $\omega_s^{-1}$.] The top and middle rows show real [blue (dark gray) and orange (light gray), respectively] and imaginary parts [cyan (light gray) and brown (dark gray), respectively] of the optimized write pulse $\eta^{(W)}_{|0/1\rangle}(t)$ for state $|0/1\rangle$ and of the generic readout pulse $\eta^{(R)}(t)$ (black and gray). The bottom row shows the cavity probability amplitude squared $|A(t)|^2$ for the resulting nonoverlapping cavity responses $A^{(R)}_{|0\rangle}(t)$ [blue (dark gray)] and $A^{(R)}_{|1\rangle}(t)$ [orange (light gray)]. The carrier frequency of all pulses $\omega_p = \omega_c = 2\pi \times 2.6915$ GHz and the coupling strength $\Omega/2\pi = 12.5$ MHz. The ratio of the powers between the readout and write pulses is 0.068 (0.013) for the case without (with) hole burning. The amplitudes of all pulses (top and middle rows) are presented in units of $\kappa/2\pi = 0.4$ MHz.

of retrieval shown in Fig. 3 is at most 0.02 for 200 noise realizations when taking the noise amplitude to be 5% of the incoming amplitude of the write pulse. These results confirm the robustness of our approach with respect to possible noise in a real physical system.

## IV. CONCLUSION AND OUTLOOK

We have presented a very efficient optimization technique applicable to different experimental realizations based on an inhomogeneously broadened spin ensemble coupled to a single cavity mode. Generalizing this scheme to the full quantum-mechanical level is the obvious next step to make our protocol an essential building block for the development of future optimal control schemes with the perspective of advancing the storage capabilities for quantum information. Given the extremely unfavorable scaling properties of composite quantum systems with particle number, any theoretical description of a quantum many-body system is an extremely challenging task. Since the identification of optimal control strategies is much harder than the mere description of a system's dynamics (the latter is naturally required for the former), optimal control is typically a viable option for rather small systems only. With our highly efficient semiclassical control technique for the non-Markovian dynamics of large hybrid quantum systems in the presence of inhomogeneous broadening, we demonstrate the capabilities and limitations of these systems for potential information storage.

## ACKNOWLEDGMENTS

We would like to thank H. Dhar and M. Zens for helpful discussions and acknowledge support by the Austrian Science Fund (FWF) through Project No. F49-P10 (SFB NextLite). F.M. acknowledges support from the European Research Council grant "odycquent."

D.O.K. and B.H. contributed equally to this work.

## APPENDIX A: VOLTERRA EQUATION FOR THE CAVITY AMPLITUDE

Our starting point is the Hamiltonian (1) of the main text from which we derive the Heisenberg equations for the cavity and spin operators $\dot{a}(t) = i[\mathcal{H}, a(t)] - \kappa a(t)$ and $\dot{\sigma}_k^-(t) = i[\mathcal{H}, \dot{\sigma}_k^-(t)] - \gamma\sigma_k^-(t)$, respectively. Here $a$ stands for the cavity annihilation operator and $\sigma_k^-$ are standard downward Pauli operators associated with the $k$th spin; $\kappa$ and $\gamma$ are the dissipative cavity and individual spin losses, respectively. (All notation is consistent with that introduced in the main text.) During the derivations we use the following simplifications and approximations valid for various experimental realizations: (i) $k_B T \ll \hbar\omega_c$ (the energy of photons of the external bath $k_B T$ is substantially smaller than that of cavity photons $\hbar\omega_c$); (ii) the number of microwave photons in the cavity remains small as compared to the total number of spins participating in the coupling (limit of low input powers of an incoming signal), so the Holstein-Primakoff-approximation $\langle\sigma_k^{(z)}\rangle \approx -1$ always holds; (iii) the effective collective coupling strength of the spin ensemble $\Omega^2 = \sum_{k=1}^N g_k^2$ ($g_k$ stands for the coupling strength of the $k$th spin) satisfies the inequality $\Omega \ll \omega_c$, justifying the rotating-wave approximation; (iv) the spatial size of the spin ensemble is sufficiently smaller than the wavelength of a cavity mode. Having introduced all these assumptions, we derive the following system of coupled first-order linear ordinary differential equations for the cavity and spin amplitudes in the

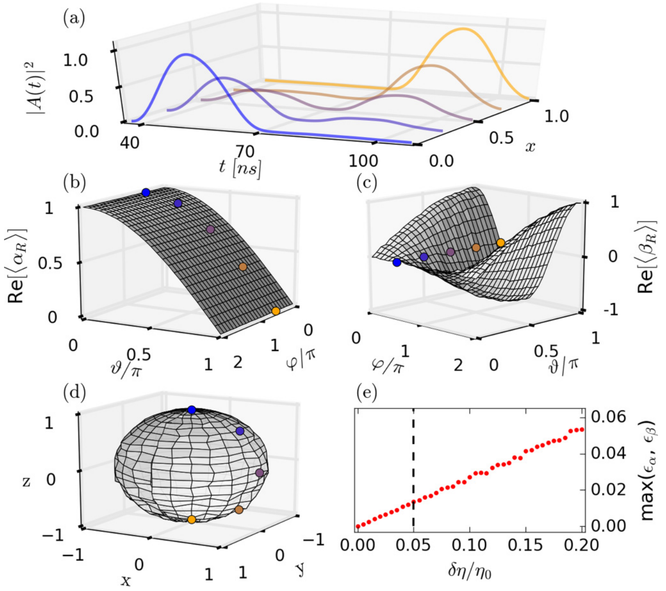

FIG. 3. (a) Retrieved cavity amplitude in the readout section, resulting from a superposition of write pulses $\alpha_x A^{(R)}_{|0\rangle}(t) + \beta_x A^{(R)}_{|1\rangle}(t)$ (normalized to a maximum value of 1) in the absence of noise with the write amplitude $\eta_0 = \kappa$. We used the rebit parametrization $\alpha_x$ and $\beta_x$ (see the text) from $x = 0$ to 1 in steps of 0.25 (with the same parameters as in Fig. 2, left column). Also shown are the retrieved average values (b) $\langle\alpha_R\rangle$ and (c) $\langle\beta_R\rangle$ (only real parts are shown) from the resulting solution $A^{(R)}(t;\alpha,\beta)$ in the presence of noise. The averaging is performed with respect to 200 noise realizations for a noise amplitude $\delta\eta/\eta_0 = 0.05$. The input configurations are parametrized as $\alpha = \cos(\vartheta/2)$ and $\beta = \sin(\vartheta/2)e^{i\varphi}$ with $\vartheta \in [0,\pi]$ and $\varphi \in [0,2\pi]$. (d) Reconstructed Bloch sphere with spatial components $r_i = (\langle\alpha_R\rangle^*,\langle\beta_R\rangle^*)\sigma_i(\langle\alpha_R\rangle,\langle\beta_R\rangle)$ for $i = x,y,z$, evaluated from the retrieved averaged parameters taken from (b) and (c), where $\sigma_i$ is the $i$th Pauli matrix. The symbols in (b)–(d) emphasize the rebit encoding from (a). The reference configurations $|0/1\rangle$ are taken from the left column of Fig. 2. (e) Maximum of the absolute errors $\epsilon_\alpha = |\alpha - \langle\alpha_R\rangle|$ and $\epsilon_\beta = |\beta - \langle\beta_R\rangle|$ in retrieval of the input configurations for different noise amplitudes $\delta\eta$. Vertical dashed line shows the noise level of the calculations in (b)–(d).

$\omega_p$-rotating frame:

$$\dot{A}(t) = -[\kappa + i\Delta_c]A(t) + \sum_{k=1}^{N} g_k B_k(t) - \eta(t), \qquad \text{(A1)}$$

$$\dot{B}_k(t) = -[\gamma + i\Delta_k]B_k(t) - g_k A(t), \qquad \text{(A2)}$$

where $A(t) \equiv \langle a(t)\rangle$ and $B_k(t) \equiv \langle\sigma_k^-(t)\rangle$. In addition, $\Delta_c = \omega_c - \omega_p$ and $\Delta_k = \omega_k - \omega_p$ are the detunings with respect to the probe frequency $\omega_p$.

By formally integrating Eq. (A2) with respect to time for the spin operators and inserting them into Eq. (A1) for the cavity operator, we get

$$\begin{aligned}\dot{A}(t) = {}& -[\kappa + i\Delta_c]A(t) + \sum_{k=1}^{N} g_k B_k(T_1)\, e^{-[\gamma+i\Delta_k](t-T_1)} \\ & - \Omega^2 \int_0^\infty d\omega\, \rho(\omega) \int_{T_1}^{t} d\tau\, A(\tau) e^{-[\gamma+i\Delta_\omega](t-\tau)} - \eta(t),\end{aligned} \qquad \text{(A3)}$$

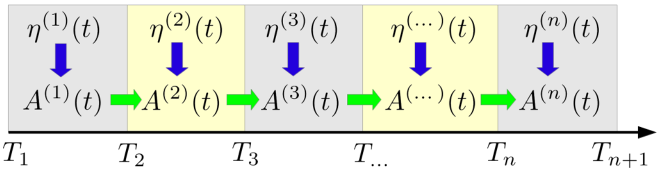

FIG. 4. Schematics of the time divisions of the cavity amplitude $A^{(n)}(t)$. The input field $\eta^{(n)}(t)$ is applied to the system in the time interval $[T_n,T_{n+1}]$ and drives the corresponding cavity amplitude $A^{(n)}(t)$ (indicated by vertical arrows). The non-Markovian contributions from previous time intervals $[T_{n-1},T_n]$ are indicated by horizontal arrows.

where $\Delta_\omega = \omega - \omega_p$, $B_k(T_1)$ is the initial spin amplitude at $t = T_1$, and $\rho(\omega) = \sum_{k=1}^{N} g_k^2 \delta(\omega - \omega_k)/\Omega^2$ stands for the continuous spectral spin distribution. As in our previous studies [29,36], we take into account the effect of an inhomogeneous broadening by modeling the spin density with a $q$-Gaussian shape $\rho(\omega) = C[1 - (1 - q)(\omega - \omega_s)^2/\Delta^2]^{1/(1-q)}$, distributed around the mean frequency $\omega_s/2\pi = 2.6915$ GHz with the parameter $q = 1.39$ and a full width at half maximum $\gamma_q/2\pi = 9.4$ MHz, where $\gamma_q = 2\Delta\sqrt{(2^q - 2)/(2q - 2)}$.

Next we formally integrate Eq. (A3) in time and simplify the resulting double integral on the right-hand side by partial integration. We also consider the case when the cavity is initially empty $A(T_1) = 0$ and all spins are in the ground state $B_k(T_1) = 0$. To speed up our numerical calculations and to separate different time sections from each other (see the main text and Appendix B for details), we divide the whole time integration into successive subintervals $T_n \leqslant t \leqslant T_{n+1}$, with $n = 1,2,\dots$ (see Fig. 4). This allows us to derive the recurrence relation for the cavity amplitude for the $n$th time interval $A^{(n)}(t)$, which depends on all previous events at $t < T_n$. Finally, we end up with the expression for $A^{(n)}(t)$,

$$A^{(n)}(t) = \int_{T_n}^{t} d\tau\, \mathcal{K}(t-\tau)A^{(n)}(\tau) + \mathcal{D}^{(n)}(t) + \mathcal{F}^{(n)}(t), \qquad \text{(A4)}$$

where the non-Markovian feedback within the $n$th time interval is provided by the kernel function $\mathcal{K}(t - \tau)$,

$$\mathcal{K}(t-\tau) = \Omega^2 \int_0^\infty d\omega\, \rho(\omega) \frac{e^{-[\gamma+i\Delta_\omega](t-\tau)} - e^{[\kappa+i\Delta_c](t-\tau)}}{[\gamma + i\Delta_\omega] - [\kappa + i\Delta_c]}. \qquad \text{(A5)}$$

The driving term $\mathcal{D}^{(n)}(t)$ in Eq. (A4),

$$\mathcal{D}^{(n)}(t) = -\int_{T_n}^{t} d\tau\, \eta^{(n)}(\tau) e^{-[\kappa+i\Delta_c](t-\tau)}, \qquad \text{(A6)}$$

includes an arbitrarily shaped, weak incoming pulse $\eta^{(n)}(t)$, defined in the time interval $[T_n,T_{n+1}]$. The memory contributions from all previous time intervals for $t < T_n$ are given both through the amplitude $A^{(n-1)}(T_n)$ and through the memory integral $\mathcal{I}^{(n)}(\omega)$, which are contained in the function

$$\mathcal{F}^{(n)}(t) = \left\{ A^{(n-1)}(T_n)e^{-[\kappa+i\Delta_c](t-T_n)} + \Omega^2 \int_0^\infty d\omega\, \rho(\omega) \frac{e^{-[\gamma+i\Delta(\omega)](t-T_n)} - e^{-[\kappa+i\Delta_c](t-T_n)}}{[\gamma+i\Delta_\omega]-[\kappa+i\Delta_c]} \mathcal{I}^{(n)}(\omega) \right\}, \tag{A7}$$

where

$$\mathcal{I}^{(n)}(\omega) = \mathcal{I}^{(n-1)}(\omega)e^{-[\gamma+i\Delta_\omega](T_n-T_{n-1})} + \int_{T_{n-1}}^{T_n} d\tau\, A^{(n-1)}(\tau)e^{-[\gamma+i\Delta_\omega](T_n-\tau)}. \tag{A8}$$

In accordance with the initial conditions introduced above at $t = T_1$, $A^{(0)}(T_1) = 0$ and $\mathcal{I}^{(1)}(\omega) = 0$, so $\mathcal{F}^{(1)}(t)$ vanishes in the first time interval $\mathcal{F}^{(1)}(t) = 0$ $(T_1 \leqslant t \leqslant T_2)$.

## APPENDIX B: OPTIMAL CONTROL BASED ON THE VOLTERRA EQUATION

In the main text we split our time interval into two parts, a write and readout section, with a variable delay section in between. In the write section, two independent optimized write pulses $\eta^{(W)}(t)$ prepare two different configurations of the spin ensemble, which are referred to as logical states $|0\rangle$ and $|1\rangle$ of the spin ensemble. It is followed by the delay section characterized by almost completely suppressed cavity responses and finally by the readout section where two logical states of the spin ensemble are retrieved and mapped on two mutually orthogonal states of the cavity field by means of the readout pulse $\eta^{(R)}(t)$ (see Fig. 5). Note that the optimized readout pulse is generic, being the same for both $|0\rangle$ and $|1\rangle$ states. For the sake of simplicity, we do not explicitly specify the delay pulse but impose on the readout pulse $\eta^{(R)}(t)$ a constraint such that the cavity responses are maximally suppressed in the delay section $[T_2,\tau_a]$ (see Fig. 5). Thus, the write and readout pulses are defined within the time intervals $[T_1,T_2]$ and $[T_2,T_3]$, respectively, in terms of the notations introduced in Appendix A and the delay section is formally absorbed into the readout section.

We then expand $\eta^{(W)}(t)$ and $\eta^{(R)}(t)$ in terms of sine functions

$$\eta^{(W)}(t) = \sum_{k=1}^{N_1} \xi_k \sin[k\omega_f(t-T_1)], \tag{B1}$$

$$\eta^{(R)}(t) = \sum_{l=1}^{N_2} \zeta_l \sin[l\omega_f(t-T_2)], \tag{B2}$$

where $\xi_k$ and $\zeta_l$ are the expansion coefficients and $\omega_f$ is the fundamental frequency. The linear property of the Volterra equation (A4) allows us to expand the cavity amplitude in the write section $A^{(W)}(t)$ in a series of time-dependent functions with the same expansion coefficients $\xi_k$ as in Eq. (B1),

$$A^{(W)}(t) = \sum_{k=1}^{N_1} \xi_k a_k^{(W)}(t). \tag{B3}$$

Here $a_k^{(W)}(t)$ are solutions of the Volterra equation

$$a_k^{(W)}(t) = \int_{T_1}^t d\tau\, K(t-\tau)a_k^{(W)}(\tau) - \int_{T_1}^t d\tau \sin[k\omega_f(\tau-T_1)]e^{-[\kappa+i\Delta_c](t-\tau)}, \tag{B4}$$

where the kernel function $\mathcal{K}(t-\tau)$ is given by Eq. (A5).

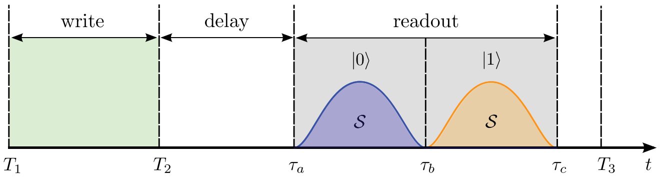

FIG. 5. Time divisions for the optimization scheme of the cavity responses $A^{(R)}_{|0\rangle}(t)$ and $A^{(R)}_{|1\rangle}(t)$. The write section $[T_1,T_2]$ is followed by the variable delay section $[T_2,\tau_a]$ and the readout section $[\tau_a,\tau_c]$. The cavity responses $A^{(R)}_{|0\rangle}(t)$ and $A^{(R)}_{|1\rangle}(t)$ reside in the first half $[\tau_a,\tau_b]$ and the second half $[\tau_b,\tau_c]$ of the readout section, respectively.

The solution in the readout section $A^{(R)}(t)$ in turn consists of two contributions

$$A^{(R)}(t) = \sum_{l=1}^{N_2} \zeta_l a_l^{(R)}(t) + \sum_{k=1}^{N_1} \xi_k \psi_k^{(R)}(t). \tag{B5}$$

Similar to the ansatz for the write section, the first term in Eq. (B5) also contains the same expansion coefficients $\zeta_l$ as the corresponding driving signal in the readout section [see Eq. (B2)] with the time-dependent functions $a_l^{(R)}(t)$ obeying the Volterra equation $(T_2 \leqslant t \leqslant T_3)$

$$a_l^{(R)}(t) = \int_{T_2}^t d\tau\, \mathcal{K}(t-\tau)a_l^{(R)}(\tau) - \int_{T_2}^t d\tau \sin[l\omega_f(\tau-T_2)]e^{-[\kappa+i\Delta_c](t-\tau)}. \tag{B6}$$

Additionally, the second term in Eq. (B5) describes the non-Markovian memory and appears in the readout section due to the energy stored in both the cavity and spin ensemble during the time interval $T_1 \leqslant t \leqslant T_2$ (write section). Therefore, it depends only on the coefficients $\xi_k$ of the write pulse (B1) and the time-dependent functions $\psi_k^{(R)}(t)$, which can be found by substituting the expressions (B3) and (B5) into Eqs. (A4)–(A8) for $n = 2$. It can be shown that these functions satisfy the Volterra equation

$$\psi_k^{(R)}(t) = \int_{T_2}^t d\tau\, \mathcal{K}(t-\tau)\psi_k^{(R)}(\tau) + f_k^{(R)}(t), \tag{B7}$$

with the feedback from the previous write section defined by

$$f_k^{(R)}(t) = a_k^{(W)}(T_2)e^{-[\kappa+i\Delta_c](t-T_2)} + \Omega^2 \int_0^\infty d\omega\, \rho(\omega) \frac{e^{-[\gamma+i\Delta_\omega](t-T_2)} - e^{-[\kappa+i\Delta_c](t-T_2)}}{[\gamma + i\Delta_\omega] - [\kappa + i\Delta_c]} \int_{T_1}^{T_2} d\tau\, a_k^{(W)}(\tau)e^{-[\gamma+i\Delta_\omega](T_2-\tau)}. \tag{B8}$$

Note that the $a_k^{(W)}(t)$ in Eq. (B8) are defined in the write section only and are known solutions of Eq. (B4).

In the main text we use two different pulses $\eta_{|0\rangle}^{(W)}(t) = \sum_{k=1}^{N_1} \xi_k^{|0\rangle} \sin[k\omega_f(t-T_1)]$ and $\eta_{|1\rangle}^{(W)}(t) = \sum_{k=1}^{N_1} \xi_k^{|1\rangle} \sin[k\omega_f(t-T_1)]$ in the write section, which are characterized by two sets of expansion coefficients from Eq. (B1). As a result, the cavity amplitudes in the write section are also represented by these sets of expansion coefficients and are given by Eq. (B3), namely,

$$\begin{aligned} A_{|0\rangle}^{(W)}(t) &= \sum_{k=1}^{N_1} \xi_k^{|0\rangle} a_k^{(W)}(t), \\ A_{|1\rangle}^{(W)}(t) &= \sum_{k=1}^{N_1} \xi_k^{|1\rangle} a_k^{(W)}(t). \end{aligned} \tag{B9}$$

Note that by injecting these pulses into the cavity, we create two independent configurations (denoted by $|0\rangle$ and $|1\rangle$) of the spin-cavity system at the beginning of the readout interval $t = T_2$.

Next we perform a readout by applying a single optimized readout pulse (B2), which is the same for the states $|0\rangle$ and $|1\rangle$. The cavity amplitudes in the readout section in turn are governed by Eq. (B5) as

$$\begin{aligned} A_{|0\rangle}^{(R)}(t) &= \underbrace{\sum_{l=1}^{N_2} \zeta_l a_l^{(R)}(t)}_{\tilde{A}^{(R)}(t)} + \underbrace{\sum_{k=1}^{N_1} \xi_k^{|0\rangle} \psi_k^{(R)}(t)}_{\tilde{A}_{|0\rangle}^{(R)}(t)}, \\ A_{|1\rangle}^{(R)}(t) &= \underbrace{\sum_{l=1}^{N_2} \zeta_l a_l^{(R)}(t)}_{\tilde{A}^{(R)}(t)} + \underbrace{\sum_{k=1}^{N_1} \xi_k^{|1\rangle} \psi_k^{(R)}(t)}_{\tilde{A}_{|1\rangle}^{(R)}(t)}, \end{aligned} \tag{B10}$$

where $\tilde{A}^{(R)}(t)$ describes the contribution from the readout pulse only, which is the same for both cavity responses and the two other terms $\tilde{A}_{|i\rangle}^{(R)}(t)$ $(i = 0,1)$ explicitly depend on the states $|0\rangle$ and $|1\rangle$ created in the write section. Thus, the cavity amplitude is determined at every moment of time by Eqs. (B3)–(B8) (and, as a consequence, all spin configurations), if all expansion coefficients $\xi_k^{|0\rangle}$, $\xi_k^{|1\rangle}$, and $\zeta_l$ are provided.

As the next step we develop an optimization scheme aiming at achieving two well-resolved cavity responses in the readout section, $A_{|0\rangle}^{(R)}(t)$ and $A_{|1\rangle}^{(R)}(t)$, as is sketched in Fig. 5. (The results of numerical calculations are presented in Fig. 2.) For this purpose we use the standard method of Lagrange multipliers by introducing the functional $\mathcal{F}(\xi_k^{|0\rangle},\xi_k^{|1\rangle},\zeta_l)$ subject to several constraints listed below and search for its minima with respect to the expansion coefficients of all three pulses. Namely, we write the expression for the functional

$$\begin{aligned} \mathcal{F}(\xi_k^{|0\rangle},\xi_k^{|1\rangle},\zeta_l) = {} & \int_{\tau_b}^{\tau_c} dt |A_{|0\rangle}^{(R)}(t)|^2 + \int_{\tau_a}^{\tau_b} dt |A_{|1\rangle}^{(R)}(t)|^2 \\ & + \left| \int_{\tau_a}^{\tau_c} dt\, A_{|0\rangle}^{(R)\star}(t) A_{|1\rangle}^{(R)}(t) \right| \\ & - \lambda_{\text{delay}}^{|0\rangle} \int_{T_2}^{\tau_a} dt |A_{|0\rangle}^{(R)}(t)|^2 - \lambda_{\text{delay}}^{|1\rangle} \\ & \times \int_{T_2}^{\tau_a} dt |A_{|1\rangle}^{(R)}(t)|^2 - \lambda_T^{|0\rangle} |A_{|0\rangle}^{(R)}(\tau_a)|^2 \\ & - \lambda_T^{|1\rangle} \left|A_{|1\rangle}^{(R)}(\tau_a)\right|^2 - \lambda_{\Delta T}^{|0\rangle} \\ & \times \left( \int_{\tau_a}^{\tau_b} dt \left|A_{|0\rangle}^{(R)}(t)\right|^2 - \mathcal{S} \right) \\ & - \lambda_{\Delta T}^{|1\rangle} \left( \int_{\tau_b}^{\tau_c} dt \left|A_{|1\rangle}^{(R)}(t)\right|^2 - \mathcal{S} \right) \\ & - \lambda_P^{|0\rangle} \left( \sum_k \left|\xi_k^{|0\rangle}\right|^2 - \mathcal{P} \right) \\ & - \lambda_P^{|1\rangle} \left( \sum_k \left|\xi_k^{|1\rangle}\right|^2 - \mathcal{P} \right), \end{aligned} \tag{B11}$$

where the $\lambda$ are the Lagrange multipliers. The first three terms in Eq. (B11) are the functions to be minimized, which ensure that the overlap between the time-binned states in the readout section is negligibly small. The rest of the terms are constraints, which additionally guarantee the following conditions to be simultaneously fulfilled: (i) The cavity responses within the delay section are maximally suppressed; (ii) the cavity at the beginning of the readout section is almost empty for both states; (iii) the integral taken with respect to the time-binned cavity amplitudes squared within the readout section has the same value $\mathcal{S}$; (iv) a net power $\mathcal{P}$ of the write pulses per fundamental period $2\pi/\omega_f$ is the same. In our numerical calculations we used the sequential least-squares programming minimization method [41] embedded in the internal python library SCIPY.OPTIMIZE to find the minima of the functional $\mathcal{F}(\xi_k^{|0\rangle},\xi_k^{|1\rangle},\zeta_l)$.

In the main text we created an arbitrary superposition of write pulses (each of which separately prepares the logical state $|0\rangle$ or $|1\rangle$) by applying the superimposed write pulse

$$\eta^{(W)}(t) = \alpha\eta_{|0\rangle}^{(W)}(t) + \beta\eta_{|1\rangle}^{(W)}(t), \tag{B12}$$

aiming to extract the encoded information (given by complex numbers $\alpha$ and $\beta$) from the solution for the cavity amplitude in the readout section designated in Fig. 5. [Note that the reading pulse $\eta^{(R)}(t)$ is always kept the same.] The solution in the readout section can be written as

$$A^{(R)}(t;\alpha,\beta) = \alpha\tilde{A}_{|0\rangle}^{(R)}(t) + \beta\tilde{A}_{|1\rangle}^{(R)}(t) + \tilde{A}^{(R)}(t), \tag{B13}$$

with all three previously established well-known amplitudes $\tilde{A}^{(R)}_{|0\rangle}(t)$, $\tilde{A}^{(R)}_{|1\rangle}(t)$, and $\tilde{A}^{(R)}(t)$ introduced in Eq. (B10). We then project our resulting solution (B13) onto the functions $A^{(R)}_{|0\rangle}(t)$ and $A^{(R)}_{|1\rangle}(t)$ from Eq. (B10), namely, we write

$$\begin{aligned}\mathcal{O}_i &= \int_{\tau_a}^{\tau_c} dt\, A^{(R)}(t;\alpha,\beta)A^{(R)*}_{|i\rangle}(t)\\ &= \alpha\mathcal{F}_{i,0} + \beta\mathcal{F}_{i,1} + \mathcal{F}_{i,R},\end{aligned} \tag{B14}$$

where the overlap integrals $\mathcal{F}_{i,q} = \int_{\tau_a}^{\tau_c} dt\, \tilde{A}^{(R)}_{|q\rangle}(t)A^{(R)*}_{|i\rangle}(t)$ with $i,q = 0,1$ and $\mathcal{F}_{i,R} = \int_{\tau_a}^{\tau_c} dt\, \tilde{A}^{(R)}(t)A^{(R)*}_{|i\rangle}(t)$. Since $\mathcal{F}_{i,q}$ and $\mathcal{F}_{i,R}$ are known we finally end up with the set of two algebraic equations

$$\mathcal{O}_0 = \alpha\mathcal{F}_{0,0} + \beta\mathcal{F}_{0,1} + \mathcal{F}_{0,R}, \tag{B15}$$

$$\mathcal{O}_1 = \alpha\mathcal{F}_{1,0} + \beta\mathcal{F}_{1,1} + \mathcal{F}_{1,R}, \tag{B16}$$

from which the retrieved values $\alpha_R$ and $\beta_R$ can be evaluated.

## APPENDIX C: RETRIEVAL OF ENCODED PARAMETERS IN THE PRESENCE OF NOISE

Here we study the influence of noise on the quality of our optimization scheme presented in the main text and introduced in Appendix B. For that purpose, we subject the previously established optimal driving amplitudes $\eta^{(W)}_{|0\rangle}(t)$, $\eta^{(W)}_{|1\rangle}(t)$, and $\eta^{(R)}(t)$ (see Appendix B) to a small perturbation represented by the driving term $\delta\eta_{\text{noise}}(t) = \delta\eta\upsilon(t)$, where $\delta\eta$ is the amplitude of perturbation and $\upsilon(t)$ stands for a Gaussian white noise of mean and correlations given by, respectively, $\langle\upsilon(t)\rangle = 0$ and $\langle\upsilon(t')\upsilon(t)\rangle = \delta(t-t')$. We then numerically integrate the Volterra equation (A3) from Appendix A with respect to time by adding the perturbation $\delta\eta_{\text{noise}}(t)$ to the corresponding deterministic optimal driving amplitudes $\eta(t)$, which in our specific case are represented by the known writing and readout amplitudes $\eta^{(W)}_{|0\rangle}(t)$, $\eta^{(W)}_{|1\rangle}(t)$, and $\eta^{(R)}(t)$. We treat the problem numerically using well-established numerical methods for integrating stochastic differential equations (see, e.g., [40]). Concisely, the stochastic contribution to the cavity amplitude is taken into account after each time step of numerical integration in the following way: $A(t_{m+1}) \rightarrow A(t_{m+1}) + \sqrt{dt}\,\delta\eta_{\text{noise}}(t_m)$, where $A(t_{m+1})$ after the arrow corresponds to the deterministic part of the cavity amplitude at $t = t_{m+1}$ obtained using the standard Runge-Kutta method and $\delta\eta_{\text{noise}}(t_m)$ is the stochastic drive taken from the previous time step. We then accumulate statistics by integrating many trajectories for different noise realizations. Next we extract the encoded parameters $\alpha_{\mathcal{R}}$ and $\beta_{\mathcal{R}}$ in the presence of noise replacing the overlap integrals in Eqs. (B15) and (B16) for the case without noise by the corresponding overlap integrals evaluated for different noise realizations. The result of calculations for the average retrieval values of $\langle\alpha_{\mathcal{R}}\rangle$ and $\langle\beta_{\mathcal{R}}\rangle$ and their absolute errors $\epsilon_\alpha = |\alpha - \langle\alpha_{\mathcal{R}}\rangle|$ and $\epsilon_\beta = |\beta - \langle\beta_{\mathcal{R}}\rangle|$ with respect to the encoded values are depicted in Fig. 3.

## APPENDIX D: NUMERICAL VALUES FOR THE OPTIMIZED READOUT PULSE COEFFICIENTS

Here we present numerical values of the coefficients $\xi_k^{|0\rangle}$, $\xi_k^{|1\rangle}$, and $\zeta_l$ of the optimal readout pulses $\eta^{(W)}_{|0\rangle}(t)$, $\eta^{(W)}_{|1\rangle}(t)$, and $\eta^{(R)}(t)$ defined by Eqs. (B1) and (B2), which are presented in the main text. We take the amplitude of the write pulses such that the net power injected into the cavity $\mathcal{P}^{(W)}_{|i\rangle} = \frac{1}{T_f}\int_0^{T_f} dt|\eta^{(W)}_{|i\rangle}(t)|^2 = \kappa^2$, with $i = 0,1$, such that it corresponds to the power provided by a coherent driving signal with the amplitude equal to the cavity decay rate $\eta = \kappa$. Specifically, using the expansion (B1) for the write pulses $\eta^{(W)}(t)$, we obtain the following expression for the power of the write pulses per fundamental period $T_f$:

$$\mathcal{P}^{(W)}_{|i\rangle} = \eta^{(W)2}\frac{1}{2}\sum_{k=1}^{N_1}|\xi_k^{|i\rangle}/\eta^{(W)}|^2 = \kappa^2, \tag{D1}$$

where $\eta^{(W)} = \kappa$ and $\frac{1}{2}\sum_{k=1}^{N_1}|\xi_k^{|i\rangle}/\kappa|^2 = 1$ due to the constraint imposed on the expansion coefficients. On the other hand, the power of the readout pulse is substantially smaller than that of the write pulses and for the case without hole burning (see left column of Fig. 2) we obtain

$$\mathcal{P}^{(R)} = \eta^{(R)2}\frac{1}{2}\sum_{k=1}^{N_2}|\zeta_l/\eta^{(R)}|^2 = 0.068\kappa^2, \tag{D2}$$

where $\eta^{(R)} = 0.26\kappa$ and again we use as the constraint $\frac{1}{2}\sum_{l=1}^{N_2}|\zeta_l/\eta^{(R)}|^2 = 1$.

The coefficients for all optimal readout pulses shown in the left column of Fig. 2 are listed in Table I. For the sake of convenience, the coefficients of the write and readout pulses are normalized to $\eta^{(W)}$ and $\eta^{(R)}$, respectively. We use $N_1 = 5$ coefficients for the write pulse and $N_2 = 10$ for the readout pulse (notation is consistent with that used in Appendices A and B). The fundamental frequency for the write pulses is given by $\omega_f = \pi/(T_2 - T_1) = \Omega_R$ and for the readout pulse we use $\omega_f = \pi/(T_3 - T_2) = \Omega_R/2$. Here the Rabi frequency $\Omega_R = 2\pi \times 13.62$ MHz and the time divisions shown in Fig. 5

TABLE I. Normalized expansion coefficients $\xi^{|i\rangle}_{k=1,\dots,5}$ (for $i = 0,1$) and $\zeta_{k=1,\dots,10}$ defined by Eqs. (B1) and (B2), which correspond to the optimal readout pulses $\eta^{(W)}_{|0\rangle}(t)$, $\eta^{(W)}_{|1\rangle}(t)$, and $\eta^{(R)}(t)$ depicted in the left column of Fig. 2. The coefficients for the write pulses are normalized to $\eta^{(W)} = \kappa$ and for the readout pulse to $\eta^{(R)} = 0.26\kappa$.

| $\xi^{\|0\rangle}_{k=1,\dots,5}$ | $\xi^{\|1\rangle}_{k=1,\dots,5}$ | $\zeta_{l=1,\dots,5}$ | $\zeta_{l=6,\dots,10}$ |
|---|---|---|---|
| $0.434 + 0.103i$ | $-0.043 - 0.013i$ | $-1.003 - 0.250i$ | $0.229 + 0.054i$ |
| $0.303 + 0.067i$ | $-0.231 - 0.055i$ | $0.820 + 0.195i$ | $0.037 + 0.007i$ |
| $1.060 + 0.259i$ | $-1.127 - 0.273i$ | $-0.017 - 0.007i$ | $-0.096 - 0.025i$ |
| $-0.152 - 0.023i$ | $0.200 + 0.044i$ | $-0.213 - 0.054i$ | $-0.174 - 0.043i$ |
| $0.682 + 0.161i$ | $-0.723 - 0.175i$ | $-0.243 - 0.061i$ | $0.105 + 0.024i$ |

TABLE II. Normalized expansion coefficients $\xi_{k=1,\ldots,4}^{|i\rangle}$ (for $i = 0,1$) and $\zeta_{k=1,\ldots,60}$ defined by Eqs. (B1) and (B2), which correspond to the optimal readout pulses $\eta_{|0\rangle}^{(W)}(t)$, $\eta_{|1\rangle}^{(W)}(t)$, and $\eta^{(R)}(t)$ depicted in the right column of Fig. 2. The coefficients for the write pulses are normalized to $\eta^{(W)} = \kappa$ and for the readout pulse to $\eta^{(R)} = 0.11\kappa$.

| $\xi_{k=1,\ldots,4}^{\|0\rangle}$ | $\xi_{k=1,\ldots,4}^{\|1\rangle}$ | $\zeta_{l=1,\ldots,15}$ | $\zeta_{l=16,\ldots,30}$ | $\zeta_{l=31,\ldots,45}$ | $\zeta_{l=46,\ldots,60}$ |
|---|---|---|---|---|---|
| $-0.227 + 0.108i$ | $1.252 - 0.161i$ | $0.066 - 0.028i$ | $-0.239 - 0.024i$ | $0.054 - 0.032i$ | $-0.036 - 0.010i$ |
| $0.017 + 0.046i$ | $0.074 + 0.050i$ | $-0.121 - 0.022i$ | $0.228 - 0.088i$ | $-0.041 - 0.014i$ | $0.059 - 0.021i$ |
| $1.014 - 0.161i$ | $-0.243 + 0.083i$ | $0.190 - 0.128i$ | $-0.170 - 0.013i$ | $0.044 - 0.029i$ | $-0.069 - 0.011i$ |
| $0.938 - 0.032i$ | $0.574 + 0.040i$ | $-0.230 + 0.010i$ | $0.161 - 0.080i$ | $-0.027 - 0.014i$ | $0.090 - 0.026i$ |
|  |  | $0.292 - 0.151i$ | $-0.109 - 0.019i$ | $0.027 - 0.025i$ | $-0.096 - 0.007i$ |
|  |  | $-0.313 + 0.033i$ | $0.107 - 0.059i$ | $-0.007 - 0.015i$ | $0.112 - 0.040i$ |
|  |  | $0.365 - 0.155i$ | $-0.066 - 0.020i$ | $0.006 - 0.020i$ | $-0.112 + 0.016i$ |
|  |  | $-0.363 + 0.028i$ | $0.073 - 0.051i$ | $0.012 - 0.020i$ | $0.122 - 0.051i$ |
|  |  | $0.398 - 0.160i$ | $-0.042 - 0.021i$ | $-0.009 - 0.017i$ | $-0.118 + 0.004i$ |
|  |  | $-0.377 - 0.001i$ | $0.058 - 0.044i$ | $0.021 - 0.022i$ | $0.122 - 0.033i$ |
|  |  | $0.395 - 0.136i$ | $-0.032 - 0.021i$ | $-0.012 - 0.009i$ | $-0.115 + 0.011i$ |
|  |  | $-0.355 - 0.009i$ | $0.025 - 0.040i$ | $0.016 - 0.021i$ | $0.117 - 0.031i$ |
|  |  | $0.358 - 0.097i$ | $-0.085 - 0.017i$ | $0.000 - 0.014i$ | $-0.108 + 0.001i$ |
|  |  | $-0.305 - 0.001i$ | $0.049 - 0.033i$ | $-0.004 - 0.018i$ | $0.107 - 0.032i$ |
|  |  | $0.298 - 0.093i$ | $-0.047 - 0.015i$ | $0.026 - 0.023i$ | $-0.095 + 0.020i$ |

are $T_1 = 0$, $T_2 = 36.72$ ns, and $T_3 = 110.15$ ns. The readout section $[\tau_a,\tau_c]$ coincides with the whole readout interval $[T_2,T_3]$.

For the case with hole burning, depicted in the right column of Fig. 2, we use $N_1 = 4$ and $N_2 = 60$. All coefficients are summarized in Table II. Here we choose the fundamental frequency for the write pulses as $\omega_f = \pi/(T_2 - T_1) = \Omega_R/2$, whereas $\omega_f = \pi/(T_3 - T_2) = \Omega_R/30$ for the readout pulse. The time divisions are $T_1 = 0$, $T_2 = 73.4$ ns, and $T_3 = 1174.9$ ns and the Rabi frequency $\Omega_R = 2\pi \times 13.62$ MHz. The readout section defined by $\tau_a = 1114.3$ ns and $\tau_c = 1153.6$ ns is delayed by approximately 1 $\mu$s with respect to the write section $[T_1,T_2]$. The power ratio of the readout pulse to the write pulse turns out to be $\mathcal{P}^{(R)}/\mathcal{P}^{(W)} = 0.013$.

[1] T. P. Harty, D. T. C. Allcock, C. J. Ballance, L. Guidoni, H. A. Janacek, N. M. Linke, D. N. Stacey, and D. M. Lucas, Phys. Rev. Lett. **113**, 220501 (2014).

[2] J. L. O'Brien, G. J. Pryde, A. G. White, T. C. Ralph, and D. Branning, Nature (London) **426**, 264 (2003).

[3] J. H. Plantenberg, P. C. de Groot, C. J. P. M. Harmans, and J. E. Mooij, Nature (London) **447**, 836 (2007).

[4] P. J. J. O'Malley *et al.*, Phys. Rev. X **6**, 031007 (2016).

[5] P. Macha, G. Oelsner, J.-M. Reiner, M. Marthaler, S. André, G. Schön, U. Hübner, H.-G. Meyer, E. Il'ichev, and A. V. Ustinov, Nat. Commun. **5**, 5146 (2014).

[6] K. V. Shulga, P. Yang, G. P. Fedorov, M. V. Fistul, M. Weides, and A. V. Ustinov, JETP Lett. **105**, 47 (2017).

[7] P. L. Stanwix, L. M. Pham, J. R. Maze, D. Le Sage, T. K. Yeung, P. Cappellaro, P. R. Hemmer, A. Yacoby, M. D. Lukin, and R. L. Walsworth, Phys. Rev. B **82**, 201201(R) (2010).

[8] R. Amsüss, C. Koller, T. Nöbauer, S. Putz, S. Rotter, K. Sandner, S. Schneider, M. Schramböck, G. Steinhauser, H. Ritsch, J. Schmiedmayer, and J. Majer, Phys. Rev. Lett. **107**, 060502 (2011).

[9] Y. Kubo *et al.*, Phys. Rev. Lett. **105**, 140502 (2010).

[10] S. Probst, H. Rotzinger, S. Wünsch, P. Jung, M. Jerger, M. Siegel, A. V. Ustinov, and P. A. Bushev, Phys. Rev. Lett. **110**, 157001 (2013).

[11] P. Rabl, D. DeMille, J. M. Doyle, M. D. Lukin, R. J. Schoelkopf, and P. Zoller, Phys. Rev. Lett. **97**, 033003 (2006).

[12] M. Afzelius, C. Simon, H. de Riedmatten, and N. Gisin, Phys. Rev. A **79**, 052329 (2009).

[13] J. Verdú, H. Zoubi, C. Koller, J. Majer, H. Ritsch, and J. Schmiedmayer, Phys. Rev. Lett. **103**, 043603 (2009).

[14] S. A. Moiseev and S. Kröll, Phys. Rev. Lett. **87**, 173601 (2001).

[15] W. Tittel, M. Afzelius, T. Chaneliere, R. L. Cone, S. Kröll, S. A. Moiseev, and M. Sellars, Laser Photon. Rev. **4**, 244 (2010).

[16] B. Kraus, W. Tittel, N. Gisin, M. Nilsson, S. Kröll, and J. I. Cirac, Phys. Rev. A **73**, 020302(R) (2006).

[17] B. Julsgaard and K. Mölmer, Phys. Rev. A **88**, 062324 (2013).

[18] C. Grezes *et al.*, Phys. Rev. X **4**, 021049 (2014).

[19] N. Gisin, S. A. Moiseev, and C. Simon, Phys. Rev. A **76**, 014302 (2007).

[20] M. U. Staudt, S. R. Hastings-Simon, M. Nilsson, M. Afzelius, V. Scarani, R. Ricken, H. Suche, W. Sohler, W. Tittel, and N. Gisin, Phys. Rev. Lett. **98**, 113601 (2007).

[21] H. de Riedmatten, M. Afzelius, M. U. Staudt, C. Simon, and N. Gisin, Nature (London) **456**, 773 (2008).

[22] M. Gündogan, P. M. Ledingham, K. Kutluer, M. Mazzera, and H. de Riedmatten, Phys. Rev. Lett. **114**, 230501 (2015).

[23] P. Jobez, I. Usmani, N. Timoney, C. Laplane, N. Gisin, and M. Afzelius, New J. Phys. **16**, 083005 (2014).

[24] S. A. Moiseev and J.-L. Le Gouët, J. Phys. B **45**, 124003 (2012).

[25] I. Novikova, N. B. Phillips, and A. V. Gorshkov, Phys. Rev. A **78**, 021802(R) (2008).

[26] D. O. Krimer, B. Hartl, and S. Rotter, Phys. Rev. Lett. **115**, 033601 (2015).

[27] S. Putz, A. Angerer, D. O. Krimer, R. Glattauer, W. J. Munro, S. Rotter, J. Schmiedmayer, and J. Majer, Nat. Photon. **11**, 36 (2017).

[28] D. O. Krimer, M. Zens, S. Putz, and S. Rotter, Laser Photon. Rev. **10**, 1023 (2016).

[29] S. Putz, D. O. Krimer, R. Amsüss, A. Valookaran, T. Nöbauer, J. Schmiedmayer, S. Rotter, and J. Majer, Nat. Phys. **10**, 720 (2014).

[30] C. U. Lei and W.-M. Zhang, Ann. Phys. (NY) **327**, 1408 (2012).

[31] W.-M. Zhang, P.-Y. Lo, H.-N. Xiong, M. W.-Y. Tu, and F. Nori, Phys. Rev. Lett. **109**, 170402 (2012).

[32] M. Tavis and F. W. Cummings, Phys. Rev. **170**, 379 (1968).

[33] K. Sandner, H. Ritsch, R. Amsüss, C. Koller, T. Nöbauer, S. Putz, J. Schmiedmayer, and J. Majer, Phys. Rev. A **85**, 053806 (2012).

[34] J. Brendel, N. Gisin, W. Tittel, and H. Zbinden, Phys. Rev. Lett. **82**, 2594 (1999).

[35] H. Primakoff and T. Holstein, Phys. Rev. **55**, 1218 (1939).

[36] D. O. Krimer, S. Putz, J. Majer, and S. Rotter, Phys. Rev. A **90**, 043852 (2014).

[37] I. Diniz, S. Portolan, R. Ferreira, J. M. Gérard, P. Bertet, and A. Aufféves, Phys. Rev. A **84**, 063810 (2011).

[38] Z. Kurucz, J. H. Wesenberg, and K. Mølmer, Phys. Rev. A **83**, 053852 (2011).

[39] J. Batle, A. R. Plastino, M. Casas, and A. Plastino, Opt. Spectrosc. **94**, 700 (2003).

[40] R. Toral and P. Colet, *Stochastic Numerical Methods: An Introduction for Students and Scientists* (Wiley-VCH, Weinheim, 2014).

[41] D. Kraft, A software package for sequential quadratic programming, DLR German Aerospace Center Institute for Flight Mechanics Report No. DFVLR-FB 88-28, 1988 (unpublished).

PHYSICS

# Ultralong relaxation times in bistable hybrid quantum systems

**Andreas Angerer,[1,2]* Stefan Putz,[1,2,3]* Dmitry O. Krimer,[4] Thomas Astner,[1] Matthias Zens,[4] Ralph Glattauer,[1] Kirill Streltsov,[1] William J. Munro,[5,6] Kae Nemoto,[6] Stefan Rotter,[4] Jörg Schmiedmayer,[1] Johannes Majer[1,7]†**

**Nonlinear systems, whose outputs are not directly proportional to their inputs, are well known to exhibit many interesting and important phenomena that have profoundly changed our technological landscape over the last 50 years. Recently, the ability to engineer quantum metamaterials through hybridization has allowed us to explore these nonlinear effects in systems with no natural analog. We investigate amplitude bistability, which is one of the most fundamental nonlinear phenomena, in a hybrid system composed of a superconducting resonator inductively coupled to an ensemble of nitrogen-vacancy centers. One of the exciting properties of this spin system is its long spin lifetime, which is many orders of magnitude longer than other relevant time scales of the hybrid system. This allows us to dynamically explore this nonlinear regime of cavity quantum electrodynamics and demonstrate a critical slowing down of the cavity population on the order of several tens of thousands of seconds—a time scale much longer than observed so far for this effect. Our results provide a foundation for future quantum technologies based on nonlinear phenomena.**

## INTRODUCTION

In nature, most physical systems are inherently nonlinear, giving rise to effects, such as bistability (*1*), chaos (*2*), solitons (*3*), and superradiance (*4*), and often appear counterintuitive when contrasted with much simpler linear systems. Amplitude bistability, one of the basic nonlinear phenomena [commonly used in optical switches nowadays (*5*)], has been extensively investigated both theoretically (*6*–*10*) and experimentally (*11*, *12*). It occurs in any medium where strong nonlinearities in the interaction between a radiation field and a polarizable medium, such as spins, exist. The nonlinearity in these systems arises from the two-level nature of the atoms coupled to the cavity mode but only shows up when driven beyond the single excitation regime. For a strong coupling between the spin system and the cavity mode, a first-order phase transition between a saturated, disordered, and de-excited, ordered ground state occurs (*13*). The coupled system switches between these two branches and shows a hysteresis depending on the history of the system.

The usual cavity quantum electrodynamics (cQED) demonstrations use atoms or trapped ions coupled to optical light fields to investigate these nonlinear effects, but the short atomic lifetimes have made it difficult to truly observe the temporal dynamics of amplitude bistability (*14*, *15*) and restricted previous studies to the steady-state behavior. In contrast, quantum engineering by hybridizing different physical systems and by exploiting their advantages (*16*–*21*) allows us to create systems with extremely long-lived emitters, making it possible to observe the bistable system during evolution. Here, we report on the observation of amplitude bistability in a cQED system composed of a superconducting resonator coupled to a long-lived electron spin ensemble formed from artificial atoms [negatively charged nitrogen-vacancy ($NV^-$) centers in diamond (*22*, *23*)]. This type of system has been studied extensively (*17*, *18*), but experiments to date have been mainly carried out in the linear regime. The present work goes beyond this linear regime and thus provides the foundation for further understanding of nonlinear physics in this type of solid-state hybrid quantum system. Moreover, the long lifetime of the spin system (*24*) allows us to study the temporal behavior of the presented effect, a regime experimentally just recently accessed (*25*, *26*).

## RESULTS

### Equations of motion from the Tavis-Cummings Hamiltonian

An ensemble of spins in a cavity is characterized by the three quantities: polarization, inversion, and the cavity amplitude. Their dynamics can be derived from the driven Tavis-Cummings Hamiltonian (*27*) for $N$ spins under the rotating wave approximation as

$$\mathcal{H} = \hbar\omega_c \boldsymbol{a}^\dagger \boldsymbol{a} + \frac{\hbar}{2}\sum\nolimits_{j=1}^{N} \omega_j \sigma_j^z + i\hbar\sum\nolimits_{j=1}^{N} g_j(\sigma_j^- \boldsymbol{a}^\dagger - \sigma_j^+ \boldsymbol{a}) + i\hbar(\eta \boldsymbol{a}^\dagger e^{-i\omega_p t} - h.c.) \qquad (1)$$

with $\boldsymbol{a}^\dagger$ and $\boldsymbol{a}$ being the creation and annihilation operators for the cavity mode of frequency $\omega_c$, respectively, and $\sigma_j^z$, $\sigma_j^+$, and $\sigma_j^-$ as the spin inversion, raising, and lowering operators, respectively, for the $j$-th spin of frequency $\omega_j$ coupled to the cavity with a single-spin coupling strength $g_j$. The last term accounts for an external cavity drive with field amplitude $\eta$ and frequency $\omega_p$.

Using a mean-field approximation, valid in the limit of large spin ensembles, $\langle \boldsymbol{a}^\dagger \sigma^- \rangle \approx a^\dagger \sigma^-$ (in the following, unbolded symbols will be used for the expectation values), we derive a set of first-order differential

---

[1] Vienna Center for Quantum Science and Technology, Atominstitut, Technische Universität Wien (TU Wien), Stadionallee 2, 1020 Vienna, Austria. [2] Zentrum für Mikro- und Nanostrukturen, TU Wien, Floragasse 7, 1040 Vienna, Austria. [3] Department of Physics, Princeton University, Princeton, NJ 08544, USA. [4] Institute for Theoretical Physics, TU Wien, Wiedner Hauptstraße 8-10/136, 1040 Vienna, Austria. [5] NTT Basic Research Laboratories, 3-1 Morinosato-Wakamiya, Atsugi, Kanagawa 243-0198, Japan. [6] National Institute of Informatics, 2-1-2 Hitotsubashi, Chiyoda-ku, Tokyo 101-8430, Japan. [7] Wolfgang Pauli Institut c/o Fakultät für Mathematik Universität Wien, Oskar Morgensternplatz 1, 1090 Vienna, Austria.
*These authors contributed equally to this work.
†Corresponding author. Email: johannes.majer@tuwien.ac.at

equations, formally equivalent to the well-known Maxwell-Bloch equations (*28*) as

$$\begin{aligned}\dot{a} &= -\kappa a + \sum\nolimits_j g_j \sigma_j^- + \eta \\ \dot{\sigma}_j^- &= -(\gamma_\perp + i\Theta_j)\sigma_j^- + g_j \sigma_j^z a \\ \dot{\sigma}_j^z &= -\gamma_\parallel(1+\sigma_j^z) - 2g_j(\sigma_j^- a^\dagger + \sigma_j^+ a)\end{aligned} \tag{2}$$

with cavity dissipation rate κ, transversal spin relaxation rate $\gamma_\perp = 1/T_2$, and longitudinal spin relaxation rate $\gamma_\parallel = 1/T_1$. The relaxation rates are ordered as $\kappa > \gamma_\perp \gg \gamma_\parallel$ such that the longitudinal decay of the spin inversion is by far the slowest process. $\Theta_j$ are the frequency detunings with respect to the ensemble central frequency to account for inhomogeneous broadening. Setting the time derivatives to zero, the steady state of this system can be written as

$$|a|^2 = \frac{\eta^2}{\kappa^2}\left(1 - \sum\nolimits_j C_j \sigma_j^z\right)^{-2}, \quad \sigma_j^z = -\left(1 + \frac{4g_j^2|a|^2\gamma_\perp}{\gamma_\parallel(\gamma_\perp^2 + \Theta_j^2)}\right)^{-1} \tag{3}$$

where the dimensionless parameter $C_j = g_j^2/[\kappa\,\gamma_\perp(1 + \Theta_j^2/\gamma_\perp^2)]$ is the single-spin cooperativity. The collective system cooperativity is given accordingly by $C_{\text{coll}} = \sum_j C_j$.

We can classify the expected system phase transition by deriving a solution for the time-dependent cavity amplitude $|a(t)|^2$. The difference in dissipation rates allows us to adiabatically eliminate the $a$ and $\sigma^{j-}$ variables (*29*), which results in a first-order differential equation for the intracavity intensity. For the giant $S_z = \sum_j \sigma_j^z$ spin in resonance ($\Theta_j = 0$) with the cavity mode, it can be written as

$$\frac{d|a|^2}{dt} = -\frac{8C_{\text{coll}}\kappa^2|a|^5}{\eta} + 8C_{\text{coll}}\kappa|a|^4 - \frac{2\kappa\gamma_\parallel}{\eta}(1 + C_{\text{coll}})|a|^3 + 2\gamma_\parallel|a|^2 \tag{4}$$

For our typical system parameters and a strong enough coupling, this equation predicts a first-order phase transition that connects a strongly driven branch and a weakly driven branch, with hysteresis and two saddle-node bifurcations (*30*) at which the transition between both branches occurs.

In contrast to amplitude bistability using a small number of emitters (*25*, *26*), in our case, the sizeable number of spins allows us to neglect quantum fluctuations, which means that a blinking between the two stable solutions does not occur on an experimentally accessible time scale.

## The hybrid quantum system

The hybrid system is shown in Fig. 1 and is composed of an electron spin ensemble formed by NV centers in diamond, loaded onto a superconducting λ/2 resonator. To thermally polarize the $N \approx 10^{12}$ electron spins to their ground state (≥99%), we put the system in a dilution refrigerator at 25 mK. Each electron spin has a zero-field splitting of $D/2\pi \approx$ 2.878 GHz and an average coupling rate of $g_0/2\pi \approx 12$ Hz to the cavity mode. We estimate the transversal relaxation rate as $\gamma_\perp/2\pi \leq 33$ kHz and the longitudinal relaxation rate as $\gamma_\parallel/2\pi \leq 3.6$ mHz (see Materials and Methods) (*18*, *24*). The superconducting resonator has a cavity linewidth of $\kappa/2\pi = (440 \pm 10)$ kHz (half width at half maximum) with a fundamental resonance frequency at $\omega_c/2\pi = 2.691$ GHz and a loaded quality factor of $Q = 3300$. An external microwave field with frequency $\omega_p$ is used to probe the hybrid system.

## Steady-state amplitude bistability

First, we search for the bistable behavior in the steady state by measuring the transmitted intensities through the cavity, defined by $|T|^2 = P_{\text{out}}/P_{\text{in}}$ as a function of the input drive intensity $P_{\text{in}} \approx \eta^2/\kappa$ and outgoing intensity $P_{\text{out}} \approx |a|^2\,\kappa$. The drive power is raised in a stepwise manner, which is slow enough to allow the system to reach a steady state for each stimulus $P_{\text{in}}$. For small excitations, the intracavity intensity is not sufficient to saturate the spin ensemble ($\sigma_j^z \approx -1$) and is thus given by $|a|^2 = \eta^2/[\kappa(1 + C_{\text{coll}})^2]$. As the power level increases, the cavity field bleaches the spins ($\sigma_j^z \approx \sigma_j^- \approx 0$) such that the Rabi splitting vanishes and the spin system decouples from the cavity (Fig. 2). The intracavity intensity $|a|^2 = \eta^2/\kappa^2$ is that of an empty cavity from which spins are completely decoupled.

This nonlinear saturation behavior is a necessary precursor to the observation of amplitude bistability. However, whether this is observable in the experiment is determined by the system's collective cooperativity. This is apparent from Eq. 3, where larger cooperativity values result in stronger nonlinearity and thus a larger phase separation.

In contrast to a homogeneously broadened spin ensemble where analytic expressions for the critical cooperativity to observe bistability exist ($C_{\text{coll}} \geq 8$) (*10*), the inhomogeneous broadening requires numerical solutions to determine the bistability threshold (see Materials and Methods). The finite width of the spin distribution markedly increases the required collective cooperativity for which bistability can be observed (*31*). In the present case of an inhomogenously broadened line with $\Gamma/2\pi = 9.5$ MHz (full width at half maximum), we predict a critical cooperativity of $C_{\text{coll}} = 42.4$. For lower values of the collective cooperativity, the intracavity intensity as a function of the input drive is a continuous function, whereas at the critical cooperativity, the system response

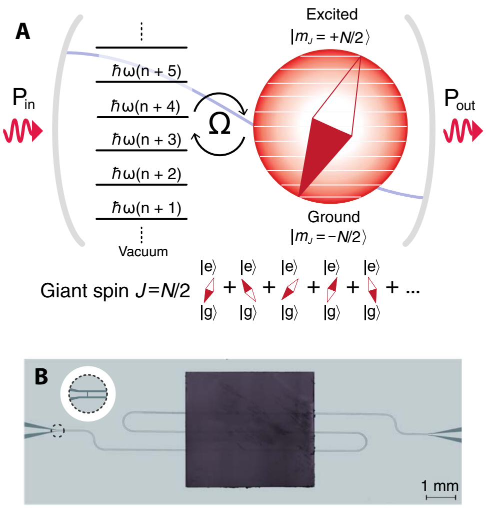

**Fig. 1. Hybrid quantum system.** (**A**) Experimental setup. Schematic illustration of our experimental setup in which an ensemble of spins (described as an effective giant spin) is inductively coupled (with a coupling rate Ω) to the cavity mode. The nonlinearity stems from the anharmonicity of this coupled spin when driven beyond its linear regime, which we probe through the transmission $|T|^2 = P_{\text{out}}/P_{\text{in}}$ of the hybrid system. (**B**) Photograph of the system consisting of a superconducting transmission line cavity with an enhanced neutron-irradiated diamond on top of it, containing a large ensemble of NV spins (black). Two coupling capacitors provide the necessary boundary conditions for the microwave radiation.

becomes a step function and, at two critical drive values $P_{\mathrm{crit}}^{\mathrm{u}}$ and $P_{\mathrm{crit}}^{\mathrm{d}}$ (see Fig. 3, B and C), the system switches between these two branches undergoing a first-order phase transition.

In Fig. 3, we show steady-state bistability measurements for three cooperativity values $C_{\mathrm{coll}} = 18$, 49, and 78. The lowest value $C_{\mathrm{coll}} = 18$ does not show bistability (Fig. 3A), but increasing the cooperativity to $C_{\mathrm{coll}} = 49$ (see Materials and Methods) allows us to observe the first signs of bistable behavior (Fig. 3B). This value is close to the expected value for the critical cooperativity of $C_{\mathrm{coll}} = 42.2$ for our system parameters. Increasing the cooperativity further to $C_{\mathrm{coll}} \approx 78$, we observe amplitude bistability (Fig. 3C) within a 2-dB range. This steady-state bistability behavior is well reproduced by a full numerical simulation, with inhomogeneous broadening taken into account (dashed lines in Fig. 3, A to C).

## Quench dynamic measurements

Given this evidence of amplitude bistability, we focus next on the temporal behavior of the hybrid system using quench dynamic measurements. We start by preparing the spin ensemble in one of the two extremal states, either polarized in the ground state or completely saturated and decoupled from the cavity. These initial states are prepared by setting the cavity input power to $P_{\mathrm{in}} = 0$ or $P_{\mathrm{in}} \gg P_{\mathrm{crit}}^{\mathrm{d}}$ for several minutes, respectively. The drive power is then nonadiabatically switched to a different drive level, and the system transmission is monitored. We repeat this measurement several times, always preparing the system in the same initial state but switching to different target drive powers. When the system is driven close to the bifurcation point ($P_{\mathrm{in}} \approx P_{\mathrm{crit}}^{\mathrm{d}}$), the time scales needed to settle in a stationary state become as long as $4 \times 10^{4}$ s, as depicted in Fig. 4.

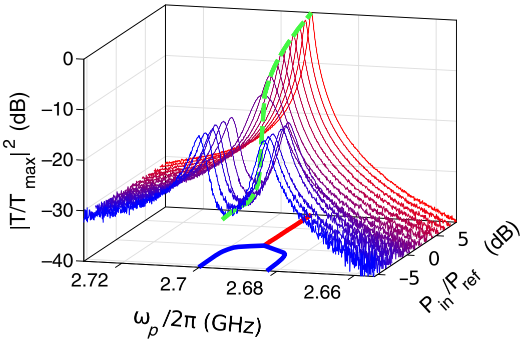

**Fig. 2. Rabi splitting under different drive powers.** Evolution of the transmission spectrum for different input drive powers $P_{\mathrm{in}}$. In the linear regime, the Rabi splitting is observable. For a drive power $P_{\mathrm{in}} \approx P_{\mathrm{ref}}$, the spin system starts to bleach and decouples from the cavity. For input drives $P_{\mathrm{in}} \gg P_{\mathrm{ref}}$, we observe the bare cavity transmission function. This behavior can be seen from the projection of the observed maximum transmission peaks on the *xy* plane. When driving the system resonantly (green dashed line) and with a large enough cooperativity, operating between these two regimes exhibits amplitude bistability.

The behavior can be linked to our model given in Eq. 4, which predicts that our system features two critical drive values $P_{\mathrm{crit}}^{\mathrm{u}}$ and $P_{\mathrm{crit}}^{\mathrm{d}}$ at which a saddle-node bifurcation occurs (*30*). For input powers between $P_{\mathrm{crit}}^{\mathrm{u}}$ and $P_{\mathrm{crit}}^{\mathrm{d}}$, two attractors coexist, and the system evolves to one of these attractors, depending on whether they are approached from below or above the bistable region. These two attractors, one with polarized and ordered spins and the other one with unordered and saturated spins, are connected by a first-order phase transition if the system cooperativity is large enough (see Fig. 3C). When driven far away from the critical drive values either in the strongly or in the weakly driven branch, the system approaches a steady state on a characteristic time scale determined by the slowest decay rate in the system—given by the longitudinal decay $\gamma_{\parallel}$ for our implementation. The system settles in a stationary state at which the external drive and dissipation are equal and opposite in effect. Close to the critical points $P_{\mathrm{crit}}^{\mathrm{d}}$ and $P_{\mathrm{crit}}^{\mathrm{u}}$, the system becomes scale-invariant and is characterized by an infinite correlation time (*32*)—an effect referred to as "critical slowing down" (*15*, *33*). In the presented experiment, we deal with a saddle-node bifurcation, where the dynamics exhibits power law divergence close to the critical drive value.

This behavior is shown in Fig. 4 (A to C) where, close to the critical drive, the system evolves toward the upper unstable fixed point, with a time derivative that can approach zero arbitrarily closely (inset in Fig. 4B). Small deviations from the critical drive lead to a speed up in the evolution until the system relaxes to a real steady state. The time it takes to go from the upper to the lower branch diverges close to the critical drive according to $t_{\mathrm{switch}} \approx |P_{\mathrm{in}} - P_{\mathrm{crit}}^{\mathrm{d}}|^{-\alpha}$, as shown in Fig. 4C, with $\alpha \approx 1.20 \pm 0.04$. For the simplest case of a saddle-node bifurcation after a cubic

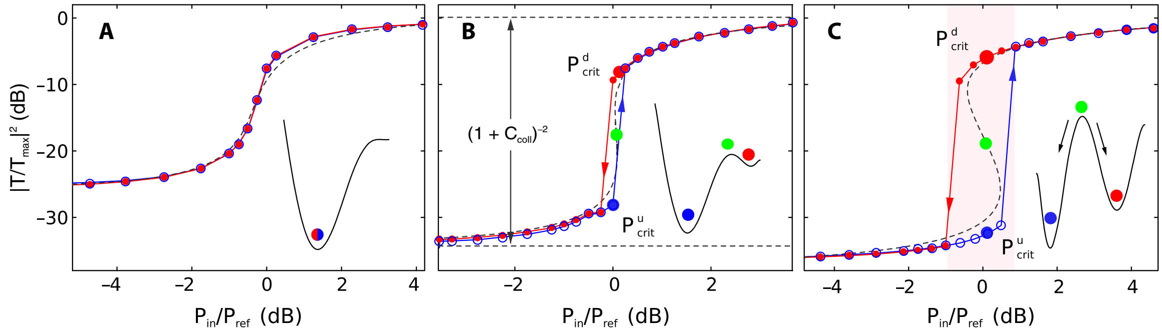

**Fig. 3. Steady-state bistability.** We measure the steady-state bistability transmission through the cavity as a function of increasing (blue) and decreasing (red) input power $P_{\mathrm{in}}$. In (**A**), the transmission measurements are plotted for the cooperativity value $C_{\mathrm{coll}} \approx 18$ and $\kappa/2\pi = 1.2$ MHz using two subensembles in resonance with the cavity. (**B**) Same transmission measurement with $C_{\mathrm{coll}} \approx 49$ and $\kappa/2\pi = 0.44$ MHz. A small bistability area is visible where the system evolves to different steady states depending on the history of the system in either upper or lower branch. (**C**) Same measurement as in (A), with an increased cooperativity of $C_{\mathrm{coll}} \approx 78$ (by using all four NV subensembles in resonance with the cavity), again with $\kappa/2\pi = 0.44$ MHz. The dashed curves are numerical solutions of Eq. 3. The dashed lines in (B) show the asymptotic solutions in the limit of large and small drive amplitudes $\eta$. Two critical values of the input power, at which a phase transition between two stable branches occurs, are characterized by a saddle-node bifurcation and labeled as $P_{\mathrm{crit}}^{\mathrm{u}}$ and $P_{\mathrm{crit}}^{\mathrm{d}}$. For all three cases, a sketch of the corresponding potential is also depicted, which shows the occurrence of either one or two stable solutions (red and blue solid circles) and one unstable solution (B and C) (green solid circles) for a fixed value of the input power. Tunneling through the potential barrier does not occur in our case because of the large system size such that the system does not switch back and forth between the steady states in the bistable area.

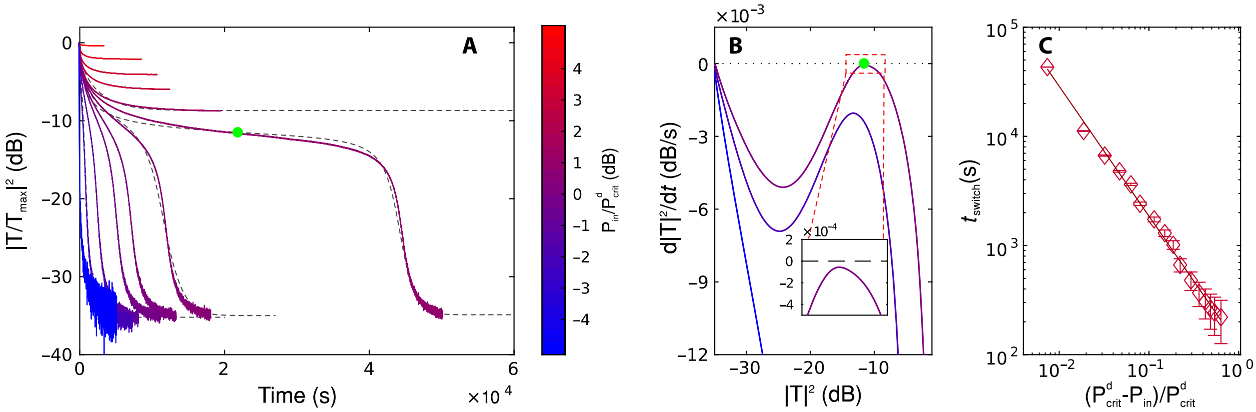

**Fig. 4. Quench dynamics measurement.** Quench dynamics of the high cooperativity $C_{coll} \approx 78$ configuration and an initial state far in the strong driving branch. In (**A**), the intracavity intensity $|T|^2/|T_{max}|^2$ is plotted over time for different drive intensities where the time to reach a steady state strongly depends on the input intensity. For drive intensities larger than a critical drive value $P^d_{crit}$ (defined as the power where the system undergoes the phase transition from the upper to the lower branch, see Fig. 3), the spin system remains saturated and sets into a state on the upper branch, whereas in the opposite case, the system evolves into a steady state on the lower branch. Close to the critical drive $P^d_{crit}$, this time scale is extremely prolonged and approaches $4 \times 10^4$ s. The dashed lines correspond to predictions from our model. In (**B**), we show the phase diagram as $d|T|^2/dt$ over $|T|^2$ for the evolution toward a steady state (black dotted line) for different input drives $P_{in}$. For drive powers close to the critical drive, the derivative approaches zero, and the dynamics becomes much slower compared to drive powers larger and smaller than the critical drive. In (**C**), the switching times between the upper and lower branch for different input drives are shown. We define the switching time $t_{switch}$ as the inverse of the smallest gradient for a given curve [green circle in (A) and (B)]. Close to the critical drive, the switching time diverges, and the time to reach a steady state becomes arbitrarily long. The solid red line is a fitting function of the form $t_{switch} \approx |P_{in} - P^d_{crit}|^{-\alpha}$ (with $\alpha = 1.20 \pm 0.04$).

function, the phase transition shows an algebraic divergence with a critical exponent $\alpha = 1$. The more complicated set of equations in the present case changes this critical exponent to the larger value $\alpha \approx 1.20 \pm 0.04$. The exact value depends on the precise structure of the so-called normal form (*34*), as given by Eq. 4 for the homogeneously broadened case. Comparing these experimental results with the full numerical solutions of Eq. 2, including inhomogeneous broadening, we observe excellent agreement (see Fig. 4A). For the quench from low-power levels to the high-power levels, we observe a similar behavior with the same critical exponent.

## DISCUSSION

In summary, we have shown how a hybrid system composed of a superconducting resonator coupled to an electron spin ensemble in diamond can be used to explore amplitude bistability in new regimes of cQED, with unusual decay rates where the spin lifetime is much longer than other decay constants in the system. This regime allows us to study the temporal evolution of the phase transition explicitly, something experimentally difficult to achieve using the standard cQED implementations. We observe a critical slowing down of the cavity population on the order of 11 hours, a time scale several orders of magnitude longer than observed so far for this effect and many orders of magnitude longer than other time scales associated with the system. Our experiment provides a foundation for the exploration of additional nonlinear phenomena in quantum metamaterials and future quantum technologies that may arise from it. One of the possible applications is microwave isolators and diodes that make use of the fact that the transmission intensity is different depending on the history of the system. For a large enough value of the collective cooperativity, our system provides an isolation of more than four orders of magnitude for a given input power in the bistable regime. By reducing the number of emitters, the nonlinearity in the system provides a way to create nonclassical states, such as spin-squeezed states, which are impossible to realize in a purely linear system. This paves the way toward possible applications in high-sensitivity magnetic field sensing and quantum metrology.

## MATERIALS AND METHODS

### Sample

The spin system was realized by enhancing a type Ib high-pressure high-temperature diamond crystal containing an initial concentration of 200 parts per million (ppm) of nitrogen, with a natural abundance of $^{13}$C nuclear isotopes. We achieved NV$^-$ centers with a total density of ≈6 ppm by 50 hours of neutron irradiation with a fluence of $5 \times 10^{17}$ cm$^{-2}$ and by annealing the crystal for 3 hours at 900°C. Excess nitrogen P1 centers ($S = 1/2$), uncharged NV$^0$ centers, and additional lattice stress are the main source of inhomogeneous broadening, which exceeds decoherence because of the naturally abundant 1.1% $^{13}$C spin bath. The characteristics of the diamond crystal and NV ensemble were initially determined at room temperature using an optical confocal microscope.

### Spin system

The NV$^-$ center is a paramagnetic point-defect center in the diamond with an electron spin $S = 1$, consisting of a nitrogen atom replacing a carbon atom in the diamond lattice and an adjacent vacancy. The ground spin triplet can be described by a simplified Hamiltonian $H = \hbar D S_z^2 + \hbar \mu B_z S_z$, with $\mu = 28$ MHz/mT and a large zero-field splitting of $D/2\pi = 2.877$ GHz. The splitting corresponds to a temperature of $D/hk_b = 138$ mK, which allows to thermally polarize the spins in the ground state at the fridge base temperature of 25 mK with up to 99% fidelity. Because of its crystallographic diamond structure, four different NV subensembles, with equal abundance (pointing in the [1, 1, 1] direction), exist. By applying $B \approx 30$ mT with either 0° or 45° relative to the [1, 0, 0] direction in the NV resonator plane, we could Zeeman-tune four or two NV subensembles into resonance with the cavity mode.

### Superconducting resonator

The microwave cavity was loaded by placing the diamond sample on top of a λ/2 transmission line resonator. The superconducting microwave cavity was fabricated by optical lithography and reactive ion etching of a 200-nm-thick niobium film sputtered on a 330-nm-thick sapphire substrate. The loaded chip was hosted and bonded to a printed circuit board enclosed in a copper sarcophagus and connected to microwave transmission lines. The cavity exhibited a linewidth of $\kappa/2\pi = 440$ kHz, which we could increase to $\kappa/2\pi = 1.2$ MHz by applying weak magnetic fields perpendicular to the resonator plane that partially quenched the superconducting material. The cavity was coupled to the environment such that the internal losses of the cavity were much smaller than the coupling losses ($\kappa_{\text{int}} \ll \kappa_{\text{ext}}$). This allowed us to approximate the total losses as $\kappa \approx \kappa_{\text{ext}}$.

### Transmission measurements

Transmission measurements were performed by recording the forward scattering parameter $|S_{21}|^2$ of the hybrid system using a standard vector network analyzer (Agilent E5071C). To perform steady-state bistability measurements, we probed the system first with increasing power levels. For each power level, we monitored the transition until a steady state was reached. We increased the drive power until the steady state lay far in the high driving branch, after which the power was lowered again in a stepwise manner. We identified bistability if the system showed different steady states when driven with increasing and decreasing power. From Eq. 3, we immediately found that the asymptotic behavior of the transmission intensity $|\mathrm{T}|^2 = |a|^2\kappa^2/\eta^2$ is described by $|\mathrm{T}_{\text{low}}|^2 = (1 + C_{\text{coll}})^{-2}$ in the single excitation regime and by $|\mathrm{T}_{\text{high}}|^2 = 1$ in the large excitation regime. The difference in the transmission between these two regimes is therefore only determined by the collective cooperativity $C_{\text{coll}} = \Sigma_j\, g_j^2/[\kappa\, \gamma_\perp(1 + \Theta_j^2/\gamma_\perp^2)]$.

### Quench dynamic measurements

Quench dynamics measurements were used to measure the temporal behavior of the observed effect. For this, we initialized the system in an initial state far in the large driving regime with a strong drive for several minutes. After this state preparation where the spin system was completely decoupled from the cavity, the drive power was nonadiabatically switched to a lower drive, with transmission monitored for different target drive levels. We monitored the transmission until the time derivative of the transmission amplitude became smaller than an arbitrarily chosen threshold, which we then identified as our steady state.

### Transversal decay rate

We used Car-Purcell-Meiboom-Gill–like sequences to get an estimate for the spin-spin relaxation time ($T_2 = 1/\gamma_\perp$). The best achievable echo times in our experiment were $T_2 = (4.8 \pm 1.6)$ μs, which we identified as a lower bound for our relaxation times. The real spin-spin relaxation times were potentially longer, but misalignment of the external dc magnetic field with respect to the $\mathrm{NV}^-$ axis and a bath of excess electron and nuclear spins in the host material limited the echo time to times shorter than the real relaxation times.

### Longitudinal decay rate

To get a value for $\gamma_\parallel$, we used the dispersive shift of the cavity mode coupled to a detuned spin system. To enter the dispersive regime, we detuned the spin system such that the detuning was much larger than the collective coupling strength Ω. The spin system acted as a refractive medium that shifted the resonance frequency if the spin system was polarized in the ground state. By applying a strong microwave tone, we excited a fraction of the $\mathrm{NV}^-$ ensemble, which led to a shift of the resonator frequency. We monitored this frequency shift over time, while the spin system relaxed back into its thermal equilibrium state with the characteristic rate $\gamma_\parallel$. This gave a lower bound for the longitudinal relaxation time of $T_1 = 44$ s (*18*), justifying the adiabatic elimination technique. The real longitudinal relaxation times were potentially longer, but spin diffusion processes by spin-spin interaction between neighboring $\mathrm{NV}^-$ center spins and additional electron spins limited the measured relaxation times to times shorter than the intrinsic longitudinal relaxation times.

### Theoretical modeling

To calculate the quench dynamics displayed in Fig. 4, we numerically solved the Maxwell-Bloch equations (Eq. 2) for the driving signals chosen nearby the first-order transition (see the main text for details) using the standard Runge-Kutta method. As an initial condition, we took the steady state given by Eq. 3, which lay on the upper branch depicted in Fig. 3C and corresponded to the limit of strong driving with $|\sigma_j^z|, |\sigma_j^-| \ll 1$. To accurately describe the dynamics and to achieve a good correspondence with experimental data, we took into account the effect of an inhomogeneous broadening by modeling the spin density with a *q*-Gaussian shape for the spin density, $\rho(\omega) = \zeta\,[1 - (1 - q)\,(\omega - \omega_s)^2/\Delta^2]^{1/(1-q)}$, distributed around the mean frequency $\omega_s/2\pi = 2.6915$ GHz, with the parameter $q = 1.39$, the width $\Delta/2\pi = 5.3$ MHz, and a normalization constant ζ. Such a shape for ρ(ω) was previously established by obtaining an excellent agreement between our theoretical model and the experiment, when treating the problem in the framework of the Volterra equation valid in the limit of weak driving signals (*35*). We then straightforwardly discretized our problem by performing the transformation $g_j = \Omega[\rho(\omega_j)/\Sigma_l\, \rho(\omega_l)]^{1/2}$, where $\Omega^2 = \Sigma_j\, g_j^2$ stands for the collective coupling strength [$\Omega/2\pi = 9.6$ MHz (Fig. 3, A and B) and 12.6 MHz (Fig. 3C)]. Because, in total, we dealt with a sizable number of spins ($N \approx 10^{12}$), we made our problem numerically tractable by dividing spins into many subgroups with approximately the same coupling strengths so that the numerical values for $g_j$ in Eq. 2 represent a coupling strength within each subgroup rather than an individual coupling strength.

### Critical cooperativity

From Eq. 3, it was straightforward to derive a condition for the threshold of bistability, which was accompanied by a negative slope of the driving strength η as a function of the transmission amplitude |a|. It is given by the following inequality

$$\frac{d\eta}{d|a|} = \kappa + \sum_k \frac{g_k^2\gamma_\parallel\gamma_\perp}{\gamma_\parallel(\gamma_\perp^2 + \Theta_k^2) + 4g_k^2|a|^2\gamma_\perp} +$$

$$\sum_k \frac{g_k^2\gamma_\parallel\gamma_\perp \cdot 8g_k^2\gamma_\perp|a|^2}{(\gamma_\parallel(\gamma_\perp^2 + \Theta_k^2) + 4g_k^2|a|^2\gamma_\perp)^2} \leq 0$$

For the simple case of a homogeneous spin ensemble, this condition could be solved analytically, giving the well-known threshold for bistability of $C_{\text{coll}} > 8$. In the case of inhomogeneous broadening, the required collective cooperativity to observe bistability increased markedly as compared to the homogeneous case (*31*). Numerical simulations show that, for the *q*-Gaussian spin distribution used in our manuscript, the effect of bistability can be observed for $C_{\text{coll}} > 42.2$, which corresponds to a collective coupling of $\Omega/2\pi = 8.86$ MHz. The threshold for bistability depends not only on the width of the distribution but also on its specific shape. Changing from a *q*-Gaussian to a Gaussian or a Lorentzian spin distribution changes the threshold to $C_{\text{coll}} > 40.8$ or $C_{\text{coll}} > 45.2$, respectively (by changing only the coupling strength while keeping all other parameters constant).

### Adiabatic elimination

Using the fact that $\gamma_{\parallel} \ll \kappa, \gamma_{\perp}$, and $\Omega$, the dynamics at large times (when $t \gg 1/\kappa$, $1/\gamma_{\perp}$, and $2\pi/\Omega$) could be considerably simplified because the cavity amplitude $a$ and the spin lowering expectation values $\sigma_j^-$ adiabatically follow the evolution of the $z$ component of the spin operator expectation value $\sigma_j^z$. By introducing the small parameter $\epsilon = \gamma_{\parallel}/\gamma_{\perp}$ and the slow dimensionless time $\tau = \gamma_{\parallel} t$, we finally derived a first-order differential Eq. 4 for the intracavity intensity $|a|^2$.

## REFERENCES AND NOTES

1. H. M. Gibbs, S. L. McCall, T. N. C. Venkatesan, A. C. Gossard, A. Passner, W. Wiegmann, Optical bistability in semiconductors. *Appl. Phys. Lett.* **35**, 451–453 (1979).
2. V. G. Benza, S. W. Koch, Symmetry breaking and metastable chaos in a coherently driven superradiant system. *Phys. Rev. A* **35**, 174–183 (1987).
3. L. F. Mollenauer, R. H. Stolen, J. P. Gordon, Experimental observation of picosecond pulse narrowing and solitons in optical fibers. *Phys. Rev. Lett.* **45**, 1095–1098 (1980).
4. R. H. Dicke, Coherence in spontaneous radiation processes. *Phys. Rev.* **93**, 99–110 (1954).
5. A. Szöke, V. Daneu, J. Goldhar, N. A. Kurnit, Bistable optical element and its applications. *Appl. Phys. Lett.* **15**, 376–379 (1969).
6. W. Casteels, F. Storme, A. Le Boité, C. Ciuti, Power laws in the dynamic hysteresis of quantum nonlinear photonic resonators. *Phys. Rev. A* **93**, 033824 (2016).
7. R. Bonifacio, P. Meystre, Transient response in optical bistability. *Opt. Commun.* **27**, 147–150 (1978).
8. R. Sawant, S. A. Rangwala, Optical-bistability-enabled control of resonant light transmission for an atom-cavity system. *Phys. Rev. A* **93**, 023806 (2016).
9. A. Dombi, A. Vukics, P. Domokos, Optical bistability in strong-coupling cavity QED with a few atoms. *J. Phys. B At. Mol. Opt.* **46**, 224010 (2013).
10. M. J. Martin, D. Meiser, J. W. Thomsen, J. Ye, M. J. Holland, Extreme nonlinear response of ultranarrow optical transitions in cavity QED for laser stabilization. *Phys. Rev. A* **84**, 063813 (2011).
11. G. Rempe, R. J. Thompson, R. J. Brecha, W. D. Lee, H. J. Kimble, Optical bistability and photon statistics in cavity quantum electrodynamics. *Phys. Rev. Lett.* **67**, 1727–1730 (1991).
12. H. J. Kimble, Strong interactions of single atoms and photons in cavity QED. *Phys. Scr.* **T76**, 127–137 (1998).
13. R. Bonifacio, L. A. Lugiato, Cooperative effects and bistability for resonance fluorescence. *Opt. Commun.* **19**, 172–176 (1976).
14. F. Mitschke, R. Deserno, J. Mlynek, W. Lange, Transients in all-optical bistability using transverse optical pumping: Observation of critical slowing down. *Opt. Commun.* **46**, 135–140 (1983).
15. E. Garmire, J. H. Marburger, S. D. Allen, H. G. Winful, Transient response of hybrid bistable optical devices. *Appl. Phys. Lett.* **34**, 374–376 (1979).
16. A. İmamoğlu, Cavity QED based on collective magnetic dipole coupling: Spin ensembles as hybrid two-level systems. *Phys. Rev. Lett.* **102**, 083602 (2009).
17. Y. Kubo, C. Grezes, A. Dewes, T. Umeda, J. Isoya, H. Sumiya, N. Morishita, H. Abe, S. Onoda, T. Ohshima, V. Jacques, A. Dréau, J.-F. Roch, I. Diniz, A. Auffeves, D. Vion, D. Esteve, P. Bertet, Hybrid quantum circuit with a superconducting qubit coupled to a spin ensemble. *Phys. Rev. Lett.* **107**, 220501 (2011).
18. R. Amsüss, Ch. Koller, T. Nöbauer, S. Putz, S. Rotter, K. Sandner, S. Schneider, M. Schramböck, G. Steinhauser, H. Ritsch, J. Schmiedmayer, J. Majer, Cavity QED with magnetically coupled collective spin states. *Phys. Rev. Lett.* **107**, 060502 (2011).
19. D. I. Schuster, A. P. Sears, E. Ginossar, L. DiCarlo, L. Frunzio, J. J. L. Morton, H. Wu, G. A. D. Briggs, B. B. Buckley, D. D. Awschalom, R. J. Schoelkopf, High-cooperativity coupling of electron-spin ensembles to superconducting cavities. *Phys. Rev. Lett.* **105**, 140501 (2010).
20. Z.-L. Xiang, S. Ashhab, J. Q. You, F. Nori, Hybrid quantum circuits: Superconducting circuits interacting with other quantum systems. *Rev. Mod. Phys.* **85**, 623–653 (2013).
21. G. Kurizki, P. Bertet, Y. Kubo, K. Mølmer, D. Petrosyan, P. Rabl, J. Schmiedmayer, Quantum technologies with hybrid systems. *Proc. Natl. Acad. Sci.* **112**, 3866–3873 (2015).
22. F. Jelezko, T. Gaebel, I. Popa, A. Gruber, J. Wrachtrup, Observation of coherent oscillations in a single electron spin. *Phys. Rev. Lett.* **92**, 076401 (2004).
23. M. W. Doherty, N. B. Manson, P. Delaney, F. Jelezko, J. Wrachtrup, L. C. L. Hollenberg, The nitrogen-vacancy colour centre in diamond. *Phys. Rep.* **528**, 1–45 (2013).
24. A. Jarmola, V. M. Acosta, K. Jensen, S. Chemerisov, D. Budker, Temperature- and magnetic-field-dependent longitudinal spin relaxation in nitrogen-vacancy ensembles in diamond. *Phys. Rev. Lett.* **108**, 197601 (2012).
25. J. M. Fink, A. Dombi, A. Vukics, A. Wallraff, P. Domokos, Observation of the photon-blockade breakdown phase transition. *Phys. Rev. X* **7**, 011012 (2017).
26. S. R. K. Rodriguez, W. Casteels, F. Storme, N. Carlon Zambon, I. Sagnes, L. Le Gratiet, E. Galopin, A. Lemaître, A. Amo, C. Ciuti, J. Bloch, Probing a dissipative phase transition via dynamical optical hysteresis. *Phys. Rev. Lett.* **118**, 247402 (2017).
27. M. Tavis, F. W. Cummings, Exact solution for an *N*-molecule—Radiation-field Hamiltonian. *Phys. Rev.* **170**, 379–384 (1968).
28. R. Bonifacio, L. A. Lugiato, in *Dissipative Systems in Quantum Optics, Topics in Current Physics* (Springer-Verlag, 1982), pp. 61–92.
29. L. Lugiato, F. Prati, M. Brambilla, *Nonlinear Optical Systems* (Cambridge Univ. Press, 2015).
30. S. H. Strogatz, *Nonlinear Dynamics and Chaos: With Applications to Physics, Biology, Chemistry, and Engineering* (Westview Press, 2001).
31. S. S. Hassan, P. D. Drummond, D. F. Walls, Dispersive optical bistability in a ring cavity. *Opt. Commun.* **27**, 480–484 (1978).
32. A. Polkovnikov, K. Sengupta, A. Silva, M. Vengalattore, *Colloquium*: Nonequilibrium dynamics of closed interacting quantum systems. *Rev. Mod. Phys.* **83**, 863–883 (2011).
33. G. Grynberg, S. Cribier, Critical exponents in dispersive optical bistability. *J. Phys. Lett. Paris* **44**, 449–453 (1983).
34. C. Kuehn, Scaling of saddle-node bifurcations: Degeneracies and rapid quantitative changes. *J. Phys. A Math. Theor.* **42**, 045101 (2009).
35. D. O. Krimer, S. Putz, J. Majer, S. Rotter, Non-Markovian dynamics of a single-mode cavity strongly coupled to an inhomogeneously broadened spin ensemble. *Phys. Rev. A* **90**, 043852 (2014).

**Acknowledgments:** We thank H. Ritsch, M. Trupke, and A. Amo for the helpful discussions. **Funding:** The experimental effort led by J.M. was supported by the Top-/Anschubfinanzierung grant of Technische Universität Wien. S.P., A.A., and T.A. acknowledge support from the Austrian Science Fund (FWF) in the framework of the Doctoral School Building Solids for Function Project W1243. D.O.K. and S.R. acknowledge funding from the Austrian Science Fund (FWF) through the Spezialforschungsbereich NextLite Project no. F49-P10. K.N. acknowledges support from the Ministry of Education, Culture, Sports, Science and Technology (MEXT) through the KAKENHI Grant-in-Aid for Scientific Research on Innovative Areas Science of hybrid quantum systems grant no. 15H05870. **Author contributions:** S.P. and D.O.K. conceived the idea, and S.P., J.S., and J.M. designed and set up the experiment. A.A., S.P., R.G., T.A., and K.S. performed the measurements under the supervision of J.M. D.O.K., M.Z., and S.R. devised the theoretical framework and provided the theoretical support for modeling the experiment. K.N. and W.J.M. provided support for the implementation of the theoretical methods. A.A. wrote the manuscript to which all authors suggested improvements. **Competing interests:** The authors declare that they have no competing interests. **Data and materials availability:** All data needed to evaluate the conclusions in the paper are present in the paper. Additional data related to this paper may be requested from the authors.

Submitted 16 May 2017
Accepted 9 November 2017
Published 8 December 2017
10.1126/sciadv.1701626

**Citation:** A. Angerer, S. Putz, D. O. Krimer, T. Astner, M. Zens, R. Glattauer, K. Streltsov, W. J. Munro, K. Nemoto, S. Rotter, J. Schmiedmayer, J. Majer, Ultralong relaxation times in bistable hybrid quantum systems. *Sci. Adv.* **3**, e1701626 (2017).

Science Advances

# Ultralong relaxation times in bistable hybrid quantum systems

Andreas Angerer, Stefan Putz, Dmitry O. Krimer, Thomas Astner, Matthias Zens, Ralph Glattauer, Kirill Streltsov, William J. Munro, Kae Nemoto, Stefan Rotter, Jörg Schmiedmayer and Johannes Majer

*Sci Adv* **3** (12), e1701626.
DOI: 10.1126/sciadv.1701626

---

PHYSICAL REVIEW A **89**, 033820 (2014)

# Route from spontaneous decay to complex multimode dynamics in cavity QED

Dmitry O. Krimer, Matthias Liertzer, and Stefan Rotter
*Institute for Theoretical Physics, Vienna University of Technology, A-1040 Vienna, Austria*

Hakan E. Türeci
*Department of Electrical Engineering, Princeton University, Princeton, New Jersey 08544, USA*
(Received 17 June 2013; published 11 March 2014)

We study the non-Markovian quantum dynamics of an emitter inside an open multimode cavity, focusing on the case where the emitter is resonant with high-frequency cavity modes. Based on a Green's-function technique suited for open photonic structures, we study the crossovers between three distinct regimes as the coupling strength is gradually increased: (i) overdamped decay with a time scale given by the Purcell modified decay rate, (ii) underdamped oscillations with a time scale given by the effective vacuum Rabi frequency, and (iii) pulsed revivals. The final multimode strong-coupling regime (iii) gives rise to quantum revivals of the atomic inversion on a time scale associated with the cavity round-trip time. We show that the crucial parameter to capture the crossovers between these regimes is the nonlinear Lamb shift, accounted for exactly in our formalism.

DOI: 10.1103/PhysRevA.89.033820 PACS number(s): 42.50.Pq, 42.50.Ar, 42.50.Ct

## I. INTRODUCTION

Controlling the emission properties of quantum systems is at the heart of a number of fields ranging from quantum information processing to single-molecule spectroscopy. In solid-state cavity QED a substantial amount of experimental effort aims at designing highly structured photonic environments in the vicinity of the emitter to achieve a high level of control over its quantum dynamics [1–4]. Much of the earlier work focuses on the resonant coupling to a single confined mode of the photonic structure that has favorable emission properties, while coupling to the rest of the modes of the photonic environment is regarded as a parasitic influence and is either discarded or bulked into a total background spontaneous emission rate in the spirit of Ref. [5]. Recent trends in experimental work, however, point towards spatially highly complex and open photonic structures, where the delineation between a cavity and the radiative environment becomes highly blurred (see, e.g., [6–8]). Such situations are more effectively described through the local density of photonic states (LDOPS) [9–15]. This more powerful and potent theoretical approach has meanwhile fueled a great deal of research on light-matter interaction in fields ranging from cavity QED to photovoltaics [16], giving rise to what may be referred to as LDOPS engineering.

While recent theoretical works have recognized the potential of this method [11–13,17], including those dealing with dispersing and absorbing media [9,18], the lack of a suitable method that allows tackling the often complex non-Markovian dynamics of a two-level-like emitter in a leaky photonic structure was a significant hurdle in revealing novel phenomena that may be at play in a host of modern-day light-confining structures such as periodic [2], deterministic aperiodic [19], and disordered photonic media [6], as well as nanoplasmonic systems [20]. Here we present a formalism for computing the full quantum dynamics of emitters in arbitrarily complex photonic structures based on a single Volterra equation with a spectral function proportional to the LDOPS. We then illustrate the possibility of calculating the LDOPS of open and complex photonic structures employing the non-Hermitian set of constant-flux (CF) states that have been introduced in Ref. [21] to describe steady-state lasing characteristics of lasers. Based on this powerful tool, we explore the dynamics of a quantum emitter in the multimode regime, i.e., when the emitter couples to several modes of the cavity. This regime is notoriously difficult because it leads to highly complex non-Markovian dynamics, but it best illustrates the potency of the method outlined here to provide insight into the various possible time scales of the emitter dynamics. In particular, we discuss a series of crossovers between three dynamical regimes as the coupling strength of the emitter is increased. Some of the aspects of these regimes have been discussed before in the literature within the limited scope of a variety of methods [9,22–27]. The beauty of our approach that we present here is that it provides a unified description, a thorough understanding, and a classification for all of these regimes, with a key parameter being the nonlinear Lamb shift.

## II. THEORETICAL MODEL

The system we study is a typical cavity QED setup consisting of a two-level system (TLS) with transition frequency $\omega_a$ placed inside a cavity. The method we present here is valid for an arbitrarily complex open cavity geometry, but for the sake of transparency we discuss here a Fabry-Pérot cavity formed by two highly reflecting mirrors (see Fig. 1). To describe the excitation dynamics of the TLS we start with the familiar Hamiltonian written in terms of the modes-of-the-universe approach [28], which makes no distinction between the cavity and its environment, $\mathcal{H} = (\hbar\omega_a/2)\sigma_z + \int d\omega\hbar\omega a^\dagger(\omega)a(\omega) + \hbar\sqrt{\gamma/\pi}\int d\omega[g(\omega,\mathbf{r})a(\omega)\sigma^+ + g^\star(\omega,\mathbf{r})a^\dagger(\omega)\sigma^-]$. Here $a^\dagger(\omega)$ and $a(\omega)$ are standard creation and annihilation operators of a photon and $\sigma^+,\sigma^-,\sigma_z$ are the Pauli operators associated with the TLS. The interaction part of $\mathcal{H}$ is written in the electric dipole and rotating-wave approximation, where $g(\omega,\mathbf{r})$ are the coupling amplitudes, and $\gamma$ stands for the coupling strength proportional to the dipole moment squared. Due to the rotating-wave approximation, nonresonant terms (proportional to $a_\lambda\sigma^-$ and $a_\lambda^\dagger\sigma^+$) are absent in this Hamiltonian such that the number of excitations is conserved. We can thus make the following ansatz for the time evolution of the system: $|\Psi(t)\rangle =$

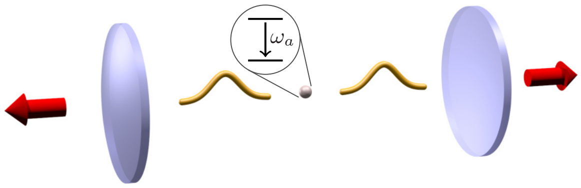

FIG. 1. (Color online) Two-level system with transition frequency $\omega_a$ inside an open cavity.

$c(t)e^{-i\omega_a t/2}|u\rangle|0\rangle + \int d\omega\, c_\omega(t)|l\rangle|1_\omega\rangle e^{-i(\omega-\omega_a/2)t}$, where the ket vectors $|u\rangle$ and $|l\rangle$ stand for the atom in the upper and lower states, respectively, and the ket vectors $|0\rangle$ and $|1_\omega\rangle$ represent the vacuum state and a single photon with the frequency $\omega$. Solving the Schrödinger equation with this ansatz $\mathcal{H}|\Psi(t)\rangle = i\hbar\partial_t|\Psi(t)\rangle$, we arrive at the Volterra equation for the excited-state amplitude of the TLS $c(t)$,

$$\dot{c}(t) = -\frac{\gamma}{\pi}\int_0^t dt' \int_0^\infty d\omega\, F(\omega) e^{-i(\omega-\omega_a)(t-t')} c(t'), \quad (1)$$

where $F(\omega) = \rho(\mathbf{r}_a,\omega)|g(\omega)|^2$ is the spectral function, featuring the LDOPS $\rho(\mathbf{r}_a,\omega)$, evaluated at the emitter position $\mathbf{r} = \mathbf{r}_a$, and $g(\omega)$ is the frequency-dependent coupling amplitude.

Note that Volterra equations as above have already been used (i) for describing a single discrete energy level coupled to a featureless continuum of states [29] as well as (ii) for the case of a TLS coupled to dispersing dielectrics [9,30]. In the former case (i) a very intuitive graphical analysis was presented including, however, a spurious integral extension towards negative frequencies. In the second case (ii) the solutions were calculated explicitly without, in turn, the insight provided by the modes of the corresponding open cavity geometry. In the following we introduce a method that is general enough to overcome the limitations of both approaches.

To make contact with the physics of an open cavity, we first evaluate the LDOPS for a one-dimensional cavity of length $L$ bounded at $x = 0,L$ by two thin semitransparent mirrors modeled by dielectric slabs of width $d \ll L$ with refractivity index $n$ (see Fig. 1). In what follows we use units where the speed of light $c = 1$. We also normalize $x$ to $L$ and measure time $t$ in units of half the cavity round-trip time and frequency $\omega$ in units of it's inverse. In the limit of $n \to \infty$ and $d \to 0$ the mirror's transparency is characterized by a factor $\eta = n^2 d$, which is related to the frequency-dependent mirror reflection amplitude as $r(\omega) = i\omega\eta/(2 - i\omega\eta)$ [31]. For such an open system the LDOPS is given exactly by the imaginary part of the Green's function [32] $\rho(x_a,\omega) = -2\omega\, \mathrm{Im}\, G^+(x_a,x_a,\omega)/\pi$, where the retarded Green's function (labeled by $+$) satisfies the Helmholtz equation $(\partial_x^2 + n^2\omega^2)G^+(x,x_a,\omega) = -\delta(x - x_a)$ for all $x \in \mathbb{R}$. Note that, due to the openness of the cavity, the LDOPS is a continuous function, corresponding to a continuum of extended modes that are notably different from the discrete set of cavity modes. An exact discrete spectral representation for the Green's function can, however, be obtained for the finite but open cavity geometry at the expense of introducing a non-Hermitian set of modes referred to as CF states, recently introduced to laser physics [21,33]. To compute the response to a monochromatic source at frequency $\omega$, CF states $\phi_m(x)$ have to be determined that satisfy $[\partial_x^2 + n^2\omega_m(\omega)^2]\phi_m(x) = 0$ with the outgoing boundary conditions $\partial_x\phi_m(x) = \pm i\omega\phi_m(x)$ at the right (with $+$) and left cavity boundary (with $-$). These states can be understood to carry a constant flux to infinity [21]. The resulting non-Hermitian eigenvalue problem features complex eigenvalues $\omega_m$ and a complete set of right ($\phi_m$) and left ($\bar{\phi}_m$) eigenvectors that parametrically depend on $\omega$ and are biorthogonal to each other, $\int_0^L dx\, n^2\bar{\phi}_m^*\phi_n = \delta_{mn}$. The spectral representation of the Green's function can then be constructed through $G^+(x,x',\omega) = -\sum_m \phi_m(x,\omega)\bar{\phi}_m^*(x',\omega)/[\omega^2 - \omega_m^2(\omega)]$, resulting in a LDOPS in the middle of the cavity that consists of a series of peaks, one for each $m$. In this picture it becomes intuitively clear that the peaks in the LDOPS, which the TLS couples to, arise when (i) the frequency $\omega$ is close to one of the CF frequencies $\omega_m$ (see the denominator in the Green's function) and (ii) the CF eigenfunction $\phi_m$ has a sizable value at the position $x_a$ of the TLS (see the numerator). The function $g(\omega)$ that determines the coupling strength to the emitter is given by $|g(\omega)|^2 = (\pi/2)\omega e^{-(\omega-\omega_a)^2/(2\omega_c^2)}$, where we have introduced a Gaussian cutoff at $\omega_c$. In our simulations we varied the cutoff frequency $\omega_c$ in a relatively large frequency interval observing qualitatively similar behavior. In what follows we present results for $\omega_c = 2\omega_a$. Putting all terms together, the spectral function in our example is given by

$$F(\omega) = \frac{2n^2\omega e^{-(\omega-\omega_a)^2}}{(n^2+1)^2 - (n^2-1)^2\cos(2\omega n d) + 2(n^4-1)\cos(\omega L)\sin^2(\omega n d) + 2n(n^2-1)\sin(\omega L)\sin(2\omega n d)}. \quad (2)$$

## III. DYNAMICAL SCENARIOS

We now proceed to solve Eq. (1) for a single excitation, initially stored in the TLS $c(0) = 1$. Applying a Laplace transform (see the Appendix), we derive the expression for the amplitude $c(t)$,

$$c(t) = \frac{\gamma}{\pi}e^{i\omega_a t}\int_0^\infty d\omega\, U(\omega)e^{-i\omega t}, \quad (3)$$

with the kernel function

$$U(\omega) = \lim_{\varepsilon\to 0^+}\frac{F(\omega)}{[\omega - \omega_a - \gamma\delta(\omega)]^2 + [\gamma F(\omega) + \varepsilon]^2} \quad (4)$$

and the nonlinear Lamb shift

$$\delta(\omega) = \frac{1}{\pi}\mathcal{P}\int_0^\infty d\tilde{\omega}\frac{F(\tilde{\omega})}{\omega - \tilde{\omega}}, \quad (5)$$

where $\mathcal{P}$ denotes the Cauchy principal value. The dominant frequency components entering the dynamics of $c(t)$ are those that are resonant in the kernel function $U(\omega)$. A *necessary* condition for such resonances to occur is that the first term in the denominator of $U(\omega)$ vanishes,

$$\frac{\omega_r - \omega_a}{\gamma} = \delta(\omega_r). \quad (6)$$

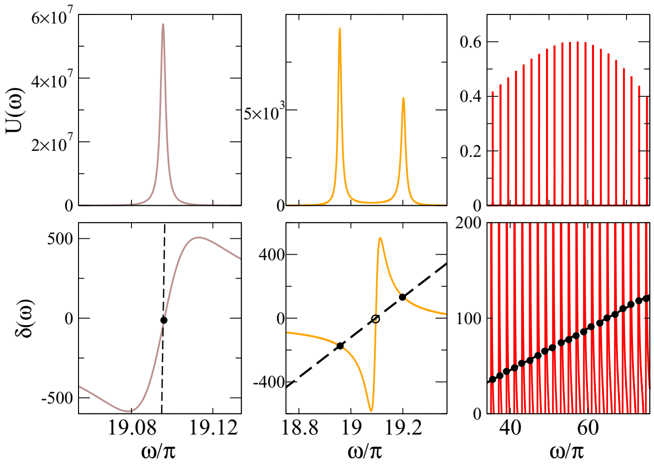

FIG. 2. (Color online) Route from the single-mode to the multimode coupling regime for different coupling strengths $\gamma$. The top row shows the dimensionless kernel function $U(\omega)$ [Eq. (4)]. The bottom row shows the dimensionless nonlinear Lamb shift $\delta(\omega)$ [Eq. (5)] for the same $\omega$ interval as above (note the different zooms for the three columns). The left column shows the weak-coupling regime for $\gamma = 4\times10^{-6}$ with a single peak in $U(\omega)$ (Purcell modified spontaneous decay). The middle column shows the strong-coupling regime for $\gamma = 2.5\times10^{-3}$ with a well-resolved Rabi splitting in $U(\omega)$ (regime of damped Rabi oscillations). The right column shows the multimode strong-coupling regime for $\gamma = 1.44$ with a multipeak structure in $U(\omega)$ consisting of almost equidistant peaks (regime of revivals). Closed circles label resonance values $\omega_r$ of the kernel $U(\omega)$ occurring at the intersections between the Lamb shift $\delta(\omega)$ and the dashed line $(\omega-\omega_a)/\gamma$. At open circles (not shown in right column) such intersections are nonresonant and do not lead to a corresponding peak in $U(\omega)$ (see the text). The transition frequency $\omega_a \approx 19\pi$ of the TLS coincides with the tenth resonance of the spectral function $F(\omega)$ [Eq. (2)]. The reflectivity parameter $\eta = 0.1$ is such that the mirror reflectivity $|r(\omega_a)|^2 = 0.9$. Frequency $\omega$ is measured here in units of the inverse half the cavity round-trip time.

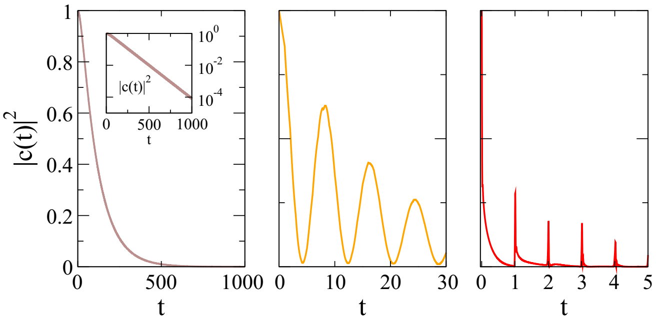

FIG. 3. (Color online) Temporal evolution of the excited-state probability $|c(t)|^2$ of the TLS for the three cases shown in Fig. 2. Time $t$ is measured here in units of half the cavity round-trip time. The left panel shows the weak-coupling regime ($\gamma = 4\times10^{-6}$) featuring spontaneous decay (also shown on a log-lin scale in the inset). The middle panel shows the strong-coupling regime ($\gamma = 2.5\times10^{-3}$) with damped Rabi oscillations. The right panel shows the multimode strong-coupling regime ($\gamma = 1.44$) featuring pulsed revivals at multiple integers of half the cavity round-trip time.

This resonance condition is satisfied at the frequencies $\omega_r$, determined by the intersection of the nonlinear Lamb shift $\delta(\omega)$ and a straight line $(\omega-\omega_a)/\gamma$ (see a corresponding graphical analysis in [29] for a simple form of a continuum). Since, according to Eq. (5), every resonance in $F(\omega)$ produces a dip followed by a peak in the Lamb shift, there may be several such intersections, corresponding to multiple solutions of Eq. (6). The corresponding resonances in the kernel $U(\omega)$ can, however, be suppressed, whenever the spectral function $F(\omega)$ has a maximum at the same resonance frequency. This is the case if the kernel $U(\omega) = 1/\gamma^2 F(\omega)$ goes through a minimum at $\omega = \omega_r$.

Based on these observations, we will now investigate the crossover from weak to strong coupling upon variation of the coupling strength $\gamma$; all other parameters, such as the spectral function $F(\omega)$ and the mirror's reflectivity factor $\eta$, will be left unchanged. At very weak coupling $\gamma = 10^{-4}$ (left panel of Fig. 2), the straight line in Eq. (6) is very steep and thus leads just to a single intersection, corresponding to a single resonance at $\omega_r \approx \omega_a$. All quantities in Eq. (4) can thus be evaluated at $\omega_a$ to very good accuracy and the kernel function reduces to a Lorentzian centered around the slightly shifted frequency $\omega_a + \gamma\delta(\omega_a)$ with the width $\gamma F(\omega_a)$. By extending the integration limit in Eq. (3) to $-\infty$, we reproduce the Purcell modified exponential decay of the TLS inversion [23], in good agreement with a numerical solution of the Volterra equation (1) (left panel in Fig. 3). This is the overdamped dynamics of the TLS in the weak-coupling limit of cavity QED.

As $\gamma$ increases to $\gamma = 2.5\times10^{-3}$ we enter the strong-coupling regime, as indicated by the straight line now being flat enough to intersect the nonlinear Lamb shift at three points (middle panel of Fig. 2). Note that these *three* intersections give rise to only *two* resonances $\omega_r$ in the kernel $U(\omega)$ since the middle frequency is very close to the resonance of $F(\omega)$ (see the discussion above). As a consequence, the kernel function $U(\omega)$ has a double-peak structure that is characteristic of the single-mode vacuum Rabi splitting [24]. This energy splitting introduces a new frequency scale, the Rabi frequency, which is easily estimated from the resonance condition (6) to be $\sqrt{2\omega_a\gamma}$. The inverse of the peak width provides the time scale at which the Rabi oscillations decay, as confirmed by independent numerical solutions of Eq. (1) (middle panel of Fig. 3).

With a further increase of the coupling strength to $\gamma = 1.44$, the straight line starts to intersect neighboring resonances of $\delta(\omega)$, involving an increasing number of cavity modes. Thus, within the multimode strong-coupling regime it is possible to couple to many cavity modes, including those that reside far away from the transition frequency $\omega_a$ (right panel of Fig. 2). Note that, similar to the situation above, only every second intersection with the Lamb shift produces a resonance in the kernel $U(\omega)$ that correspondingly takes on a multipeaked profile. If, as in our case, these peaks also have an equidistant spacing to each other, then the interference between these resonant modes produces a train of pulses in the probability of the excited state $|c(t)|^2$, corresponding to pulsed revivals of the TLS inversion (right panel of Fig. 3). With the revival time being equal to half the cavity round-trip time, the straightforward explanation of this phenomenon is the repetitive emission and subsequent reabsorption of radiation

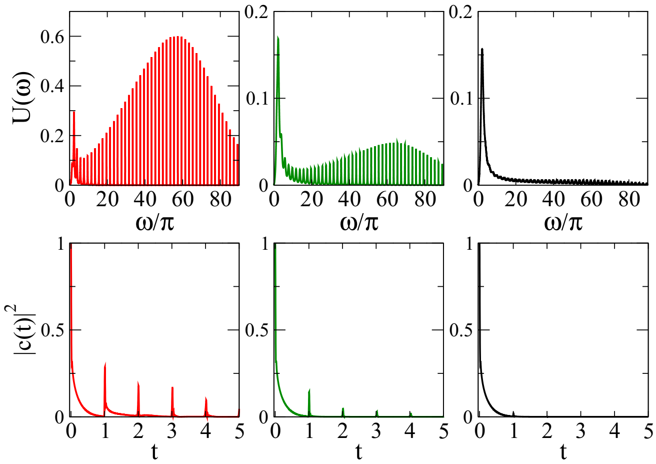

FIG. 4. (Color online) Destruction of the multimode strong-coupling regime by broadening of the peaks in the spectral function (2). The left column shows the mirror reflectivity parameter $\eta = 0.9$ (as in right panel of Fig. 2). The middle column shows $\eta = 0.3$. The right column shows $\eta = 0.015$. The top row shows the dimensionless kernel function $U(\omega)$. The bottom row shows the corresponding excited-state probability $|c(t)|^2$ of the TLS versus normalized time $t$. The transition frequency $\omega_a \approx 19\pi$ and the coupling strength $\gamma = 1.44$ are the same as in the right panels of Figs. 2 and 3.

by the TLS, when it is back-reflected by the cavity boundaries. As such, this effect relies on the fact that the phases acquired from all possible paths starting from and returning to the position of the TLS differ only by integer multiples of $2\pi$, a condition that strongly depends on the position of the TLS in the cavity. Indeed, if we move the TLS away from the cavity center, a much more irregular type of dynamics emerges (not shown). We also checked explicitly on the limitations that the revival effect is subject to in terms of the cavity opening. For that purpose we performed numerical simulations for cavities with smaller values of the mirror's reflectivity factor $\eta = 0.3, 0.015$ (Fig. 4). We observe that for decreasing values of $\eta$ the overlap between neighboring resonant peaks in $U(\omega)$ increases until they merge into a single wide resonance. As a result, the revivals in the inversion of the TLS die out when all resonances merge to a single peak, at which point the decay will be just a simple exponential decay, no matter how large the coupling strength $\gamma$ is.

## IV. COMPARISON WITH A SYSTEM-AND-BATH FORMALISM

To verify the validity of the above results, we recalculated the temporal decay in all of the three regimes from above using a recently developed system-and-bath approach [34]. Under the rotating-wave and Born approximations this approach can, in principle, also be reduced to a single Volterra equation as in Eq. (1). We have, however, been able to go beyond the Born approximation by solving a coupled set of Volterra equations for the TLS and damped cavity modes explicitly numerically. These equations very well illustrate how costly it becomes numerically to obtain the solutions for the temporal decay without the Laplace transform employed above and how little insight one gets into these solutions when they have to be explicitly integrated in time. The fact that we obtain very similar results (for all the scenarios obtained above) with this more complex approach confirms in turn the validity of the simple and insightful strategy presented in the previous sections.

### A. Total Hamiltonian

Our starting point is a Hamiltonian that includes altogether five contributions from the resonator, the external region, the TLS and the interaction of the resonator with the external region and of the TLS with the resonator [see Eq. (81) in [34]],

$$\begin{aligned}\mathcal{H} = {}& \sum_\lambda \hbar\omega_\lambda a_\lambda^\dagger a_\lambda + \int d\omega\, \hbar\omega\, b^\dagger(\omega) b(\omega) + \frac{\hbar\omega_a}{2}\sigma_z \\ &+ \hbar \sum_\lambda \int d\omega [\mathcal{W}_\lambda(\omega) a_\lambda^\dagger b(\omega) + \mathcal{W}_\lambda^\star(\omega) a_\lambda b^\dagger(\omega)] \\ &+ \sum_\lambda [g_\lambda a_\lambda \sigma^+ + g_\lambda^\star a_\lambda^\dagger \sigma^-]. \end{aligned} \quad (7)$$

Note that the form of this Hamiltonian is a bit simpler as compared to the one presented in [34] as we do not consider multiple scattering channels outside the cavity.

The Hermitian resonator modes are described by a discrete set of operators $a_\lambda$ and corresponding eigenfrequencies $\omega_\lambda$, whereas the external radiation field corresponds to a continuous set of operators $b(\omega)$ and frequencies $\omega$. The operators obey the usual canonical commutation relations (see Sec. II D in [34] for more details). The resonator and external region communicate with each other via the coupling matrix elements $\mathcal{W}_\lambda(\omega)$ defined as the expectation value of the operator $\mathcal{L}_{PQ}$ sandwiched between the resonator and external modes [see Eq. (52a) in [34]]. This coupling operator is determined through the Feshbach projection formalism, which consists of separating space in two regions, the resonator $Q$ and the external region $P$. Finally, the action of the operator $\mathcal{L}$ onto an arbitrary function $\phi$ is written as the decomposition $\mathcal{L}\phi = \mathcal{L}_{QQ}\mu + \mathcal{L}_{QP}\nu + \mathcal{L}_{PQ}\mu + \mathcal{L}_{PP}\nu$, where the functions $\mu$ and $\nu$ reside inside the resonator and the external regions, respectively. Correspondingly, the operators $\mathcal{L}_{QP}$ and $\mathcal{L}_{PQ}$ act in the vicinity of the boundaries between the resonator and external region (see Secs. II B and III C for more details). The key point is that the total operator $\mathcal{L}$, the cavity operator $\mathcal{L}_{QQ}$, and external region operator $\mathcal{L}_{PP}$ are *Hermitian* operators in their regions of definition. The operators $\sigma_z$, $\sigma^+$, and $\sigma^-$ are the standard Pauli operators that describe the TLS and $\omega_a$ stands for its transition frequency. The coupling amplitude $g_\lambda$ is given by

$$g_\lambda = -i\left(\frac{\hbar\omega_\lambda}{2}\right)^{1/2} \boldsymbol{\mu} \cdot \mathbf{u}_\lambda(\mathbf{r_a}), \quad (8)$$

where $\boldsymbol{\mu}$ is the dipole strength of the transition, $\mathbf{u}_\lambda(\mathbf{r})$ stands for the eigenfunctions of $\mathcal{L}_{QQ}$, and $\mathbf{r_a}$ is the location of the TLS.

It should be noted that in the Hamiltonian (7) the rotating-wave approximation has already been applied in the following ways. (i) The nonresonant terms in the system-and-bath part of Hamiltonian [i.e., terms proportional to $a_\lambda^\dagger b^\dagger(\omega)$ and $a_\lambda b(\omega)$] are neglected. This approximation is valid if the damping rates of the cavity resonances are substantially smaller than the frequencies of interest. For our purpose this approximation is indeed well fulfilled since the revival regime that we aim to describe occurs exactly in this limit. (ii) Also the nonresonant terms in the atom-field interaction (i.e., terms proportional to $a_\lambda^\dagger\sigma^+$ and $a_\lambda\sigma^-$) are neglected, which is a commonly used approximation.

### B. Volterra equations

Since the Hamiltonian (7) conserves the total number of atom and field excitations (due to the above rotating-wave approximation) we can set up the following ansatz for our solution to the Schrödinger equation:

$$\begin{aligned}|\Psi(t)\rangle &= c(t)e^{-i\omega_a t/2}|u\rangle|0\rangle\\ &\quad+\sum_\lambda c_\lambda(t)|l\rangle|1_\lambda\rangle e^{-i(\omega_\lambda-\omega_a/2)t}\\ &\quad+\int d\omega c(\omega,t)e^{-i(\omega-\omega_a/2)t}|l\rangle|1(\omega)\rangle,\end{aligned}\tag{9}$$

where the ket vectors $|u\rangle$ and $|l\rangle$ stand for the atom in the upper and lower states, respectively. In Eq. (9) the ket vectors $|0\rangle$, $|1_\lambda\rangle$, and $|1(\omega)\rangle$ represent the vacuum state of the electromagnetic field, a single photon in cavity mode $\lambda$, and a single photon in the external region with frequency $\omega$, respectively. We assume that the system at time $t = 0$ is in the initial state $|u\rangle|0\rangle$. After straightforward algebra we derive the following set of coupled differential equations for the probability amplitudes $c(t)$, $c_\lambda(t)$, and $c(\omega,t)$ introduced in Eq. (9):

$$\dot{c}(t) = -\frac{i}{\hbar}\sum_\lambda g_\lambda e^{-i(\omega_\lambda-\omega_a)t}c_\lambda(t),\tag{10a}$$

$$\begin{aligned}\dot{c}_\lambda(t) &= -\frac{i}{\hbar}g_\lambda^\star e^{i(\omega_\lambda-\omega_a)t}c(t)\\ &\quad-i\int d\omega\mathcal{W}_\lambda(\omega)e^{-i(\omega-\omega_\lambda)t}c(\omega,t),\end{aligned}\tag{10b}$$

$$\dot{c}(\omega,t) = -i\sum_\lambda \mathcal{W}_\lambda^\star(\omega)e^{-i(\omega_\lambda-\omega)t}c_\lambda(t).\tag{10c}$$

The initial conditions are $c(0) = 1$ and $c_\lambda(0) = c(\omega,0) = 0$.

Next, we formally integrate Eq. (10c) and plug the result into Eq. (10b), which allows us to exclude the external region from the consideration such that we finally obtain the set of equations

$$\dot{c}(t) = -\frac{i}{\hbar}\sum_\lambda g_\lambda e^{-i(\omega_\lambda-\omega_a)t}c_\lambda(t),\tag{11a}$$

$$\begin{aligned}\dot{c}_\lambda(t) &= -\frac{i}{\hbar}g_\lambda^\star e^{i(\omega_\lambda-\omega_a)t}c(t)-\int d\omega\sum_{\lambda'}\mathcal{W}_\lambda(\omega)\mathcal{W}_{\lambda'}^\star(\omega)\\ &\quad\times e^{-i(\omega-\omega_\lambda)t}\int_0^t d\tau\, e^{-i(\omega_\lambda'-\omega)\tau}c_{\lambda'}(\tau).\end{aligned}\tag{11b}$$

### C. Markov approximation

To simplify matters, we apply the so-called Markov approximation in Eq. (11b) with respect to the cavity amplitudes $c_\lambda(t)$ such that memory effects with regard to the outcoupling to the external radiation field are disregarded. (Note that, most importantly, the memory effects within the cavity are still carried along.) Specifically, we shift the initial time of integration to $-\infty$, let $c_\lambda(t') \approx c_\lambda(t)$, and, assuming subsequent integration with respect to $\omega$, make use of the relation

$$\begin{aligned}&e^{-i(\omega-\omega_\lambda)t}\lim_{\sigma\to 0}\frac{e^{i(\omega-\omega_{\lambda'}-i\sigma)\tau}}{\omega-\omega_{\lambda'}-i\sigma}\Bigg|_{\tau=-\infty}^{\tau=t}\\ &\quad\to e^{-i(\omega_{\lambda'}-\omega_\lambda)t}\left[\mathcal{P}\left(\frac{1}{\omega-\omega_{\lambda'}}\right)+i\pi\delta(\omega-\omega_{\lambda'})\right].\end{aligned}\tag{12}$$

The differential equations for $c(t)$ and $c_\lambda(t)$ are then

$$\dot{c}(t) = -\frac{i}{\hbar}\sum_\lambda g_\lambda e^{-i(\omega_\lambda-\omega_a)t}c_\lambda(t),\tag{13a}$$

$$\begin{aligned}\dot{c}_\lambda(t) &= -\frac{i}{\hbar}g_\lambda^\star e^{i(\omega_\lambda-\omega_a)t}c(t)\\ &\quad+\sum_{\lambda'}\Gamma_{\lambda\lambda'}(\omega_{\lambda'})e^{-i(\omega_{\lambda'}-\omega_\lambda)t}c_{\lambda'}(t),\end{aligned}\tag{13b}$$

where the matrix elements of the damping matrix $\Gamma_{\lambda\lambda'}$ are given by

$$\begin{aligned}\Gamma_{\lambda\lambda'}(\omega_{\lambda'}) &= -\pi\mathcal{W}_\lambda(\omega_{\lambda'})\mathcal{W}_{\lambda'}^\star(\omega_{\lambda'})\\ &\quad+i\mathcal{P}\int d\omega\frac{\mathcal{W}_\lambda(\omega)\mathcal{W}_{\lambda'}^\star(\omega)}{\omega-\omega_{\lambda'}},\end{aligned}\tag{14}$$

which should be calculated in a discrete set of eigenfrequencies $\omega_\lambda$ only. The second term in Eq. (14) is similar to a Lamb shift in that it accounts for a shift of the cavity resonances in an open system with respect to the positions in the corresponding closed system. Next we formally integrate Eqs. (13a) and (13b) and end up with a set of coupled integral Volterra equations

$$\begin{aligned}c(t) &= 1-\frac{i}{\hbar^2}\sum_\lambda\frac{g_\lambda g_\lambda^\star}{\omega_\lambda-\omega_a}\int_0^t d\tau[e^{-i(\omega_\lambda-\omega_a)(t-\tau)}-1]c(\tau)\\ &\quad+\frac{1}{\hbar}\sum_{\lambda\lambda'}\frac{g_\lambda\Gamma_{\lambda\lambda'}(\omega_\lambda')}{\omega_\lambda-\omega_a}\int_0^t d\tau[e^{-i(\omega_\lambda-\omega_a)(t-\tau)}-1]\\ &\quad\times e^{-i(\omega_\lambda'-\omega_a)\tau}c_\lambda'(\tau),\end{aligned}\tag{15}$$

$$\begin{aligned}c_\lambda(t) &= -\frac{ig_\lambda^\star}{\hbar}\int_0^t d\tau\, e^{i(\omega_\lambda-\omega_a)\tau}c(\tau)\\ &\quad+\sum_{\lambda'}\Gamma_{\lambda\lambda'}(\omega_\lambda')\int_0^t d\tau e^{-i(\omega_{\lambda'}-\omega_\lambda)\tau}c_{\lambda'}(\tau).\end{aligned}\tag{16}$$

### D. One-dimensional dielectric cavity

We solve Eqs. (15) and (16) numerically for the geometry shown in Fig. 1. Specifically, we consider the one-dimensional cavity of length $L$ now bounded at $x = -L,0$ by two thin semitransparent mirrors modeled by dielectric slabs of width $d \ll L$ with refractivity index $n$. Using the fact that the TLS couples only to those modes that are symmetric with respect to the center of the cavity (where the TLS is located), we replace our original geometry by a more simple one. This new cavity runs within $[-L/2,0^-]$ with Neumann boundary conditions at the position of the TLS $\partial_x u_\lambda(x = -L/2) = 0$. On the right cavity edge we impose (for the closed system $Q$) a Dirichlet boundary condition $u_\lambda(x = 0^-) = 0$ to remove a singular contribution of the operator $\mathcal{L}_{QQ}$ at this point [see, e.g., Eq. (52a) in [31]]. The corresponding cavity eigenvalue problem

$$\frac{d^2}{dx^2} u_\lambda(x) + \omega_\lambda^2 u_\lambda(x) = 0 \tag{17}$$

is finally solved with the eigenvalues $\omega_\lambda = \pi(2\lambda - 1)/L$ ($\lambda = 1,2,\dots$) and with the eigenvectors (inside the cavity)

$$u_\lambda = \sqrt{\frac{2}{L}} \cos\left[\omega_\lambda \left(x + \frac{L}{2}\right)\right]. \tag{18}$$

The coupling amplitudes between the TLS and the cavity modes (8) reduce to

$$g_\lambda = i\mu\sqrt{\frac{\hbar\omega_\lambda}{L}} f_c(\omega_\lambda). \tag{19}$$

In the limit of $n \to \infty$ and $d \to 0$, keeping the mirror's transparency factor $\eta = n^2 d$ finite, the channel modes (outside the resonator) coincide with those calculated in [31] [see Eqs. (55)– (58) therein],

$$\nu(\omega,x) = \frac{1}{\sqrt{2\pi}}\left(e^{-i\omega x} + \frac{i - \eta\omega}{i + \eta\omega} e^{i\omega x}\right). \tag{20}$$

To couple these cavity modes in the bounded domain $Q$ to the unbounded domain $P$ we require the coupling elements $\mathcal{W}_\lambda(\omega)$ that enter the damping matrix $\Gamma_{\lambda\lambda'}$,

$$\mathcal{W}_\lambda(\omega) = \frac{(-1)^\lambda}{1 - i\eta\omega}\sqrt{\frac{\omega_\lambda}{\pi\omega L}} f_c(\omega_\lambda). \tag{21}$$

Here and in Eq. (19) we introduce the cutoff function $f_c(\omega_\lambda) = e^{-(\omega_\lambda - \omega_a)^2/(4\omega_c^2)}$ to eliminate the interaction with high-frequency modes in the same way as was done in Sec. II. To ensure the convergence of the integral in Eq. (14) also in the low-frequency limit, we integrate from a frequency above zero but below the first cavity resonance. Finally, we plug the obtained expressions into Eqs. (14)–(16) and solve them numerically with the initial conditions $c(0) = 1$ and $c_\lambda(0) = 0$.

The results of our calculations are shown in Fig. 5 for two typical values of the coupling strength within both the regime of Rabi oscillations and the regime of revivals. We normalize time to half the cavity round-trip time $L/c$ and find again the revivals occurring at integer multiples of these values. Note in particular the very good correspondence that we find between the results obtained from the model based on the CF state representation of the LDOPS within a single Volterra equation (1) and the system-and-bath formalism given by Eqs. (15) and (16) above. This close correspondence confirms the validity of our calculations and the difference in complexity between the two calculations demonstrates the usefulness of the simple and accessible approach presented in Sec. III.

## V. CONCLUSION AND OUTLOOK

To summarize, we have shown how the emission process of a two-level atom changes as a function of its coupling strength to the electromagnetic field of an open multimode resonator. Solving the Volterra equation for the temporal decay through Laplace transform allowed us to obtain the decay dynamics together with a corresponding graphical analysis that provides an intuitive understanding of the different regimes observed. On top of the familiar exponential decay and damped Rabi oscillations in the weak- and strong-coupling regimes, respectively, we identify, for very strong coupling, a regime where the emitter couples to multiple modes, leading to pulsed revivals of its initial excitation. We expect that these predictions can be explicitly verified in various physical systems dealing with a two-level-like emitter inside an open multimode cavity. In particular, we have circuit QED setups in mind (e.g., [6,35–37]), for which the coupling strength can be tuned by engineering the two-level system appropriately.

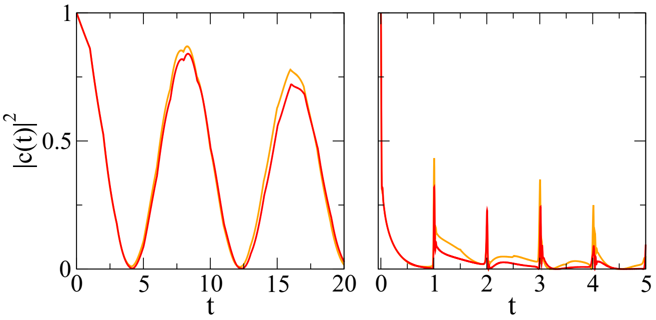

FIG. 5. (Color online) Comparison between the results obtained from a single Volterra equation [dark gray (red) curves] and from the system-and-bath formalism [gray (orange) curves]. The calculations are performed for the 1D geometry presented in Fig. 1 with the mirror reflectivity parameter set to $\eta = 0.18$. The left panel shows $\gamma = 2.5 \times 10^{-3}$ (regime of Rabi oscillations) and the right panel $\gamma = 1.44$ (multimode strong-coupling regime). Time $t$ is measured in units of half the cavity round-trip time.

## ACKNOWLEDGMENTS

The authors would like to thank R. Luger, M. Malekakhlagh, and C. Viviescas for helpful discussions. Financial support from the Vienna Science and Technology Fund through Project No. MA09-030 (LICOTOLI), the Austrian Science Fund through Projects No. F25-P14 (SFB IR-ON) and No. F49-P10 (SFB NextLite), the National Science Foundation through the NSF CAREER Grant No. DMR-1151810, and the Swiss NSF through Grant No. PP00P2-123519/1 is gratefully acknowledged. We also profited from free access to the computational resources of the Vienna Scientific Cluster.

## APPENDIX: LAPLACE TRANSFORM OF THE VOLTERRA EQUATION

We solve the Volterra equation (1) by means of the standard Laplace transform method (see [38,39], where different modal weight functions have been considered), multiplying it by $e^{-st}$ and integrating both sides of the equation with respect to time from 0 to $\infty$. Here $s = \sigma + i\omega$ is the complex variable so that we reformulate our problem by solving it in the complex plane of $s$. After straightforward calculations, the algebraic equation for the Laplace transform $\tilde{c}(s) = \int_0^\infty dt\, e^{-st} c(t)$ is derived,

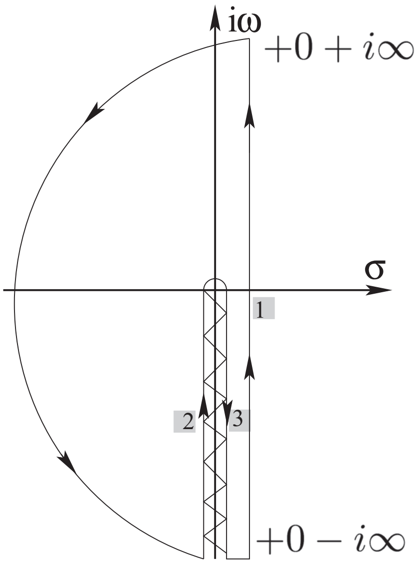

FIG. 6. Contour completion in the complex plane $s = \sigma + i\omega$ for the calculation of the inverse Laplace transform (A2). Those contours that give nonzero contribution are designated by numbers.

which is solved by

$$\tilde{c}(s) = \frac{1}{s + \frac{\gamma}{\pi}\int_0^\infty d\omega \frac{F(\omega)}{s + i(\omega - \omega_a)}}. \tag{A1}$$

Next we perform the inverse Laplace transformation $c(t) = \frac{1}{2\pi i}\int_{\sigma - i\infty}^{\sigma + i\infty} ds\, e^{st}\tilde{c}(s)$ and obtain the formal solution for the amplitude $c(t)$,

$$c(t) = \frac{e^{i\omega_a t}}{2\pi i}\int_{\sigma - i\infty}^{\sigma + i\infty} \frac{e^{st} ds}{s + i\omega_a + G(s)}, \tag{A2}$$

with

$$G(s) = \frac{\gamma}{\pi}\int_0^\infty \frac{d\omega\, F(\omega)}{s + i\omega}, \tag{A3}$$

where $\sigma > 0$ should be chosen such that the real parts of all singularities of $\tilde{c}(s)$ are smaller than $\sigma$. It can be shown that the function

$$J(\omega) = \lim_{\sigma \to 0^+} [G(\sigma + i\omega) - G(-\sigma + i\omega)] \tag{A4}$$

is nonzero for $-\infty < \omega \leqslant 0$. Therefore, the function $G(s)$ and, as a consequence, the whole integrand in Eq. (A2) exhibit a jump along the negative part of the imaginary axis, which is a branch cut. By equating the denominator of Eq. (A2) to zero $s + i\omega_a + G(s) = 0$, the poles $s_j$ are shown to satisfy the equation

$$\omega_j + \omega_a = \frac{\gamma}{\pi}\int_0^\infty d\omega \frac{F(\omega)}{\omega + \omega_j}, \quad \sigma_j = 0. \tag{A5}$$

Thus, the poles (if at all existing) can be located on the imaginary axis only. Moreover, we strictly prove, using a graphical analysis and the fact that $F(\omega) \geqslant 0$, that only a single simple pole can reside in the positive imaginary axis that leads to undamped oscillations at infinite time. For values of the coupling strength $\gamma$ larger than considered in this paper, such a scenario emerges in the equations but is not considered here. Thus, to evaluate the original integral (A2), we apply Cauchy's theorem to a closed contour shown in Fig. 6. We prove similarly to Jordan's lemma that the arc contribution is negligible and the contribution of the small semi-circle around $s = 0$ is also zero. Therefore, the only paths that remain are those around the branch cut and the one we are looking for (see Fig. 6). Thus, we derive the following expression for the amplitude $c(t)$:

$$c(t) = \frac{e^{i\omega_a t}}{2\pi i}\int_0^\infty d\omega\, e^{-i\omega t}[\Phi_-(\omega) - \Phi_+(\omega)], \tag{A6}$$

where

$$\Phi_\pm(\omega) = \lim_{\sigma \to 0^+}\left\{\frac{1}{\omega - \omega_a + i\left[\frac{\gamma}{\pi}\int_0^\infty \frac{d\tilde{\omega} F(\tilde{\omega})}{\pm\sigma + i(\tilde{\omega} - \omega)} \pm \sigma\right]}\right\}. \tag{A7}$$

Employing the Sokhotski-Plemelj theorem, the integral in the denominator of Eq. (A7) is rewritten in the limit of $\sigma \to 0$ as

$$\int_0^\infty \frac{d\tilde{\omega}\, F(\tilde{\omega})}{\pm\sigma + i(\tilde{\omega} - \omega)} = -i\left\{\mathcal{P}\int_0^\infty \frac{d\tilde{\omega}\, F(\tilde{\omega})}{\tilde{\omega} - \omega} \pm i\pi F(\omega)\right\},$$

We finally end up with Eqs. (3)–(5) for the amplitude $c(t)$ (see Sec. III).

---

[1] G. Khitrova *et al.*, Nat. Phys. **2**, 81 (2006).

[2] S. Noda, M. Fujita, and T. Asano, Nat. Photon. **1**, 449 (2007).

[3] A. Wallraff *et al.*, Nature (London) **431**, 162 (2004).

[4] M. Agio, Nanoscale **4**, 692 (2012).

[5] H. J. Carmichael, R. J. Brecha, M. G. Raizen, H. J. Kimble, and P. R. Rice, Phys. Rev. A **40**, 5516 (1989).

[6] L. Sapienza *et al.*, Science **327**, 1352 (2010).

[7] P. V. Ruijgrok *et al.*, Opt. Express **18**, 6360 (2010).

[8] X.-W. Chen, M. Agio, and V. Sandoghdar, Phys. Rev. Lett. **108**, 233001 (2012).

[9] H. T. Dung, L. Knöll, and D.-G. Welsch, Phys. Rev. A **62**, 053804 (2000).

[10] N. Vats, S. John, and K. Busch, Phys. Rev. A **65**, 043808 (2002).

[11] M. Wubs and A. Lagendijk, Phys. Rev. E **65**, 046612 (2002).

[12] T. Ochiai, J. I. Inoue, and K. Sakoda, Phys. Rev. A **74**, 063818 (2006).

[13] V. S. C. Manga Rao and S. Hughes, Opt. Lett. **33**, 1587 (2008).

[14] R. Pierrat and R. Carminati, Phys. Rev. A **81**, 063802 (2010).

[15] X.-W. Chen, V. Sandoghdar, and M. Agio, Phys. Rev. Lett. **110**, 153605 (2013).

[16] A. Polman and H. A. Atwater, Nat. Mater. **11**, 174 (2012).

[17] P. T. Kristensen, J. Mørk, P. Lodahl, and S. Hughes, Phys. Rev. B **83**, 075305 (2011).

[18] M. Khanbekyan, D.-G. Welsch, C. Di Fidio, and W. Vogel, Phys. Rev. A **78**, 013822 (2008); Phys. Scr. **T135**, 014015 (2009).

[19] S. V. Boriskina, A. Gopinath, and L. Dal Negro, Physica E **41**, 1102 (2009).

[20] D. E. Chang, A. S. Sorensen, P. R. Hemmer, and M. D. Lukin, Phys. Rev. Lett. **97**, 053002 (2006).

[21] H. E. Tureci, A. D. Stone, and B. Collier, Phys. Rev. A **74**, 043822 (2006).

[22] V. Weisskopf and E. Wigner, Z. Phys. **63**, 54 (1930).

[23] E. M. Purcell, Phys. Rev. **69**, 681 (1946).

[24] E. T. Jaynes and F. W. Cummings, Proc. IEEE **51**, 89 (1963).

[25] P. W. Milonni, J. R. Ackerhalt, H. W. Galbraith, and M. L. Shih, Phys. Rev. A **28**, 32 (1983).

[26] R. W. F. van der Plank and L. G. Suttorp, Phys. Rev. A **54**, 2464 (1996).

[27] A. Carmele, J. Kabuss, F. Schulze, S. Reitzenstein, and A. Knorr, Phys. Rev. Lett. **110**, 013601 (2013).

[28] R. J. Glauber and M. Lewenstein, Phys. Rev. A **43**, 467 (1991).

[29] C. Cohen-Tannoudji, J. Dupont-Roc, and G. Grynberg, *Atom-Photon Interactions* (Wiley-VCH, Weinheim, 2004), Complement CIII.

[30] I. V. Bondarev, G. Ya. Slepyan, and S. A. Maksimenko, Phys. Rev. Lett. **89**, 115504 (2002).

[31] C. Viviescas and G. Hackenbroich, J. Opt. B **6**, 211 (2004).

[32] E. N. Economou, *Green's Functions in Quantum Physics*, 3rd ed., Springer Series in Solid-State Sciences Vol. 7 (Springer, Berlin, 2006).

[33] H. E. Türeci, L. Ge, S. Rotter, and A. D. Stone, Science **320**, 643 (2008).

[34] C. Viviescas and G. Hackenbroich, Phys. Rev. A **67**, 013805 (2003).

[35] K. Srinivasan and O. Painter, Nature (London) **450**, 862 (2007).

[36] J. M. Fink *et al.*, Nature (London) **454**, 315 (2008).

[37] A. A. Houck *et al.*, Phys. Rev. Lett. **101**, 080502 (2008).

[38] K. F. Riley, M. P. Hobson, and S. J. Bence, *Mathematical Methods for Physics and Engineering* (Cambridge University Press, Cambridge, 2006).

[39] P. R. Berman and G. W. Ford, in *Advances in Atomic, Molecular, and Optical Physics*, edited by E. Arimondo, P. R. Berman, and C. C. Lin (Elsevier, Amsterdam, 2010), Vol. 59, Chap. 5, pp. 175–221.

PHYSICAL REVIEW A **92**, 053801 (2015)

# Analytical study of quantum-feedback-enhanced Rabi oscillations

Julia Kabuss,[1] Dmitry O. Krimer,[2] Stefan Rotter,[2] Kai Stannigel,[3] Andreas Knorr,[1] and Alexander Carmele[1,3]
[1]*Nichtlineare Optik und Quantenelektronik, Institut für Theoretische Physik, Technische Universität Berlin, Hardenbergstraße 36, 10623 Berlin, Germany*
[2]*Institute for Theoretical Physics, Vienna University of Technology, Wiedner-Hauptstraße 8-10/136, A-1040 Vienna, Austria*
[3]*Institute for Quantum Optics and Quantum Information, Technikerstraße 21, 6020 Innsbruck, Austria*

(Received 20 March 2015; published 2 November 2015)

We present an analytical solution of the single-photon quantum feedback in a cavity quantum electrodynamics system based on a half-cavity setup coupled to a structured continuum. Our exact analytical expression constitutes an important benchmark for quantum-feedback models and allows us to unravel the necessary conditions for the previously reported numerical result that a single-emitter-cavity system, which is initially in the weak-coupling regime, can be driven into the strong-coupling regime via the proposed quantum-feedback mechanism [A. Carmele *et al.*, Phys. Rev. Lett. **110**, 013601 (2013)]. We specify the phase relations between the cavity mode and the delay time and state explicitly the theoretical limit for a feedback effect in the single-photon regime. Via the photon-path representation, we prove that the stabilization phenomenon relies on a destructive interference effect and we discuss the stabilization time in the weak- and strong-coupling limits.

DOI: 10.1103/PhysRevA.92.053801 PACS number(s): 42.50.Pq, 42.50.Ar, 02.30.Ks, 42.50.Ct

## I. INTRODUCTION

The basic phenomenon at the heart of any quantum information processing network is the coherent exchange of photonic and atomic excitations by means of a single emitter in a microcavity. Advances in the design and fabrication of microcavities allow very high quality factors and have enabled multiple studies of cavity quantum electrodynamics (CQED) in the strong-coupling limit [1–7]. Several applications have been proposed and already realized, such as single-photon transistors, two-photon gateways, parametric down-conversion, and the generation and detection of individual microwave photons [8–11]. Furthermore, several quantum gate proposals rely on a natural quantum interface between flying qubits (photons) and stationary qubits (e.g., atoms). Here the photons allow for secure quantum communication over long distances, whereas atoms can be used for the manipulation and storage of quantum information [11].

Application of CQED techniques requires that a single-atom–single-photon coupling exceeds any photon loss and radiative decay processes, such as spontaneous emission or photon leakage. So, besides technological progress to increase the quality factor of the cavities, a promising alternative is to identify strategies to control and exploit potentially advantageous properties of the environment coupling, which go beyond the conventional effects of the environment such as dissipation and undesired information loss.

A possible mechanism to stabilize qubits and desired quantum states is quantum feedback based on the repeated action of a sensor-controller-actuator loop. In such a case, a quantum system is driven to a target state via the external control [12,13] such that continuous measurements allow stabilization of the target state, e.g., by a modification of the pumping strength. In addition to these extrinsic control setups, experiments start to explore a variety of intrinsic delayed feedback control schemes, e.g., by using an external mirror in front of a nanocavity [14]. Intrinsic quantum feedback is not based on a continuous measurement process, but controls the quantum state by shaping the environment appropriately [15–21].

Here we discuss how the initial weak atom-cavity coupling is driven into the strong-coupling regime. In contrast to Ref. [21], here we evaluate the quantum-feedback mechanism analytically to specify the conditions for this stabilization phenomenon, in particular the phase relation between the cavity mode and the delay time imposed by the external mirror. Furthermore, we state the theoretical limit for a feedback effect on the single-excitation level and extend our investigation from the weak- to the strong-coupling regime. By expanding our solution with the von Neumann series, we can demonstrate that the effect relies on a destructive interference effect of incoming and outgoing photon wave packages and illustrate this in a photon-path representation picture. Our proposed control scheme has potential applications for quantum error correction [22], quantum gate purifying [23], and quantum feedback [13].

## II. MODEL

The system consists of a microcavity system of length $L'$ with a two-level emitter coupled to a single-cavity mode (see Fig. 1). Furthermore, the cavity exhibits photon loss due to its coupling to external modes. An external mirror, placed at a distance of $L$, introduces a boundary condition to the external mode structure and causes a feedback of lost cavity photons into the cavity. We assume that the microcavity length $L' \ll L$ is very short in comparison to $L$ to allow a single-mode description for the emitter-cavity interaction. This kind of quantum self-feedback can be realized via a shaped mode continuum in a photonic waveguide. Due to the finite cavity-mirror distance $L$ and the quasicontinuous mode structure of the semi-infinite lead, a delay mechanism is introduced into the system at $\tau = \frac{2L}{c_0}$, with $c_0$ being the speed of light in vacuum. To describe the corresponding physics we work with the following Hamiltonian within the rotating-wave and dipole approximations [24]:

$$H/\hbar = -\gamma(\sigma^- a^\dagger + \sigma^+ a) - \int dk G(k,t) a^\dagger d_k + G^*(k,t) d_k^\dagger a, \tag{1}$$

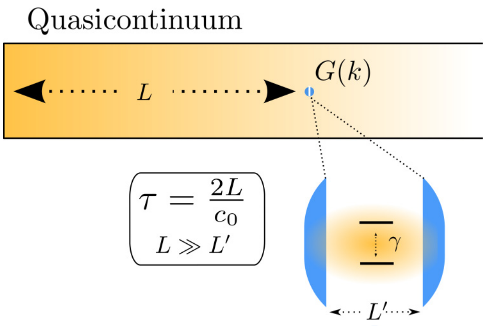

FIG. 1. (Color online) Implementation of an intrinsic quantum-feedback mechanism via a quasicontinuum, realized by a photonic crystal waveguide with length $L$, which is supposed to be considerably larger than the cavity length $L'$. The waveguide is a half cavity and allows the exchange of cavity photons with waveguide photons due to the photon leakage $G(k)$. The photons inside the cavity interact with a single emitter (coupling strength $\gamma$).

where a rotating frame is chosen in correspondence to the free-energy contribution of the Hamiltonian. The emitter is described via the Pauli matrices with $\sigma^{+(-)}$ being the raising and lowering operators of the two-level system (TLS), respectively. In the following, the atomic energy is assumed to be on resonance with the single-cavity mode. A photon annihilation (creation) in the cavity is described with the bosonic operator $a^\dagger$ $(a)$ and $\gamma$ is the coupling between the two-level system and the cavity mode. The coupling strength between the emitter and the field mode is assumed to be of the order of $\gamma = 50\ \mu\text{eV}$ [2,25,26]. The cavity photons interact with the external modes $d_k^{(\dagger)}$ in front of the mirror via the tunnel Hamiltonian coupling elements $G(k,t)$. Due to the rotating frame and the interference with the backreflected signal from the mirror, these coupling elements depend both on time $t$ and on the wave number $k$, resulting in the expression $G(k,t) = G_0 \sin(kL) \exp[i(\omega_0 - \omega_k)t]$, where $G_0$ is the bare tunnel coupling strength and $\omega_0$ and $\omega_k$ stand for the frequencies of a single-cavity mode and half-cavity modes, respectively. As we will see below, this specific form of $G(k,t)$ will determine the nature of the feedback on the cavity.

### A. Single-photon limit

If no other pump mechanism or loss channels are introduced, the system dynamics described by the Hamiltonian (1) can be solved in the Schrödinger picture, following Refs. [27,28]. In the single-photon limit, the total wave function reads

$$|\Psi\rangle = c_e|e,0,\{0\}\rangle + c_g|g,1,\{0\}\rangle + \int dk\, c_{g,k}|g,0,\{k\}\rangle, \tag{2}$$

where $|e,0,\{0\}\rangle$ denotes the excited state of the two-level system with the cavity and the waveguide being in the vacuum state, $|g,1,\{0\}\rangle$ stands for a single photon residing in the cavity and the two-level system as well as the radiation field in the waveguide being in the ground state. Finally, $|g,0,\{k\}\rangle$ describes the ground state of the two-level system with exactly one photon in the waveguide of mode $k$. The variables $c_e,c_g,c_{g,k}$ denote the corresponding amplitudes of the three different states above.

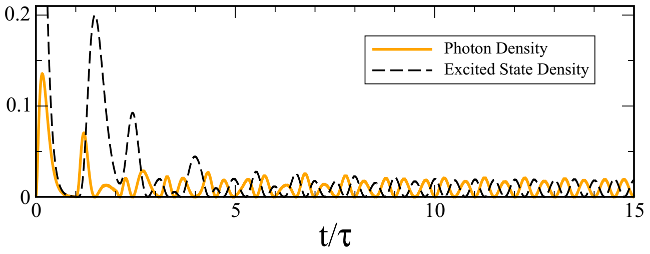

FIG. 2. (Color online) Excited-state density $|c_e(t)|^2$ of the two-level system (black dashed line) and the photon density inside the cavity $|c_g(t)|^2$ (orange solid line) in the quasicontinuum model. The quantum-feedback mechanism ($\kappa/\gamma = 2$) induces a regular oscillation pattern at multiples of $\tau = 2\pi/\gamma$.

Applying the Schrödinger equation, we arrive at the following set of linear partial differential equations:

$$\partial_t c_e = i\gamma c_g, \tag{3}$$

$$\partial_t c_g = i\gamma c_e + i\int dk\, G(k,t) c_{g,k}, \tag{4}$$

$$\partial_t c_{g,k} = iG^*(k,t) c_g. \tag{5}$$

First, we numerically solve this coupled set of differential equations assuming that initially at $t_0 = 0$ the TLS is in the excited state $c_e(t_0) = 1$ and there are no photons inside the cavity $c_g(t_0) = 0$ or in the external region $c_{g,k}(t_0) = 0$. To introduce a delay time corresponding to $\tau = 2L/c_0 = 2\pi/\gamma$, we choose a mirror resonator distance $L = \pi c_0/\gamma$.

The results for the dynamics of the excited state and photon density are shown in Fig. 2. In the time interval $[0,\tau]$ we find the conventional exponential decay as described by the Wigner-Weisskopf model in the weak-coupling limit. After the first round-trip $\tau = 2L/c_0$, the photon density and after a small delay also the excited-state density are driven by the quantum feedback. In this time interval $[\tau,2\tau]$, the amplitude of the photon density is smaller than the amplitude of the excited case, since the damping mechanism acts only on the photons inside the cavity. However, for longer times, the asymmetry between the amplitudes of the excited state and the photon density vanishes, so the system sets into a state of coherent Rabi oscillations characterized by approximately equal maxima of both densities (see the asymptotic dynamics for $t/\tau \geqslant 8$ in Fig. 2). In this long-time limit, the amplitude for the cavity photon population stabilizes at around 15% of the maximum photon population in the first time interval $[0,\tau]$. This remarkable effect has been reported in Ref. [21] and will now be analyzed analytically and thereby explained in more detail. In particular, we will focus on the following two specific questions: (i) How sensitive is this effect on the chosen parameters, in particular on the choice of the time delay? (ii) Can the oscillation amplitude be increased or is there an intrinsic limit? To answer these questions, we will first derive a simplified picture of the dynamics by solving Eqs. (3)–(5) in the Markovian limit.

### B. Analytical quantum feedback

The initial decay and the subsequent oscillations observable in Fig. 2 indicate that the underlying physical processes that govern this system consist of both a typical (Markovian) cavity loss and a (non-Markovian) memory kernel with significant contributions around multiples of the delay time $\tau$. Assuming that the rotating-wave approximation and the quasicontinuum assumption hold, the coupling to the external modes can be eliminated from the problem. To achieve this, Eq. (5) is integrated formally and inserted into Eq. (4), resulting in the following expression:

$$\partial_t c_g = i\gamma c_e - \kappa c_g + \kappa c_g(t-\tau)\Theta(t-\tau)e^{i\omega_0\tau}, \tag{6}$$

with $\kappa = \pi G_0^2/2c_0$. This reduced expression has the advantages of being easily solvable numerically and being amenable to an analytical solution through a Laplace transformation. With the initial conditions that neither cavity nor continuum photons are present in the beginning, i.e., $c_e(0) = 1$, the equations read after Laplace transformation

$$sc_e(s) = 1 + i\gamma c_g(s), \tag{7}$$

$$sc_g(s) = i\gamma c_e(s) - \kappa c_g(s) + \kappa c_g(s)e^{-(s-i\omega_0)\tau}, \tag{8}$$

where $s$ is the complex frequency parameter of the Laplace transformation. As can be seen from Eq. (6), the solution consists of a dynamical component without the mirror-induced feedback $t \leqslant \tau$ and one with the feedback for $t > \tau$.

We now derive a solution for the photon-assisted ground state for $t \leqslant \tau$, which is the cavity-damped Jaynes-Cummings model [29]

$$c_g(s) = \frac{i\gamma}{s^2 + \gamma^2 + \kappa s} = \frac{i\gamma}{(s+\kappa/2)^2 + \gamma^2 - \kappa^2/4}. \tag{9}$$

This leads directly to the damped Jaynes-Cummings solutions in the time domain as expected for times $t \leqslant \tau$, when the cavity system is not affected by the feedback mechanism:

$$c_g(t) = i\frac{\sin[\sqrt{1-(\kappa/2\gamma)^2}\gamma t]}{\sqrt{1-(\kappa/2\gamma)^2}}e^{-\kappa/2t}. \tag{10}$$

Note that, due to the cavity damping, not only is the amplitude reduced but also the Rabi oscillation frequency is reduced by a factor of $\sqrt{1-(\kappa/2\gamma)^2}$. The cavity loss leads inevitably to an effectively reduced value for the coupling strength and as a result, the frequency of damped Rabi oscillations decreases. As we will see below, this restriction is lifted if a feedback mechanism is present.

Now we solve the dynamics for times $t > \tau$. This leads to an additional term in the denominator. By using a geometric series expansion, i.e., $(1-q)^{-1} = \sum_n q^n$ for $q < 1$ and $n \to \infty$, Eq. (9) can be written as

$$\begin{aligned} c_g(s) &= i\gamma\left(1 - \frac{\kappa s\exp[-(s-i\omega_0)\tau]}{(s+\kappa/2)^2+\gamma^2-\kappa^2/4}\right)^{-1} \\ &\quad\times [(s+\kappa/2)^2+\gamma^2-\kappa^2/4]^{-1} \\ &= i\gamma\sum_n\left(\frac{\kappa s\exp[-(s-i\omega_0)\tau]}{(s+\kappa/2)^2+\gamma^2-\kappa^2/4}\right)^n \\ &\quad\times [(s+\kappa/2)^2+\gamma^2-\kappa^2/4]^{-1}. \end{aligned} \tag{11}$$

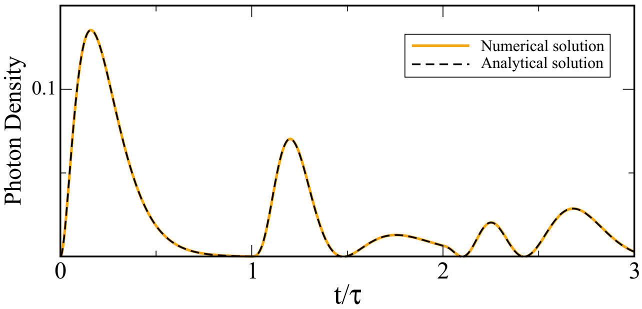

FIG. 3. (Color online) Comparison between numerical calculation and the Laplace transformed analytical solution valid until $t = 3\tau$ with $\kappa/\gamma = 2$.

Due to the linearity of the Laplace transformation, the solution in the time domain can be obtained via the method of partial fraction expansion and the convolution property. However, the expression is very lengthy and must be calculated for every time interval $[n\tau,(n+1)\tau]$, separately. Since we are interested in the weak-coupling regime, we can choose the parameter to be $\gamma = \kappa/2$ to simplify the expression into

$$c_g(s) = \frac{i\kappa/2}{(s+\kappa/2)^2}\sum_n\left(\frac{\kappa s e^{(i\omega_0 - s)\tau}}{(s+\kappa/2)^2}\right)^n. \tag{12}$$

Using now the binomial series and Laplace transformation $n!/(s-a)^{n+1} \to t^n \exp[at]$, we get an expression in the time domain

$$\begin{aligned} c_g(t) = \frac{i}{2}\sum_{n=0}^{\infty} n!2^{n+1}e^{-\kappa/2(t-n\tau)+i\omega_0 n\tau}\Theta(t-n\tau)\sum_{k=0}^{n} \\ \times\frac{(-1)^k}{k!(n-k)!}\frac{[\kappa/2(t-n\tau)]^{n+1+k}}{(n+1+k)!}. \end{aligned} \tag{13}$$

In Fig. 3 the numerical solution of Eq. (3) coupled with Eq. (6) is compared with the analytical solution (13) for the time interval $[0,3\tau]$. The excellent agreement found between these two solutions confirms the validity of our calculations. For longer times, more terms from the series expansion (13) contribute to the solution via $\Theta(t-n\tau)$, but the analytical solution become very lengthy, i.e., for $t \in [0,n\tau]$ up to $n(n-1)$ terms contribute. As the next step, we derive the long-time behavior using the residuum method.

### C. Long-time solution

The long-time dynamics of the coupled system is directly related to the singularities in the contour integral of the Laplace transformed function [30]. To demonstrate this explicitly, we need to find the singularities of the photon-assisted ground-state amplitude

$$c_g(s) = \frac{i\gamma}{s^2+\gamma^2+\kappa s - \kappa s e^{-(s-i\omega_0)\tau}}. \tag{14}$$

The singularities are found by setting the denominator to zero. We assume a pure oscillation behavior in the long-time limit, i.e., where $s$ is purely imaginary. We set $s = \pm i\gamma$ and get

$$-\gamma^2 + \gamma^2 \pm i\gamma\kappa(1 - e^{\mp i\gamma\tau}e^{i\omega_0\tau}) = 0, \tag{15}$$

from which it immediately follows that

$$e^{i(\omega_0 \mp \gamma)\tau} = 1. \tag{16}$$

We now need to find a delay time $\tau$ in a way that for $\pm i\gamma$ this equation is valid. As it turns out, the corresponding singularity condition can be matched for the following two cases:

$$\exp(i\gamma\tau) = \exp(i\omega_0\tau) = 1, \tag{17}$$

$$\exp(-i\gamma\tau) = \exp(i\omega_0\tau) = 1. \tag{18}$$

In order to satisfy these conditions we observe that we can freely choose the delay time with respect to the coupling strength by adjusting the length $L$ between the cavity and mirror accordingly. For instance, if we choose $\gamma\tau = 2\pi m$ and at the same time tune the resonance frequency such that $\omega_0\tau = 2\pi l$, where $l,m$ are integer numbers, then the conditions (17) and (18) are satisfied. [Note that there are also three other obvious constraints on $\tau$ and $\gamma$ to satisfy the conditions (17) or (18), but they are not discussed below.] As a result, we achieve a purely coherent asymptotic solution with a minimum of dephasing and a maximum amplitude, corresponding to the fact that the pole does not contain any decaying term. Indeed, we derive the following expression for the asymptotic behavior of the photon density inside the cavity:

$$\begin{aligned} c_g^{(i)}(t) &= \frac{1}{2\pi i}\oint ds\, c_g(s)e^{st} \approx \sum_{\text{poles}} \text{Res}[c_g(s)e^{st}] \\ &= \sum_{\pm} \lim_{s\to\pm i\gamma} \frac{(s \pm i\gamma)\exp(s2n\pi/\gamma)i\gamma}{(s+i\gamma)(s-i\gamma)+\kappa s[1-\exp(-s2m\pi/\gamma)]}. \end{aligned} \tag{19}$$

Using now L'Hôpital's rule and taking the limits $s \to \pm i\gamma$, the solution for $c_g(t)$ reads

$$c_g(t) = \frac{i\sin[\gamma t]}{1+\kappa m\pi/\gamma}. \tag{20}$$

In Fig. 4 the numerical solution and the analytical long-time solution is plotted for $\tau = 2\pi/\gamma$ (i.e., when $m = 1$) up to several $\tau$. The agreement is excellent with the long-time solution accurately recovering the amplitude and the oscillation frequency of the numerical solution. Interestingly, for $\kappa = 0$, we recover the Jaynes-Cummings solution as in Eq. (10) with $\kappa = 0$. In contrast to Eq. (10), we see, however, that the cavity loss does not modify the frequency of vacuum Rabi oscillations, which is now equal to the coupling strength $\gamma$, and only damps the corresponding amplitude. In this context, we discover a maximum amplitude for the feedback effect via this proposed mechanism. It is seen that Eq. (20) yields the following amplitude of the quantum-feedback-induced Rabi oscillations for $\tau = 2\pi/\gamma$: $1/(1+\kappa\pi/\gamma)^2$. Therefore, with $\kappa = 2\gamma$, the maximum amplitude is approximately 0.02, in correspondence with Fig. 4, which is 15% of the maximum photon amplitude in the first time interval $[0,\tau]$. With these results at hand, we can now also answer the questions raised above.

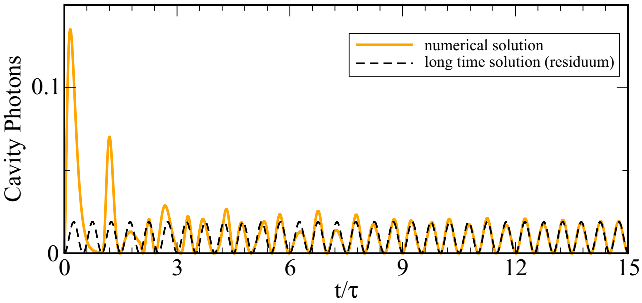

FIG. 4. (Color online) Comparison between the numerics (orange curve) and long-time solution determined by the residuum contribution only (black curve) for an initially excited TLS $c_e(0) = 1$ and $\kappa/\gamma = 2$. After several $\tau$, the analytical long-time solution and the numerics coincide. Note that the long-time solution is only valid for $t \gg 10\tau$. We plotted the solution for short times only for illustration purposes.

(i) The effect of stabilized Rabi oscillations in the long-time limit depends strongly on the chosen time delay $\tau$, which has to be chosen so as to satisfy one of the conditions (17) and (18) that lead to asymptotically undamped Rabi oscillations. Furthermore, the factor $\exp(i\omega_0\tau)$ plays a crucial role to decide whether quantum feedback leads to a stabilized Rabi oscillation or to a damped feedback situation. However, the effect depends only quantitatively (rather than qualitatively) on the cavity loss $\kappa$ and coupling strength $\gamma$, besides the obvious restriction that both of them are unequal to zero.

(ii) For a given ratio between the coupling strength and the cavity loss $x = \kappa/\gamma$, there is a maximum amplitude that is given for the above case by $(1 + x\pi)^{-2}$.

### D. Photon-path representation

To give an intuitive explanation for this effect of recovered Rabi oscillations in the weak-coupling limit, we visualize the resulting cavity dynamics in the framework of the photon-path representation [31,32]. For this purpose we rewrite the system of equations of motion (7) and (8) in the Laplace domain as

$$\begin{pmatrix} c_e(0) \\ c_g(0) \end{pmatrix} = s(1-\mathbb{L})\begin{pmatrix} c_e(s) \\ c_g(s) \end{pmatrix}, \tag{21}$$

with the scattering matrix

$$\mathbb{L} = \begin{pmatrix} 0 & i\frac{\gamma}{s} \\ i\frac{\gamma}{s} & -\frac{\kappa}{s}(e^{-\tau s}-1) \end{pmatrix}. \tag{22}$$

Due to the nonzero determinant, the matrix can be inverted and using the Neumann expansion, we get, for $||\mathbb{L}|| < 1$,

$$\begin{aligned} \begin{pmatrix} c_e(s) \\ c_g(s) \end{pmatrix} &= \frac{1}{s}\sum_{n=0}^{\infty}\mathbb{L}^n\begin{pmatrix} c_e(0) \\ c_g(0) \end{pmatrix} \\ &= \sum_{n=0}^{\infty}\left[\frac{(i\gamma)^n}{s^{n+1}}\begin{pmatrix} 0 & 1 \\ 1 & \frac{\kappa}{i\gamma}(e^{-\tau s}-1) \end{pmatrix}^n\right]\begin{pmatrix} c_e(0) \\ c_g(0) \end{pmatrix}. \end{aligned} \tag{23}$$

Now the dynamics is written in a very complicated manner but in a way that the photon path (represented by scattering processes due to $\mathbb{L}$) becomes visible. With this expansion, one can represent the dynamics as a series of single-scattering events by multiple application of the matrix, which swaps the excitation from $c_e$ to $c_g$ and includes the cavity loss and the gain from the feedback. This becomes especially apparent

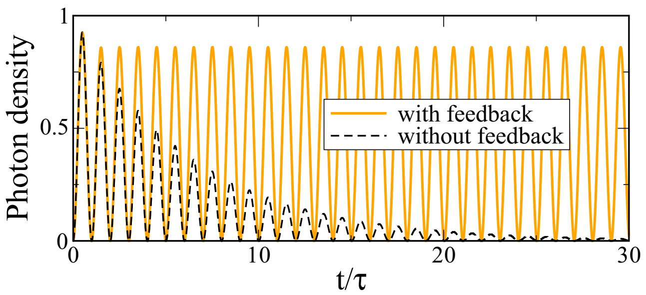

FIG. 5. (Color online) Fast stabilization of Rabi oscillations of the cavity photon number in the strong-coupling limit $\gamma = 20\kappa$ after only one round-trip $\tau$, when the feedback from the waveguide is present (orange curve). Initially, the excitation is stored in the TLS $[c_e(0) = 1]$.

when writing down the single terms of the Laplace transform and then transforming them back into the time domain. In particular, for the ground-state probability such an expansion reads (only terms up to $t^3$ are kept)

$$\begin{aligned} c_g(t) = {} & \frac{(i\gamma)}{1!} - \frac{(i\gamma)\kappa}{2!}t^2 + \frac{(i\gamma)^3}{3!}t^3 + \frac{(i\gamma)\kappa^2}{3!}t^3 + \cdots \\ & + \frac{(i\gamma)\kappa}{2!}(t-\tau)^2\theta(t-\tau) \\ & - \frac{(2i\gamma)\kappa^2}{3!}(t-\tau)^3\theta(t-\tau) + \cdots . \end{aligned} \tag{24}$$

From the structure of this expansion it follows that undamped Rabi oscillations can be viewed as a result of an interference between incoming and outgoing photonic paths provided $\tau = 2\pi/\gamma$. In other words, the strong-coupling feature is produced by a destructive interference effect of the photon paths at the point within the waveguide, where the tunneling event between the cavity and waveguide takes place. This expansion explains furthermore that it takes a minimum time for this effect to unfold, since at least two dissipatively interacting waves need to be in the waveguide.

### E. Strong-coupling limit

To complete the picture, we investigate the proposed feedback mechanism via a quasicontinuum in the strong-coupling limit. In Fig. 5 the dynamics with and without feedback is plotted for a coupling strength $\gamma = 20\kappa$. Clearly, Rabi oscillations are visible with and without feedback. If no feedback is present, however, the amplitude of the Rabi oscillations are damped fast without changing the frequency. With a feedback and a chosen delay time of $\tau = \pi/2\gamma$, on the other hand, the amplitude loss is stopped at very early times already: Already after one round-trip the amplitude stays constant for all times, if no other loss mechanism inside or between the mirror and cavity is present. We explain the acceleration of the stabilization feature by the fact that for the strong-coupling regime the incoming and outgoing photons already interfere efficiently after one round-trip. In contrast, in the weak-coupling limit the in and out tunneling does not overlap for the first three round-trips and as a consequence interference takes place at longer times only. If we choose a larger round-trip time $\tau$, also in the strong-coupling regime, a higher number of round-trips $n\tau$ is necessary to reach the point of stabilized Rabi oscillations.

## III. CONCLUSION AND OUTLOOK

We have discussed an approach to stabilize single-emitter CQED via a quantum feedback mechanism induced by an external mirror. Our analytical solution shows that depending on the chosen parameters, an intrinsic limit of the feedback effects exists. For a system initially in the weak-coupling regime (before the feedback modifies the system dynamics) we demonstrate that the quantum feedback can at most recover approximately 15% of the maximum cavity occupancy in the first time interval. Our analytic calculations demonstrate furthermore that the quantum-feedback-induced Rabi oscillations are indeed coherent and follow a typical differential delay equation with an appropriate inhomogeneity to drive the system into the strong-coupling regime. Our results extend the set of exact analytical solutions in the field of coherent atom CQED and form a starting point to establish a framework for a theoretical description of coherent quantum feedback.

## ACKNOWLEDGMENTS

We would like to thank N. Naumann and S. Hein for helpful discussions. We acknowledge support from Deutsche Forschungsgemeinschaft through SFB 910 “Control of self-organizing nonlinear systems.” D.O.K. and S.R. were supported by the Austrian Science Fund (FWF) through project No. F49-P10 (SFB NextLite). A.C. gratefully acknowledges support from Alexander von Humboldt Foundation through the Feodor-Lynen program.

---

[1] K. Hennessy, A. Badolato, M. Winger, D. Gerace, M. Atature, S. Gulde, S. Falt, E. L. Hu, and A. Imamoglu, Nature (London) **445**, 896 (2007).

[2] J. McKeever, A. Boca, A. D. Boozer, J. R. Buck, and H. Kimble, Nature (London) **425**, 268 (2003).

[3] S. Putz, D. O. Krimer, R. Amsüss, A. Valookaran, T. Nöbauer, J. Schmiedmayer, S. Rotter, and J. Majer, Nat. Phys. **10** (2014).

[4] D. O. Krimer, M. Liertzer, S. Rotter, and H. E. Türeci, Phys. Rev. A **89**, 033820 (2014).

[5] J. Fink, M. Göppl, M. Baur, R. Bianchetti, P. Leek, A. Blais, and A. Wallraff, Nature (London) **454**, 315 (2008).

[6] I. Schuster, A. Kubanek, A. Fuhrmanek, T. Puppe, P. Pinske, K. Murr, and G. Rempe, Nat. Phys. **4**, 382 (2008).

[7] A. Carmele, B. Vogell, K. Stannigel, and P. Zoller, New J. Phys. **16**, 063042 (2014).

[8] D. Chang, A. Sorenson, E. Demler, and M. Lukin, Nat. Phys. **3**, 807 (2007).

[9] M. A. Nielsen and I. L. Chuang, *Quantum Computation and Quantum Information* (Cambridge University Press, Cambridge, 2000).

[10] C. Monroe, Nature (London) **416**, 238 (2002).

[11] P. Zoller, T. Beth, D. Binosi, R. Blatt, H. Briegel *et al.*, Eur. Phys. J. D **36**, 203 (2005).

[12] X. Zhou, I. Dotsenko, B. Peaudecerf, T. Rybarczyk, C. Sayrin, S. Gleyzes, J. M. Raimond, M. Brune, and S. Haroche, Phys. Rev. Lett. **108**, 243602 (2012).

[13] H. Wiseman and G. Milburn, *Quantum Measurement and Control* (Cambridge University Press, Oxford, 2006).

[14] F. Albert, C. Hopfmann, S. Reitzenstein, C. Schneider *et al.*, Nat. Commun. **2**, 366 (2011).

[15] W. Kopylov, C. Emary, E. Schöll, and T. Brandes, New J. Phys. **17**, 013040 (2015).

[16] A. Grimsmo, A. Parkins, and B. Skagerstam, New J. Phys. **16**, 065004 (2014).

[17] P. Strasberg, G. Schaller, T. Brandes, and M. Esposito, Phys. Rev. E **88**, 062107 (2013).

[18] K. Pyragas and V. Novičenko, Phys. Rev. E **88**, 012903 (2013).

[19] S. M. Hein, F. Schulze, A. Carmele, and A. Knorr, Phys. Rev. Lett. **113**, 027401 (2014).

[20] F. Schulze, B. Lingnau, S. M. Hein, A. Carmele, E. Schöll, K. Lüdge, and A. Knorr, Phys. Rev. A **89**, 041801 (2014).

[21] A. Carmele, J. Kabuss, F. Schulze, S. Reitzenstein, and A. Knorr, Phys. Rev. Lett. **110**, 013601 (2013).

[22] P. W. Shor, Phys. Rev. A **52**, R2493 (1995).

[23] S. J. van Enk, J. I. Cirac, and P. Zoller, Phys. Rev. Lett. **79**, 5178 (1997).

[24] D. Walls and G. Milburn, *Quantum Optics* (Springer, Berlin, 2007).

[25] A. Laucht, N. Hauke, A. Neumann, T. Günthner, F. Hofbauer, A. Mohtashami, K. Müller, G. Böhm, M. Bichler, M.-C. Amann *et al.*, J. Appl. Phys. **109**, 102404 (2011).

[26] C. Berger, U. Huttner, M. Mootz, M. Kira, S. W. Koch, J.-S. Tempel, M. Aßmann, M. Bayer, A. M. Mintairov, and J. L. Merz, Phys. Rev. Lett. **113**, 093902 (2014).

[27] U. Dorner and P. Zoller, Phys. Rev. A **66**, 023816 (2002).

[28] R. J. Cook and P. W. Milonni, Phys. Rev. A **35**, 5081 (1987).

[29] C. Gardiner and P. Zoller, *Quantum Noise* (Springer, Berlin, 1991).

[30] D. O. Krimer, S. Putz, J. Majer, and S. Rotter, Phys. Rev. A **90**, 043852 (2014).

[31] G. Alber, J. Z. Bernád, M. Stobińska, L. L. Sánchez-Soto, and G. Leuchs, Phys. Rev. A **88**, 023825 (2013).

[32] C. Stampfer, S. Rotter, J. Burgdörfer, and L. Wirtz, Phys. Rev. E **72**, 036223 (2005).